Imperial College London

Department of Electrical and Electronic Engineering

Design of Wireless Power Transfer Systems in the Presence of Living Objects

Christopher Howe Kwan

October 2018

A thesis submitted for the degree of Doctor of Philosophy of Imperial College London and the Diploma of Imperial College.

Abstract

Many existing wireless power transfer (WPT) systems are designed for a free-space environment with efficiency maximisation as the primary objective. However, in the presence of living objects, the design of such systems needs to consider modifications to the magnetic link and field distributions due to the interaction between the system and biological tissue. Parameters that maximise link efficiency in air should be changed to regain optimal system operation. Furthermore, additional design constraints are required to minimise adverse health effects and meet safety requirements.

Firstly, this thesis presents an overview of the design of WPT systems in air, using link efficiency-led principles in conjunction with high-frequency soft-switching power electronics. This is followed by a summary of safety considerations applicable to WPT systems, and a simulation study to evaluate the compliance of a wirelessly-powered drone demonstrator to safety limits.

Wireless power for high-power implantable medical devices is then studied. A general link efficiency expression is derived for arbitrary tuning capacitance and receiver load. A coil model is devised, incorporating a frequency- and tissue type-dependent series resistance for losses due to a magnetic field. Varying frequency, number of coil turns, tuning method and receiver load can lead to improved link efficiency, lower tissue heating and reduced temperature rises.

Whilst WPT for high-power implantable medical devices is feasible only over short distances, the range can be extended for low-power medical implants and wearable devices. The development of a position-insensitive long-range WPT system is reported, in which an ultra-low power open-loop flyback impedance emulator maintains maximum power transfer, and transmitter power modulation using wireless feedback prevents receiver damage when moving close to the transmitter. For such systems, a method of detecting living objects in a coil's near field is found to be possible, which could be used in foreign object detection for safety purposes.

Acknowledgements

I would like to express my sincere gratitude to my supervisor Paul Mitcheson for his valuable guidance and advice throughout my PhD studies. His aptitude and passion for electrical engineering has inspired me greatly. I would also like to thank my co-supervisor Alessandro Astolfi who, along with Paul Mitcheson, introduced me to the exciting field of wireless power transfer for medical devices.

In addition, I would like to take this opportunity to thank David Yates, with whom I have beeen able to discuss various technical aspects of my work in great detail.

I wish to acknowledge former and current members of the Wireless Power Lab (Samer Aldhaher, Alwyn Elliott, James Lawson, George Kkelis, Juan Arteaga Saenz and Lingxin Lan).

I am grateful for my wife Xiaomei and my daughter Jade (who was born during the latter half of my PhD studies), both of whom have supported me throughout my journey as a research student.

I owe my parents a great debt of gratitude, for without their unconditional support, none of this would be possible.

The following sources of funding are acknowledged: The Department of Electrical and Electronic Engineering, Imperial College London provided financial support for the PhD programme. Funding is gratefully acknowledged from Her Majesty's Government for the work on the long-range inductive power transfer system and on the detection of living objects with high-frequency magnetic fields.

Declarations

I herewith certify that all material in this thesis which is not my own work has been properly acknowledged.

The copyright of this thesis rests with the author and is made available under a Creative Commons Attribution Non-Commercial No Derivatives licence. Researchers are free to copy, distribute or transmit the thesis on the condition that they attribute it, that they do not use it for commercial purposes and that they do not alter, transform or build upon it. For any reuse or redistribution, researchers must make clear to others the licence terms of this work.

Contents

List of Abbreviations **13**

List of Figures **15**

List of Tables **21**

1 Introduction **25**

1.1 Background 27

1.1.1 Inductive power transfer for low-power medical implants 27

1.1.2 Coil optimisation and system design 29

1.1.3 Wireless power for high-power medical devices 31

1.1.4 Evaluation of safety 34

1.1.5 Long range inductive power transfer 36

1.2 Research areas and thesis outline 37

2 Overview of wireless power transfer system design in air **41**

2.1 Coil characteristics and coupling 42

2.1.1 Self-inductance of a coil 42

2.1.2 Coil resistance 43

2.1.3 Coil Q factor 43

2.1.4 Mutual inductance and coupling 44

2.2 Link efficiency maximisation 44

2.3 Power electronics 47

2.3.1 Semiconductors 47

2.3.2 Inverters . . . 48
2.3.3 Rectifiers . . . 53
2.3.4 Receiver load emulation . . . 57
2.4 Example of a system in air . . . 58
2.5 Summary . . . 59

3 Human safety considerations 61
3.1 Effects of exposure on humans . . . 62
3.2 Guidelines, standards and regulations . . . 63
3.2.1 Electromagnetic field exposure . . . 63
3.2.2 Device immunity and temperature rises . . . 68
3.2.3 MRI compatibility . . . 69
3.3 The wirelessly-powered drone . . . 70
3.4 Summary . . . 75

4 Wireless power delivery for high-power implantable medical devices 77
4.1 System and link analysis . . . 78
4.1.1 Conditions for maximum link efficiency . . . 78
4.1.2 A general link efficiency expression . . . 81
4.1.3 Coil currents and voltages . . . 86
4.2 Design methods and simulations . . . 88
4.2.1 Simulation overview and configuration . . . 92
4.2.2 Frequency and coil geometry . . . 94
4.2.3 Using resonant tuning equations . . . 108
4.2.4 Magnetic field distribution . . . 109
4.2.5 Variation of receiver load . . . 113
4.3 Design trade-offs . . . 123
4.4 Summary . . . 125

5 Wireless power experiments in salt water solution 127
5.1 Coils, coating and salt water preparation . . . 128

5.2 Impedance measurements and link parameters . . . 130
5.3 Power electronics . . . 137
5.4 Thermal insulation and temperature measurement . . . 143
5.5 Results . . . 145
5.6 Simulation verification . . . 146
5.7 Summary . . . 152

6 Towards long-range powering of low-power medical implants and wearables 153

6.1 Motivation . . . 154
6.2 System specifications and simulations . . . 155
6.3 Impedance emulation . . . 161
6.3.1 Buck topology . . . 161
6.3.2 Buck-boost topology . . . 163
6.3.3 Flyback topology . . . 165
6.4 Transmitter power control . . . 170
6.5 Class E inverter board modifications . . . 171
6.6 Results . . . 173
6.7 Safety . . . 175
6.8 System comparison . . . 176
6.9 An approach to detection of living objects . . . 176
6.9.1 Theory and modelling . . . 177
6.9.2 Simulation study . . . 179
6.9.3 Experimental work . . . 184
6.10 Summary . . . 184

7 Conclusion 187

7.1 Main research outcomes . . . 188
7.2 Comparison with other work . . . 190
7.3 Publications, patents and presentations . . . 192

7.4 Future work 194

References **197**

List of Abbreviations

A4WP Alliance for Wireless Power

AC alternating current

AIMD active implantable medical device

AL action level

AM amplitude modulation

ASK amplitude-shift keyring

BPSK binary phase-shift keyring

DBPSK differential binary phase-shift keyring

DC direct current

ELV exposure limit value

EM electromagnetic

EMF electromotive force

ESR equivalent series resistance

EU European Union

FSK frequency-shift keyring

GaN gallium nitride

ICNIRP International Commission on Non-Ionizing Radiation Protection

IEEE Institute of Electrical and Electronics Engineers

IPT inductive power transfer

ISM industrial, scientific and medical

LC inductor-capacitor

Li lithium

LVAD left ventricular assist device

MOSFET metal–oxide–semiconductor field-effect transistor

PCB printed circuit board

PDMS polydimethylsiloxane

RF radio frequency

RL resistor-inductor

RMS root mean square

SAR specific absorption rate

Si silicon

SiC silicon carbide

WPT wireless power transfer

ZCS zero-current switching

ZVS zero-voltage switching

List of Figures

2.1 Block diagram of IPT system 45

2.2 Variation of coil Q factor with frequency (2-turn 50 cm diameter copper coil) 47

2.3 Semi-resonant Class E inverter from [2] 49

2.4 Simulated and measured drain-source voltage for semi-resonant Class E inverter with $V_{\text{in}} = 60\,\text{V}$ [2] 50

2.5 Class E inverter with a saturable reactor [53] 50

2.6 Class EF_2 or Class E/F_3 inverter. [56] 51

2.7 Comparison of normalised voltage and current waveforms of different inverters classes. [56] 52

2.8 A voltage-driven low dv/dt Class E rectifier [57] 53

2.9 Simulated voltage-driven Class E rectifier waveforms: [Top] Voltage across D_r; [Bottom] Current through D_r (solid) and C_r (dotted) [57] 54

2.10 Current driven Class E low dv/dt half wave rectifier [48] 55

2.11 Reverse bias voltage across diode in current driven Class E rectifier [48] . 56

2.12 Current driven Class D half wave rectifier [48] 56

2.13 Reverse bias voltage across diode in current driven Class D rectifier [48] . 57

2.14 A 6.78 MHz system designed using link efficiency-led principles 59

3.1 (Blue) Variation of magnetic field strength with distance on axis from transmitter pad in vertical direction (Drone and receiver at 150 mm); (Brown) IEEE maximum permissible exposure value; (Red) ICNIRP reference level 72

3.2 (Blue) Variation of magnetic field strength with distance in horizontal direction from outer edge of transmitter pad; (Brown) IEEE maximum permissible exposure value; (Red) ICNIRP reference level 73
3.3 SAR distribution with Nelly's head 40 cm above transmitter coil 74
3.4 SAR distribution with Nelly's head 10 cm from the transmitter coil's outer edge in the horizontal direction 75

4.1 Wireless power transfer system as two-port network with Z-parameters . 79
4.2 Equivalent circuit of reciprocal two-port network in terms of Z-parameters 80
4.3 Equivalent circuit of reciprocal two-port network in terms of Z-parameters with an attached load Z_L at the receiver end 82
4.4 Receiver coil, with 0.3 mm encapsulation shown in green 89
4.5 Position of encapsulated receiver coil in human body model (cross-section, side view) 89
4.6 Position of encapsulated receiver coil in human body model (cross-section, top view) 90
4.7 Smaller transmitter coil for short-range power transfer 90
4.8 Larger transmitter coil for longer-range power transfer 91
4.9 Variation of receiver coil Q factor with number of turns and frequency . . 96
4.10 Variation of smaller transmitter coil Q factor with number of turns and frequency 97
4.11 Variation of larger transmitter coil Q factor with number of turns and frequency 98
4.12 Link efficiency at 6.78 MHz in short-range scenario: variation with number of turns 98
4.13 Link efficiency at 13.56 MHz in short-range scenario: variation with number of turns 99
4.14 Link efficiency at 6.78 MHz in longer-range scenario: variation with number of turns 99

4.15 Link efficiency at 13.56 MHz in longer-range scenario: variation with number of turns 100
4.16 Receiver coil Q factor ($N_{RX} = 2$) 101
4.17 Smaller transmitter coil Q factor ($N_{TX} = 4$) 101
4.18 Maximum link efficiency of system with 4-turn smaller transmitter coil and 2-turn receiver coil 102
4.19 Equivalent circuit model of coil inside human body 103
4.20 Variation of coupling factor with number of turns of the transmitter coil, for the short-range scenario with $N_{RX} = 2$ 107
4.21 Variation of overall magnetic flux density, the magnetic flux density due to smaller transmitter coil and the magnetic flux density due to receiver coil with distance on axis from transmitter coil (receiver coil and human body at 2 cm). 112
4.22 Variation of overall magnetic flux density, the magnetic flux density due to larger transmitter coil and the magnetic flux density due to receiver coil with distance on axis from transmitter coil (receiver coil and human body at 30 cm). 112
4.23 Variation of overall magnetic flux density (blue), flux density due to transmitter (yellow), and flux density due to receiver coil (orange) with load resistance (at centre of receiver coil), for short-range scenario 116
4.24 Variation of overall magnetic flux density (blue), flux density due to transmitter (yellow), and flux density due to receiver coil (orange) with load resistance (at centre of receiver coil), for longer-range scenario 116
4.25 SAR distribution: maximum link efficiency (short-range scenario) 118
4.26 SAR distribution: increased load (short-range scenario) 118
4.27 Temperature distribution (°C): maximum link efficiency (short-range scenario) 119
4.28 Temperature distribution (°C): increased load (short-range scenario) . . . 120
4.29 SAR distribution: maximum link efficiency (longer-range scenario) 120

4.30 SAR distribution: increased load (longer-range scenario) 121
4.31 Temperature distribution (°C): maximum link efficiency (longer-range scenario) 122
4.32 Temperature distribution (°C): increased load (longer-range scenario) . . 122

5.1 Transmitter coil PCB 128
5.2 Receiver coil PCB 129
5.3 Equivalent circuit of reciprocal two-port network in terms of complex impedance parameters, with the receiver end shorted. 132
5.4 Current driven Class D rectifier PCB 137
5.5 Schematic diagram of receiver system 138
5.6 Simulated current-driven Class D rectifier waveforms: [Top] Input (solid) and output (dotted) voltage; [Bottom] Input (solid) and output (dotted) current 140
5.7 Schematic diagram of load independent Class EF inverter and coil 141
5.8 Simulated load-independent Class EF inverter waveforms: [Top] Switch voltage; [Bottom] Output current 142
5.9 Polystyrene foam holder insulating the salt water solution in the tank . . 143
5.10 Thermal imager capture showing thermistor probe heating up in the salt water solution 144
5.11 Scatter plot of experimental results, showing temperature rise of salt water solution with both original and increased DC load 145
5.12 Experimental setup modelled in CST Microwave Studio 147
5.13 SAR distribution with original load 148
5.14 Variation of magnetic field strength with distance on axis from transmitter, when original load is used 149
5.15 SAR distribution with increased load 149
5.16 Variation of magnetic field strength with distance on axis from transmitter, when increased load is used 150
5.17 Temperature distribution with original load 151

5.18 Temperature distribution with increased load 151
5.19 Variation of temperature with time for original (solid) and increased (dashed) load at centre of receiver coil 151

6.1 Variation of coupling factor with distance on axis from transmitter coil (from simulation) 156
6.2 Variation of link efficiency with distance on axis from transmitter coil (from simulation) 156
6.3 Semi-resonant Class E inverter from [2] 157
6.4 Voltage across MOSFET switch of Class E inverter ($V_{\text{in}} = 16.0\,\text{V}$, $I_{\text{TX}} = 27.0\,\text{A}$) 158
6.5 Equivalent circuit of parallel-tuned receiver with tuning capacitor and load 158
6.6 Variation of magnetic flux density per square root of receiver power in mW with distance on axis from transmitter (receiver at 6 m) 160
6.7 Buck converter 162
6.8 Buck-boost converter 164
6.9 Flyback converter 165
6.10 Simulated current through primary winding of flyback transformer 167
6.11 Simulated current through secondary winding of flyback transformer . . . 167
6.12 Simulated voltage across diode at secondary side of flyback transformer . 168
6.13 Variation of emulated impedance of flyback impedance emulator with input voltage 169
6.14 Variation of efficiency of flyback impedance emulator with input voltage . 169
6.15 Transmitter coil and electronics 170
6.16 Transmitter power modulation flow diagram 171
6.17 Old Class E inverter board damaged by arcing 172
6.18 Heat sink of old Class E inverter board damaged by arcing 172
6.19 New Class E inverter board 173
6.20 Receiver coil and electronics - schematic diagram 174
6.21 Receiver coil and electronics - photograph 174

6.22 Received power with distance between transmitter and receiver coil . . . 175
6.23 Simulation setup for detection of a human sized block by a transmitter coil 179
6.24 Variation of the imaginary part of the magnetic field with distance along coil central axis, with block of fat placed at distances between 2 m and 5 m 180
6.25 Variation of the imaginary part of the magnetic field with distance along coil central axis, with block of fat placed at distances between 5 m and 10 m 181
6.26 Variation of the real part of transmitter coil voltage with distance between fat block and transmitter, between 2 m and 5 m 181
6.27 Variation of the real part of transmitter coil voltage with distance between fat block and transmitter, between 5 m and 10 m 182
6.28 Variation of the real part of transmitter coil voltage with distance between polypropylene block and transmitter, between 50 cm and 10 m 183
6.29 Variation of MOSFET drain-source voltage with distance between standing person and transmitter coil (Transmitter power: 50 W) 184

List of Tables

1.1 Typical power consumption of various implantable medical devices 26

2.1 Comparison of normalised output power of different resonant inverter classes 52

3.1 ICNIRP 1998 SAR limits: general public and occupational exposure . . . 64

3.2 ICNIRP 2010 internal electric field limits: general public and occupational exposure 65

3.3 ICNIRP 2010 reference levels for non-thermal effects: general public and occupational exposure 65

3.4 ICNIRP 1998 reference levels for thermal effects: general public and occupational exposure 65

3.5 IEEE C95.1-2005 maximum permissible exposure levels: general public and occupational exposure 67

3.6 SAR limits from IEC 60601-2-33 70

3.7 Temperature limits from IEC 60601-2-33 70

3.8 Transmitter and receiver coil characteristics for the drone system at 13.56 MHz 71

3.9 Link characteristics and parameters for drone system at 13.56 MHz, over a distance of 15 cm (received power: 15 W) 72

4.1 Maximum link efficiency and turns combination for each scenario and frequency 98

4.2 Dielectric properties of several tissue types at 6.78 MHz 103

4.3 Conductivity of several tissue types at the first two ISM bands 105

4.4 Maximum link efficiency for each frequency, and receiver coil turns from 1 to 2 (in the short-range scenario, $N_{\mathrm{TX}} = 4$) 106
4.5 Maximum SAR and temperature, H-field at centre of receiver coil and power dissipation for each frequency, and N_{RX} from 1 to 2 (in the short-range scenario, $N_{\mathrm{TX}} = 4$) 106
4.6 Comparison of system parameters with optimal tuning and resonant tuning at 6.78 MHz 108
4.7 Comparison of system parameters with optimal tuning and resonant tuning at 13.56 MHz 108
4.8 Maximum SAR and temperature for each frequency and tuning type (in the short-range scenario, $N_{\mathrm{TX}} = 4$, $N_{\mathrm{RX}} = 2$) 109
4.9 High level design trade-offs (↑: increases, ↓: decreases, ⋆: decreases at 6.78 MHz and increases at 13.56 MHz, ⋈: increases at 6.78 MHz and decreases at 13.56 MHz, ‡: increases with $N_{\mathrm{RX}} = 1$ and decreases with $N_{\mathrm{RX}} = 2$, ◯: decreases with $N_{\mathrm{RX}} = 1$ and increases with $N_{\mathrm{RX}} = 2$) . . . 123

5.1 Measurements of coil resistance and inductance in air and salt water at 13.56 MHz with impedance analyser 131
5.2 Coil Q factors in air and salt water 131
5.3 Comparison of mutual impedance between system in air and in salt water 133
5.4 Coupling factor of system in air and in salt water 133
5.5 Link parameters for system in air 134
5.6 Link parameters for a system in salt water solution, using both optimal tuning and resonant tuning 134
5.7 Reflected impedance on transmitter of a system in air, a system in salt water with ‘optimal tuning’, and a system in salt water with ‘resonant tuning’ 135
5.8 Link parameters for a system in salt water solution, using real tuning . . 136
5.9 Comparison of currents and voltages for system in air and in salt water . 136

5.10 Comparison of link parameters of system with original load (using resonant tuning) and increased load (1.5 times original load) 137
5.11 Receiver system parameters 138
5.12 Simulated Class D rectifier waveform values 139
5.13 Transmitter system parameters 141
5.14 Power dissipation in coils and salt water with original load 148
5.15 Power dissipation in coils and salt water with increased load 149
5.16 Comparison of temperature rises of experiment and simulation 152

6.1 Simulated transmitter and receiver coil properties at 3 MHz 155
6.2 Components values for semi-resonant Class E inverter 157
6.3 Tuning and loading parameters for maximising link efficiency at 6 m . . . 159
6.4 Comparison of coil and link parameters 176

7.1 Comparison of other systems in literature with similar specifications for wirelessly powering an left ventricular assist device (LVAD) 191

Chapter 1

Introduction

The aim of the PhD project is to investigate the design methods for a wireless power transfer (WPT) system in the presence of living objects. The implementation of WPT systems in free-space or air has been well documented in a number of sources, in which the main design objective is to maximise link efficiency [1, 2, 3]. However, in the presence of living objects, designing a WPT system requires a consideration of the interaction between the system and biological tissue, which can affect the magnetic link and modify the field distributions. In contrast to air or vacuum, biological tissue is electrically conductive, which enables the high frequency magnetic fields used by WPT systems to generate eddy currents inside the tissue. Consequently, parameters that maximised link efficiency in air need to be changed to regain optimal system operation. In addition, additional design constraints need to be imposed on a system, in order to minimise adverse thermal (energy absorption in biological tissue) and non-thermal (stimulation of nervous system) health effects and meet safety requirements.

These design methods are especially necessary for designing WPT systems with a power receiver coil located inside the body of a patient, in order to deliver power to an implantable medical device. The feasibility of such a transcutaneous energy transfer system for supplying energy to a mechanical circulatory support device such as a LVAD is the main focus of this thesis. The objectives are then to analyse, design and simulate a WPT system for LVADs. The work contributes towards enabling the wireless powering

of the medical devices inside the body with a power transmitter external to the patient.

A significant issue with existing heart pumps (including both LVADs and total artificial hearts) is that the physical drive-line used to power the device punctures the skin, potentially leaving it exposed to infection and contamination. In addition, due to the presence of an open wound, the patient's mobility is severely restricted. The research into wireless power delivery for high-power medical implants will improve the lives of patients who need to have an artificial organ or a medical implant fitted. Inductive power transfer (IPT) through the skin can significantly decrease the risk of infection, if such a system can be small enough to be implanted into the body and still operate reliably and safely. Another advantage of incorporating this technology into medical implants is that the patients would be able to experience a greater freedom to move around.

Table 1.1 shows the typical power consumption of various implantable medical devices [4, 5, 6, 7]. Whilst wireless power delivery for high-power implantable medical devices ($> 5\,\mathrm{W}$) is feasible only over short distances (a few cm), low-power implants ($< 100\,\mathrm{mW}$) can be powered wirelessly over greater distances ($0.5\,\mathrm{m}$ to $6\,\mathrm{m}$). Therefore, this thesis also reports the development of a long-range IPT system for remotely powering a network of sensors (e.g. situated within a room) reliably as the distance between the transmitter and the receiver varies. Such a system can also be used to charge the batteries of or supply power to small low-power medical implants inside a patient or to wearable devices on the clothing worn by a person. Due to the low power and energy requirements of these types of devices (in contrast to an LVAD), the range of power transfer can be extended to beyond a coil diameter that is typical of mid-range higher power applications. This is because the operation of such a system can still be feasible despite a significant reduction in link efficiency at large distances.

Device	Power
Pacemaker and ICDs	$10\,\mu\mathrm{W}$ to $1\,\mathrm{mW}$
Retinal prosthesis	$45\,\mathrm{mW}$
Left ventricular assist device	$5\,\mathrm{W}$ to $25\,\mathrm{W}$

Table 1.1: Typical power consumption of various implantable medical devices

In addition, for long-range IPT systems, the coil's near field region could be used to

detect living objects, which could be used in foreign object detection for safety purposes. This method, which uses high-frequency magnetic fields, will also be of great use in emergency and disaster response scenarios, in which an accurate means of locating trapped persons underneath collapsed buildings following an earthquake or explosion are desired. The use of this new approach together with convention methods can speed up the process of identifying the location of human beings, which means that more lives can potentially be saved whenever disasters occur.

1.1 Background

1.1.1 Inductive power transfer for low-power medical implants

There are many examples of inductive links being used in various types of low-power implanted devices. In [8], a 5-turn 3.5 cm diameter PCB coil was used as a receiver for an inductive link designed for implantable medical devices. It operated over a range of 1.5 cm, using a frequency of 10 MHz. Data was also sent via the same link using binary phase-shift keyring (BPSK) modulation, at a data rate of 1.12 Mbps. The receiver electronics consumed 610 µW.

In [9], an implantable stimulator-telemeter for the control of paralysed muscles was developed, which used a frequency of 6.78 MHz to transfer up to 120 mW of power over a distance of 2.5 cm. Data was transferred over the same link using the load shift keyring-circuit configuration modulation technique.

In [10], a intravascular blood pressure sensor utilised a 27 MHz inductive link to transfer both power (2 mW received power with a 5 cm single loop) and data (1 kBd) over a distance of 9 cm. The data modulation employed was pulse-position-modulated amplitude modulation (AM).

Visual neuroprosthesis can also benefit from wireless power and data transfer using an inductive link. An example is given in [11], which describes a cortex simulation system. The sensor consumed 50 mW of power and the range of transfer was 1 cm to 2 cm. The forward link carried both power and data; it had a data rate of 1 Mbps with frequency-

shift keyring (FSK) modulation and used a frequency of 10.333 MHz. The reverse link used differential binary phase-shift keyring (DBPSK) modulation with a data rate of 156.25 kbps and a carrier frequency of 5 MHz. The receiver consisted of a Litz wire planar coil, with a 3 cm diameter neodymium magnet inside the coil. The overall efficiency was 28 %.

A retinal prosthesis system has been developed in [12], which consisted of an intraocular unit that receives both power and data from the extraocular unit. It used a frequency of between 1 MHz and 10 MHz to deliver 5 mW of power and data at a rate of 25 kbps to 250 kbps. The same link was used for power and the data received by the intraoculuar unit. The data was sent using pulse width modulation and amplitude-shift keyring (ASK).

Inductive links have also been used in neural recording systems, as illustrated in [13]. The receiver in their system consisted of 120 turns, and had a diameter of 4.7 mm and a height of 2.5 mm. The electronics in the receiver side consumed 90 mW. The operating frequency was 2 MHz and the link range was 5 mm. The data modulation scheme used was AM and the data was encoded using a pulse-width modulation technique with a resulting data rate of 125 kbps.

A millimetre-sized neural recording tag uses a 1 mm^3 implantable loop antenna at 400 MHz to transfer up to 90 mW over a distance of up to 30 mm. The authors performed simulations to determined whether limits on tissue heating (specific absorption rate (SAR)) have been met by the transmit antenna.

In [14], an implanted microsystem for neural stimulation and recording operating at a carrier frequency of 4 MHz had a receiver power of up to 3.6 mW and a data transfer rate of 60 kbps with the use of ASK. The distance between the transmitter and receiver was 8 mm.

From these examples, it can be observed that many of the systems had both power and data transferred over the same magnetic link. Reverse telemetry was also employed to allow bidirectional data communication, and many systems used load modulation techniques to achieve this. However, these implanted devices had low received power,

and power was transferred over short distances of up to a few centimetres. Also, most of the research focused on reducing the power consumption of the implant electronics (such as the sensors and data processing circuitry).

The approach that this thesis will take is significantly different to those in the aforementioned examples. Instead of focussing on minimising the power consumption of the implant electronics, the design goal of the research work is to maximise the link efficiency of the system. This can be done by optimising the magnetic link such as selecting the optimal frequency and coil geometry to achieve the maximum coil Q factors and coupling factor for a certain distance and constraints on coil dimensions. For a short-range system designed to supply power to an LVAD with a power consumption of up to 15 W, the desired range is 2 cm, the maximum dimension of the implanted receiver coil is 5 cm, and the maximum dimension of the transmitter coil is 10 cm. In general, larger coils lead to higher coupling and link efficiencies. However, the coils also have to be designed with patient comfort in mind, so there are restrictions on their size. There are also additional design constraints to ensure that the WPT system is safe. After optimising the coils and magnetic link, the end-to-end efficiency can then be maximised by designing and implementing power electronics that are able to operate efficiently and reliably at the chosen frequency.

1.1.2 Coil optimisation and system design

In order to improve the link efficiency of a WPT system with an implanted receiver, it is essential that the receiver coil is optimised in order to maximise the Q factor. Therefore, accurate models of coils in the human body are required in order to predict the performance of the resulting system. In addition, the main constraint on the receiver coil geometry is usually the outer dimension as the coil is intended to be implanted under the skin or deeper inside the body.

Optimising printed spiral coils was demonstrated in [15], where an iterative design procedure was followed to obtain values of the fill factor and trace width of both the transmitter coil and the receiver coil, and of the size of the transmitter coil, in order to

maximise the link efficiency. The modelling, simulation and measurement of the coils were performed in air at frequencies of 1 MHz and 5 MHz and did not take into account human body effects.

In [16], the processes of modelling and optimisation of printed spiral coils for a 1 cm × 1 cm implant were undertaken in the presence of a muscle tissue environment. Power was transferred over a distance of 1 cm and at a frequency of 13.56 MHz. In addition to the design process described in their earlier work [15], the thickness of the biocompatible coating (ceramic, parylene or medical-grade silicone) was also optimised. The revised coil model contains an additional parasitic capacitance to account for the high relative permittivity of the tissue material, and a parallel resistance due to dielectric losses in the tissue. However, there is no series resistance representing the eddy current losses in the tissue due to the magnetic field.

In [17], it was observed that the Q factor of an implanted receiver coil tended to decrease with the number of turns due to losses in the biological tissue; hence, the link efficiency of the overall system would be maximised with a receiver coil having few turns.

The analysis and optimisation process for a 4-coil system for biomedical implants is given in [18]. The coils were made from several layers of multi-stranded Litz wire, instead of being printed on a printed circuit board (PCB). The design parameters included the number of strands of Litz wire in a bunch and the number of turns per layer. The authors also studied the variation of Q factor and link efficiency with frequency and distance. Their receiver consisted of a 22 mm implanted coil, which was used in their prototype system, operating at 700 kHz with an efficiency of greater than 80 % over a range of 10 mm to 20 mm.

Expressions for the maximum power transfer efficiency of a near-field coupled power-transfer system and the required tuning capacitance and receiver load to achieve it have been derived in [19]. These expressions differ from the maximal link efficiency equations in [1], due to the presence of conductive media such as human tissue. In terms of the two-port z-parameters of the system, it means that the real part of the mutual impedance Z_{21} is non-zero in the presence of living objects.

The effect of the variation of receiver loading, frequency, number of turns of receiver coil and the transmitter coil radius on various system performance parameters and tissue losses was covered in [20], in which the design method for the delivery of power to millimetre-sized biomedical implants was described.

The above-mentioned examples examined the various aspects of coil and system design that influence overall link efficiency. In this thesis, a holistic design method that enables accurate analysis and optimal design of a WPT system with an implanted receiver coil will be devised, by combining together the results and findings found in the literature:

- Inclusion of tissue environment and biocompatible coating/encapsulation.
- Equivalent circuit modelling of receiver coil in human tissue environment which includes the effects of coil ohmic losses, dielectric losses, eddy current losses, and increased parasitic capacitance.
- Use of expressions for maximum link efficiency, tuning capacitance and optimal load for WPT systems in conductive media.
- Optimisation of coil geometry (size, number of turns, trace width, turn spacing) to improve Q factor and maximum link efficiency.
- Optimisation of frequency to maximise link efficiency.
- Variation of the receiver load to reduce tissue heating.

1.1.3 Wireless power for high-power medical devices

In review papers that cover the current status and future trends of left ventricular assist devices [21] and total artificial hearts [22], the incorporation of wireless power transfer technology is particularly desired as it leads to the removal of the driveline incision which has been a site of infections. The successful application of IPT to such devices would result in a fully implantable mechanical circulatory support device. Such heart blood pumps require higher levels of power than implants that perform sensing or stimulation functions, as these devices contain motors that pump blood around the body. For example, the

Thoratec HeartMate II LVAD requires a nominal power of 14 W [23]. Also, in order to allow patients greater mobility, the range of operation needs to be extended to beyond the few centimetres that low power medical implants offer. For example, the transmitter coil could be placed under a mattress or behind a chair; the distances required in this scenario would be around 30 cm to 50 cm.

The review papers in [24, 25], presented a history of and the need for the use of transcutaneous energy transmission in mechanical circulatory support devices and an overview of how such technology works. In addition, they outlined the current state-of-the-art and described future trends towards a fully implantable device and their associated challenges with regards to tissue heating, energy storage and the overall size of the system. Whilst the incorporation of wireless power transfer has been trialled in several commercial LVADs (Arrow LionHeart and AbioCor TAH), the challenges of high temperatures and tissue heating were encountered especially under misaligned conditions and increased distances where there is reduced efficiency [26]. In [24], it was identified that power-transfer efficiency improvements are important as energy loss generates heat in the system, which can damage the surrounding tissues.

LVADs have been considered as a potential application of IPT by several research groups. In [5, 26, 27], a 7.65 MHz system was designed to power a HeartMate II (running at a speed equivalent to a required power of 8 W) over a distance of 1 m between the transmitter and receiver. Their system contained 5 coils: two coils at the transmitter side, two coils at the receiver side (one implanted in the body with a 9.5 cm diameter and one worn on a jacket or a vest), and a relay coil to extend the range of operation and coverage within a house (there could be several of these relay coils within a house) [5]. The system efficiency was between 40 % and 50 %. Their work also considered tissue heating effects of such systems and the applicable electromagnetic (EM) safety limits [5, 27], but their simulations studies only involved the transmitter coil and the human body model.

There are some IPT systems for LVADs that use frequencies in the 100 kHz range, but operate over very short distances (only across the tissue/ skin barrier). In [28], 15 W was received with an efficiency of 82 % over a separation distance of 20 mm. The operating

frequency was 178 kHz, the receiver coil diameter was 50 mm and the coil thickness was 5 mm. In vivo experiments were conducted, in which the receiver coil was implanted in sheep. Temperature rises were recorded: there was an increase of 3.4 °C on the coil surface and a rise of 0.8 °C 20 mm from the coil. The losses and temperature rises for the system were studied in [29]. They identified the main causes of heating as the conduction losses (including skin and proximity effect) in the coils, and conduction and switching losses in the power electronics (inverter and rectifier) and other circuit components (e.g. tuning capacitors). They did not consider the heating as a result of the interaction between the high-frequency electromagnetic field and the electrically conductive tissue, even though they operated at a frequency above 100 kHz.

Another system [30] used an inductive link frequency of 163 kHz to send 25 W to a receiver 5 mm away from the transmitter. The receiver coil diameter was 53 mm and consisted of 12 turns of Litz wire around a ferrite core. The efficiency of the system in air was 87.3 %, and a rise of temperature of 9.1 °C was recorded on the ferrite core. It was acknowledged that the temperature rise of the receiver when implanted in the body might be lower due to the cooling action of blood flow.

In [31], a four-coil WPT system for a ventricular assist device was developed and implemented, with a frequency of operation of 8 MHz. Both the transmitter coil and receiver coil were made from Litz wire. The receiver had a diameter of less than 60 mm and thickness of less than 1.6 mm. The transmitter, having a diameter of 200 mm, was designed to be embedded in a shirt. It was therefore made flexible to allow for deformation due to human movement; a deformation could lead to a change in coupling and self inductance of the coil. The authors analysed the change in link efficiency at different levels of deformation, and found that with maximum deformation the efficiency dropped by 10 %. The overall efficiency at without any deformation was greater than 75 % at distances of less than 60 mm.

These examples are show different approaches to powering high-power implantable medical devices, each with its own advantages and disadvantages. In this thesis, the design approach for a WPT system for high-power medical implants will have the following

characteristics:

- The system will use a higher frequency in the multi-MHz range, preferably in the industrial, scientific and medical (ISM) band (6.78 MHz or 13.56 MHz). At these frequencies, there is no need to use expensive Litz wire to achieve higher coil Q factors; PCB coils with a few number of turns could be used instead. At higher frequencies, the power electronics can be miniaturised as well due to the use of smaller components. Since the coil Q factors and link efficiency of the system are greater at higher frequencies, there is no need to use ferrite cores to enhance the coupling factor.

- Two coils will be used in the system: the implanted receiver coil and an external transmitter coil (either vest worn or placed under a mattress or behind a chair). Some systems use a four-coil system, with the transmitter and receiver end each having a pair of coils. This is done for impedance matching purposes, but can be avoided with properly designed power electronics. A two-coil system is less complex as it has fewer coils, and analysis in [32] shows that the two-coil and four-coil systems have identical performance characteristics.

- The design and analysis process will use 3D EM and thermal simulations with accurate human body models to ensure that the system is safe. The simulations will include the full system, and not just the transmitter coil and human body model.

1.1.4 Evaluation of safety

An early study on how the power absorbed in a human body varies with the frequency of the EM field to which the body was exposed was presented in [33], where a person was modelled as a homogeneous sphere. The material of the sphere was assumed to be muscle with a total mass of 70 kg; hence, the sphere had an effective radius of 25.57 cm. The person was exposed to a plane wave field with an incident power of $1\,\mathrm{mW\,cm^{-2}}$, and it was found that power absorbed increased with approximately the square of frequency

up to 20 MHz.

With increases in computing power and advances in simulation technology, it is possible to perform 3D full-wave EM field simulations with realistic heterogeneous human body models to evaluate the safety of a system. The method of simulating tissue heating and calculating SAR is presented in [34]. In summary, a finite-difference time domain simulation of a human male voxel model exposed to a plane wave was performed, and the resulting SAR in the body was calculated over a range of frequencies. SAR is difficult to measure since it is internal to the body; the paper also mentioned the external field values (also known as reference levels) that could be used to show compliance with the SAR limits. In addition to tissue heating, there are non-thermal effects of human exposure to EM fields that involve the stimulation of muscles, nerves and sensory organs. In [35] a female human body voxel model was used in simulations to determine the induced current densities and internal electric fields when exposed to an external uniform field.

There are many different safety guidelines, standards and regulations that apply to WPT systems in the presence of living objects. In [36, 37], the standards and guidelines that apply to WPT systems for implantable medical devices were identified, including SAR, device surface temperature rises and device immunity to EM fields. The authors in [36] performed simulations of a system to evaluate its safety at two operating frequencies, 650 kHz and 13.56 MHz. They studied the distribution of the magnetic fields, electric fields and SAR, and compared the simulation results with the limits. However, they did not perform thermal simulations of the system to evaluate compliance with temperature rise limits, which will be detailed in Chapter 3.

An example of calculating SAR of a strongly coupled 4-coil WPT system for implantable biomedical devices using EM field simulations is given in [38]. The system split into two resonant modes, such that link efficiency had local minima at two different frequencies. It was found that operating at the higher frequency mode, where the resonator magnetic fields are out-of-phase, resulted in higher SAR.

In [39], the authors evaluated the SAR levels arising from the exposure of a human body to a WPT system, by performing simulations with various high resolution voxel

human body models. They considered the transmitter-generated magnetic field, but did not include the implanted receiver in their simulations, which would have generated its own magnetic field. In addition, the authors performed experiments on a phantom, in which the electric field strength of the tissue-simulating dielectric material was measured when exposed a magnetic field generated by the transmitter coil current 1 cm away. The measurements were then compared with an EM field simulation of the experimental setup with the phantom and transmitter coil, where it was found that a current of 0.44 A (which is of the same order of magnitude as that used in the simulations with human body models) was required to reach a SAR value of $2\,\mathrm{W\,kg^{-1}}$.

1.1.5 Long range inductive power transfer

Far-field approaches to transferring power with EM fields over long distances (up to 10 m) suffer from many drawbacks that limit their potential to remotely power a network of sensors. Methods with dedicated transmitters that radiate power are generally quite inefficient. Employing antennas with narrow beam patterns can result in improvements in efficiency as the receivers are able to intercept a larger amount of the radiated energy. An example of these types of systems can be found in [40], where hundreds of µW could be transmitted over a distance of 1 m. However, the directivity of the antennas means that the freedom of movement of such receivers is severely restricted.

Ambient radio frequency (RF) energy harvesters are another candidate for far-field energy transfer; these do not require a separate transmitter as the energy is derived from mobile base stations, making them especially advantageous in urban environments. However, received power levels are limited to tens of µW as demonstrated in [41] with cm-scale antennas for harvesting energy from the following frequency bands: DTV (470 MHz to 610 MHz), GSM900 (880 MHz to 915 MHz and 925 MHz to 960 MHz), GSM1800 (1710 MHz to 1785 MHz and 1805 MHz to 1880 MHz) and 3G (1920 MHz to 1980 MHz and 2110 MHz to 2170 MHz).

IPT systems, which operate in the near field, are a particularly attractive alternative to existing far-field techniques for transferring power with EM fields over long distances

(up to 10 m). In a previous system [42], it was shown that more than 10 mW could be transferred to a load up to 6 m from the transmitter using near-field IPT.

1.2 Research areas and thesis outline

Chapter 1 introduced the aims, motivations and scope of the PhD research. It also presented a review of background material and literature regarding the topics to be discussed in this thesis.

In Chapter 2, an overview of the design methods for an IPT system in air or free-space is detailed, where the goal is to maximise link efficiency by varying the frequency, and the efficient soft-switching high-power electronics are then designed around the chosen frequency. This is in stark contrast to traditional methods of design, where frequency of operation is restricted to those that permit the feasible and efficient operation of hard-switching power converter topologies. However, the link efficiency of a system may be nowhere near its potential maximum at such low frequencies, unless heavy ferrite cores are used to shape the magnetic fields in order to increase coupling.

The aim of Chapter 3 is to introduce the adverse health effects of human body exposure to the high-frequency magnetic field employed by WPT systems, which are broadly categorised into non-thermal and thermal types. It also describes the various guidelines, standards and regulations that are applicable to WPT systems in the presence of humans and other living objects. Understanding these safety restrictions and limits is important as they can greatly influence the design parameters and constraints of WPT systems at different frequencies. With a wirelessly-powered drone as an example, numerical simulations are presented to illustrate how compliance with the guidelines can be evaluated. These simulations, when used with human body models, are useful for investigating the potential effects of a WPT system, in terms of tissue heating, temperature rises and stimulation of the nervous system.

Chapter 4 details the process of designing a WPT system for high-power implantable medical devices, namely LVADs and artificial hearts. Several analysis tools are developed,

including a general link efficiency expression for an arbitrary tuning capacitance and receiver load given a set of two-port Z-parameters, an equivalent model of an implanted coil which incorporates an additional series frequency- and tissue type-dependent resistance representing the eddy current losses in the body, and the mathematical relationship between the receiver load and the overall magnetic field inside the human body. Parameters such as frequency, tuning method, coil geometry and receiver load are varied to determine their effect on system performance (i.e. link efficiency) and safety (internal electric field, tissue heating and temperature rises). Reductions in tissue heating and temperature rises can be achieved by selecting the combination of frequency and coil turns that balances tissue losses (due to EM field energy absorption) with coil dissipation. A method of reducing temperature rises and SAR is presented, which involves setting the receiver load away from its optimal value to reduce both eddy current losses and coil dissipation. Electromagnetic and thermal simulations are performed both as a design and optimisation tool and as a means of evaluating safety and compliance with regulations and guidelines.

Chapter 5 describes experimental work in salt water solution which validates the theory that increasing the receiver load can result in lower temperature rises, by reducing eddy current losses in the conductive medium and receiver coil dissipation (as described in Chapter 4).

Chapter 6 presents work towards a long range method of reliably powering low-power medical implants, wearable devices and sensor networks. An ultra-low power open-loop flyback impedance emulator is designed to maintain maximum power transfer despite being relatively far from the transmitter coil. A method of transmitter power modulation using wireless data feedback is implemented to prevent receiver damage when moving close to the transmitter. Furthermore, an approach to detecting living objects using WPT technology and high-frequency magnetic fields is introduced, with experiments using the existing coil in this chapter to illustrate the concept. This approach is based on the fact that the interaction of a high-frequency magnetic field with conductive biological tissue generates an additional magnetic field, which induces a detectable voltage in the coil. The amplitude and phase response of the additional magnetic field and voltage

can provide information regarding the distance and material composition of the object of interest.

In Chapter 7, conclusions of the thesis are given and the main research outcomes and findings are summarised. Recommendations for future work are described, and a list of publications and presentations is provided.

Chapter 2

Overview of wireless power transfer system design in air

Before methods of designing wireless power transfer (WPT) systems in the presence of living objects are discussed, it is important to review the design principles for WPT systems in free space or air. These systems tend to be weakly coupled and utilise receiver resonance to achieve maximum link efficiency for a particular frequency. Traditionally, systems have been limited to using frequencies in the 100s of kHz range as the associated power electronics have not been able to operate efficiently at higher frequencies due to excessive switching losses. However, significant improvements to link efficiency can usually be achieved by increasing the frequency of operation to the multi-MHz range.

Fortunately, recent improvements in power electronics (inverters and rectifiers) mean that they can now operate at higher frequencies efficiently using soft-switching techniques and state-of-the-art semiconductor devices. Therefore, by increasing the frequency of operation to the multi-MHz range, improvements to link efficiency can be achieved without compromising the overall end-to-end system efficiency significantly.

The WPT systems described in this thesis make use of air-core coils. Coils with ferrite cores can be heavy and thus not very portable. In addition, their directed magnetic flux leads to a restricted freedom of movement for both the transmitter and receiver sides due to the need for accurate coil alignment. Therefore, there are many situations in which

air-core coils, with their wide flux coverage, are more suitable for WPT applications.

This chapter presents an overview of design principles for an inductive power transfer (IPT) system in air. Firstly, it reviews some expressions of the properties of a coil and of mutual coupling between two coils. It then outlines how secondary resonance, the use of an optimal load, and optimal frequency selection are required to achieve maximum link efficiency. Several types of high-frequency power electronics, including inverters and rectifiers, are described which are able to run efficiently at the chosen operating frequency. Lastly, through using the design methods described in this chapter, an 6.78 MHz industrial, scientific and medical (ISM)-band IPT was implemented, and the results are presented at the end of this chapter.

2.1 Coil characteristics and coupling

2.1.1 Self-inductance of a coil

Equation (2.1) gives the external inductance of a multi-turn helical coil, whose height is small compared to its radius [43]:

$$L = N^2 R \mu_0 \left[\ln\left(\frac{8R}{a}\right) - 2 \right] \tag{2.1}$$

where a is the conductor radius, N is the number of turns, R is the coil radius, and μ_0 is the permeability of free space. The formula is accurate for coils with $a << R$. It can be seen that the inductance increases with the square of the number of turns.

In [44], the inductance of the flat circular spiral coil is approximated by:

$$L = \frac{a^2 n^2}{203200a + 279400c} \tag{2.2}$$

where n is the number of turns, a is the average coil radius and c is the difference between the outer and inner coil radius. The formula is accurate to within 5 % for coils with $c > 0.2a$.

Additional formulae for flat spiral coil inductances can be found in [45].

2.1.2 Coil resistance

The frequency-dependent series loss resistance of a multi-turn helical coil is given in [44]. It involves multiplying the direct current (DC) resistance of the coil by a factor in order to obtain an alternating current (AC) resistance, which takes into account both the skin effect and proximity effect of a coil. The AC-to-DC resistance ratio is:

$$\frac{\text{AC resistance}}{\text{DC resistance}} = H + u\left(\frac{d_0}{c}\right)^2 G \tag{2.3}$$

where H is the resistance ratio of isolated wire, G is a proximity effect factor, u is a constant based on the number of turns and d_0/c is the ratio of wire diameter to spacing between centres of adjacent turns. The values of H, G, and u can be found in lookup tables in [44]. The formula is for helical coils whose height is small compared with its radius, and with a few turns that are not too closely spaced ($\frac{d_0}{c} \leq 0.6$).

The radiation resistance R_{rad} of a multi-turn circular coil is given by [46]:

$$R_{\text{rad}} = N^2 \eta \frac{\pi}{6} \left(k^2 a^2\right)^2 \tag{2.4}$$

where η is the impedance of free space, N is the number of turns, k is the wavenumber and is equal to $\frac{2\pi}{\lambda}$ where λ is the wavelength, and a is the coil radius. Radiation resistance represents the energy radiated from the coil [44].

The sum of the loss resistance (dissipation in the coil which heats it up) and the radiation resistance gives the total combined series resistance of a coil.

2.1.3 Coil Q factor

The Q factor of a coil is:

$$Q = \frac{\omega L}{R} \tag{2.5}$$

where L is the inductance of the coil, R is the total resistance of the coil, and ω is the frequency of operation multiplied by 2π.

2.1.4 Mutual inductance and coupling

One way of calculating the mutual impedance between two coils is given in Equation (2.6), which is derived from dividing the magnetic flux linkage at the receiver coil by the current generated in the transmitter coil [43]:

$$M = \frac{\mu_0 \pi N_{TX} N_{RX} a_{TX}^2 a_{RX}^2}{2\left(d^2 + a_{TX}^2\right)^{\frac{3}{2}}} \tag{2.6}$$

where μ_0 is the permeability of free space, N_{TX} is the number of turns of the transmitter coil, N_{RX} is the number of turns of the receiver coil, a_{TX} is the transmitter coil radius, a_{RX} is the receiver coil radius, and d is the distance between the transmitter coil and the receiver coil. However, it assumes that the receiver is small enough compared with the coil separation distance, such that the magnetic field over the receiver coil is constant.

The coupling factor of a pair of coils is calculated by using Equation (2.7):

$$k = \frac{M}{\sqrt{L_{\mathrm{TX}} L_{\mathrm{RX}}}} \tag{2.7}$$

where L_{TX} is the inductance of the transmitter coil and L_{RX} is the inductance of the receiver coil. Although changing the number of turns of a helical coil changes the mutual inductance and the self-inductances of the coils, there is no significant overall effect on the coupling factor, as the coil turns cancel out in the expression for coupling factor.

Mutual inductance can be calculated more accurately from the use of magnetic vector potentials, as demonstrated by [43, 47].

2.2 Link efficiency maximisation

IPT involves the transfer of power between a transmitter coil and a receiver coil using a high frequency magnetic field. A block diagram of an IPT system is shown in Figure 2.1. The inverter converts the DC input into an AC current in order to drive the transmitter coil. The alternating magnetic field generated by the current in the transmitter coil passes through the receiver coil which induces an electromotive force (EMF) within the

coil. Attached to the receiver coil is a rectifier, which converts the AC voltage of the coil to a DC output. A load emulation circuit (which may take the form of a DC-to-DC converter) presents the rectifier and the receiver coil with the optimal load in order to maintain maximum link efficiency, even as coupling factor or loading changes. Lastly, at the output of the load emulator is the actual DC load, which can also be energy storage such as a battery.

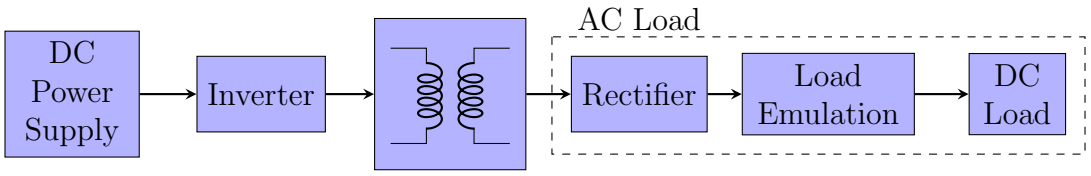


Figure 2.1: Block diagram of IPT system

With the coils acting as a weakly-coupled air-core transformer, efficiency can deteriorate rapidly with distance. To maximise link efficiency, receiver resonance should be used to cancel the secondary leakage inductance, and the optimal load should be presented to the receiver's resonant tank.

For a series tuned secondary, receiver resonance can be achieved by attaching a tuning capacitance in series with the receiver coil inductance such as to cancel the impedance of the receiver coil inductance [1]:

$$C_{\text{tune,ser}} = \frac{1}{\omega^2 L_{\text{RX}}} \tag{2.8}$$

For a parallel tuned secondary, the tuning capacitance in parallel with the secondary coil for achieving resonance is given by [1]:

$$C_{\text{tune,par}} = \frac{1}{\omega^2 L_{\text{RX}}} \frac{\alpha_{\text{opt,par}}^2}{\alpha_{\text{opt,par}}^2 + 1} \tag{2.9}$$

where

$$\alpha_{\text{opt,par}} = \frac{Q_{\text{RX}}}{\sqrt{1 + k^2 Q_{\text{TX}} Q_{\text{RX}}}} \tag{2.10}$$

where Q_{TX} is the Q factor of the transmitter coil, and Q_{RX} is the Q factor of the receiver coil.

The optimal load for a series resonant secondary is given by Equation (2.11) [48]. For a parallel resonant secondary, the optimal load is given by Equation (2.12) [1].

$$R_{\text{opt,ser}} = \omega L_{\text{RX}} \left(\frac{\sqrt{1 + k^2 Q_{\text{TX}} Q_{\text{RX}}}}{Q_{\text{RX}}} \right) \tag{2.11}$$

$$R_{\text{opt,par}} = \frac{1}{\omega C_{\text{tune,par}}} \left(\frac{Q_{\text{RX}}}{\sqrt{1 + k^2 Q_{\text{TX}} Q_{\text{RX}}}} \right) \tag{2.12}$$

As a result of using either form of secondary tank resonance, the maximum link efficiency can be evaluated using Equation (2.13) [1]:

$$\eta_{\text{link}} = \frac{k^2 Q_{\text{TX}} Q_{\text{RX}}}{\left(1 + \sqrt{1 + k^2 Q_{\text{TX}} Q_{\text{RX}}}\right)^2} \tag{2.13}$$

From Equation (2.13), it can be seen that the key to improving link efficiency is by increasing the product $k^2 Q_{\text{TX}} Q_{\text{RX}}$. Coupling is weak with air-core coils, and if the coupling factor is assumed to remain constant (i.e. with fixed separation distance and coil geometries), the link efficiency can be maximised by choosing an operating frequency that maximises the product of the Q factors of the coils. Figure 2.2 illustrates the relationship between the Q factor and the frequency of a 2-turn 50 cm diameter copper coil. Increasing the frequency of operation of the IPT system leads to a rise in Q factor, but only up to a certain point (10 MHz in this example) after which the coil's far-field radiation starts to dominate, causing the Q factor to drop [49]. This is because the loss resistance increases with the square root of frequency, whilst the radiation resistance increases with the fourth power of frequency [2]. If the transmitter and the receiver coils are identical ($Q_{\text{TX}} = Q_{\text{RX}}$) then the operating frequency is selected to maximise the Q factor of the coils. If the coils are not identical, then the optimal frequency will be dominated by that which maximises the Q factor of the larger coil (the one with the lower optimal frequency) [2], because radiation resistance rises much more quickly than loss resistance does with frequency.

The advantages of air-core coils can also be seen in longer range applications (up to 10 m between transmitter and receiver coils) where a network of sensors with milliwatt-

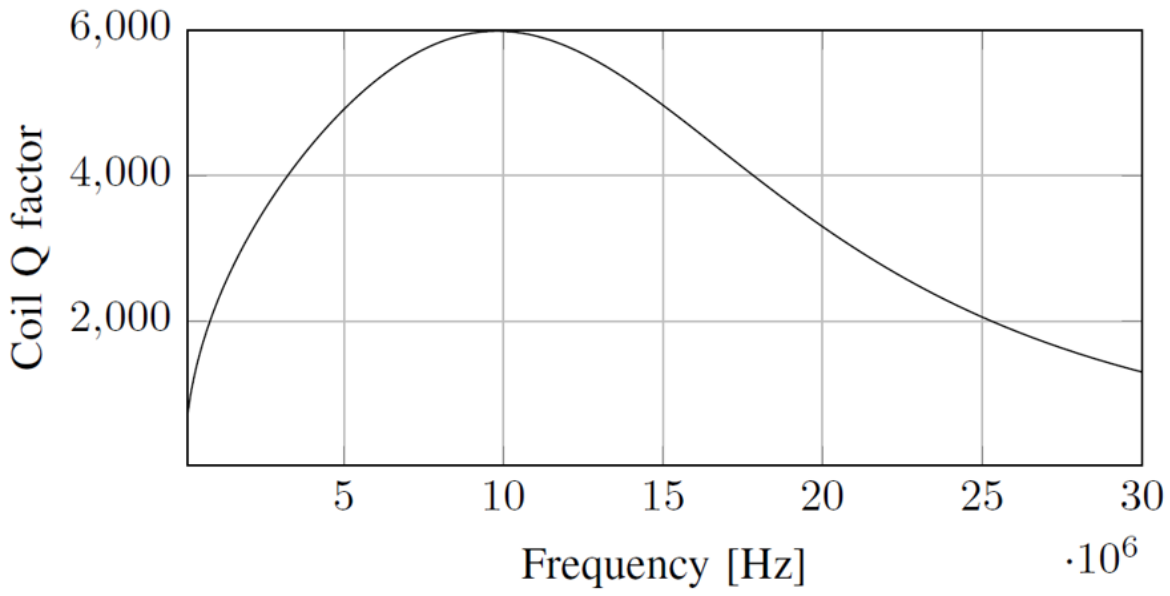


Figure 2.2: Variation of coil Q factor with frequency (2-turn 50 cm diameter copper coil)

level consumption could be remotely powered [42]. In these situations, the superior tolerance to angular offsets and transverse displacements compared to coils with ferrite cores is essential to being able to supply power to multiple sensor nodes concurrently. Furthermore, the reduction in size and weight of the coils due to the absence of the ferrite core means that the wireless sensors can be kept small and lightweight.

Once the link efficiency of the IPT has been maximised, it does not necessarily follow that the overall efficiency of the system will be increased as well, as switching losses of the power electronics in both the inverter and rectifier circuits could rise with frequency. Therefore, efficient high-frequency, soft-switching power electronics are desired. These circuits rely on fast semiconductor devices.

2.3 Power electronics

2.3.1 Semiconductors

Due to the high frequency, high voltage and high current requirements of the power electronics, the task of selecting appropriate semiconductor devices is not trivial. As mid-range high power IPT systems operate near the limits of the capabilities of traditional silicon (Si) devices, wide-bandgap semiconductor materials such as silicon carbide (SiC)

and gallium nitride (GaN) ought to be considered due to their superior characteristics as power devices, e.g. faster switching rates and higher breakdown field strengths. Alternatively, specialist high-speed radio frequency (RF) metal–oxide–semiconductor field-effect transistors (MOSFETs) such as those from IXYS RF can be incorporated into designs. For example, the IXYS RF IXZ4DF12N100 has a total rise and fall time of 7.5 ns [50], whilst the combined rise and fall times of high-voltage MOSFETs from International Rectifier are typically at least 40 ns [51].

An IXYS RF power MOSFET combined with gate driver (IXZ4DF12N100) was used in the Class E inverter of the mid-range IPT system that will be presented at the end of this chapter. Cree SiC Schottky diodes (C3D10170 and C3D10060) were used in the Class D and Class E rectifiers that will be described later in this section.

The packaging of the devices used in the power electronics can influence the performance of the inverter and rectifier circuits. The Cree C3D10170 SiC Schottky diode in the rectifier comes in a TO-247-2 package [52], which has long, narrow leads, adding stray inductances to the circuit. Contrastingly, the IXYS RF IXZ4DF12N100 module for the inverter has a surface-mount low-inductance package which means that parasitic effects, which could potentially reduce the switching speeds, can be minimised. It also has a low intrinsic gate resistance, leading to a decrease in rise and fall times, and enabling faster switching of the devices.

2.3.2 Inverters

Conventional hard-switching inverters are not suitable for IPT systems when operating in the MHz region. Since the switching time of the devices becomes comparable to the period of the driving signal, the result is that they can be inefficient at higher frequencies. Soft-switching inverters, such as Class D and Class E inverters, address this issue by employing zero-voltage switching (ZVS) to minimise power dissipation in the MOSFET during switching. This is achieved by preventing concurrent high voltage across and high current through the MOSFET. A disadvantage of Class D inverters, which are popular with low-power systems adhering to Qi or Alliance for Wireless Power (A4WP) standards,

is that they have lower output power compared to Class E inverters for the same input voltage and output load. Another issue is that they require a floating gate drive due to the presence of a high-side switching device. However, in contrast to Class E inverters, Class D inverters are able to operate over a larger load range with ZVS if the switching frequency is below the resonant frequency of the output load network.

Figure 2.3 depicts the Class E inverter in semi-resonant operation mode [2] used to drive the transmitter coil. In this topology, the transmitter resonant tank is tuned to a slightly higher frequency than the secondary resonant tank to keep the primary tank impedance inductive, a requirement for Class E operation. The parallel combination of the capacitor C_{res} (in Figure 2.3) and the transmitter coil (L_{TX} and R_{TX}) forms an impedance transformer, which causes the load impedance to appear larger, leading to an increase in driver efficiency. Figure 2.4 shows the simulated and measured drain-source voltage of the MOSFET of the Class E semi-resonant inverter running at 6 MHz. In this scenario, the input voltage is fixed at $V_{\text{in}} = 60\,\text{V}$ which results in an input power of $P_{\text{in}} = 90\,\text{W}$ and a maximum drain-source voltage of up to 250 V. As the maximum drain-source voltage is at least four times greater than the input voltage, the voltage stress on the MOSFET is high. The drain-source voltage goes to zero gradually before the MOSFET turns on, demonstrating zero-voltage switching which allows for highly-efficient switching at MHz frequencies.

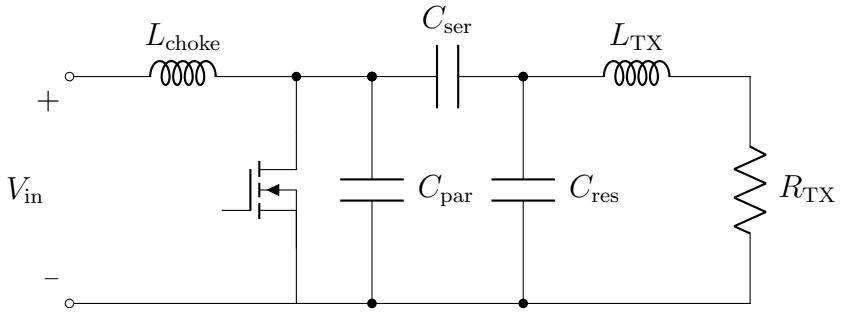


Figure 2.3: Semi-resonant Class E inverter from [2]

Class E inverters may also include a saturable reactor [53] to tune for optimum switching operation when a change in the load occurs (see Figure 2.5). A saturable reactor is essentially an AC-to-AC transformer consisting of a primary and a secondary winding,

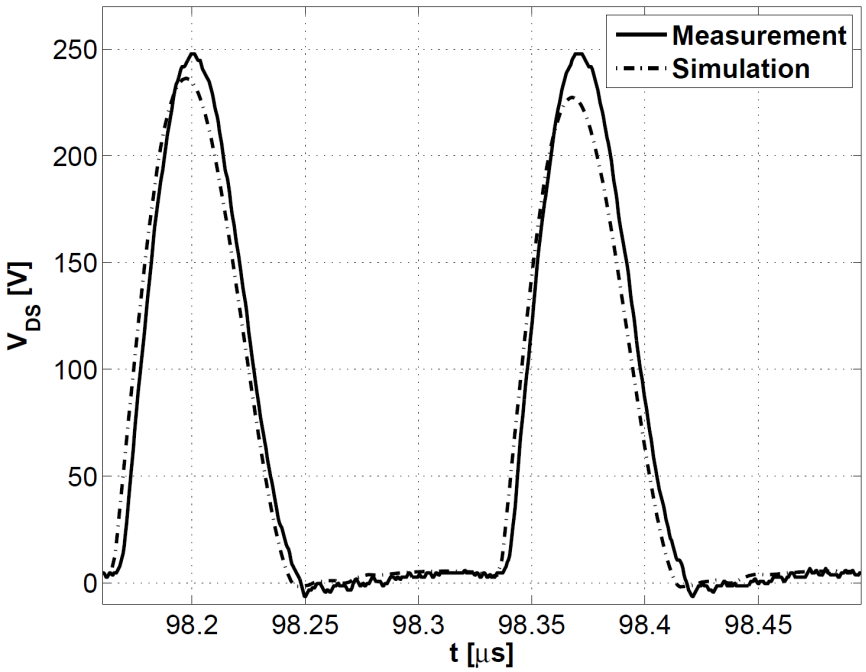


Figure 2.4: Simulated and measured drain-source voltage for semi-resonant Class E inverter with $V_{\text{in}} = 60\,\text{V}$ [2]

both wound on a single magnetic core. It operates by applying a low DC current in one winding, which causes the magnetic core's permeability to decrease, and therefore effectively changing the impedance of the second winding. The tuning procedure relies on varying the switching frequency and the effective reactance of capacitor C_{par} in Figure 2.5 via the saturable reactor.

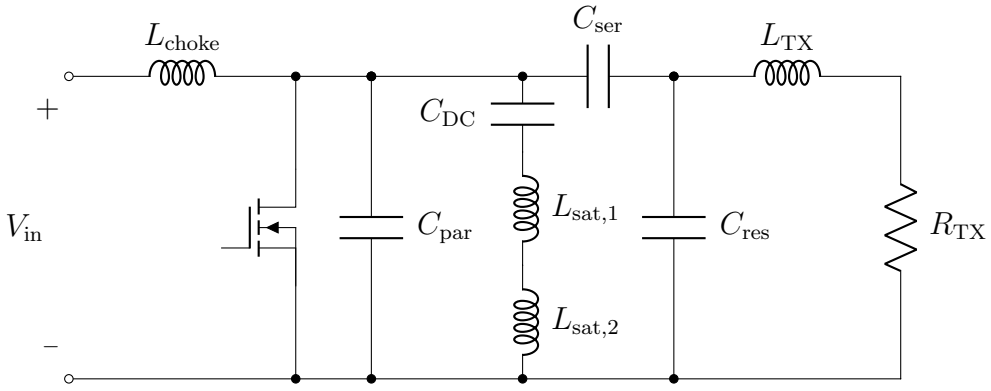


Figure 2.5: Class E inverter with a saturable reactor [53]

Although Class E inverters can achieve ZVS and zero-current switching (ZCS) operation, their voltage and current stresses can be large compared to other inverters. It has been reported in [54, 55] that adding a series LC resonant network in parallel with the

MOSFET can reduce its voltage or current stresses and therefore improve the efficiency of the inverter. The added inductor-capacitor (LC) network is tuned to either the second or third harmonic of the switching frequency. Adding resonant networks in inverters is a common technique used in Class F and Class F^{-1} inverters to shape the MOSFET drain voltage and current waveform. This hybrid configuration of Class E switching with a resonant network has been referred to as the Class EF_2 inverter when the added resonant LC network is tuned to the second harmonic, or the Class E/F_3 inverter when the added resonant LC network is tuned to the third harmonic. Figure 2.6 shows the circuit diagram of the Class EF_2 or Class E/F_3 inverter; inductor L_2 and capacitor C_2 form the added resonant network and their values are set such that their resonant frequency is either twice or three times the switching frequency [56]. Figure 2.7 compares the waveforms of the Class EF_2 and Class E/F_3 inverters with the Class E inverter. The Class EF_2 inverter results in lower voltage stresses across the MOSFET whereas the Class E/F_3 inverter results in lower current stresses through the MOSFET.

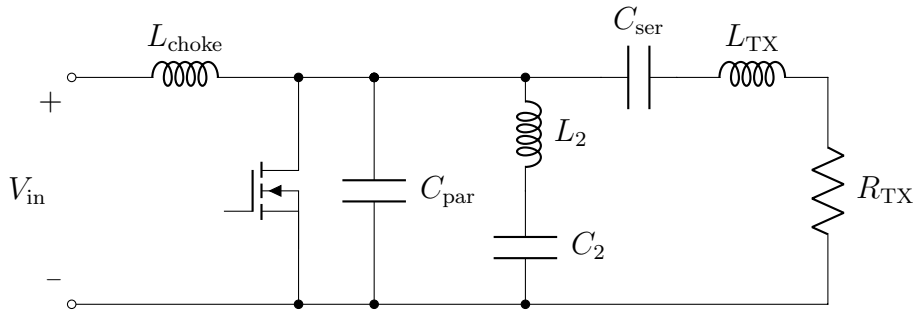
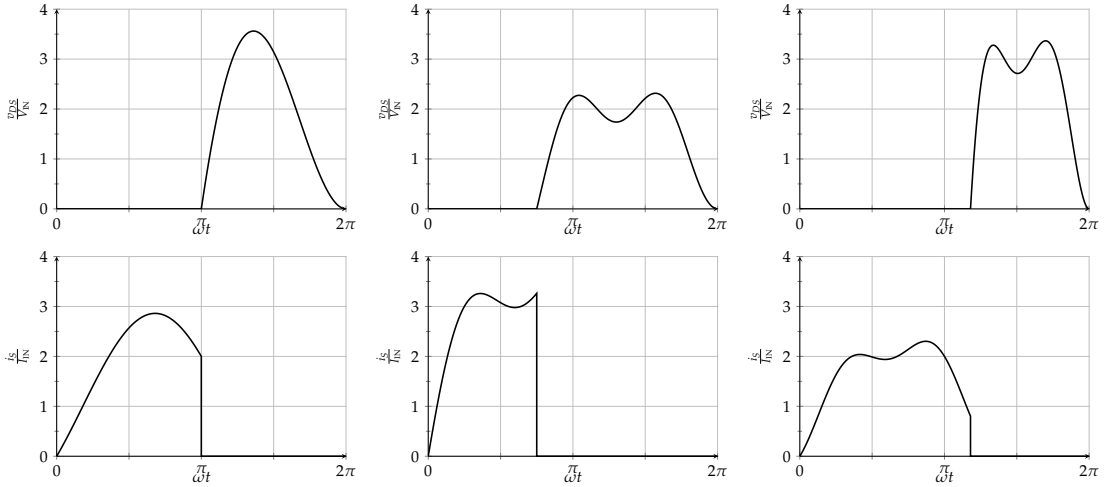


Figure 2.6: Class EF_2 or Class E/F_3 inverter. [56]

Table 2.1 shows a comparison of the normalised output power of the Half-Bridge Class D ZVS, the Class D ZCS, the Class E, the Class EF_2 and the Class E/F_3 inverters.



(a) Class E (b) Class EF_2 (c) Class E/F_3

Figure 2.7: Comparison of normalised voltage and current waveforms of different inverters classes. [56]

Inverter Class	**Normalised Output Power** $\left(\frac{P_o R_L}{V_i^2}\right)$
Half-Bridge Class D ZVS	0.2026
Class D ZCS	4.9348
Class E	0.5768
Class EF_2	0.6105
Class E/F_3	1.0760

Table 2.1: Comparison of normalised output power of different resonant inverter classes

2.3.3 Rectifiers

Rectifiers can suffer from significant diode reverse recovery losses in the MHz region if they are hard-switched. The use of soft-switching rectifiers avoids the requirement of a hard recovery and almost eliminates the associated losses with re-establishing reverse blocking function. Class E rectifiers are soft-switching topologies; one such circuit topology with low dv/dt that is voltage-driven is shown in Figure 2.8 [57].

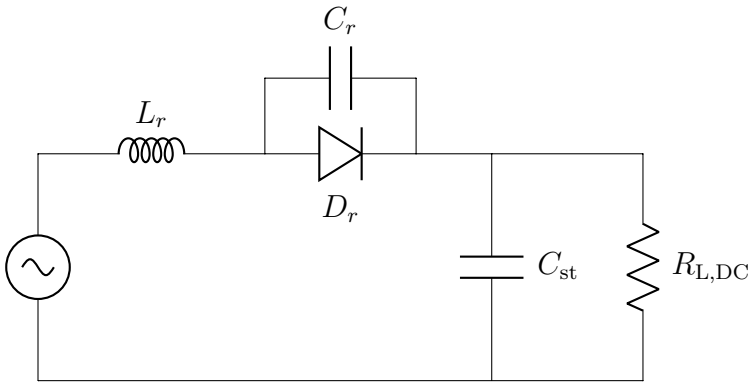


Figure 2.8: A voltage-driven low dv/dt Class E rectifier [57]

This specific Class E topology contains an inductor L_r in series with a parallel connection of a capacitor C_r and a diode D_r. The inductor L_r is in resonance with the capacitor C_r at the operating frequency of the system. Therefore, the L_r-C_r-D_r connection provides half-wave rectification. Output filtering is performed by the first-order low-pass filter consisting of the stabilising capacitor C_{st} and the output load $R_{\text{L,DC}}$. Any leakage inductance from the secondary coil can be absorbed into L_R. In addition, the diode-capacitor parallel combination means that the diode's junction capacitance can be absorbed into C_r.

When designing a Class E rectifier, the primary objective is to ensure that the rectifier's input impedance, R_{in}, is equal to the optimal load R_{opt}. Since the rectifier depicted in Figure 2.8 is a voltage-driven Class E rectifier for a parallel-tuned secondary, the optimal load is given by $R_{\text{opt,par}}$ in Equation (2.12). The input impedance R_{in} relates to the output load $R_{\text{L,DC}}$ of the Class E rectifier by Equation (2.14), where M is the AC-to-DC gain [58]:

$$R_{\text{L,DC}} = 2M^2 R_{\text{in}} \tag{2.14}$$

Figure 2.9 shows the waveforms of the Class E rectifier. The top plot is the rectifier's diode voltage, whilst the bottom plot shows the current through the diode D_r (solid) and the capacitor C_r (dotted). In this scenario, the rectifier is integrated in the IPT system described in [2]. The input voltage of the rectifier, which is the sinusoidal voltage across the parallel-tuned receiver coil, has an amplitude of 1.5 kV. The output voltage is under 400 V DC. An issue with this topology is that it circulates DC current, generating losses in the receiving coil and resonant inductor. The voltage across the diode is large compared to the output voltage of the rectifier; the high voltage stresses are due to the high receiver coil voltages at the input of the rectifier.

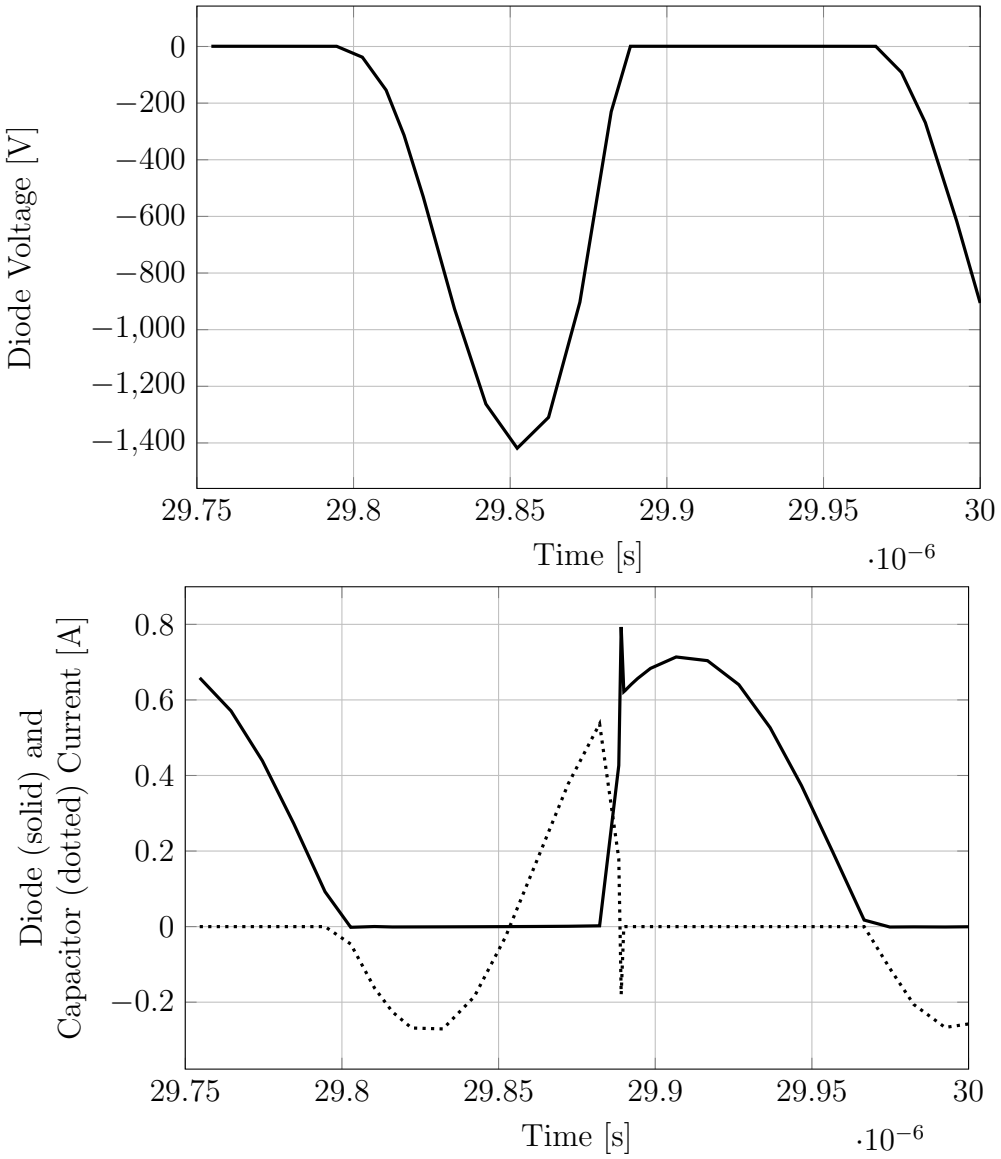


Figure 2.9: Simulated voltage-driven Class E rectifier waveforms: [Top] Voltage across D_r; [Bottom] Current through D_r (solid) and C_r (dotted) [57]

Another type of Class E rectifier is shown in Figure 2.10 [48]. This half-wave low dv/dt Class E rectifier is current driven, so it is suitable for a series-tuned receiver. The rectifier consists of a capacitor-diode network connected to a second-order output filter. This filter is made up of an inductor L_f, a capacitor C_f and the output load $R_{\mathrm{L,DC}}$, and provides load-independent filtering. For this rectifier, C_d acts as a snubber capacitor and therefore ensures zero voltage at turn on and turn off and zero rate of voltage change at turn off. There is no resonant inductor compared to the previous Class E rectifier topology.

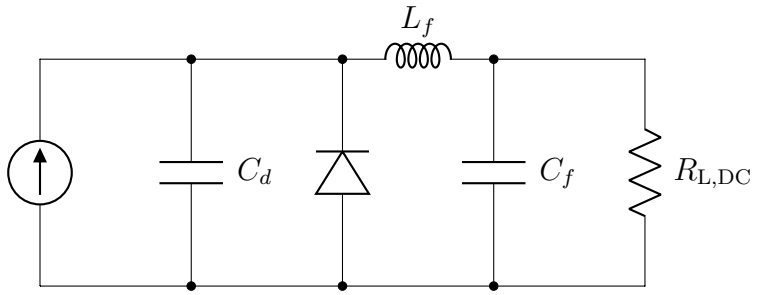


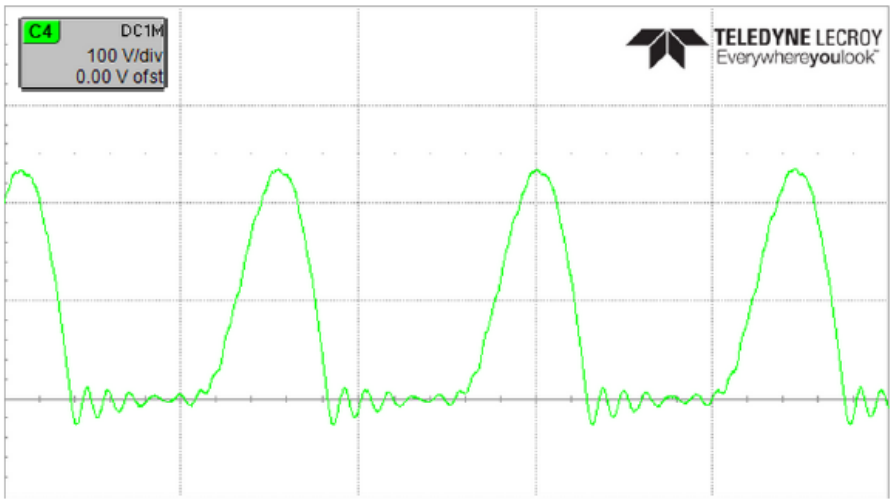
Figure 2.10: Current driven Class E low dv/dt half wave rectifier [48]

The relationship between the input impedance R_{in} of this current-driven rectifier and its output load $R_{\mathrm{L,DC}}$ is given by Equation (2.15), where K_I is the AC-to-DC current gain:

$$R_{\mathrm{L,DC}} = \frac{R_{\mathrm{in}}}{2K_I^2} \tag{2.15}$$

Due to the use of soft-switching operation, this topology results in excessive semiconductor stresses, because the voltage across the diode is greater than that across the output load, and the current through the diode consists of the input AC current superimposed on the output DC current [48]. Figure 2.11 shows the measured reverse bias voltage across the diode for this topology with an output power of 100 W, using the Cree C3D10060 SiC Schottky diodes [48]. On the other hand, soft-switching operation enables the use of larger diodes that are slower, because of the elimination of reverse recovery effects [48].

Although conventional hard-switching rectifier can be inefficient in the multi-MHz region, Class D rectifiers with SiC Schottky diodes have shown to be usable in the MHz



[D]: *Class-E*; R_{dc}=26Ω; C_d=220pF

Figure 2.11: Reverse bias voltage across diode in current driven Class E rectifier [48]

region. An example of such a topology is shown in Figure 2.12, which is a half-wave Class D rectifier consisting of two diodes [48]. It is also current driven, making it appropriate for series-resonant receivers.

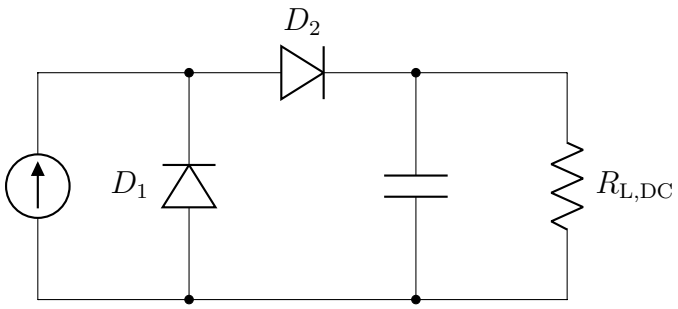


Figure 2.12: Current driven Class D half wave rectifier [48]

The input impedance of this current-driven rectifier is affected only by its output load, and the relationship is given by Equation (2.16):

$$R_{\mathrm{L,DC}} = \frac{\pi^2 R_{\mathrm{in}}}{2} \tag{2.16}$$

The advantages of the Class D rectifier, which include a simpler design process, lower cost implementation, higher tolerance to DC load variation and better semiconductor utilisation, are more noticeable in higher voltage operation, where semiconductor parasitic effects are minimised. Figure 2.13 shows the measured reverse bias voltage across the

diode for this topology with an output power of 100 W, using the Cree C3D10060 SiC Schottky diodes [48]. There is better semiconductor utilisation, as the diodes are stressed to the input current during conduction and stressed to the output voltage when reverse-biased [48]. However, the square wave voltage could introduce switching losses, if the reverse recovery time is comparable to the period [48].

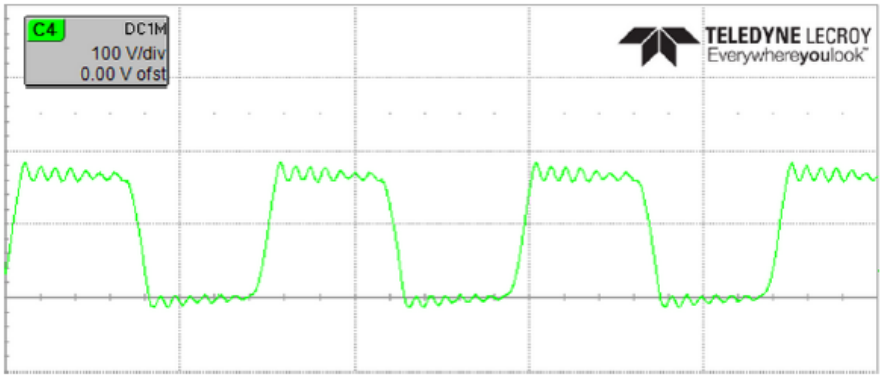


Figure 2.13: Reverse bias voltage across diode in current driven Class D rectifier [48]

2.3.4 Receiver load emulation

As shown in Equations (2.14), (2.15) and (2.16), the Class D and Class E rectifiers have an input resistance which depends on the load attached to its output. Therefore, in order to attain maximum link efficiency, a load emulation circuit should be attached to the output of the rectifier, so that the rectifier (and the receiver's resonant tank) is always presented with the optimal load, given by Equation (2.11) for a series-tuned secondary and Equation (2.12) for a parallel-tuned secondary. Otherwise, a change in the level of current draw in the load would result in a drop in efficiency and receiver power.

Such a circuit may take the form of a DC-to-DC converter, such as the Buck converter, which can be controlled to achieve optimal loading. This is done by measuring the voltage at the output of the rectifier and dividing by the desired load in order to obtain the current demand. This current demand is then compared with the actual measured current in order to obtain an error signal with which the duty cycle of the Buck converter can be adjusted to emulate the desired load.

In addition, from Equations (2.11) and (2.12), it can be seen that optimal load varies with the coupling factor, which in turn changes with the distance between the transmitter and receiver coils. Hence, the load emulation circuit should be controlled in such a way that the optimal load is always emulated even as distance changes, in order to ensure maximal link efficiency.

In the case of longer range systems (up to 10 m between the transmitter and receiver coils) such as those for wireless sensor network applications, the coupling coefficient is extremely low, which means that the optimal load varies little with distance and is dominated by the complex conjugate of the receiver's resonant tank impedance. In these scenarios, receiver power is typically very small (in the tens of mW range), so an open-loop type of load emulation circuit is preferred; this type of circuit eliminates the power consumption of any active control circuitry required for a closed-loop system. Examples of suitable ultra-low power open-loop load emulators include the buck-boost and the fly-back converter operating in discontinuous conduction mode [59], and are explained in more detail in Chapter 6.

2.4 Example of a system in air

A 6.78 MHz mid-range IPT system capable of transferring 120 W of power across a distance of 30 cm with a DC-to-load efficiency of approximately 70 % has been implemented and demonstrated. This system was designed with principles introduced in this chapter. The experimental setup is shown in Figure 2.14. The transmitter coil is a 30 cm 3-turn air-core coil made from copper piping. A Class E inverter in semi-resonant operation was selected to drive the transmitter coil, with the IXYS RF IXZ4DF12N100 combined gate driver and MOSFET module used as the switching device. The receiver coil is a 20 cm 5-turn air-core coil, also made from copper piping. The chosen rectifier topology is the voltage-driven Class E low dv/dt rectifier, utilising the Cree C3D10180 SiC Schottky diode. These methods have resulted in a reduction of losses and an improvement in efficiency of the power electronics. Consequently, this mid-range IPT system is able to

operate feasibly in the MHz region, leading to an increase in coil Q factors ($Q_{\mathrm{TX}} = 1270$ and $Q_{\mathrm{RX}} = 1100$), link efficiency (95 %), and overall DC-to-load efficiency (70 %).

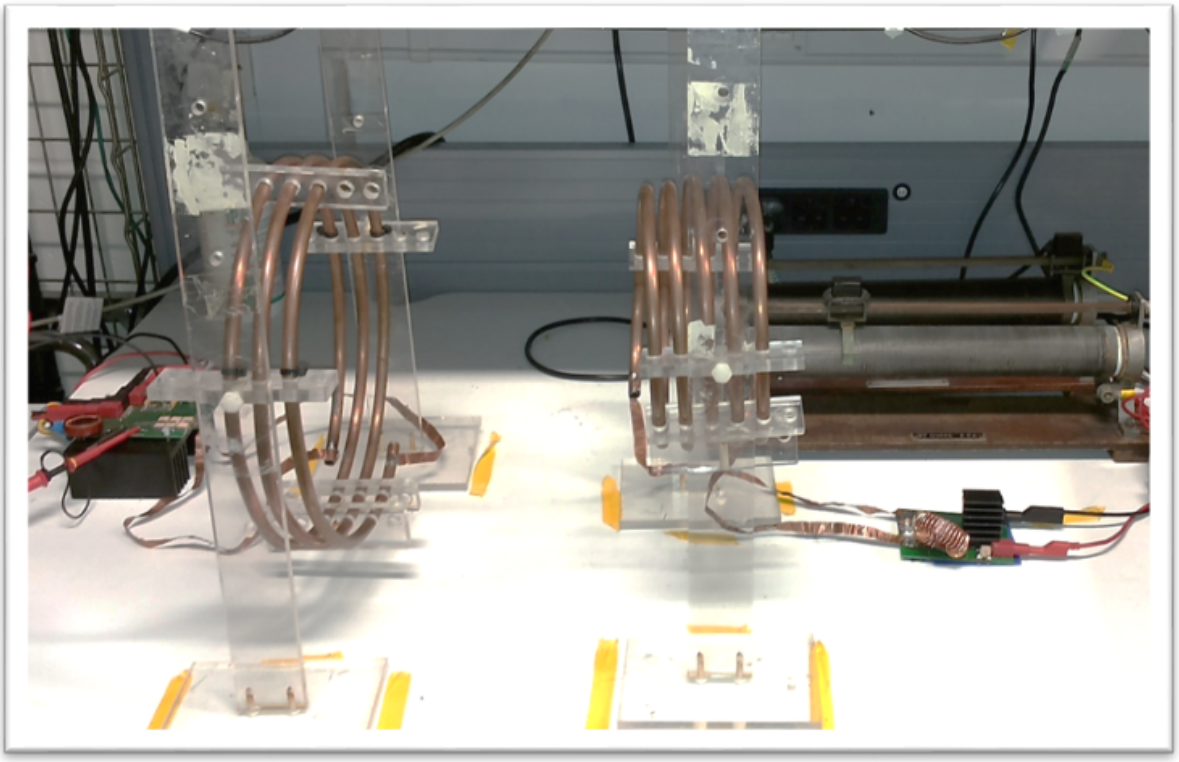


Figure 2.14: A 6.78 MHz system designed using link efficiency-led principles

2.5 Summary

The design of a lightweight and portable IPT system calls for the use of air-core coils in favour of coils with ferrite cores. The weak coupling of air-core coils suggests that the operating frequency should be increased to the multi-MHz region to maximise link efficiency. However, the efficiency of power electronics will tend to decrease with frequency, unless suitable high frequency power converters are utilised. Inverters that are appropriate for multi-MHz frequencies include the Class E semi-resonant inverter, the Class E inverter with a saturable reactor, and the Class EF_2 or Class E/F_3 inverter. Class D or Class E rectifiers may be used to rectify the high-frequency coil voltage. Different types of semiconductor devices need to be considered, including GaN, SiC and specialist high-speed RF Si devices. Receiver load emulation may be needed to maintain maximum link

efficiency by emulating the optimal load seen by the rectifier and the receiver's resonant tank. The regulations on human exposure to electromagnetic (EM) fields, which will be described in Chapter 3, may also influence IPT design and usage scenario, and ultimately encourage the design of a highly-efficient system. By following the link efficiency-led design principles in this chapter, a mid-range IPT system can be designed with maximum link efficiency and overall DC-to-load efficiency.

Chapter 3

Human safety considerations

The successful design of a wireless power transfer (WPT) system in the presence of living objects requires an understanding of the types of effects such systems have on living objects such as human beings. As a WPT system utilises a high-frequency magnetic field to deliver power, the adverse health effects arise mainly from the interaction between the magnetic field and the conductive human tissue, which generates heat in the tissue. There are also additional contributions to tissue heating, stemming from the electric field caused by the coil's high voltages, and, especially for wirelessly-powered medical implants, heat dissipation in the coil. Lastly, internal electric fields in the body can be a cause of non-thermal nervous system effects. The relative importance of each type of effect depends on, among other factors, the frequency of operation of the WPT system.

There are guidelines and regulations that limit the exposure of the general public and occupational workers to high-frequency electromagnetic fields. WPT systems need to adhere to these limits, but there may be exceptions for medical purposes where the risk of the effects of exposure is outweighed by the benefits arising from the medical treatment. In addition, there exists standards that govern the heat and maximum temperature rises that can be produced by active implantable medical devices (AIMDs), as well as the immunity of such devices to electromagnetic fields.

Evaluation of the compliance of a WPT system to the safety guidelines and limits can be performed using numerical simulations. This is illustrated practically by the

assessment of the safety of a wirelessly-powered drone/quadcopter demonstrator using 3D full-wave electromagnetic simulations with human body models. These simulations are able to show whether the relevant limits for general public exposure have been met. This wirelessly-powered drone, which has been developed by the author's research group, is used to showcase the technology developed within the research group to the visitors in the laboratory, and to attendees at trade shows and at conferences. Therefore, it is vital to ensure people viewing the exhibit are not subjected to electromagnetic field levels that would exceed limits.

This chapter describes the effects of exposure of humans and other living objects to a WPT system. It outlines some of the guidelines, regulation and standards with which such systems should be compliant, in order to be considered safe in the presence of living objects. Lastly, it demonstrates, with a practical example of a wirelessly-powered quadcopter, how safety and adherence to safety limits can be evaluated using numerical simulations.

3.1 Effects of exposure on humans

In addition to the challenges of operating efficiently in the MHz region that was addressed in Chapter 2, the design of inductive power transfer (IPT) systems must also consider limits on electromagnetic (EM) field levels that are in place in order to protect humans from the adverse health effects of exposure to EM fields. For exposure to wireless power transfer systems, these effects may arise due to the interaction of the high frequency magnetic field with the conductive biological tissue.

The adverse health effects of EM field exposure can be broadly categorised into two types: non-thermal and thermal. Non-thermal effects [60] are due to exposure to EM fields below 10 MHz, causing stimulation of muscles, nerves and sensory organs as a result of an induced electric field in the body.

In terms of thermal effects, exposure to EM fields at frequencies above 100 kHz can cause tissue heating due to energy absorption [60]. There are two main mechanisms

of heating that are directly caused by EM fields. Firstly, a high-frequency magnetic field produces eddy currents in conductive human tissue, heating it up. Secondly, the alternating current (AC) voltage across the coil and between the coil turns generate a time-varying electric field which passes through conductive tissue, causing dielectric heating.

In addition to these two thermal effects that are directly caused by EM field exposure, a source of heating for a wirelessly-powered implantable medical device is heat dissipation in the implanted receiver coil. This is a result of current flowing through the coil's own loss resistances.

The combination of eddy current heating, dielectric heating and (for wirelessly-powered medical implants) coil dissipation will lead to a rise in the temperature of human body tissue. Any increase of more than 1 °C is considered unsafe [61]. Therefore, temperature rises should be minimised as far as possible by decreasing heating by all three mechanisms, but a consequence of doing so may be a deterioration in link efficiency.

Working at 6.78 MHz (first industrial, scientific and medical (ISM) band) means that both thermal and non-thermal effects need to be taken account of when designing such IPT systems. At 13.56 MHz (second ISM band), only thermal effects require consideration.

3.2 Guidelines, standards and regulations

3.2.1 Electromagnetic field exposure

A number of guidelines, standards and regulations exist to minimise the adverse effects of human exposure to EM fields. The applicability of a particular set of standards or guidelines depends, among other things, on the region (e.g. U.S.A. or the European Union (EU)) and the usage scenario (i.e. general public, occupational or medical exposure). Also, these guidelines cover a wide range of frequencies, from static/direct current (DC) and low frequency fields (such as overhead power lines at 50 Hz) to microwave radiation in the GHz range. In this thesis, only the first two ISM bands at 6.78 MHz and 13.56 MHz are

considered, as these multi-MHz frequencies are commonly used for IPT systems operating with high link efficiency.

The International Commission on Non-Ionizing Radiation Protection (ICNIRP) has published a widely-accepted set of guidelines to minimise the risks of exposure of humans to electromagnetic fields [61, 62] There are limits for both general public exposure and occupational exposure, where those for the latter are generally less stringent. Compared to the general public, it is expected that workers are more aware of when they are exposed to EM fields, and understand the causes and risks of exposure in order to take appropriate precautions.

ICNIRP defines basic restrictions, which are directly related to established health effects (i.e. tissue heating and nerve stimulation). These quantities, which are generally difficult to measure directly as they are internal to the body, must not be exceeded. The particular basic restriction which relates to thermal effects is the specific absorption rate (SAR). It is specified in the 1998 Guidelines and is relevant for frequencies greater than 100 kHz. Table 3.1 shows the SAR limits for both general public and occupational exposure; the same values apply to both the 6.78 MHz and 13.56 MHz ISM bands. These values are averaged over any six-minute period, and the localised SAR values are averaged over 10 g of tissue.

	General Public	Occupational
Whole-body average SAR	$0.08\,\mathrm{W\,kg^{-1}}$	$0.4\,\mathrm{W\,kg^{-1}}$
Localised SAR (head and trunk)	$2\,\mathrm{W\,kg^{-1}}$	$10\,\mathrm{W\,kg^{-1}}$
Localised SAR (limbs)	$4\,\mathrm{W\,kg^{-1}}$	$20\,\mathrm{W\,kg^{-1}}$

Table 3.1: ICNIRP 1998 SAR limits: general public and occupational exposure

The basic restriction for non-thermal effects is the internal electric field induced in the body. These are mentioned in the 2010 Guidelines for frequencies under 10 MHz, and so do not apply to IPT systems operating at 13.56 MHz. Table 3.2 shows the internal electric field limits for both general public and occupational exposure at 6.78 MHz; these values are expressed in root mean square (RMS). For a particular type of tissue, the 99th percentile value of the electric field is used to evaluate compliance; this is to minimise the effects of computational artefacts due to meshing and the use of human body models.

	General Public	Occupational
Internal electric field (6.78 MHz)	$915\,\mathrm{V\,m^{-1}}$	$1831\,\mathrm{V\,m^{-1}}$

Table 3.2: ICNIRP 2010 internal electric field limits: general public and occupational exposure

Because basic restrictions are difficult to measure directly, ICNIRP also defines reference levels. These quantities are the external and unperturbed (measured without the human body present) electric field and magnetic field. The reference levels for non-thermal effects are taken from 2010 Guidelines and are shown in Table 3.3 for 6.78 MHz, whilst those for thermal effects at both ISM bands are taken from 1998 Guidelines and are given in Table 3.4. The thermal effect reference levels are to be averaged over a six-minute period.

	General Public	Occupational
Electric field strength (6.78 MHz)	$83\,\mathrm{V\,m^{-1}}$	$170\,\mathrm{V\,m^{-1}}$
Magnetic field strength (6.78 MHz)	$21\,\mathrm{A\,m^{-1}}$	$80\,\mathrm{A\,m^{-1}}$

Table 3.3: ICNIRP 2010 reference levels for non-thermal effects: general public and occupational exposure

	General Public	Occupational
Electric field strength (6.78 MHz)	$33.4\,\mathrm{V\,m^{-1}}$	$90.0\,\mathrm{V\,m^{-1}}$
Magnetic field strength (6.78 MHz)	$0.108\,\mathrm{A\,m^{-1}}$	$0.236\,\mathrm{A\,m^{-1}}$
Electric field strength (13.56 MHz)	$28\,\mathrm{V\,m^{-1}}$	$61\,\mathrm{V\,m^{-1}}$
Magnetic field strength (13.56 MHz)	$0.0730\,\mathrm{A\,m^{-1}}$	$0.160\,\mathrm{A\,m^{-1}}$

Table 3.4: ICNIRP 1998 reference levels for thermal effects: general public and occupational exposure

The 1998 Guidelines also contained basic restrictions for non-thermal effects in terms of the current density in the head and trunk, along with their corresponding external reference levels. However, the non-thermal effect limits in the 1998 Guidelines have been superseded by those in the 2010 Guidelines, which are based on the internal electric fields.

Compliance with these reference levels ensures compliance with the respective basic restrictions. However, if the reference levels are exceeded, it does not necessarily follow that the corresponding basic restriction will be exceeded as well. In these cases, further tests are needed to prove compliance with the basic restrictions such as performing 3D

computational EM simulations with accurate human body models. In addition, working at 6.78 MHz means that the reference levels due to both the non-thermal and the thermal effects need to be considered. In effect, it means that if field strengths are below the non-thermal effect reference level but above the thermal effect reference level, then only the thermal effect basic restriction (i.e. SAR) has to be evaluated.

The reference levels tend to be very conservative and incorporate a high safety margin. This is because it assumes small variations in electric and magnetic field strengths across the whole body. However, for WPT systems, which operate in the near field, the distribution of the magnetic field will be non-uniform. Since a person is likely to be situated close to the source of the magnetic field, areas of high field strengths tend to be very localised, and restricted to small regions of the body.

The underlying physical phenomenon that dictate the thermal effect basic restrictions and reference levels set by ICNIRP is that exposure to EM fields should not lead to a more than 1 °C rise in body temperature, as higher temperatures would result in adverse biological effects.

A EU directive [60] was adopted on 26 June 2013 by the European Parliament and the Council of Europe, which sets out limits on the exposure of workers to EM fields. This Directive was transposed into UK law on 1 July 2016 (as the Control of Electromagnetic Fields at Work Regulations 2016). The safety limits are based on the 1998 and 2010 ICNIRP limits [61, 62]. The Directive defines exposure limit values (ELVs) which ICNIRP calls basic restrictions. It also defines action levels (ALs), which are referred to as reference levels by ICNIRP.

In the US, the Institute of Electrical and Electronics Engineers (IEEE) C95.1-2005 standard is generally adhered to as safety guidance for human body exposure to electromagnetic fields [63]. As with ICNIRP, the IEEE standard also defines basic restrictions as those that are based on established adverse health effect. For thermal effects (relevant for frequencies greater than 100 kHz), the basic restriction quantity is also SAR, and the limits are identical to those of ICNIRP for both the general public and workers.

The IEEE standard also defines maximum permissible exposure values, which have the

same meaning as ICNIRP's reference levels and are derived from the basic restrictions. The maximum permissible exposure values for thermal effects at both 6.78 MHz and 13.56 MHz are given in Table 3.5; these values are expressed in RMS and are to be averaged over a six-minute period (except for the general public electric field strength reference level, which is to be averaged over a 30-minute period).

	General Public	Occupational
Electric field strength (6.78 MHz)	$122\,\mathrm{V\,m^{-1}}$	$272\,\mathrm{V\,m^{-1}}$
Magnetic field strength (6.78 MHz)	$2.40\,\mathrm{A\,m^{-1}}$	$2.40\,\mathrm{A\,m^{-1}}$
Electric field strength (13.56 MHz)	$60.8\,\mathrm{V\,m^{-1}}$	$136\,\mathrm{V\,m^{-1}}$
Magnetic field strength (13.56 MHz)	$1.20\,\mathrm{A\,m^{-1}}$	$1.20\,\mathrm{A\,m^{-1}}$

Table 3.5: IEEE C95.1-2005 maximum permissible exposure levels: general public and occupational exposure

It is interesting to note that even though the IEEE standard and the ICNIRP guidelines have identical basic restrictions for thermal effects, the IEEE standard reference levels are generally less stringent that those of the ICNIRP guidelines.

Within the IEEE standard, there are no basic restrictions or maximum permissible exposure values for non-thermal effects at frequencies above 5 MHz. Hence, non-thermal effects arising from internal electric fields do not need to be considered when evaluating compliance with the IEEE standards at the first two ISM bands.

In reality, depending on the power requirements of the application, it may not be possible to deliver enough power to a load whilst at the same time keeping external electric and magnetic field levels within the reference levels and/or the induced electric fields and SAR within the basic restrictions. Hence, it would be necessary to define an exclusion zone, outside of which it would be safe for humans to be physically present.

Naturally, for wirelessly powering a medical implant, it would not make sense to define an exclusion zone at the receiving end for meeting the limits, since the device and receiver coil are implanted inside the body. In addition, as will be studied in Chapter 4, the presence of the human body with an implanted wireless power receiver can change the magnetic field distribution greatly, so reference levels are not very useful in evaluating compliance of wirelessly-powered medical implants. In these cases it is essential that computational EM simulations are performed to determine a system's safety. In fact,

the ICNIRP guidelines' definition of general public exposure excludes exposure during medical procedures and the IEEE standards do not apply to patients under the direction of medical professionals.

Nevertheless, these EM field limits and regulations imply that it is important to design IPT systems with high link efficiencies, so that the required level of power can be delivered to the receiver load with minimal magnetic field.

3.2.2 Device immunity and temperature rises

In order for any AIMD to be CE-marked (so that it can be traded on the EEA market) it needs to comply with Directive 90/385/EEC on AIMDs [64]. With respect to EM fields, that directive states that 'Devices must be designed and manufactured in such a way as to remove or minimize as far as possible: ... risks connected with reasonably foreseeable environmental conditions such as magnetic fields, external electrical influences, electrostatic discharge, pressure or variations in pressure and acceleration'. AIMDs that are designed to meet the CENELEC EN 45502-1 standard [65] comply with the Directive in terms of EM field immunity. The EN 45502-1 standard says that devices need to meet the General Public Reference Levels from Council Recommendation 1999/519/EC [66], which are in turn based on the 1998 ICNIRP reference levels. These were given in Table 3.4. Effectively, this standard requires an exclusion zone to be set up for any WPT system, outside of which the field levels are below the ICNIRP 1998 reference levels in order to ensure that any AIMD such as a cardiac pacemaker still functions properly.

As previously mentioned for a wirelessly-powered medical implant, the combined heating from eddy current heating, dielectric heating and coil dissipation causes an overall temperature rise in the human tissue. Eddy current heating and dielectric heating are a result of the direct interaction between the high frequency electromagnetic fields and the electrically conductive human tissue, so the exposure limits set by the ICNIRP guidelines and the IEEE standard should ensure temperature rises in the body are within the limits. However, for a medical implant with a wireless power receiver, there is heat dissipation in the coil due to relatively large currents flowing through the coil. This source of heat-

ing is not a direct effect of exposure to electromagnetic fields, but makes a significant contribution to the overall temperature rise of the human tissue via direct contact with the device. In order to meet the EN 45502-1 standard for CE marking, another aspect that applies to wirelessly-powered implants is that a maximum temperature rise of 2 °C on the outer surface of the medical device is permitted.

In addition, for WPT systems with an implanted receiver operating at below 100 kHz, even though there are no thermal effects to evaluate, temperature rises still need to be analysed due to coil dissipation.

3.2.3 MRI compatibility

In the past, it was standard medical practice for patients with implants to be excluded from access to MRI due to safety concerns [67]. However, in recent years, many implant manufacturers have been designing their medical devices to be 'MR conditional', which means that they are safe to use in an MRI environment within certain limits specified on implant labelling [67].

The design of an implanted receiver coil and the associated power electronics should consider MRI compatibility. The relevant standards for the safety of humans and medical implants in an MRI environment include IEC 62570 (Standard practice for marking medical devices and other items for safety in the magnetic resonance environment), IEC 60601-2-33 (Particular requirements for the basic safety and essential performance of magnetic resonance equipment for medical diagnosis), and ISO/TS 10974 (Assessment of the safety of magnetic resonance imaging for patients with an active implantable medical device) [68].

An MRI scan utilises the combination of a static magnetic field (typically 0.2 T to 3 T), a time-varying gradient magnetic field (in the extremely low frequency (ELF) region, with slew rates in the range of $20\,\mathrm{T\,m^{-1}\,s^{-1}}$ to $150\,\mathrm{T\,m^{-1}\,s^{-1}}$) and an radio frequency (RF) magnetic field (typically in the tens of MHz) [69]. Due to the variety of frequencies present, there are multiple effects on the human body and the implantable medical devices. As this thesis focuses on WPT systems for medical implants, the effects of and

limits on the RF magnetic fields will be discussed in this section, since the frequencies of these magnetic fields are similar to the ones used for WPT systems. Information on the static and ELF regions is available in the standards [68, 70, 71, 62] and other resources [69].

The RF magnetic field will cause tissue heating due to energy absorption and the IEC 60601-2-33 standard specifies limits in terms of SAR, temperature rises and maximum temperature. These are summarised in Tables 3.6 and 3.7. Normal operating mode means there is no physiological stress to patients, whilst First-level controlled mode means there may be physiological stress caused to patients which needs to be controlled by medical supervision [70].

	SAR ($W\,kg^{-1}$)				
		Partial body		Localised region	
Operating mode	Whole body	Any	Head	Head and trunk	Extremities
Normal	2	2-10	3.2	10	20
First-level controlled	4	4-10	3.2	10	20

Table 3.6: SAR limits from IEC 60601-2-33

	Temperature limits (°C)		
Operating mode	Max. core temp.	Max. local tissue temp.	Rise of core temp.
Normal	39	39	0.5
First-level controlled	40	40	1

Table 3.7: Temperature limits from IEC 60601-2-33

3.3 The wirelessly-powered drone

The wirelessly-powered drone was developed within the Wireless Power Lab to showcase the application of wireless power technology in flying vehicles and to illustrate the associated design obstacles (e.g. reliable operation under variable coupling) [72, 73]. It has been demonstrated in the laboratory as well as various conferences and trade shows, where members of the general public are able to see the system running live. Due to the close proximity of spectators to the drone flying while being powered wirelessly, it is

important to evaluate the safety of the system with respect to the general public exposure limits of the ICNIRP guidelines and IEEE standards.

The operating frequency is 13.56 MHz, which is in one of the unlicensed ISM bands. At this frequency, only the thermal effects of exposure need to be considered, so 3D EM simulations of the drone system with the human body model are performed to calculate SAR. The process of setting up, configuring and performing simulations will be described in detail in Chapter 4.

The transmitter pad consists of a 20 cm outer diameter 2-turn printed circuit board (PCB) coil, with 1 oz copper (equivalent trace thickness of 35 µm). The receiver coil consists of the copper-plated propeller guards of the Hubsan H107L X4 quadcopter, with a maximum dimension of 15.8 cm. The furthest distance between the two coils is 15 cm.

The demonstrator is placed in a 40 cm × 40 cm × 40 cm perspex box, with the transmitter coil sitting at the bottom of the box. Therefore, the minimum distance a person is situated from the system is 10 cm from the side of the transmitter coil's outer edge (or 20 cm from the centre of the transmitter coil in the horizontal direction), and 40 cm above the transmitter coil (25 cm above the receiver coil/drone at its maximum height from the transmitter).

Table 3.8 shows the characteristics of the coils at 13.56 MHz from simulation. Also obtained from simulations are the link characteristics and tuning parameters at 13.56 MHz for a distance of 15 cm using resonant tuning for maximum link efficiency (explained in Chapter 2); these values are given in Table 3.9. The received power is assumed to be 15 W.

	Transmitter coil	Receiver coil
Inductance	1.08 µH	431 nH
Resistance	103 mΩ	145 mΩ
Q factor	888	253

Table 3.8: Transmitter and receiver coil characteristics for the drone system at 13.56 MHz

By configuring the simulation set-up with the tuning capacitance, optimal load and transmitter current given in Table 3.9, it is possible to obtain magnetic field strength distributions in order to evaluate compliance with the thermal effect reference levels.

Parameter	Value
Coupling factor	3.29 %
Maximum link efficiency	88.0 %
Tuning capacitance	320 pF
Optimal load	2.26 Ω
Reflected resistance	1.51 Ω
Transmitter coil current	4.60 A

Table 3.9: Link characteristics and parameters for drone system at 13.56 MHz, over a distance of 15 cm (received power: 15 W)

Figure 3.1 shows the variation in the magnetic field strength with distance on axis from the transmitter pad (in the vertical direction), which has been obtained from simulation (blue). The drone and receiver coil are situated 15 cm above the transmitter coil. Also shown are the reference level from ICNIRP (red) and the maximum permissible exposure value from IEEE (brown), for the general public exposure scenario.

The magnetic field strength is within the ICNIRP reference level limit when a person is situated more than 72.2 cm above the transmitter pad, and is within the IEEE maximum permissible exposure limit when a person is more than 32.5 cm above the transmitter pad.

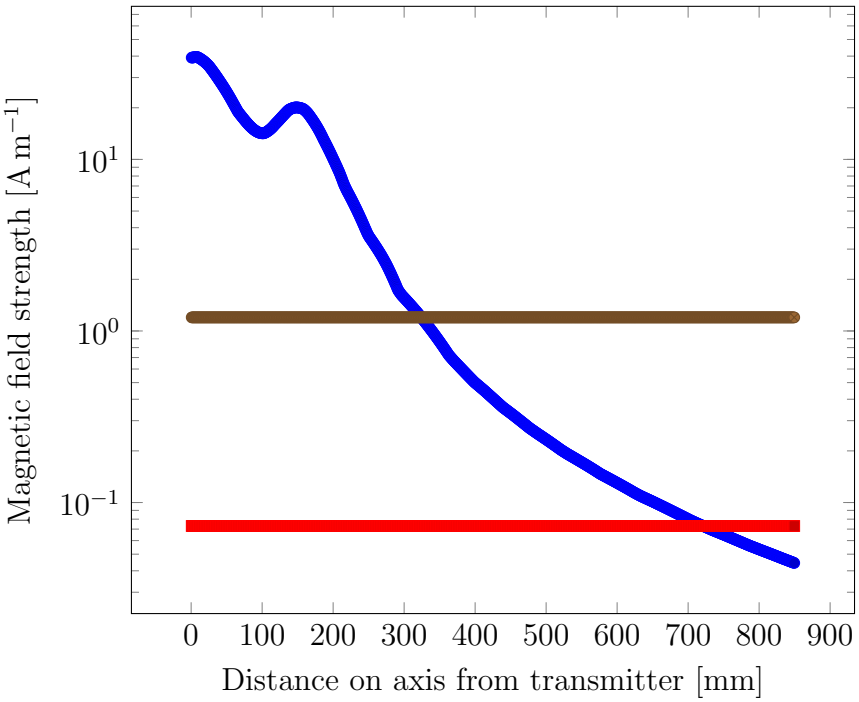


Figure 3.1: (Blue) Variation of magnetic field strength with distance on axis from transmitter pad in vertical direction (Drone and receiver at 150 mm); (Brown) IEEE maximum permissible exposure value; (Red) ICNIRP reference level

Figure 3.2 shows the variation in the magnetic field strength with distance in the horizontal direction from the outer edge of the transmitter pad, which has been obtained from simulation (blue). Also shown are the reference level from ICNIRP (red) and the maximum permissible exposure value from IEEE (brown), for general public exposure.

The magnetic field strength is within ICNIRP reference level limit when a person is situated more than 46.4 cm away from the outer edge of the transmitter pad in the horizontal direction, and is within the IEEE maximum permissible exposure limit when a person is more than 13.3 cm away from the outer edge of the transmitter pad in the horizontal direction.

The distance from the outer edge of the transmitter pad in the horizontal direction at which the magnetic field strength is within the ICNIRP reference level is 46.4 cm. The magnetic field strength is within the IEEE standard at 13.3 cm from the outer edge of the transmitter pad in the horizontal direction.

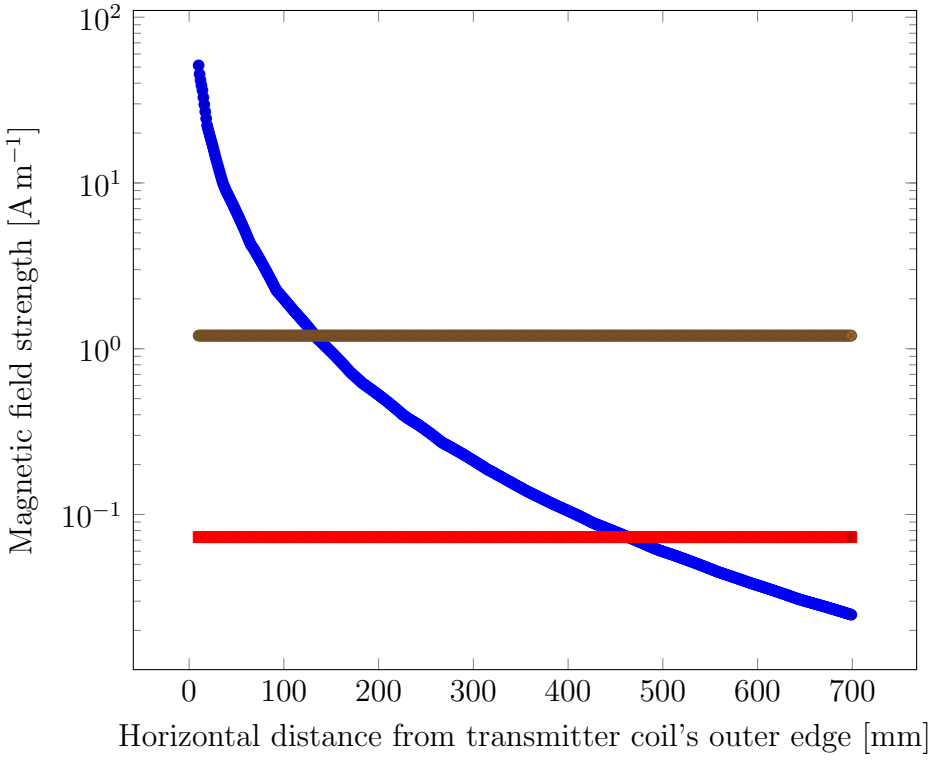


Figure 3.2: (Blue) Variation of magnetic field strength with distance in horizontal direction from outer edge of transmitter pad; (Brown) IEEE maximum permissible exposure value; (Red) ICNIRP reference level

According to the IEEE standard, the drone system is considered to be safe as the

person is exposed to fields below the maximum permissible exposure values, even at the edge of the box. However, since the ICNIRP reference levels are exceeded even when the person is at the edge of the box, it is important to perform simulations with a human body model in order to determine whether the SAR levels meet the basic restriction limits.

Figure 3.3 shows the SAR distribution in the Nelly human body model when Nelly's head is situated 40 cm above the transmitter coil (and 25 cm above the receiver coil). The maximum SAR when Nelly is in this position is 0.000 681 364 W kg^{-1} (at the neck/shoulder region).

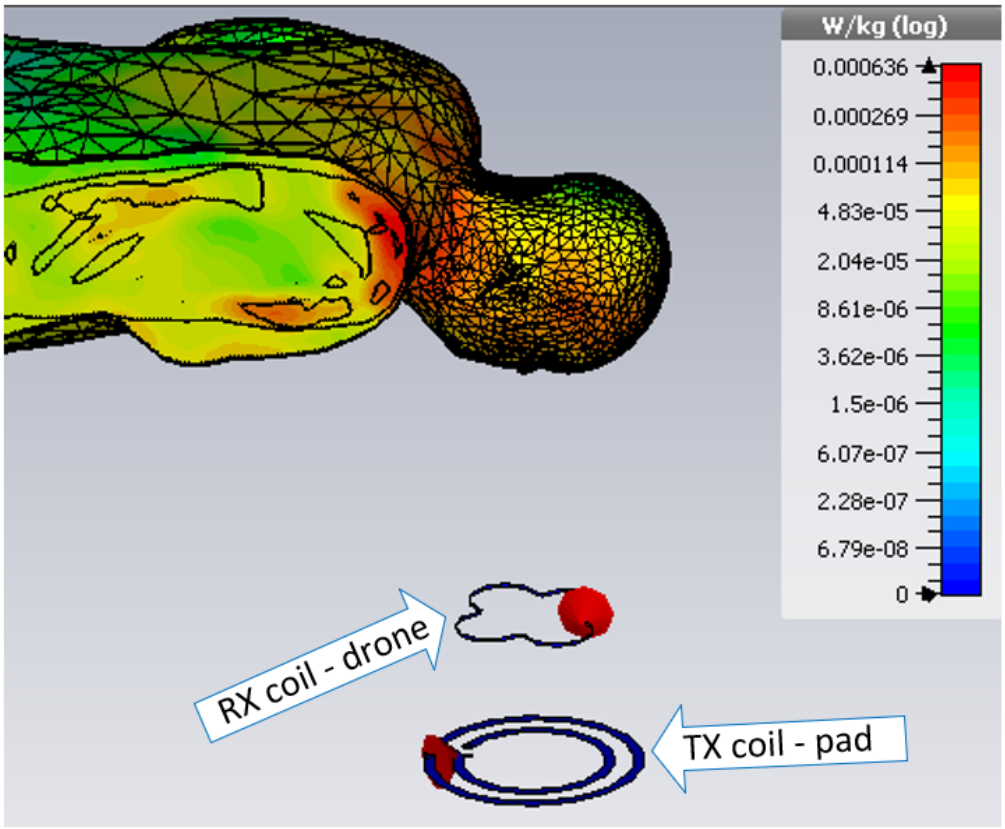


Figure 3.3: SAR distribution with Nelly's head 40 cm above transmitter coil

Figure 3.4 shows the SAR distribution in Nelly, when her head is 10 cm from the transmitter coil's outer edge in the horizontal direction. The maximum SAR when Nelly is in this position is 0.003 42 W kg^{-1} (at the forehead).

Despite external magnetic fields exceeding the ICNIRP reference levels for general public exposure, the SAR levels are still extremely low compared to the basic restrictions.

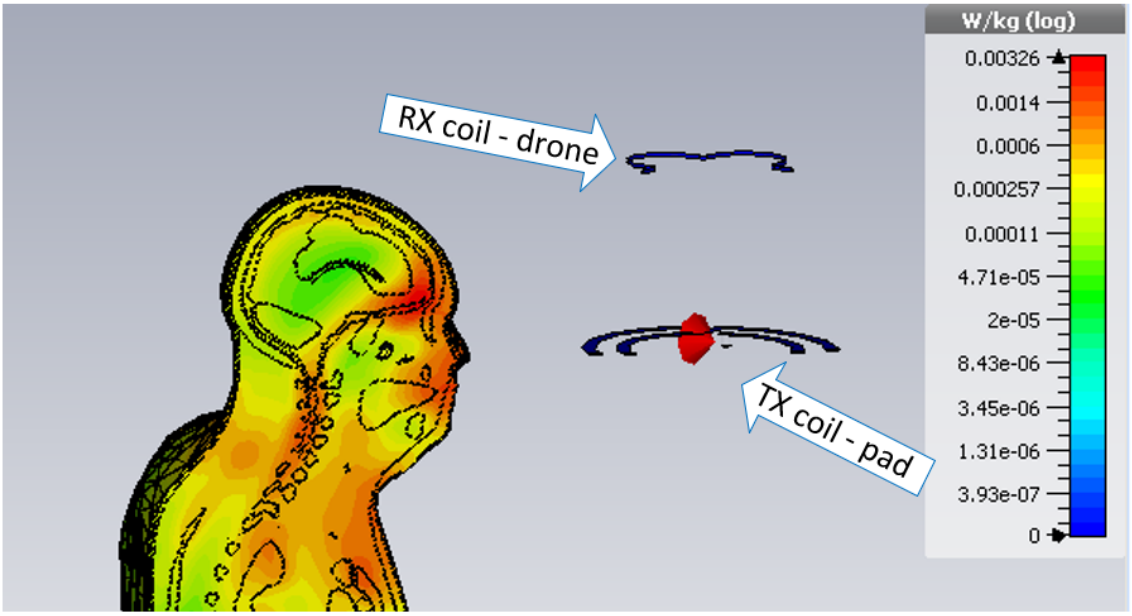


Figure 3.4: SAR distribution with Nelly's head 10 cm from the transmitter coil's outer edge in the horizontal direction

This shows how conservative the reference levels are for scenarios where human body exposure to high magnetic fields is very localised.

3.4 Summary

With respect to the design of WPT systems for implantable medical devices, the following safety limits will be used as design constraints in the next chapter: maximum temperature rise of 2 °C (from EN 45502-1), maximum SAR of 0.08 W kg^{-1} (whole body), 2 W kg^{-1} (head and trunk), and 4 W kg^{-1} (limbs) (from ICNIRP 1998 - General Public), and maximum internal electric field of 915 V m^{-1} (from ICNIRP 2010 - 6.78 MHz systems only).

To ensure compatibility of the implanted receiver system within MRI environments, electromagnetic and thermal simulations of the human body model and the medical implant situated inside the MRI scanner will need to be performed to ensure the SAR and temperature limits specified in Tables 3.6 and 3.7 are not exceeded, along with the limits on the static magnetic fields and the time-varying gradient magnetic field. These simulations are not within the scope of this thesis, but will need to be performed to make

sure that the implant is 'MR conditional'.

In this chapter, the thermal and non-thermal effects of human exposure to the high-frequency magnetic field generated by a WPT system were described. In addition, for WPT systems with an implanted receiver, the additional coil dissipation's contribution to overall temperature rise was highlighted. The standards and guidelines that govern the exposure of humans to EM fields, the maximum temperature rise of the surface of an AIMD, an AIMD's immunity to external EM fields, and MRI compatibility were outlined. Lastly, using the Wirelessly-Powerered Drone experimental demonstrator as an example, the process of evaluating a WPT system's compliance with safety limits with 3D EM field simulations was shown. The concepts, methods and procedures presented in this chapter are important for understanding what additional constraints and objectives are relevant when designing a WPT system for high-power medical implants; this will be the topic of the following chapter.

Chapter 4

Wireless power delivery for high-power implantable medical devices

The design of wireless power transfer (WPT) systems in free-space or air has been well documented in a number of sources, in which the main design objective is to maximise link efficiency [1, 2, 3]. The conditions for optimising the link efficiency of such WPT systems were explained in Chapter 2.

However, for systems with a receiver coil and electronics implanted inside a patient, the interaction between the high-frequency magnetic fields employed by WPT systems and the electrically conductive biological tissue of the human body modifies the magnetic link and the field distributions. Parameters that were chosen to be optimal in air, such as frequency, coil geometry and receiver load, may need to be altered so that the system achieves maximum link efficiency in the presence of the human body.

Furthermore, additional constraints and requirements have to be imposed, which include reducing specific absorption rate (SAR), internal electric fields and tissue temperature rises in order to meet relevant safety limits. These constraints are needed to minimise the adverse health effects of a wirelessly-powered medical implant on the human body (the safety constraints and the causes of the health effects were explained in detail in

Chapter 3). They will influence more significantly the design of higher-power biomedical devices such as ventricular assist devices and total artificial hearts (with the former typically requiring approximately 14 W average power [23]); the design of WPT systems for such devices is the focus of this chapter. Changing the design criteria allows a system to be safer in the presence of human beings and to comply with relevant regulations. Electromagnetic and thermal simulations with human body models are able to show the effect of new design principles on not only the link efficiency of the system, but also SAR, the internal electric field, and tissue temperature rises experienced by patients fitted with these implants [74].

This chapter explores how the presence of living objects affects the characteristics of the coils and the magnetic link of a WPT system, and how the parameters that optimise the system in air differ from those for a system in which a receiver is implanted in a patient. It also details the additional design constraints imposed on such systems, arising from the need to meet safety limits. Results from electromagnetic and thermal simulations are presented which illustrate the improvements to link efficiency and safety of a system with these new parameters.

4.1 System and link analysis

4.1.1 Conditions for maximum link efficiency

The conditions for maximising the link efficiency of a WPT system in air were laid out in Chapter 2. However, if the receiver of such a system is implanted inside a human body, the expressions for the tuning capacitance and the optimal load for achieving the theoretical maximum link efficiency will be different from a system in air. This is due to the presence of a conductive medium, which alters the model of a wireless power transfer system.

A WPT system can be considered as a two-port network, as illustrated in Figure 4.1. Port 1 represents the transmitter end and Port 2 denotes the receiver end of the WPT system. Two-port S-parameters (whether obtained via measurement with vector net-

work analysers or from numerical simulations) for such a network can be converted to Z-parameters using the equations in (4.1) [75], with Z_0 denoting the characteristic impedance, which is $50\,\Omega$ in the simulations presented in this chapter.

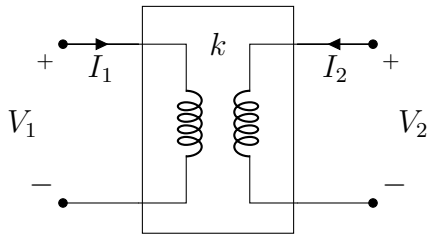


Figure 4.1: Wireless power transfer system as two-port network with Z-parameters

$$\begin{aligned}
Z_{11} &= \frac{(1+S_{11})(1-S_{22})+S_{12}S_{21}}{(1-S_{11})(1-S_{22})-S_{12}S_{21}}Z_0 \\
Z_{12} &= \frac{2S_{12}}{(1-S_{11})(1-S_{22})-S_{12}S_{21}}Z_0 \\
Z_{21} &= \frac{2S_{21}}{(1-S_{11})(1-S_{22})-S_{12}S_{21}}Z_0 \\
Z_{22} &= \frac{(1-S_{11})(1+S_{22})+S_{12}S_{21}}{(1-S_{11})(1-S_{22})-S_{12}S_{21}}Z_0
\end{aligned} \tag{4.1}$$

The current-to-voltage relationships for this network are shown in Equations (4.2) and (4.3):

$$V_1 = Z_{11}I_1 + Z_{12}I_2 \tag{4.2}$$

$$V_2 = Z_{21}I_1 + Z_{22}I_2 \tag{4.3}$$

Since a WPT system is a reciprocal network ($Z_{12} = Z_{21}$), it can be represented by the equivalent circuit shown in Figure 4.2 [75]. The two-port complex impedance quantities in Figure 4.2 can be defined in terms of reactances, resistances and inductances, as given by Equations (4.4), (4.5) and (4.6).

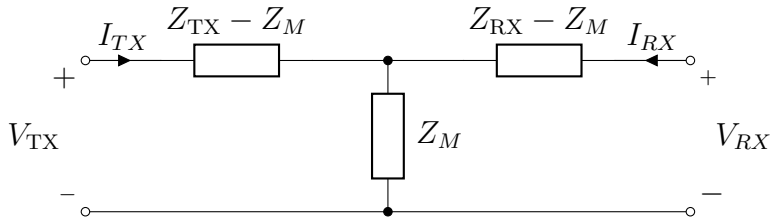


Figure 4.2: Equivalent circuit of reciprocal two-port network in terms of Z-parameters

$$Z_{\mathrm{TX}} = R_{\mathrm{TX}} + jX_{\mathrm{TX}} = R_{\mathrm{TX}} + j\omega L_{\mathrm{TX}} \tag{4.4}$$

$$Z_{\mathrm{RX}} = R_{\mathrm{RX}} + jX_{\mathrm{RX}} = R_{\mathrm{RX}} + j\omega L_{\mathrm{RX}} \tag{4.5}$$

$$Z_{\mathrm{M}} = R_{\mathrm{M}} + jX_M = R_{\mathrm{M}} + j\omega M \tag{4.6}$$

ω is the frequency of operation multiplied by 2π. Z_{TX} represents the complex impedance of the transmitter coil and consists of its combined resistances, R_{TX}, and its self-inductance, L_{TX}. Z_{RX} is the complex impedance of the receiver coil and consists of its combined resistances, R_{RX}, and its self-inductance, L_{RX}. Z_M denotes the complex mutual impedance between the transmitter and receiver coils. In air, Z_M is purely imaginary and is equal to $j\omega M$, where M is the mutual inductance. However, in the presence of conductive media, the real part of Z_M, defined as a mutual resistance and denoted by R_M, is typically non-zero. This is mainly due to an additional magnetic field generated by eddy currents in the human body, which are induced by the transmitter-generated magnetic field; this additional magnetic field, which is 90° out-of-phase with the magnetic field generated by the transmitter coil, induces another electromotive force (EMF) in the receiver coil.

The current-to-voltage relationships for the reciprocal network in Figure 4.2 in terms of its complex impedances are given by Equations (4.7) and (4.8).

$$V_{\mathrm{TX}} = Z_{\mathrm{TX}} I_{\mathrm{TX}} + Z_M I_{\mathrm{RX}} \tag{4.7}$$

$$V_{\mathrm{RX}} = Z_M I_{\mathrm{TX}} + Z_{\mathrm{RX}} I_{\mathrm{RX}} \tag{4.8}$$

V_{TX} in Equation (4.7) is the voltage of the transmitter coil and V_{RX} in Equation (4.8) is the voltage of the receiver coil. I_{TX} is the current through the transmitter coil and I_{RX} is the current through the receiver coil. The induced EMF in the receiver coil, V_{ind}, is

represented in Equation (4.8) by $Z_M I_{\mathrm{TX}}$.

The expressions for optimal load and tuning capacitance to attain maximum efficiency for a series-tuned system have been derived in [19] using ABCD parameters and are given by Equations (4.9) and (4.10), respectively.

$$R_{L,opt} = \frac{\sqrt{\left(R_{\mathrm{TX}}R_{\mathrm{RX}} + (\omega M)^2\right)\left(R_{\mathrm{TX}}R_{\mathrm{RX}} - R_M^2\right)}}{R_{\mathrm{TX}}} \tag{4.9}$$

$$C_{tune,opt} = \frac{1}{\omega^2\left(L_{\mathrm{RX}} - \frac{MR_M}{R_{\mathrm{TX}}}\right)} \tag{4.10}$$

In air, where R_M is equal to zero, Equations (4.9) and (4.10) simplify to expressions that were presented in Chapter 2 for the tuning capacitance that resonates with the receiver coil and for the optimal load.

The maximum link efficiency of this 2-port network is given by Equations (4.11) and (4.12).

$$\eta_{\max} = \frac{\chi}{\left(1 + \sqrt{1+\chi}\right)^2} \tag{4.11}$$

$$\chi = \frac{|Z_M|^2}{R_{\mathrm{TX}}R_{\mathrm{RX}} - R_M^2} \tag{4.12}$$

In air, where $R_M = 0$, Equation (4.12) becomes $\chi = k^2 Q_{\mathrm{TX}} Q_{\mathrm{RX}}$ and the expression for maximum link efficiency reduces to Equation (2.13) in Chapter 2.

4.1.2 A general link efficiency expression

If the same expressions for the tuning capacitance and optimal load in air (using resonant tuning) were used for a WPT system with an implanted receiver, the maximum link efficiency equation for air given in Chapter 2 would no longer be valid. This is because when a WPT system operates in the presence of living objects, the real part of the mutual impedance can no longer be assumed to be zero, due to additional magnetic fields

generated by the circulating eddy currents in the human body. In addition, it would be interesting to find out how attaching a non-optimal load resistance to the receiver affects the link efficiency. Therefore, a more generalised link efficiency expression for a system must be derived for any load resistance and tuning capacitance, given the Z-parameters of a two-port network.

Firstly, let a complex load impedance Z_L be written as in Equation (4.13), where R_L is the load resistance, X_L is the reactance of the tuning capacitor and C_{tune} is the tuning capacitance.

$$Z_L = R_L + jX_L = R_L - \frac{j}{\omega C_{\text{tune}}} \tag{4.13}$$

If Z_L is attached to the receiver end as shown in Figure 4.3, the relationship between the voltage and current at the receiver end is given by Equation (4.14).

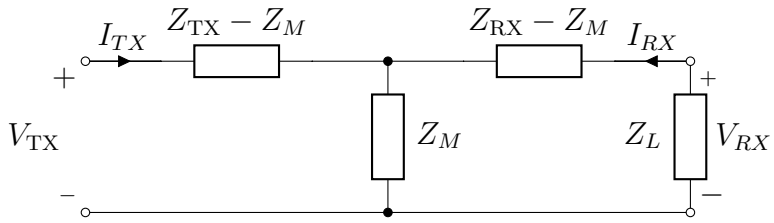


Figure 4.3: Equivalent circuit of reciprocal two-port network in terms of Z-parameters with an attached load Z_L at the receiver end

$$V_{\text{RX}} = -I_{\text{RX}} Z_L \tag{4.14}$$

Equation (4.8) then becomes:

$$-I_{\text{RX}} Z_L = Z_M I_{\text{TX}} + Z_{\text{RX}} I_{\text{RX}} \tag{4.15}$$

Rearranging Equation (4.15) for I_{RX} gives the following:

$$I_{\text{RX}} = -\frac{Z_M}{Z_{\text{RX}} + Z_L} I_{\text{TX}} \tag{4.16}$$

Plugging Equation (4.16) into Equation (4.7), the following equation is obtained:

$$V_{\mathrm{TX}} = Z_{\mathrm{TX}} I_{\mathrm{TX}} - \frac{Z_M^2}{Z_{\mathrm{RX}} + Z_L} I_{\mathrm{TX}} \tag{4.17}$$

The total input impedance of the two port network is therefore:

$$Z_{\mathrm{IN}} = \frac{V_{\mathrm{TX}}}{I_{\mathrm{TX}}} = Z_{\mathrm{TX}} - \frac{Z_M^2}{Z_{\mathrm{RX}} + Z_L} \tag{4.18}$$

The link efficiency of the system is the ratio between the receiver load power and the transmitted power. The received load power is given in Equation (4.19).

$$P_R = \frac{\Re\left(Z_L\right) |I_{\mathrm{RX}}|^2}{2} \tag{4.19}$$

The transmitted power is given in Equation (4.20).

$$P_T = \Re\left(Z_{\mathrm{TX}} - \frac{Z_{\mathrm{M}}^2}{Z_{\mathrm{RX}} + Z_L}\right) \frac{|I_{\mathrm{TX}}|^2}{2} \tag{4.20}$$

The link efficiency can therefore be expressed as in Equation (4.21):

$$\begin{aligned} \eta_{\mathrm{link}} = \frac{P_R}{P_T} &= \frac{\Re\left(Z_L\right) |I_{\mathrm{RX}}|^2}{\Re\left(Z_{\mathrm{TX}} - \frac{Z_{\mathrm{M}}^2}{Z_{\mathrm{RX}} + Z_L}\right) |I_{\mathrm{TX}}|^2} \\ &= \frac{R_L |I_{\mathrm{RX}}|^2}{R_{\mathrm{TX}} - \Re\left(\frac{Z_{\mathrm{M}}^2}{Z_{\mathrm{RX}} + Z_L}\right) |I_{\mathrm{TX}}|^2} \end{aligned} \tag{4.21}$$

Note that from Equation (4.16):

$$\begin{aligned} \frac{|I_{\mathrm{RX}}|^2}{|I_{\mathrm{TX}}|^2} &= \left|\frac{I_{\mathrm{RX}}}{I_{\mathrm{TX}}}\right|^2 \\ &= \left|\frac{Z_M}{Z_{\mathrm{RX}} + Z_L}\right|^2 \\ &= \frac{|Z_M|^2}{|Z_{\mathrm{RX}} + Z_L|^2} \\ &= \frac{R_M^2 + X_M^2}{\left(R_{\mathrm{RX}} + R_L\right)^2 + \left(X_{\mathrm{RX}} + X_L\right)^2} \end{aligned} \tag{4.22}$$

Also,

$$\begin{aligned}
&\Re\left(\frac{Z_{\mathrm{M}}^2}{Z_{\mathrm{RX}}+Z_L}\right)\\
&=\Re\left(\frac{R_M^2-X_M^2+j2R_MX_M}{R_{\mathrm{RX}}+R_L+j(X_{\mathrm{RX}}+X_L)}\right)\\
&=\Re\left(\frac{R_M^2-X_M^2+j2R_MX_M}{R_{\mathrm{RX}}+R_L+j(X_{\mathrm{RX}}+X_L)}\cdot\frac{R_{\mathrm{RX}}+R_L-j(X_{\mathrm{RX}}+X_L)}{R_{\mathrm{RX}}+R_L-j(X_{\mathrm{RX}}+X_L)}\right)\\
&=\frac{(R_M^2-X_M^2)(R_{\mathrm{RX}}+R_L)+2R_MX_M(X_{\mathrm{RX}}+X_L)}{(R_{\mathrm{RX}}+R_L)^2+(X_{\mathrm{RX}}+X_L)^2}
\end{aligned}\tag{4.23}$$

Hence, from Equations (4.21), (4.22), and (4.23), Equation (4.24) can be obtained, which gives a general expression for link efficiency of a two port network in terms of its z-parameters, when a resistive load R_L and a reactive load X_L are connected in series to the output.

$$\begin{aligned}
\eta_{\mathrm{link}}=\frac{R_L(R_M^2+X_M^2)}{R_{\mathrm{TX}}\left((R_{\mathrm{RX}}+R_L)^2+(X_{\mathrm{RX}}+X_L)^2\right)\\
+(X_M^2-R_M^2)(R_{\mathrm{RX}}+R_L)-2R_MX_M(X_{\mathrm{RX}}+X_L)}
\end{aligned}\tag{4.24}$$

Out of interest, the optimal load parameters for a WPT system can be calculated directly from the Z-parameters of the two-port network (as opposed to the ABCD parameters in [19]). The derivation involves finding values of X_L and R_L that maximise η_{link}.

Firstly, by inspection, it can be seen that in order to maximise η_{link} with respect to X_L, the denominator of Equation (4.24) needs to be minimised with respect to X_L.

The derivative of the denominator in Equation (4.24) with respective to X_L is:

$$2R_{\mathrm{TX}}(X_{\mathrm{RX}}+X_L)-2R_MX_M \tag{4.25}$$

Setting the expression in (4.25) to zero and re-arranging for $X_L=X_{\mathrm{L,opt}}$, the reactive load required for maximising link efficiency is obtained:

$$X_{\mathrm{L,opt}}=\frac{R_MX_M}{R_{\mathrm{TX}}}-X_{\mathrm{RX}} \tag{4.26}$$

The equivalent tuning capacitance is then calculated using:

$$C_{\text{tune,opt}} = \frac{-j}{\omega X_{\text{L,opt}}} \tag{4.27}$$

The maximum link efficiency with respect to the resistive load R_L can be found by substituting $X_L = X_{\text{L,opt}}$ into Equation (4.24) and differentiating the resulting link efficiency expression with respect to R_L:

$$\eta_{\text{link}} = \frac{A_1 R_L}{A_2 R_L^2 + A_3 R_L + A_4} \tag{4.28}$$

where

$$\begin{aligned} A_1 &= R_{\text{TX}}(R_M^2 + X_M^2) \\ A_2 &= R_{\text{TX}}^2 \\ A_3 &= 2R_{\text{TX}}^2 R_{\text{RX}} + R_{\text{TX}} X_M^2 - R_{\text{TX}} R_M^2 \\ A_4 &= R_{\text{TX}}^2 R_{\text{RX}}^2 + R_{\text{TX}} X_M^2 R_{\text{RX}} - R_{\text{TX}} R_M^2 R_{\text{RX}} - R_M^2 X_M^2 \end{aligned} \tag{4.29}$$

$$\frac{\mathrm{d}\eta_{\text{link}}}{\mathrm{d}R_L} = \frac{A_1(A_2 R_L^2 + A_3 R_L + A_4) - A_1 R_L(2A_2 R_L + A_3)}{(A_2 R_L^2 + A_3 R_L + A_4)^2} \tag{4.30}$$

Assume that the denominator of derivative of the link efficiency in Equation (4.30) is non-zero. Letting the numerator of Equation (4.30) equal to zero, and rearranging for $R_L = R_{\text{L,opt}}$ gives the load resistance for maximising link efficiency:

$$R_{L,opt} = \frac{\sqrt{(R_{\text{TX}} R_{\text{RX}} + X_M^2)\,(R_{\text{TX}} R_{\text{RX}} - R_M^2)}}{R_{\text{TX}}} \tag{4.31}$$

One can observe that if $R_M = 0$ for a system in air or free-space, then Equations (4.31) and (4.26) for optimal load and series tuning capacitance reduce to those for resonant coupling and maximum link efficiency in air that were introduced in Chapter 2.

The input impedance of the circuit in Figure 4.3 was derived and is given by Equation (4.18). From this equation, it can be seen that the input impedance consists of the transmitter coil's own impedance Z_{TX} and the reflected impedance, Z_{refl}, which is given

by Equation (4.32).

$$Z_{\text{refl}} = -\frac{Z_M^2}{Z_{\text{RX}} + Z_L} \tag{4.32}$$

The reflected impedance can now be calculated for any load resistance and tuning capacitance, given the mutual impedance and the impedance of the receiver coil.

4.1.3 Coil currents and voltages

The currents through and the voltages across the coils for a wireless power transfer system given the received power P_{RX}, load resistance R_L and tuning capacitance C_{tune} and the impedance parameters of the two-port network (Z_{TX}, Z_{RX} and Z_{M}) can now be derived.

The current through the receiver coil I_{RX} in terms of the received power P_{RX} and load resistance R_L is calculated by the following equation:

$$I_{\text{RX}} = -\sqrt{\frac{2P_{\text{RX}}}{R_L}} \tag{4.33}$$

The voltage across the receiver coil V_{RX} is given by the following equation:

$$\begin{aligned} V_{\text{RX}} &= -I_{\text{RX}} Z_L \\ &= -I_{\text{RX}} \left(R_L - \frac{j}{\omega C_{\text{tune}}} \right) \\ &= \sqrt{\frac{2P_{\text{RX}}}{R_L}} \left(R_L - \frac{j}{\omega C_{\text{tune}}} \right) \end{aligned} \tag{4.34}$$

The required induced EMF at the receiver coil due to a current at the transmitter coil is given by:

$$\begin{aligned} V_{\text{ind}} &= -I_{\text{RX}} \left(Z_{\text{RX}} + Z_L \right) \\ &= -I_{\text{RX}} \left(R_{\text{RX}} + j\omega L_{\text{RX}} - \frac{j}{\omega C_{\text{tune}}} + R_L \right) \\ &= \sqrt{\frac{2P_{\text{RX}}}{R_L}} \left(R_{\text{RX}} + j\omega L_{\text{RX}} - \frac{j}{\omega C_{\text{tune}}} + R_L \right) \end{aligned} \tag{4.35}$$

The transmitter coil current needed to induce the required EMF at the receiver coil

is given by:

$$\begin{aligned} I_{\mathrm{TX}} &= \frac{V_{\mathrm{ind}}}{Z_M} \\ &= \frac{1}{R_M + j\omega M}\sqrt{\frac{2P_{\mathrm{RX}}}{R_L}}\left(R_{\mathrm{RX}} + j\omega L_{\mathrm{RX}} - \frac{j}{\omega C_{\mathrm{tune}}} + R_L\right) \end{aligned} \tag{4.36}$$

Lastly, the transmitter coil voltage is given by:

$$\begin{aligned} V_{\mathrm{TX}} &= I_{\mathrm{TX}}Z_{\mathrm{TX}} + I_{\mathrm{RX}}Z_M \\ &= \frac{R_{\mathrm{TX}} + j\omega L_{\mathrm{TX}}}{R_M + j\omega M}\sqrt{\frac{2P_{\mathrm{RX}}}{R_L}}\left(R_{\mathrm{RX}} + j\omega L_{\mathrm{RX}} - \frac{j}{\omega C_{\mathrm{tune}}} + R_L\right) \\ &\quad - \sqrt{\frac{2P_{\mathrm{RX}}}{R_L}}\left(R_M + j\omega M\right) \end{aligned} \tag{4.37}$$

It is possible to select a load resistance that minimises the voltage across the receiver coil. This can be done to limit the electric fields present in the human body caused by the receiver coil. The square of the absolute value of the receiver coil voltage is:

$$\begin{aligned} |V_{\mathrm{RX}}|^2 &= \frac{2P_{\mathrm{RX}}}{R_L}\left(R_L^2 + \left(\frac{1}{\omega C_{\mathrm{tune}}}\right)^2\right) \\ &= 2P_{\mathrm{RX}}R_L + \frac{2P_{\mathrm{RX}}}{R_L}\left(\frac{1}{\omega C_{\mathrm{tune}}}\right)^2 \end{aligned} \tag{4.38}$$

Differentiating Equation (4.38) and equating to zero gives:

$$\begin{aligned} \frac{\mathrm{d}\,|V_{\mathrm{RX}}|^2}{\mathrm{d}R_L} &= 0 \\ 2P_{\mathrm{RX}} - \frac{2P_{\mathrm{RX}}}{R_L^2}\left(\frac{1}{\omega C_{\mathrm{tune}}}\right)^2 &= 0 \end{aligned} \tag{4.39}$$

Rearranging Equation (4.39) for R_L gives:

$$R_L = \frac{1}{\omega C_{\mathrm{tune}}} \tag{4.40}$$

If resonant tuning is used, where $-\frac{j}{\omega C_{\mathrm{tune}}} = j\omega L_{\mathrm{RX}}$, then Equation (4.40) can be

expressed as:

$$R_L = \omega L_{\mathrm{RX}} \tag{4.41}$$

The resulting expression for V_{RX} with the load resistance given in Equation (4.40) is:

$$V_{\mathrm{RX}} = \sqrt{\frac{4P_{\mathrm{RX}}}{\omega C_{\mathrm{tune}}}} \tag{4.42}$$

4.2 Design methods and simulations

In this section, design methods taking into account the safety issues and the interaction between WPT systems and the human body discussed in Chapter 3 are introduced.

In the analyses and simulations that follow, it is assumed that both the transmitter coil and the receiver coil are planar square spirals with a thin, rectangular cross-section. The thickness of the conductor is assumed to be 70 µm, which is the typical trace thickness of printed circuit boards (PCBs) constructed with 2 oz copper.

The receiver coil, being implanted in the chest area 1 cm underneath the outer surface of the skin, has a maximum outer dimension of 5 cm for patient comfort and is of the same order of magnitude as the size of left ventricular assist devices (LVADs). It is encapsulated in polydimethylsiloxane (PDMS), a type of medical-grade silicone, to prevent direct electrical contact with the biological tissue; the thickness of this coating is 300 µm, which is the optimal thickness for PCBs in human tissue [16]. The trace width is chosen to be 3 mm, with a trace spacing of 3 mm. The receiver coil is intended to be implanted a maximum of 1 cm inside the abdomen within the subcostal region (under the ribs); this is where existing driveline incisions for LVADs are situated. The depth of the coil need not be too great, as wires can run from the coil to the LVAD located in the thoracic region. Figure 4.4 is a diagram of the encapsulated receiver coil. Figures 4.5 and 4.6 show the position of the receiver inside the human body model (side-view and top-view, respectively).

In terms of the transmitter coil and the coil separation distance, two different scenarios are analysed and simulated. In both scenarios, it is assumed that there is perfect

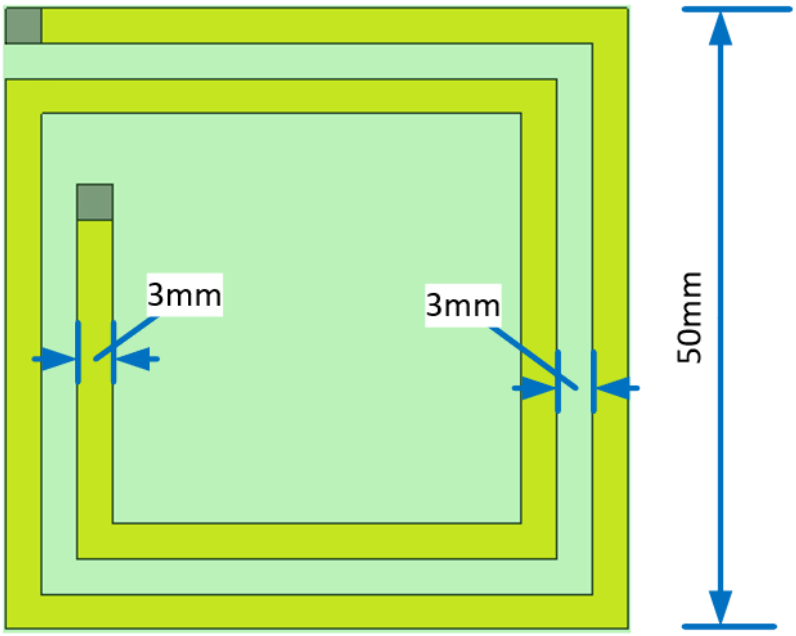


Figure 4.4: Receiver coil, with 0.3 mm encapsulation shown in green

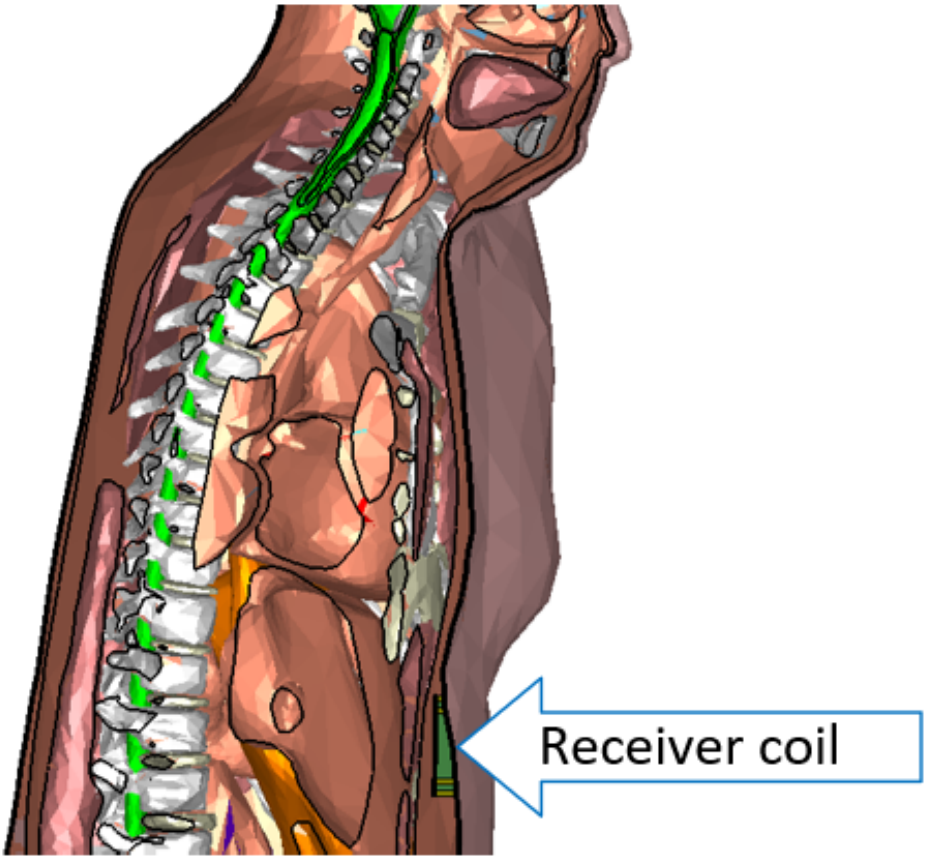


Figure 4.5: Position of encapsulated receiver coil in human body model (cross-section, side view)

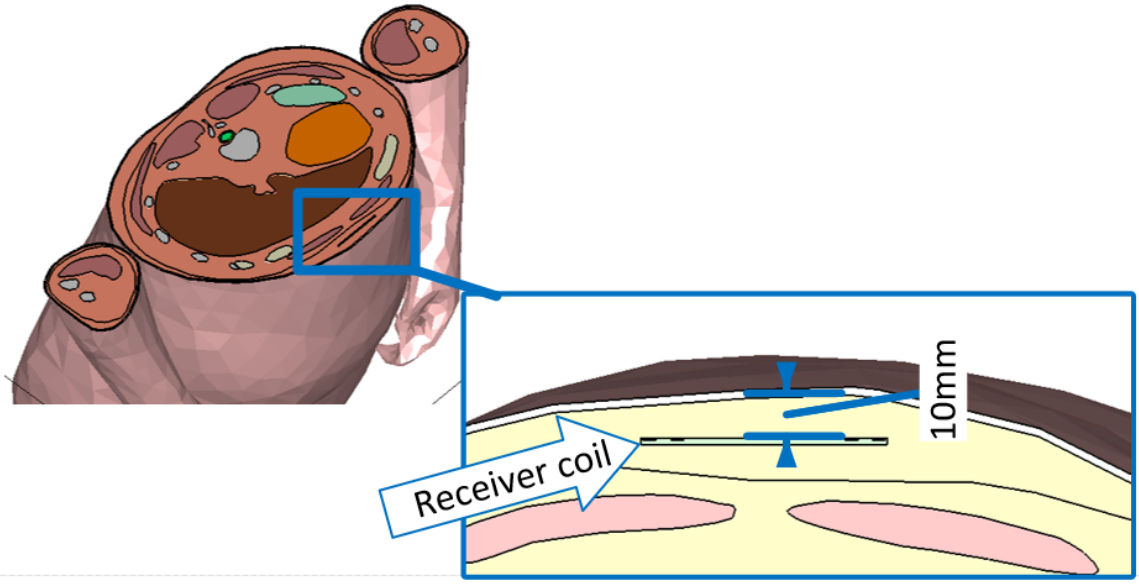


Figure 4.6: Position of encapsulated receiver coil in human body model (cross-section, top view)

alignment between the transmitter coil and the receiver coil. The first case involves a short-range power transfer between a small external transmitter and an implanted receiver. The transmitter coil is designed to be worn on the body in a vest and has a maximum outer dimension of 10 cm. This size allows for good magnetic field coverage and offset tolerance, but most importantly is small enough to ensure patient comfort and freedom to move around when the vest is worn. The trace width of the transmitter coil is 4 mm, with a trace spacing of 4 mm. Figure 4.7 shows a diagram of this transmitter coil. The maximum distance between the two coils is 2 cm (centre of coils on axis).

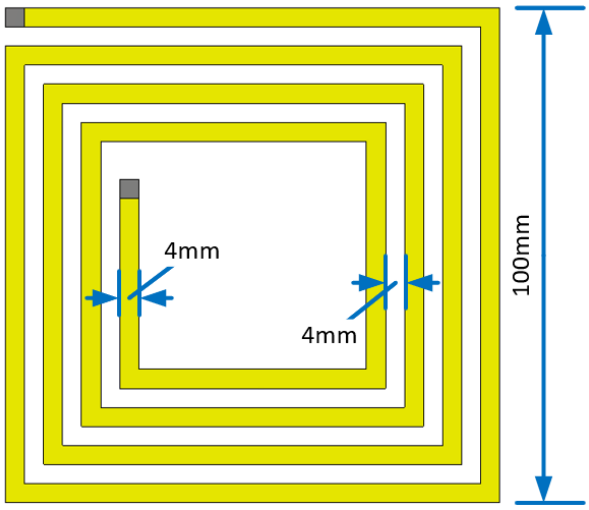


Figure 4.7: Smaller transmitter coil for short-range power transfer

The second scenario consists of a transmitter situated further away from the receiver coil and the patient; the maximum distance between the coils is 30 cm. For longer distances, the transmitter coil needs to be much larger to maintain adequate flux coverage across the receiver coil. For this case, a maximum dimension of 50 cm is chosen. The trace width of the transmitter coil is 15 mm, with a trace spacing of 10 mm. Figure 4.8 shows a diagram of this transmitter coil. This setup has the advantage of being able to power an implantable medical device without wearing an additional vest on the body, thus eliminating the weight of the transmitter coil, power electronics and batteries that the patient would have had to carry on them. The implant could be powered whilst the patient is sitting down or sleeping, with the transmitter placed behind a chair or underneath a mattress.

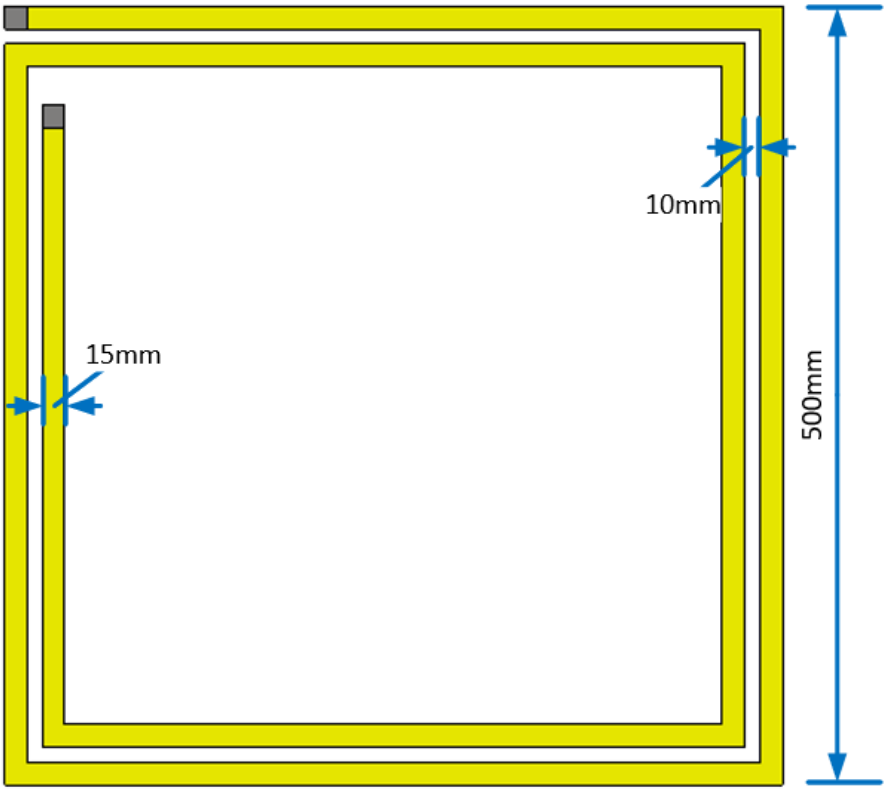


Figure 4.8: Larger transmitter coil for longer-range power transfer

Planar spiral coils are preferred as implants due to the small volume that they occupy under the skin or in the chest cavity. They can be easily manufactured as they are able to be printed on a substrate like a PCB. Planar flat coils are also chosen for the transmitter pad, as it would also be preferable to have something lightweight and thin on

the surface of the body for patient comfort or against furniture. Helical coils add volume and, therefore, do not work well as vest coils or implantable coils, or as an unobtrusive addition to existing furnishings.

The received power is 15 W, which is the maximum amount required by LVADs [23]. The receiver coil is series tuned, and it is assumed in both the simulations and analyses that the receiver load does not dissipate any heat.

The effects of varying the following parameters on link efficiency and heating will be studied in this chapter: frequency, number of turns, tuning configuration and receiver load.

4.2.1 Simulation overview and configuration

Electromagnetic field simulations are carried out with CST Microwave Studio, a well-known commercial full-wave 3D high-frequency electromagnetic (EM) field simulator. It offers two types of solvers: the transient solver (using the Finite Integration Technique) and the frequency domain solver (using the Finite Element Method). The HUGO human body voxel model and those from the CST Voxel Family (Gustav, Laura, Katja (pregnant), baby, child, etc.) can only be used with the hexahedral structured mesh and transient solver. The consequence is that simulations with small details (e.g. the implanted receiver coil trace) but large overall dimensions (e.g. the human body) may take a long time to simulate, but it is nevertheless required when running simulations with voxel models to calculate the electromagnetic fields and SAR in the body. A range of voxel resolutions is available for use; the smallest voxel size that can be simulated is $1\,\text{mm} \times 1\,\text{mm} \times 1\,\text{mm}$.

However, if voxel models are not required, the frequency domain solver is generally more suitable for inductive power transfer (IPT) scenarios. This is because the frequency domain solver uses an unstructured tetrahedral mesh, so small details do not greatly slow down the overall simulation time, especially for electrically small structures. CAD human body models, such as Nelly, are available for use with the frequency domain solver to evaluate SAR and electromagnetic fields in a body. As very thin coils are being

used for the implanted receiver and the structures are electrically small compared to the wavelegth, the frequency domain solver with the Nelly human body model will be used in simulations in this chapter. According to the CST Studio Suite Help Documentation, Nelly is 'based on the work of the National Library of Maryland's research laboratory, who dissected, then photographed, a frozen female corpse.' [76]. The dielectric properties of the various types of biological tissues are generated using a macro provided by CST, and these are based on a 4-Cole-Cole model with parameters for each tissue type given by Gabriel et al. [77]. The dielectric properties of the metals are also provided by CST, whilst those of the silicone coating were obtained from other references [78]. Simulations that do not involve the human body are also run with the frequency domain solver.

A 1-coil S-parameter simulation can be performed in order to find out a coil's inductance and resistances (assuming a resistor-inductor (RL) coil model with an inductance L in series with a frequency-dependent resistance R), from which the Q factor can be evaluated over a range of frequencies. The resistance of a coil consists of a combination of the coil's skin effect and radiation losses, as well as eddy current losses and dielectric losses due to interaction of electromagnetic field with biological tissue.

A 2-coil S-parameter simulation can be used to find the mutual impedance between the transmitter and receiver coils at a desired separation distance. The theoretical maximum link efficiency, the required optimal load resistance, the tuning capacitance and the transmitter current for delivering 15 W to the receiver load at a particular frequency can then be derived from the Z-parameters of the two-port network.

After performing a 2-coil S-parameter simulation and calculating the link parameters to deliver 15 W to the receiver load at a certain frequency, the fields need to be combined in order to obtain the correct SAR and internal electric field for a particular load resistance and received power. Lastly, thermal simulations can be performed with the correct losses to obtain the corresponding temperature rises. Instead of re-running the entire simulation again with the capacitor and resistor attached to the receiver end as a lumped element, CST provides a circuit simulator, where circuit elements can be attached to the external ports of a EM field simulation block, for which S-parameters have already been calculated.

Using the circuit simulator, it is a straightforward process to attach the tuning capacitor and the receiver load to the receiver end of the two-port network. The transmitter coil is driven by a current source, which is configured appropriately to provide the correct magnetic field for the desired power to be consumed in the load. This method is valid for as long as the system can be considered linear (non-linearities may be introduced through the use of ferrites at high power levels where saturation may occur due to large currents and magnetic fields).

Thermal simulations are performed to find out the magnitude and distribution of the temperature rises in the human body due to the combination of dielectric heating, eddy current heating and coil resistive losses. These simulations are performed using CST MPhysics Studio, using the power loss distributions (surface losses for lossy metals and electric volume losses for normal dielectric materials) calculated from CST Microwave Studio. The thermal properties of air, copper and the various types of biological tissues are provided by CST, whilst those of the silicone coating are obtained from other references [78]. The thermal solver from CST MPhysics Studio also takes into account various biological cooling and heating mechanisms, including blood perfusion and basal metabolism, using a bioheat equation [76]. Convection of heat from the human body model to the surroundings was considered, and the convective heat transfer coefficients are obtained from [79].

4.2.2 Frequency and coil geometry

Chapter 2 explained how the resistance of a coil is frequency dependent. In air, the total resistance consists of AC coil losses (incorporating both the skin effect and proximity effect) and radiation losses. In the presence of a human body, there are two main additional losses. One source of losses is caused by eddy currents in the biological tissue, which is a result of the coil's high frequency magnetic field passing through the human body. Another source of losses is the dielectric loss due to the voltages between turns and across the coil, which produce electric fields that pass through conductive tissue. How these losses and coil Q factors vary with different parameters such as frequency, number

of coil turns and distance will be explored within this chapter. However, since WPT systems make use of a high-frequency magnetic field to deliver power, it is the tissue eddy current losses that will make up the bulk of the additional losses, and therefore will be the focus of this chapter.

The selection of frequency is mainly influenced by three factors. Firstly, it may be chosen to maximise link frequency, which in turn is influenced by the coils Q factors and the coupling factor of the magnetic link. The Q factor of a coil is frequency-dependent, but does not increase linearly with frequency. This is because a coil's resistance, which generally rises with frequency, is composed of alternating current (AC) coil losses and radiation losses, in addition to the human body losses as a result of eddy currents and high voltages. (Coil inductance is assumed to be constant with frequency.)

Secondly, the frequency selection should also consider the efficiency of the power electronics. Typically, switching losses increase with frequency, as the rise and fall times of the switching devices become comparable to the switching time. However, recent developments in highly efficiency soft-switching resonant inverters and rectifiers means that operating at high frequencies becomes feasible and efficient.

Thirdly, the frequency is chosen considering the interaction between the high-frequency magnetic field and the human body, and vice-versa. Compared with air, the Q factor of the coils is lower when placed in the vicinity of the body; this difference in Q factor is greater at higher frequencies. Therefore, the frequency at which link efficiency is maximised would be much lower than that for a system in air. Another issue to consider is how the amount of heating and the magnitude of temperature rises change at different frequencies for the same received power. In addition, it is preferable to operate at industrial, scientific and medical (ISM) band frequencies as they are unlicensed. 6.78 MHz and 13.56 MHz, the first two ISM bands, will be considered and compared throughout this chapter.

In the presence of the human body, the Q factors of the implanted receiver coil and both types of transmitter coil vary with the number of turns, at both 6.78 MHz and 13.56 MHz.

Figure 4.9 shows the Q factor of the human-implanted receiver coil, obtained from electromagnetic simulation using CST Microwave Studio. For both ISM band frequencies, it falls with the number of turns, which means a single turn loop has the greatest Q factor. The receiver coil, being placed under the skin, is surrounded by conductive tissue, so the losses in the human body are causing the Q factor to deteriorate quite significantly with the number of turns. In addition, the coil Q factors are generally lower at 13.56 MHz than at 6.78 MHz. At a higher frequency, the eddy current losses in the human body are greater, causing the Q factor to be smaller, and to deteriorate more rapidly with the number of turns.

Also shown in Figure 4.9 is the Q factor of the receiver coil in air at both frequencies. In air, the Q factor increases with the number of turns until it reaches a peak at 3 turns, after which it drops. This occurs at both of the ISM band frequencies. The Q factors at 13.56 MHz are greater than those at 6.78 MHz for all number of turns from 1 to 4. When implanted in the human body, the Q factor of the receiver coil is generally lower than that in air, due to the extra losses from being in the presence of the human body.

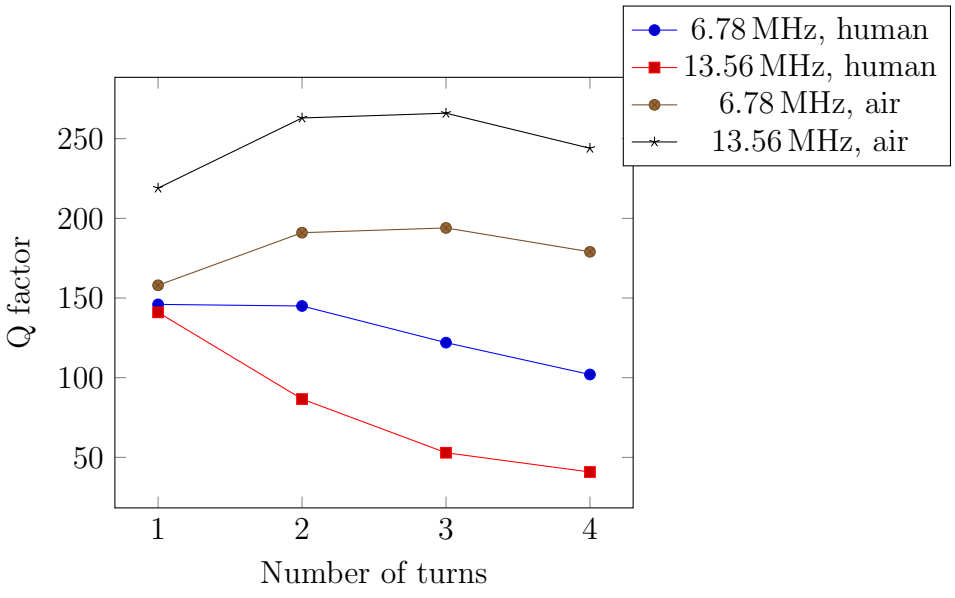


Figure 4.9: Variation of receiver coil Q factor with number of turns and frequency

Figure 4.10 shows the variation of the Q factor of the smaller transmitter coil with the number of turns, as used in the short-range scenario. At 1 and 2 turns, the Q factors of the coil at 13.56 MHz are greater than the corresponding values at 6.78 MHz. However,

at 3 and 4 turns, the Q factors of the coil at 13.56 MHz are lower than those at 6.78 MHz. At 6.78 MHz, the Q factor increases with number of turns, but at 13.56 MHz, the Q factor only increases from 1 to 3 turns, after which it starts to fall.

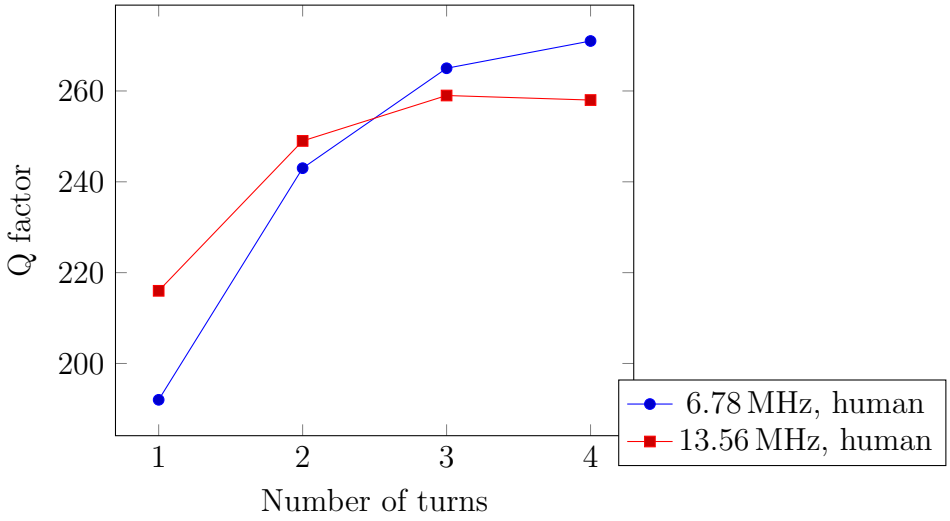


Figure 4.10: Variation of smaller transmitter coil Q factor with number of turns and frequency

Figure 4.11 shows the variation of the Q factor of the larger transmitter coil with the number of turns, as used in the longer-range scenario. Only 1- and 2-turn coils are considered, as this type of coil has a greater electrical length especially at 13.56 MHz. Therefore, with a higher number of turns, radiation would become more dominant [42]. Also, the parasitic capacitance is larger with this type of coil, so the system would be operating much closer to the transmitter coil's self-resonant frequency. In the presence of a human body, with only 1 turn, the Q factor of the coil at 13.56 MHz is greater than that at 6.78 MHz. With 2 turns the coil Q factor is greater at 6.78 MHz than at 13.56 MHz.

Figures 4.12, 4.13, 4.14 and 4.15 show the link efficiency for all combinations of turns, for the following scenarios and frequencies: short-range 6.78 MHz, short-range 13.56 MHz, longer-range 6.78 MHz and longer-range 13.56 MHz. Table 4.1 shows for each frequency and scenario the maximum link efficiencies and the turns combination used to achieve them.

The variation of the coil Q factors and system link efficiency over a range of frequencies can be studied further by running a broadband S-parameter simulation. Figure 4.16 shows the variation of the Q factor of a 2-turn receiver coil with frequency from 1 MHz

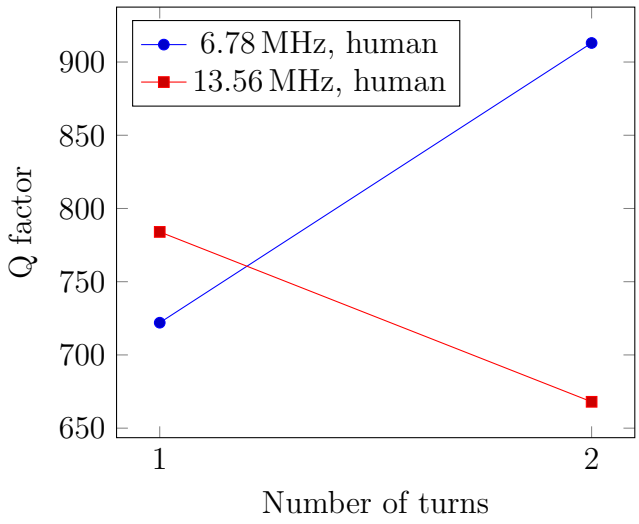


Figure 4.11: Variation of larger transmitter coil Q factor with number of turns and frequency

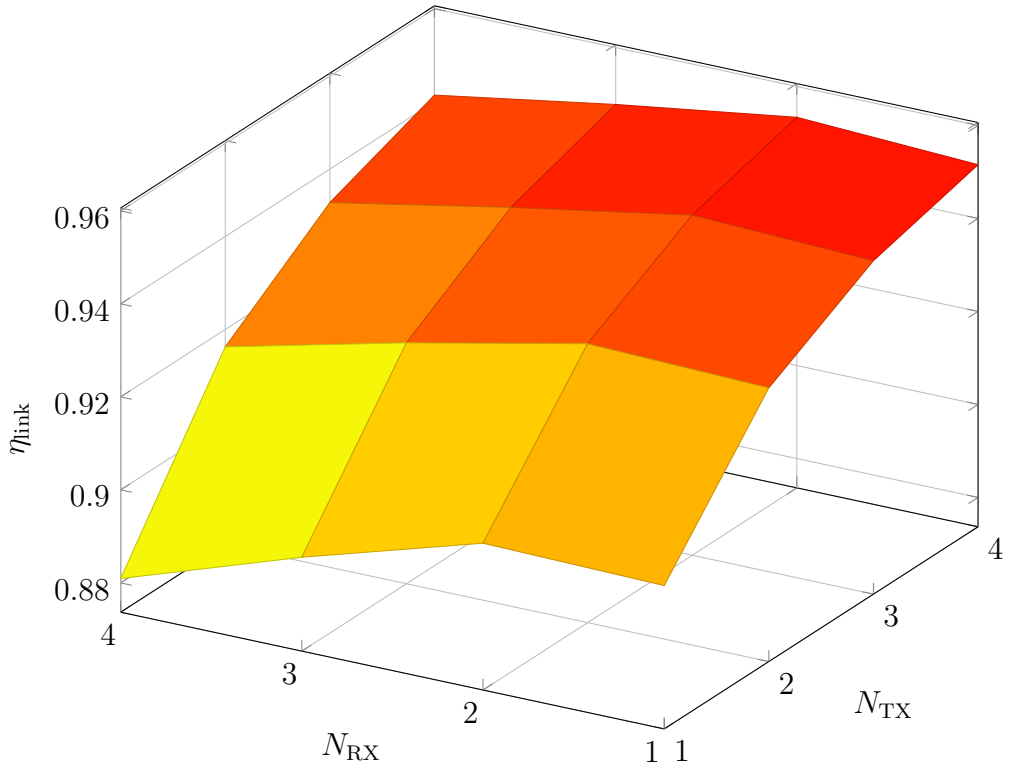


Figure 4.12: Link efficiency at 6.78 MHz in short-range scenario: variation with number of turns

Scenario	Frequency	N_{TX}	N_{RX}	η_{link}
Short-range	6.78 MHz	4	2	0.953
Short-range	13.56 MHz	4	1	0.952
Longer-range	6.78 MHz	2	2	0.316
Longer-range	13.56 MHz	2	1	0.305

Table 4.1: Maximum link efficiency and turns combination for each scenario and frequency

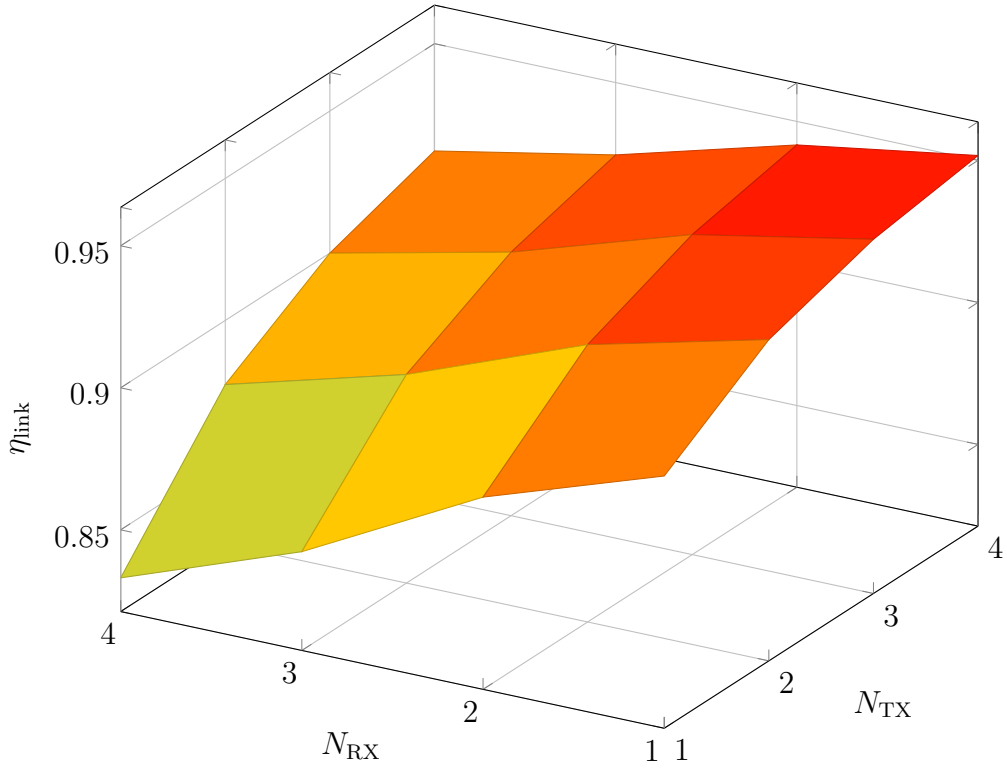


Figure 4.13: Link efficiency at 13.56 MHz in short-range scenario: variation with number of turns

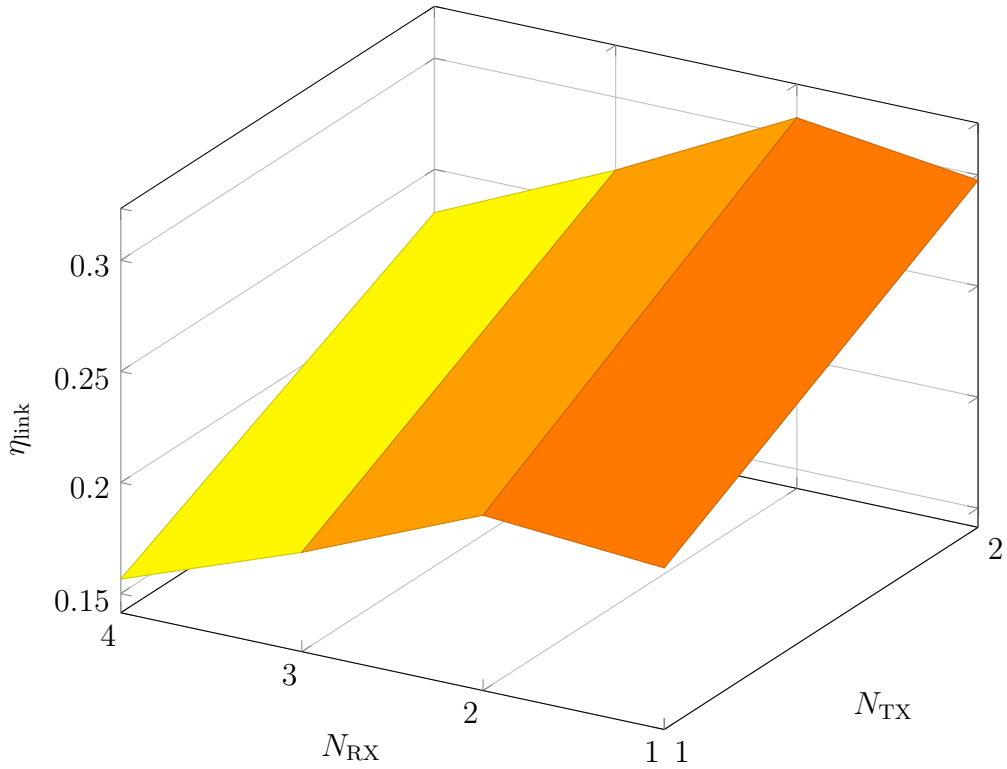


Figure 4.14: Link efficiency at 6.78 MHz in longer-range scenario: variation with number of turns

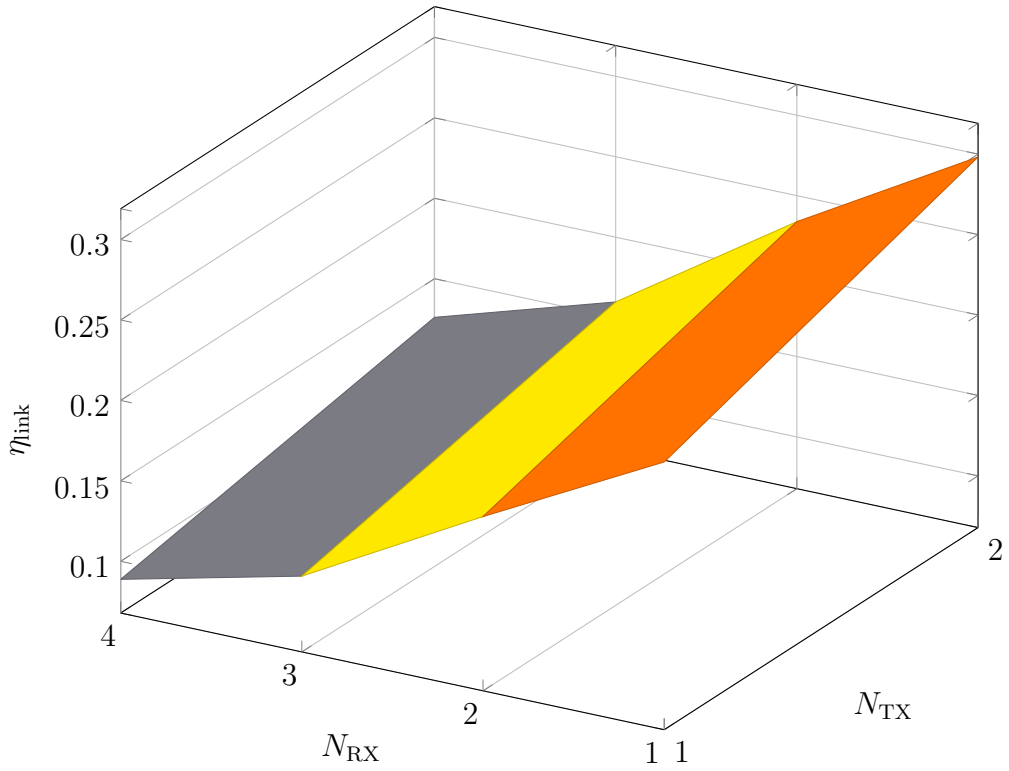


Figure 4.15: Link efficiency at 13.56 MHz in longer-range scenario: variation with number of turns

to 20 MHz, both in air and when implanted in the human body. Figure 4.17 shows the variation of the Q factor of a 4-turn transmitter coil over the same frequency range. In the presence of the human body, the maximum Q factor of the implanted receiver coil is 147 at a frequency of 5.77 MHz and the maximum Q factor of the transmitter coil is 269 at a frequency of 8.18 MHz. At those frequencies, the receiver Q factor in air is 179 and the transmitter Q factor in air is 365. The negative effect of the presence of the human body on the Q factor is very clear, especially at higher frequencies.

Figure 4.18 shows the resulting link efficiency of the short-range system over the same frequency range. The maximum link efficiency of the system in the presence of the human body is 0.953 at a frequency of 7.18 MHz, which is in between the frequencies that maximise the Q factor of the two coils. At the same frequency, the maximum link efficiency of the system in air is 0.964. Again, the presence of the human body causes the link efficiency to deteriorate, and this effect is more pronounced at higher frequencies.

Figure 4.19 is an equivalent circuit model of a coil that is implanted in the human body. In air, the coil model consists only of the series combination of L_{coil} (inductance of

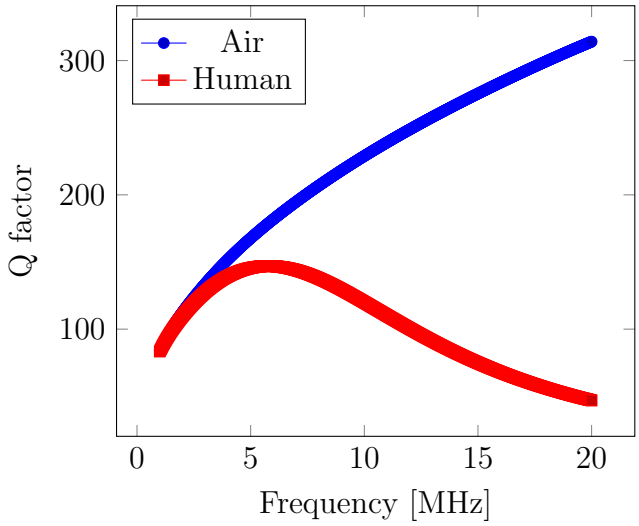


Figure 4.16: Receiver coil Q factor ($N_{\mathrm{RX}} = 2$)

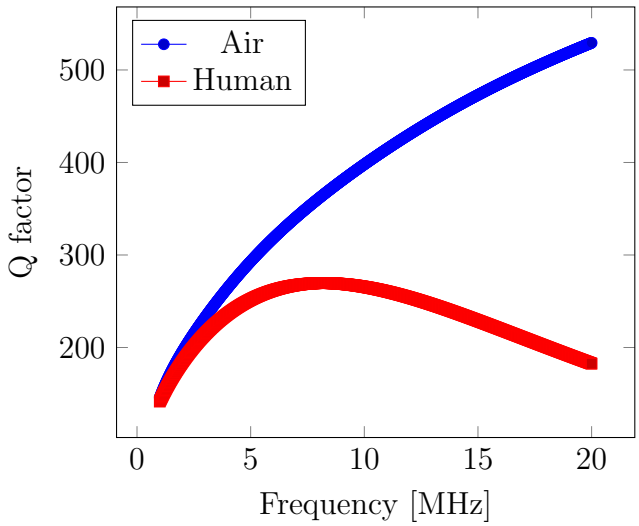


Figure 4.17: Smaller transmitter coil Q factor ($N_{\mathrm{TX}} = 4$)

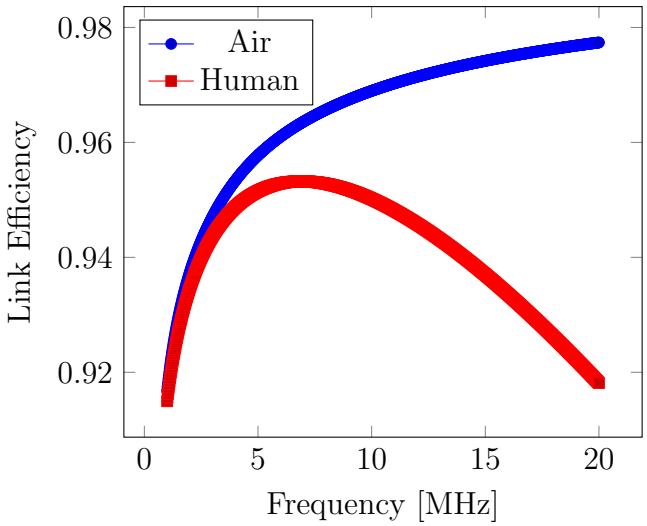


Figure 4.18: Maximum link efficiency of system with 4-turn smaller transmitter coil and 2-turn receiver coil

the coil) and R_{coil} (combination of the AC loss and the radiation resistances of the coil). However, in the presence of a human body, there is an additional series resistance R_{body} which represents the losses due to eddy currents circulating in the body and a parallel capacitance C_{body} due to the relative permittivity of the surrounding tissue material. Both R_{body} and R_{coil} are frequency dependent. C_{body} does have an ESR associated with it representing the dielectric losses due to the electric fields in the conductive tissue. This value depends on the frequency-dependent complex permittivity or loss tangent of the tissue surrounding it, and can be calculated by Equation (4.43), where $\tan\delta$ is the loss tangent of the surrounding tissue. Table 4.2 shows the relative permittivity, conductivity and loss tangent of several tissue types at 6.78 MHz. The effect of the ESR of the parasitic capacitance is small, as the main form of heating is from eddy currents due to magnetic fields, so it will be ignored.

$$\text{ESR} = \frac{\tan\delta}{\omega C_{\text{body}}} \tag{4.43}$$

The values of C_{body} and R_{body} can be obtained via simulations of the coil in air and in the presence of the human body. Firstly, a simulation of the coil in air gives the value of L_{coil} and R_{coil}. Secondly, a simulation of the coil in the presence of a human body gives an equivalent coil impedance Z_{eq}, consisting of a resistor R_{eq} in series with an inductor

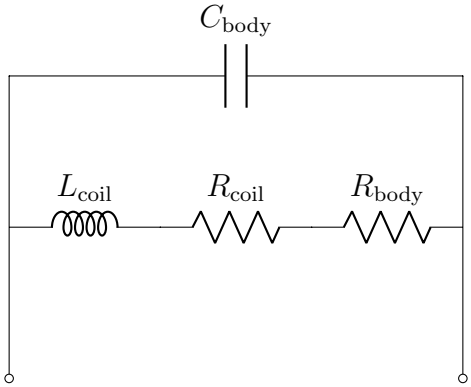


Figure 4.19: Equivalent circuit model of coil inside human body

Tissue type	Relative permittivity	Conductivity	Loss tangent
Fat	16.318	$0.027\,775\,\text{S}\,\text{m}^{-1}$	4.5129
Muscle	233.27	$0.602\,10\,\text{S}\,\text{m}^{-1}$	6.8431
Skin (dry)	478.4	$0.147\,12\,\text{S}\,\text{m}^{-1}$	0.8153

Table 4.2: Dielectric properties of several tissue types at 6.78 MHz

L_{eq}.

An expression for the equivalent coil impedance, in term of the quantities in the circuit in Figure 4.19 can be derived:

$$\begin{aligned}
Z_{\text{eq}} &= R_{\text{eq}} + j\omega L_{\text{eq}} \\
&= \frac{(R_{\text{all}} + j\omega L_{\text{coil}})\frac{1}{j\omega C_{\text{body}}}}{R_{\text{all}} + j\omega L_{\text{coil}} + \frac{1}{j\omega C_{\text{body}}}} \\
&= \frac{R_{\text{all}} + j\omega L_{\text{coil}}}{1 - \omega^2 L_{\text{coil}} C_{\text{body}} + j\omega R_{\text{all}} C_{\text{body}}} \\
&= \frac{R_{\text{all}}(1 - \omega^2 L_{\text{coil}} C_{\text{body}}) + \omega^2 L_{\text{coil}} R_{\text{all}} C_{\text{body}} + j\omega L_{\text{coil}}(1 - \omega^2 L_{\text{coil}} C_{\text{body}}) - j\omega R_{\text{all}}^2 C_{\text{body}}}{(1 - \omega^2 L_{\text{coil}} C_{\text{body}})^2 + (\omega R_{\text{all}} C_{\text{body}})^2} \\
&= \frac{R_{\text{all}} + j\omega L_{\text{coil}}(1 - \omega^2 L_{\text{coil}} C_{\text{body}}) - j\omega R_{\text{all}}^2 C_{\text{body}}}{(1 - \omega^2 L_{\text{coil}} C_{\text{body}})^2 + (\omega R_{\text{all}} C_{\text{body}})^2}
\end{aligned} \tag{4.44}$$

where

$$R_{\text{all}} = R_{\text{coil}} + R_{\text{body}} \tag{4.45}$$

Equating the real and imaginary parts of the equivalent coil impedance in Equa-

tion (4.44) gives a pair of simultaneous equations:

$$R_{\text{eq}} = \frac{R_{\text{all}}}{(1-\omega^2 L_{\text{coil}} C_{\text{body}})^2 + (\omega R_{\text{all}} C_{\text{body}})^2} \tag{4.46}$$

$$L_{\text{eq}} = \frac{L_{\text{coil}}(1-\omega^2 L_{\text{coil}} C_{\text{body}}) - R_{\text{all}}^2 C_{\text{body}}}{(1-\omega^2 L_{\text{coil}} C_{\text{body}})^2 + (\omega R_{\text{all}} C_{\text{body}})^2} \tag{4.47}$$

Since there are two equations (Equations (4.46) and (4.47)) with two unknowns (C_{body} and R_{body}), it is possible for the solutions to be found:

$$C_{\text{body}} = \frac{\sqrt{(\sigma_1 - 2\omega L_{\text{coil}} R_{\text{eq}})(\sigma_1 + 2\omega L_{\text{coil}} R_{\text{eq}})} + \sigma_1 - 2\omega^2 L_{\text{coil}} L_{\text{eq}}}{2\omega^2 L_{\text{coil}} \sigma_1} \tag{4.48}$$

$$R_{\text{body}} = \frac{\sigma_1 - \sqrt{(\sigma_1 - 2\omega L_{\text{coil}} R_{\text{eq}})(\sigma_1 + 2\omega L_{\text{coil}} R_{\text{eq}})}}{2R_{\text{eq}}} - R_{\text{coil}} \tag{4.49}$$

where

$$\sigma_1 = R_{\text{eq}}^2 + (\omega L_{\text{eq}})^2 \tag{4.50}$$

For a 2-turn receiver coil at 6.78 MHz, the first simulation in air gives $L_{\text{coil}} = 322\,\text{nH}$ and $R_{\text{coil}} = 71.3\,\text{m}\Omega$. The second simulation in the human body provides the following values: $L_{\text{eq}} = 324\,\text{nH}$ and $R_{\text{eq}} = 95.2\,\text{m}\Omega$. The resulting additional parasitic capacitance due to the human tissue is $C_{\text{body}} = 9.61\,\text{pF}$ and the additional coil series resistance due to the eddy currents in the human tissue is $R_{\text{body}} = 22.8\,\text{m}\Omega$.

Note that R_{body} represents the additional reflected resistance of the human body losses on the receiver coil. To understand the effect of changing the frequency on the power losses in the human body, it is useful to define another resistance R_{eddy}. What R_{eddy} represents is the overall resistance that the eddy currents in the human body pass through, due to an induced voltage in the body caused by an external magnetic field from a coil. Therefore, a human body can also be modelled as a receiver with a separate induced voltage across R_{eddy}. The eddy currents in the body are approximately 90° out-of-phase with respect to the transmitter coil current and magnetic field, as with the current in the receiver coil and load. This added reflected resistance due to the human

body eddy current losses on the receiver coil can be represented by:

$$R_{\text{body}} = \frac{(\omega M_{\text{body}})^2}{R_{eddy}} \tag{4.51}$$

where M_{body} is the hypothetical mutual inductance between the coil and the human body.

The numerator of the Equation (4.51) increases with the square of frequency. Also, conductivity of most tissue types increases with frequency (see Table 4.3), so R_{eddy} in the denominator will decrease accordingly with frequency. The overall effect is that increasing the frequency makes the reflected resistance R_{body} larger, which causes the coil Q factor to fall. Taking muscle as an example, its conductivity changes from $0.6021\,\text{S}\,\text{m}^{-1}$ at 6.78 MHz to $0.628\,18\,\text{S}\,\text{m}^{-1}$ at 13.56 MHz. This represents a decrease in R_{eddy} of 4.33%, when the frequency is doubled. Putting these changes together, there is an expected increase in the reflected resistance R_{body} of 4.17 times on the receiver coil when operating frequency is increased from 6.78 MHz to 13.56 MHz.

	Conductivity $\text{S}\,\text{m}^{-1}$	
Tissue type	6.78 MHz	13.56 MHz
Fat	0.027775	0.030354
Muscle	0.6021	0.62818
Skin (dry)	0.14712	0.23802

Table 4.3: Conductivity of several tissue types at the first two ISM bands

Looking back at the short-range results in Table 4.1, despite the small variation in maximum link efficiency between the two ISM band frequencies, there may still be a significant difference in heating (SAR) and temperature rise. In addition, it is important to find out whether using receiver coils with a different number of turns that do not result in maximum link efficiency for a particular frequency, leads to lower SAR and temperature rise. Table 4.4 shows the maximum link efficiencies for the short-range scenario, for each of the ISM band frequencies and receiver coil turns from 1 to 2 (using a 4-turn transmitter coil).

Table 4.5 shows the simulated maximum SAR (averaged over 10 g of tissue) and maximum temperature in the human body for each of these combinations. Also shown are the magnetic field strength at the centre of the receiver coil, the power dissipation

Frequency	N_{RX}	η_{link}
6.78 MHz	1	0.952
6.78 MHz	2	0.953
13.56 MHz	1	0.952
13.56 MHz	2	0.942

Table 4.4: Maximum link efficiency for each frequency, and receiver coil turns from 1 to 2 (in the short-range scenario, $N_{\mathrm{TX}} = 4$)

in the entire human body model P_{body}, and the receiver coil dissipation $P_{\text{coil-RX}}$. It is assumed that the ambient temperature is 20 °C and the initial temperature of the human body is 37 °C.

Frequency	N_{RX}	Max. SAR	Max. Temp	H-field	P_{body}	$P_{\text{coil-RX}}$
6.78 MHz	1	1.80 W kg^{-1}	39.5 °C	93.3 A m^{-1}	96.9 mW	343 mW
6.78 MHz	2	3.43 W kg^{-1}	38.9 °C	124 A m^{-1}	139 mW	286 mW
13.56 MHz	1	8.76 W kg^{-1}	39.3 °C	61.5 A m^{-1}	266 mW	257 mW
13.56 MHz	2	13.8 W kg^{-1}	39.6 °C	75.0 A m^{-1}	454 mW	178 mW

Table 4.5: Maximum SAR and temperature, H-field at centre of receiver coil and power dissipation for each frequency, and N_{RX} from 1 to 2 (in the short-range scenario, $N_{\mathrm{TX}} = 4$)

Higher SAR does not necessarily equate to higher temperature rises in the body. At 6.78 MHz, by increasing the turns from 1 to 2, the maximum SAR has risen from 1.80 W kg^{-1} to 3.43 W kg^{-1}. However, the maximum temperature in the body has dropped from 39.5 °C to 38.9 °C. Even though a higher number of turns means the magnetic field in the centre of the receiver coil has increased from 93.3 A m^{-1} to 124 A m^{-1} (leading to an increase in the dielectric losses in the human body from 96.9 mW to 139 mW), the coil dissipation has dropped from 0.343 W to 0.286 W. Coil dissipation plays an important role in the magnitude of temperature rises in the body, but this information is not captured by SAR, which is only concerned with the direct interaction of EM fields with the conductive human tissue. The difference in temperature rises and maximum SAR between 1 and 2 receiver coil turns is also not clear from the comparison of link efficiencies only, so relying on link efficiency is not sufficient to ensure lowest SAR or temperature rise.

Increasing the frequency or the number of coil turns leads to greater tissue heat absorption due to an EM field but lower heat dissipation due to coil currents. Therefore,

the optimal selection of frequency and number of turns should be made so as to balance out tissue heat absorption and coil dissipation.

In addition, with a receiver coil turn of 1, even though the maximum SAR at 13.56 MHz is significantly greater than that at 6.78 MHz, the maximum temperature rise does not reflect this difference in SAR, as it drops slightly from 39.5 °C at 6.78 MHz to 39.3 °C at 13.56 MHz. Again, this is due to the fall in coil dissipation from 343 mW at 6.78 MHz to 257 mW at 13.56 MHz, despite a rise in the dielectric loss in the entire human body from 96.9 mW at 6.78 MHz to 266 mW at 13.56 MHz

In the short range system, where the coil separation is small and the transmitter loop area is not very large compared to the receiver loop area, coupling factor does indeed change with the number of turns, as shown in Figure 4.20. The expression for mutual inductance in Equation (2.6) is not valid for this case, as the magnetic field cannot be considered to be constant over the area of the receiver coil. In addition, in the case of a spiral coil, the average length of one side of the coil decreases and the average or effective area of the coil changes with the number of turns. A more accurate means of calculating mutual inductance of planar spiral coil is available in [80].

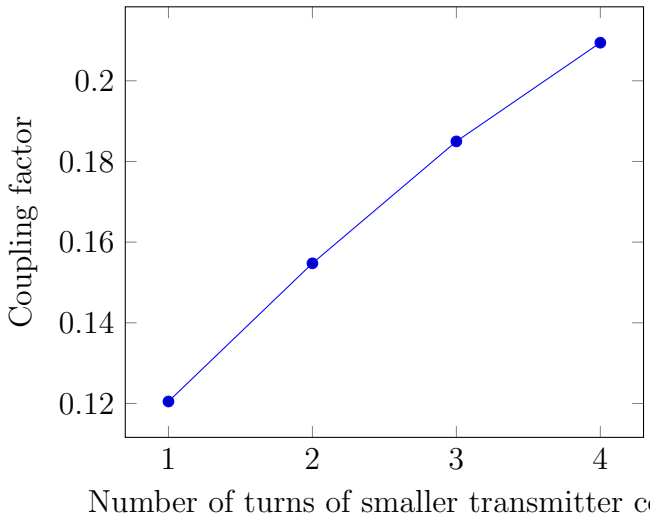


Figure 4.20: Variation of coupling factor with number of turns of the transmitter coil, for the short-range scenario with $N_{\mathrm{RX}} = 2$

4.2.3 Using resonant tuning equations

It would be interesting to see the effect of using the load resistance and tuning capacitance expressions in Chapter 2 for a system in air (referred to as 'resonant tuning'), instead of the optimal tuning expressions for maximum link efficiency described in this chapter. Tables 4.6 and 4.7 show the change in the system parameters when switching from the optimal tuning expressions to the resonant tuning expressions, at two different frequencies (ISM band frequencies of 6.78 MHz and 13.56 MHz, respectively) with the short range scenario, $N_{\mathrm{TX}} = 4$ and $N_{\mathrm{RX}} = 2$. As the receiver coil is not very deeply implanted, the distances are small and the coil areas are not very large, the effect of switching the tuning mode on the maximum link efficiency may actually be quite minimal, especially at lower frequencies. In comparison, the tolerances of real-life components, such as the values of the tuning capacitors and the non-linearities introduced by the voltage-dependent capacitance of the rectifier diodes would be more significant. For example, the Vishay QUAD HIFREQ series surface mount capacitors used in the experiments that will be described in Chapter 5 have a tolerance of 10% [81].

Parameter	Optimal tuning	Resonant tuning
C_{ser}	1.79 nF	1.70 nF
R_L	3.88 Ω	3.94 Ω
η_{link}	95.3%	95.3%
I_{TX}	1.69 A	1.68 A
$Z_{TX-refl}$	$(10.7 - 1.88\mathrm{j})\,\Omega$	$(10.9 - 0.0889\mathrm{j})\,\Omega$

Table 4.6: Comparison of system parameters with optimal tuning and resonant tuning at 6.78 MHz

Parameter	Optimal tuning	Resonant tuning
C_{ser}	484 pF	420 pF
R_L	9.28 Ω	10.0 Ω
η_{link}	94.2%	93.8%
I_{TX}	1.35 A	1.30 A
$Z_{TX-refl}$	$(16.9 - 7.04\mathrm{j})\,\Omega$	$(18.2 - 0.442\mathrm{j})\,\Omega$

Table 4.7: Comparison of system parameters with optimal tuning and resonant tuning at 13.56 MHz

The reflected impedance seen at the transmitter coil needs to be considered, as this could affect the operation of the inverters that are used to drive the coils with a high frequency AC current. Optimal tuning leads to a larger negative reactance appearing at the transmitter coil than resonant tuning. As this reactance is in series with the coil inductance, it serves to reduce the inductance seen by the coil driver circuit. For example, this reduction in inductance across the output of the load independent Class EF inverter [82] could affect its ability to maintain zero-voltage switching and constant current output.

In addition, there is a difference in terms of heating (maximum SAR) and temperature rise in the human body between optimal tuning and resonant tuning, as shown in Table 4.8. Using the resonant tuning expressions in Chapter 2 for a system in air gives a higher level of SAR and tissue temperature rise.

Frequency	Tuning	Max. SAR	Max. Temp
6.78 MHz	Optimal	3.43 W kg^{-1}	38.9 °C
6.78 MHz	Resonant	3.73 W kg^{-1}	39.2 °C
13.56 MHz	Optimal	13.8 W kg^{-1}	39.6 °C
13.56 MHz	Resonant	17.0 W kg^{-1}	40.3 °C

Table 4.8: Maximum SAR and temperature for each frequency and tuning type (in the short-range scenario, $N_{\mathrm{TX}} = 4$, $N_{\mathrm{RX}} = 2$)

4.2.4 Magnetic field distribution

For wirelessly-powered implanted medical devices, tissue heating is caused not only by the magnetic field generated by the transmitter, but also, and more significantly, by the resistive losses in the receiver coil and the magnetic field generated by the receiver coil. Therefore, simulations and experimental measurements involving only the human body and the transmitter coil are not sufficient to ensure compliance of the overall system with the safety regulations. IPT makes use of near-field coupling, so the presence of the receiver coil can significantly disturb the magnetic field generated by the transmitter.

The magnetic field strength due to a current through a square coil can be calculated using Biot-Savart law. For a square transmitter coil with N_{TX} turns, whose average length of one side is $2a_{\mathrm{TX}}$, and with a coil current of I_{TX}, the magnetic field strength $H_{\mathrm{TX}}(z)$ at a

distance z on axis from the centre of the transmitter coil is given by Equation (4.52) [83]:

$$H_{\mathrm{TX}}(z) = \frac{2I_{\mathrm{TX}}a_{\mathrm{TX}}^2 N_{\mathrm{TX}}}{\pi\left(a_{\mathrm{TX}}^2 + z^2\right)\left(2a_{\mathrm{TX}}^2 + z^2\right)^{\frac{1}{2}}} \tag{4.52}$$

Note that as the distance of the receiver coil from the transmitter coil z becomes much greater than the size of the transmitter coil a_{TX}, the magnetic field approaches that of a magnetic dipole and falls with the cube of distance from the transmitter.

For the square receiver coil that is situated at a distance D on axis from the transmitter coil, the magnetic field strength $H_{\mathrm{RX}}(z)$ can be found by using Equation (4.53), where I_{RX} is the receiver coil current, $2a_{\mathrm{RX}}$ is the average length of one side of the receiver coil, and N_{TX} is the number of turns:

$$H_{\mathrm{RX}}(z) = \frac{2I_{\mathrm{RX}}a_{\mathrm{RX}}^2 N_{\mathrm{RX}}}{\pi\left(a_{\mathrm{RX}}^2 + (D-z)^2\right)\left(2a_{\mathrm{RX}}^2 + (D-z)^2\right)^{\frac{1}{2}}} \tag{4.53}$$

The average length $2a$ of one side of the square coil can be found in simulation by injecting a known current I_0 into the coil and finding the magnetic field strength $H_0(0)$ at the centre of the coil with N turns. The average length is therefore given by Equation (4.54), which is the Biot-Savart law for a square coil at location $z = 0$:

$$2a = \frac{2\sqrt{2}I_0 N}{\pi H_0(0)} \tag{4.54}$$

Substituting Equation (4.33) into Equation (4.53), the following equation for the magnetic field strength generated by the receiver coil is obtained:

$$H_{\mathrm{RX}}(z) = -\sqrt{\frac{2P_{\mathrm{RX}}}{R_L}}\frac{2a_{\mathrm{RX}}^2 N_{\mathrm{RX}}}{\pi\left(a_{\mathrm{RX}}^2 + (D-z)^2\right)\left(2a_{\mathrm{RX}}^2 + (D-z)^2\right)^{\frac{1}{2}}} \tag{4.55}$$

In addition, by substituting Equations (4.33) and (4.16) into Equation (4.52), the following equation for the magnetic field strength generated by the transmitter coil is obtained:

$$H_{\mathrm{TX}}(z) = -\sqrt{\frac{2P_{\mathrm{RX}}}{R_L}}\frac{Z_{\mathrm{RX}} + Z_L}{Z_M}\frac{2a_{\mathrm{TX}}^2 N_{\mathrm{TX}}}{\pi\left(a_{\mathrm{TX}}^2 + z^2\right)\left(2a_{\mathrm{TX}}^2 + z^2\right)^{\frac{1}{2}}} \tag{4.56}$$

Note that Equation (4.56) is complex, which indicates a phase difference between the transmitter and receiver magnetic fields. To obtain the overall magnetic field strength variation with distance from the transmitter coil $H_{\text{overall}}(z)$, the sum of Equations (4.52) and (4.53) is taken:

$$H_{\text{overall}}(z) = H_{\text{TX}}(z) + H_{\text{RX}}(z) \tag{4.57}$$

The magnetic field strength (H) in units of A m^{-1} can be converted to magnetic flux density (B) in units of T using the following equation, assuming no use of magnetic materials):

$$B = \mu_0 H \tag{4.58}$$

Figure 4.21 shows the variation of overall magnetic flux density with distance on axis from the smaller transmitter coil ($N_{\text{TX}} = 4$), when the receiver coil ($N_{\text{RX}} = 2$) and human body are 20 mm away from the transmitter coil. Figure 4.22 shows the variation of overall magnetic flux density with distance on axis from the larger transmitter coil ($N_{\text{RX}} = 2$), when the receiver coil ($N_{\text{RX}} = 2$) and human body are 30 cm away from the transmitter coil. For either system, the frequency of operation is 6.78 MHz). Note that the figures show the absolute value, or the magnitude, of the magnetic field. The variation of the magnetic flux density generated by the transmitter coil and the magnetic flux density generated by the receiver coil are also shown. The receiver in the human body can give rise to magnetic fields inside the body that are higher than if a receiver coil were not present in the human body. Therefore, an implanted receiver would cause additional heating in the body. In addition, it is interesting to note that the magnetic field at the centre of the receiver coil is greater than that at the centre of the transmitter coil, albeit very localised.

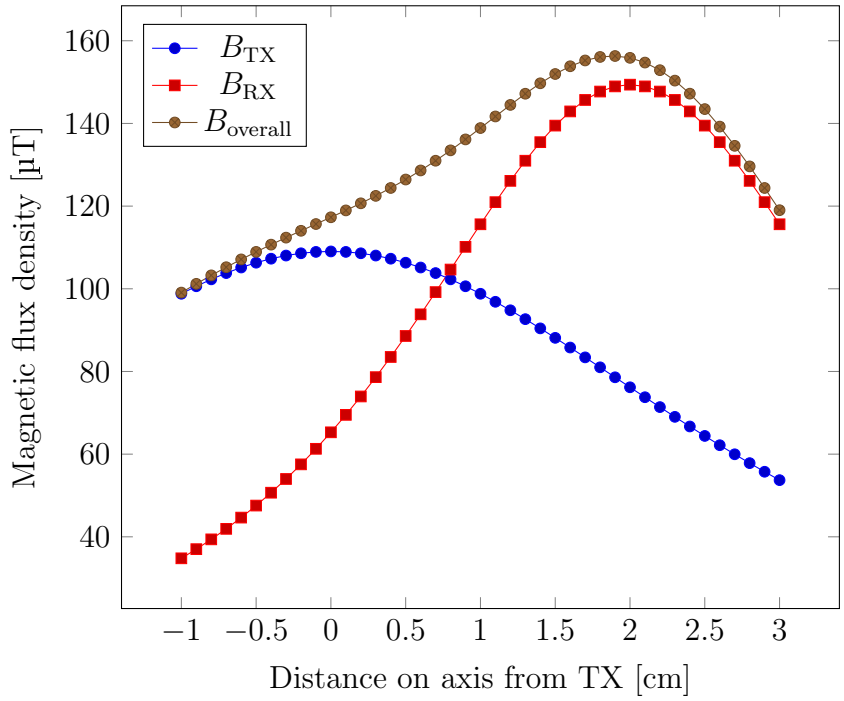


Figure 4.21: Variation of overall magnetic flux density, the magnetic flux density due to smaller transmitter coil and the magnetic flux density due to receiver coil with distance on axis from transmitter coil (receiver coil and human body at 2 cm).

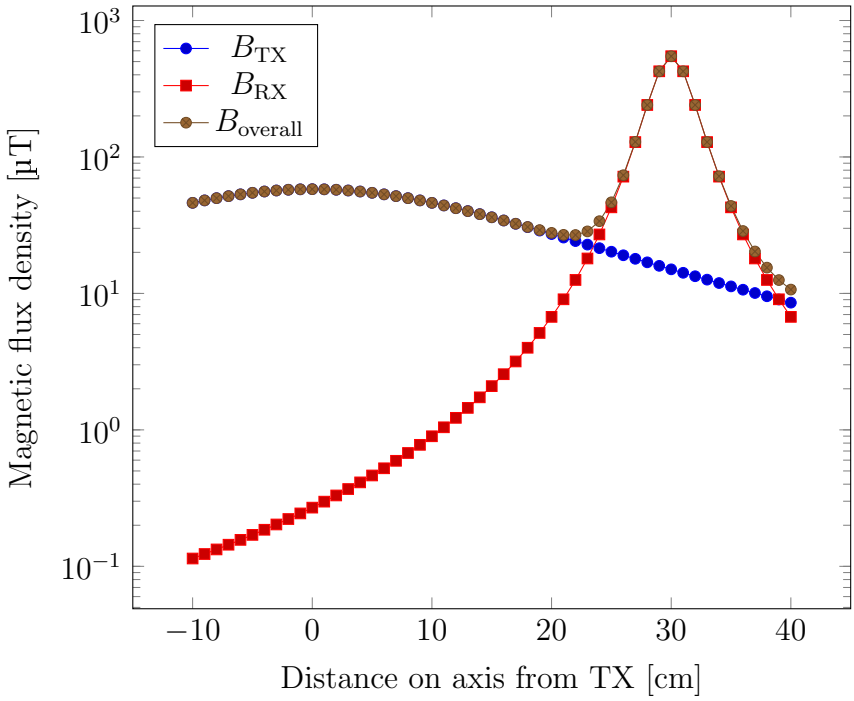


Figure 4.22: Variation of overall magnetic flux density, the magnetic flux density due to larger transmitter coil and the magnetic flux density due to receiver coil with distance on axis from transmitter coil (receiver coil and human body at 30 cm).

4.2.5 Variation of receiver load

The overall magnetic field at the centre of the receiver coil inside the body can be considered as a combination of the magnetic field generated by the transmitter coil and the magnetic field that is a result of current flowing through the receiver coil [74].

The magnetic field at the centre of the receiver coil due to the receiver coil current, $H_{\mathrm{RX}}(0)$, can be calculated using the Biot-Savart Law for a square coil. The expression is shown in Equation (4.59), where N_{RX} is the number of turns of the receiver coil, and $2a_{\mathrm{RX}}$ is the average length of one side of the coil. The process of finding the average length of the side of a coil over all its turns from simulation was described in Section 4.2.4.

$$H_{\mathrm{RX}}(0) = \sqrt{\frac{P_L}{R_L}} \frac{2N_{\mathrm{RX}}}{\pi a_{\mathrm{RX}}} \tag{4.59}$$

For $H_{TX}(D)$, the magnetic field at the centre of the receiver coil produced by the transmitter coil at a distance D away from the receiver coil, it is possible to obtain its expression using the Biot-Savart law equation in (4.56). Alternatively, another expression for this can be obtained that only depends on the receiver coil (i.e. without any reference to the transmitter coil or the mutual coupling).

Firstly, the induced voltage at the receiver coil can be calculated using Faraday's Law of Induction, and the expression in time-harmonic form is given by Equation (4.60), where Φ is the total flux over the area of the receiver coil.

$$V_{\mathrm{ind}} = -j\omega N_{\mathrm{RX}} \Phi \tag{4.60}$$

Since the coil area is square, the total magnetic flux is simply the magnetic flux density at the centre of the receiver coil due to the transmitter coil, $B_{\mathrm{TX}}(D)$, multiplied by the square of the average length of one side: $\Phi = B_{TX}(D) \times (2a)^2$. $B_{\mathrm{TX}}(D)$ is assumed to be constant over the area bounded by the receiver coil. Therefore, the induced voltage can be written as:

$$V_{\mathrm{ind}} = -j\omega N_{\mathrm{RX}} B_{\mathrm{TX}}(D) \times (2a_{\mathrm{RX}})^2 \tag{4.61}$$

The required induced voltage at the receiver coil to deliver 15 W of power to the receiver load can also be written as the product of the receiver coil current and the sum of the load impedance and receiver coil impedance. Hence, induced voltage is also given by Equation (4.62).

$$\begin{aligned} V_{\text{ind}} &= -I_{\text{RX}}(Z_{\text{RX}} + Z_L) \\ &= \sqrt{\frac{2P_L}{R_L}}(Z_{\text{RX}} + Z_L) \end{aligned} \tag{4.62}$$

Equating Equations (4.61) and (4.62), and letting $B_{TX}(D) = \mu_0 H_{TX}(D)$, the magnitude of the magnetic field at the centre of the coil caused by the transmitter coil is given in Equation (4.63)

$$H_{\text{TX}}(D) = -j\sqrt{\frac{2P_L}{R_L}}\frac{(Z_{\text{RX}} + Z_L)}{\mu_0 \omega N_{\text{RX}}(2a_{\text{RX}})^2} \tag{4.63}$$

Therefore, the total magnetic field at the centre of the receiver coil is given by Equation (4.64).

$$\begin{aligned} H_{\text{overall}} &= H_{\text{TX}}(D) + H_{\text{RX}}(0) \\ &= -j\sqrt{\frac{2P_L}{R_L}}\frac{(Z_{\text{RX}} + Z_L)}{\mu_0 \omega N_{\text{RX}}(2a_{\text{RX}})^2} + \sqrt{\frac{P_L}{R_L}}\frac{2N_{\text{RX}}}{\pi a_{\text{RX}}} \end{aligned} \tag{4.64}$$

Assuming the use of secondary resonance tuning (where $X_{\text{L}} = -X_{\text{RX}}$) and that the mutual impedance is predominantly imaginary ($X_M \gg R_M$), the transmitter-generated magnetic field $B_{\text{TX}}(D)$ and the receiver-generated magnetic field $B_{\text{RX}}(0)$ are 90° out of phase. Therefore, the overall magnetic field is evaluated by adding the transmitter-generated and receiver-generated magnetic fields in quadrature. The equation for the overall magnetic flux density is given by (4.65).

$$H_{\text{overall}} = \sqrt{\frac{2P_L}{R_L}\frac{(R_{\text{RX}} + R_L)^2}{16\mu_0^2\omega^2 N_{\text{RX}}^2 a_{\text{RX}}^4} + \frac{P_L}{R_L}\frac{4N_{\text{RX}}}{\pi^2 a_{\text{RX}}^2}} \tag{4.65}$$

The magnetic field strength in units of A m^{-1} can be converted to magnetic flux density in units of T using Equation (4.58), assuming no use of magnetic materials.

As a WPT system relies on a high frequency magnetic field to deliver power, the primary cause of SAR will be the magnetic field through the conductive tissue. Reducing the overall magnetic field should decrease SAR near the receiver, but it may possibly lead to additional heating in the tissue in other areas due to increased transmitter coil currents.

Figure 4.23 shows how the overall magnetic field, the field due to the transmitter coil, and the field due to the receiver coil (at the centre of the receiver coil) vary with the load resistance attached to the receiver's resonant tank, for the short-range scenario where link efficiency is maximised with $R_L = 3.87\,\Omega$. Figure 4.24 shows how the overall magnetic field, the field due to the transmitter coil, and the field due to the receiver coil (at the centre of the receiver coil) vary with the load resistance, for the longer-range scenario where link efficiency is maximised with $R_L = 0.181\,\Omega$. Both figures assume a constant received power of $P_L = 15\,\mathrm{W}$ and an operating frequency of $6.78\,\mathrm{MHz}$.

It can be seen from either figure that overall magnetic field initially drops with load resistance (coinciding with the lowering of the loaded Q factor of the receiver), but then reaches a minimum (at $7.3\,\Omega$ for short range and $9.23\,\Omega$ for longer-range) before increasing again. Hence, there exists a load resistance for which magnetic field is minimised, which means localised SAR is near its lowest at this point if electric fields do not increase significantly. This minimiser, R_L^*, can be evaluated using (4.66). It is important to note that R_{RX} is a function of ω, N_{RX} and a_{RX} as well.

$$R_L^* = \frac{\sqrt{\left(4\sqrt{2}\omega N_{\mathrm{RX}}^2 a_{\mathrm{RX}}\mu_0\right)^2 + (\pi R_{\mathrm{RX}})^2}}{\pi} \tag{4.66}$$

Apart from heating caused by magnetic fields inducing eddy currents in the conductive human tissue, another source of heating is the power dissipation (P_{diss}) due to the current flowing in the receiver coil I_{RX}. The power dissipated in the receiver coil is calculated by:

$$P_{\mathrm{diss}} = \frac{|I_{\mathrm{RX}}|^2 R_{\mathrm{coil}}}{2} \tag{4.67}$$

R_{coil} denotes the coil's own loss resistances (AC losses due to skin effect and proximity

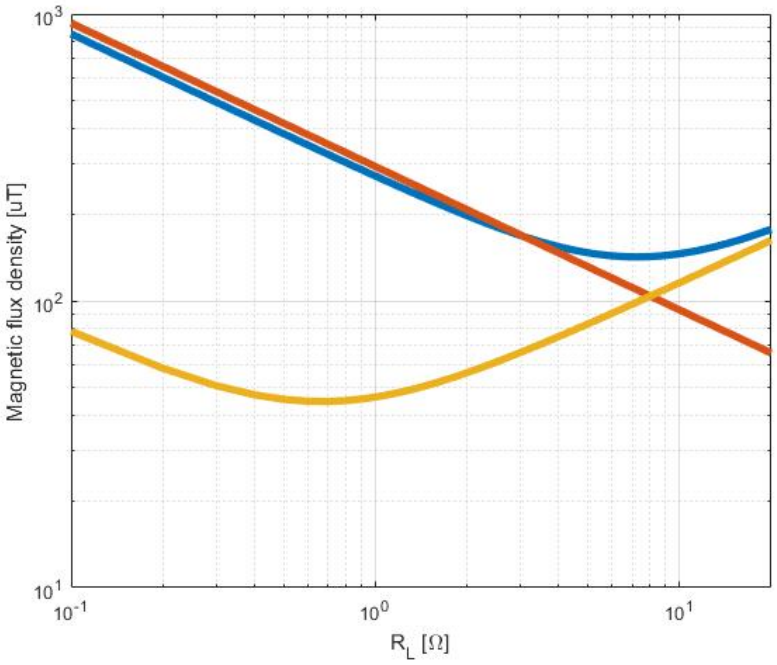


Figure 4.23: Variation of overall magnetic flux density (blue), flux density due to transmitter (yellow), and flux density due to receiver coil (orange) with load resistance (at centre of receiver coil), for short-range scenario

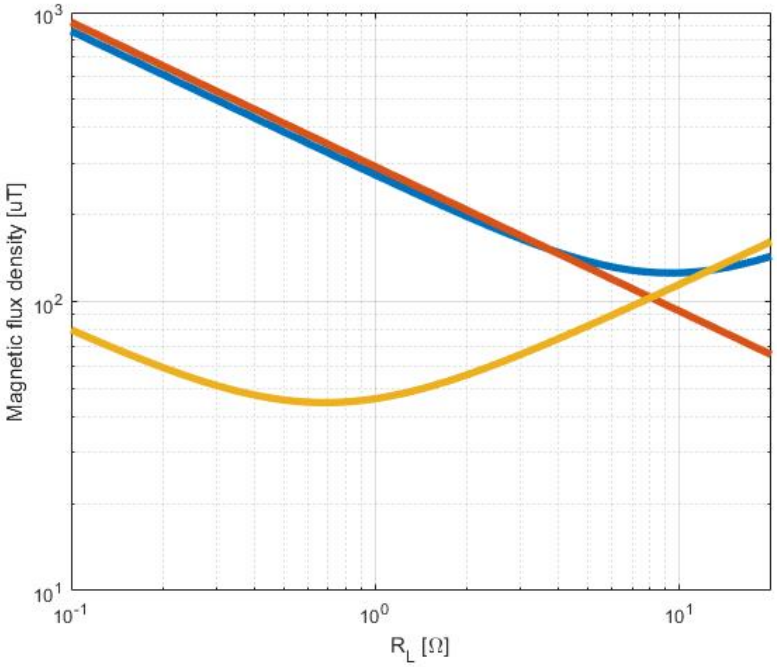


Figure 4.24: Variation of overall magnetic flux density (blue), flux density due to transmitter (yellow), and flux density due to receiver coil (orange) with load resistance (at centre of receiver coil), for longer-range scenario

effect). It is used in the calculation of coil dissipation, as the coil's combined resistance R_{RX} also consists of the radiation resistance and the losses in the conductive tissue due to induced eddy currents. R_{coil} can be obtained in simulation by finding the difference between the coil's resistance when the coil is modelled as a lossy metal and the coil's resistance when the coil is modelled as a perfect electrical conductor.

The key to reducing coil dissipation is to make the receiver coil current smaller. With Equation (4.33), the coil dissipation can be expressed as:

$$\begin{aligned} P_{\mathrm{diss}} &= \frac{\left(\sqrt{\frac{2P_{\mathrm{RX}}}{R_L}}\right)^2 R_{\mathrm{coil}}}{2} \\ &= \frac{P_{\mathrm{RX}} R_{\mathrm{coil}}}{R_L} \end{aligned} \tag{4.68}$$

Therefore, for a fixed receiver power, increasing the load resistance R_L would lead to a fall in the heating of the surrounding tissue due to power dissipation from the receiver coil's losses.

The following simulations show the effect of changing load on the SAR and the tissue temperature rises for both the short-range and the longer-range scenario. The frequency of operation used in these simulations is 6.78 MHz.

For the first short-range simulation, the load resistance is chosen such that it would maximise link efficiency. Thereby, by using (4.31), R_L is set to 3.87 Ω. To deliver 15 W to this load, a transmitter coil current of 1.69 A is required. Figure 4.25 shows the cross-sectional distribution of SAR through the centre of the receiver coil and the chest area of the Nelly model. The maximum SAR in this plot is 3.43 $\mathrm{W\,kg^{-1}}$. The link efficiency of this set-up is 95.3 %, the receiver coil current is 2.78 A and the magnetic flux density at the centre of the receiver coil is 155 µT.

The second short-range simulation aims to reduce the SAR in the chest area by reducing the overall magnetic field at the centre of the receiver coil and the level of coil dissipation, as described in Section 4.2.5. If R_L is set to 5.81 Ω (1.5 times the optimal load value), the transmitter coil current needs to be increased to 2.03 A to maintain the delivery of 15 W to the load. Figure 4.26 shows the cross-sectional distribution of SAR

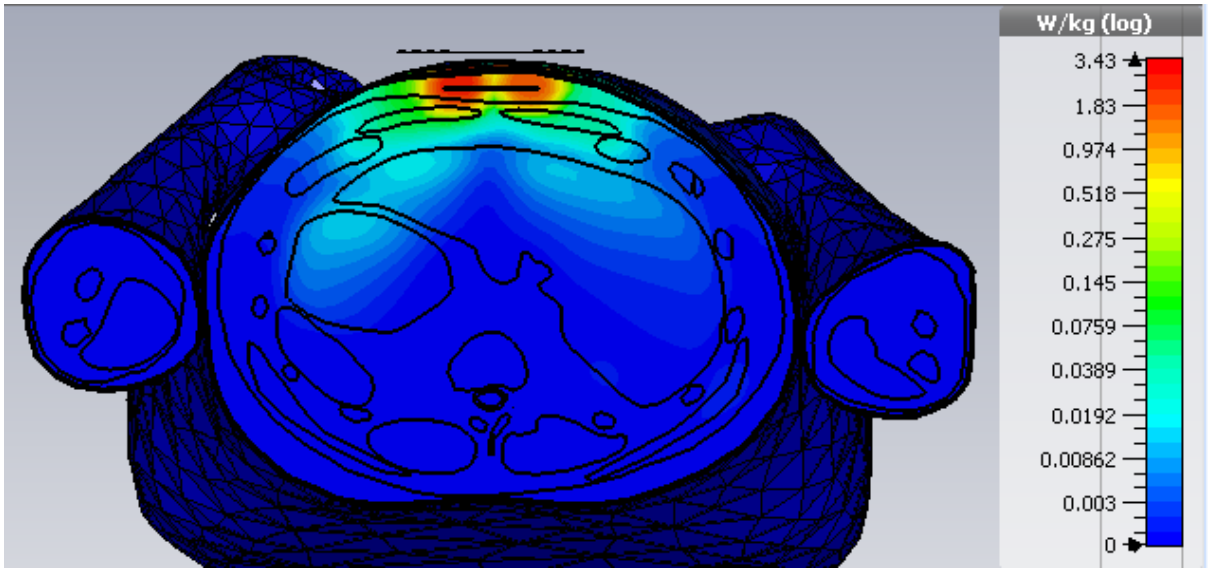


Figure 4.25: SAR distribution: maximum link efficiency (short-range scenario)

through the centre of the receiver coil and the chest area of the Nelly model for these values. The maximum SAR in this plot has decreased to 2.57 W kg^{-1}. The link efficiency of this new set-up has decreased slightly to 95.0 %, the receiver coil current is 2.27 A and the magnetic flux density at the centre of the receiver coil is 146 µT.

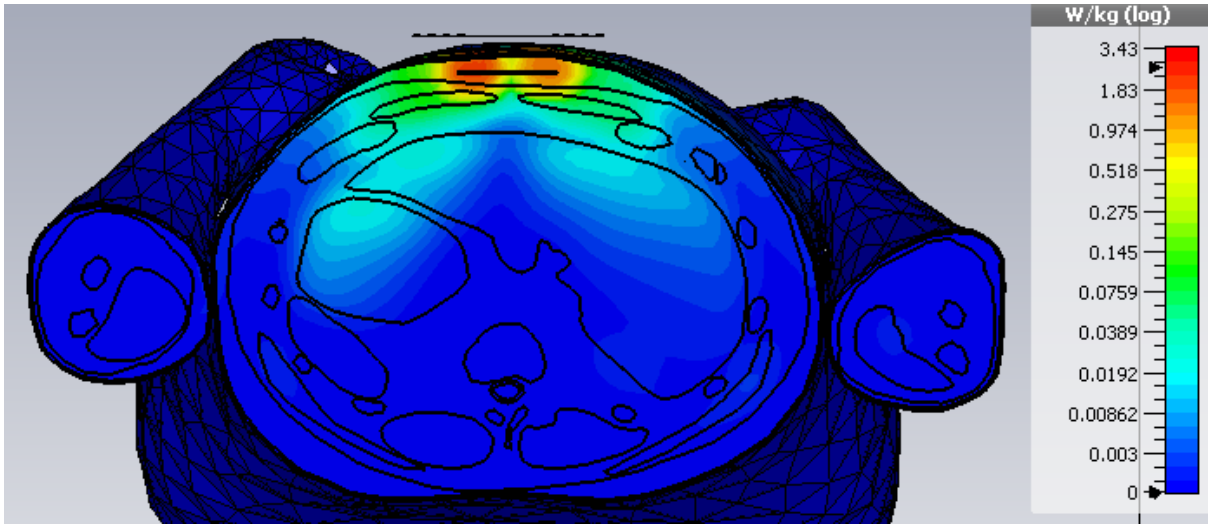


Figure 4.26: SAR distribution: increased load (short-range scenario)

Internal electric fields in the body will also need to be investigated to ensure that their limits are not exceeded, since the frequency of operation is 6.78 MHz. For the case of optimal tuning for maximum link efficiency, the 99th percentile value of the internal electric field is 17.6 V m^{-1} (root mean square (RMS)). The corresponding value for the increased load case is 20.2 V m^{-1} (RMS). For either case, the internal electric field is well

within the International Commission on Non-Ionizing Radiation Protection (ICNIRP) basic restrictions for non-thermal effects in the 2010 Guidelines.

Figure 4.27 shows the cross-sectional temperature distribution through the centre of the receiver coil and the chest area of the Nelly model for the simulation, in which the load resistance was chosen such that it would maximise link efficiency. The maximum temperature of the tissue in this plot is 38.9 °C, which means that there is an increase of 1.9 °C from a normal body temperature of 37.0 °C.

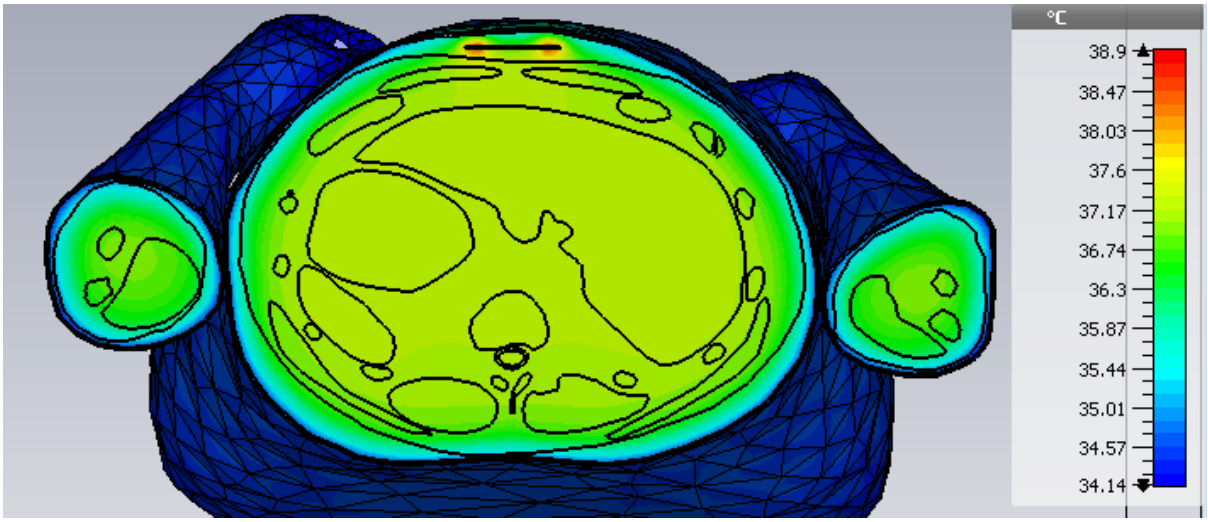


Figure 4.27: Temperature distribution (°C): maximum link efficiency (short-range scenario)

If the load resistance is set to 5.81 Ω in order to increase the receiver efficiency and to reduce the magnetic field at the centre of the receiver coil (as explained in Section 4.2.5), the resulting temperature distribution plot is shown in Figure 4.28. The maximum temperature of the tissue in this scenario is 38.2 °C, which means that there is a rise in body temperature of only 1.2 °C.

For the first longer-range simulation, the load resistance is chosen such that it would maximise link efficiency. Therefore, by using (4.31), R_L is set to 0.181 Ω. To deliver 15 W to this load, a transmitter coil current of 14.4 A is required. Figure 4.29 shows the cross-sectional distribution of SAR through the centre of the receiver coil and the chest area of the Nelly model. The maximum SAR in this plot is 47.7 W kg^{-1}. The link efficiency of this set-up is 31.6 %, the receiver coil current is 12.9 A and the magnetic flux density at the centre of the receiver coil is 687 µT.

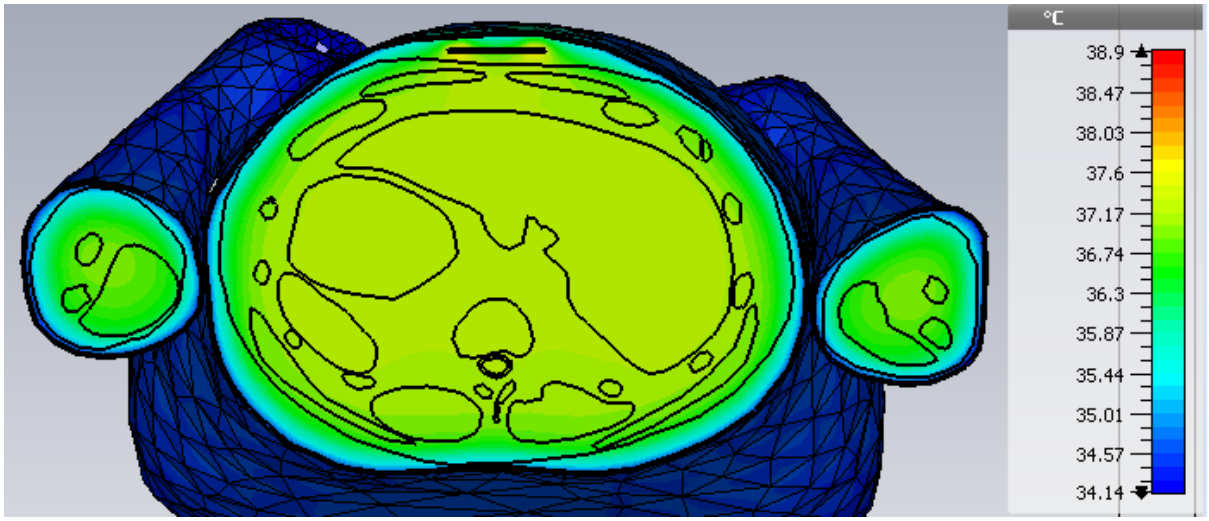


Figure 4.28: Temperature distribution (°C): increased load (short-range scenario)

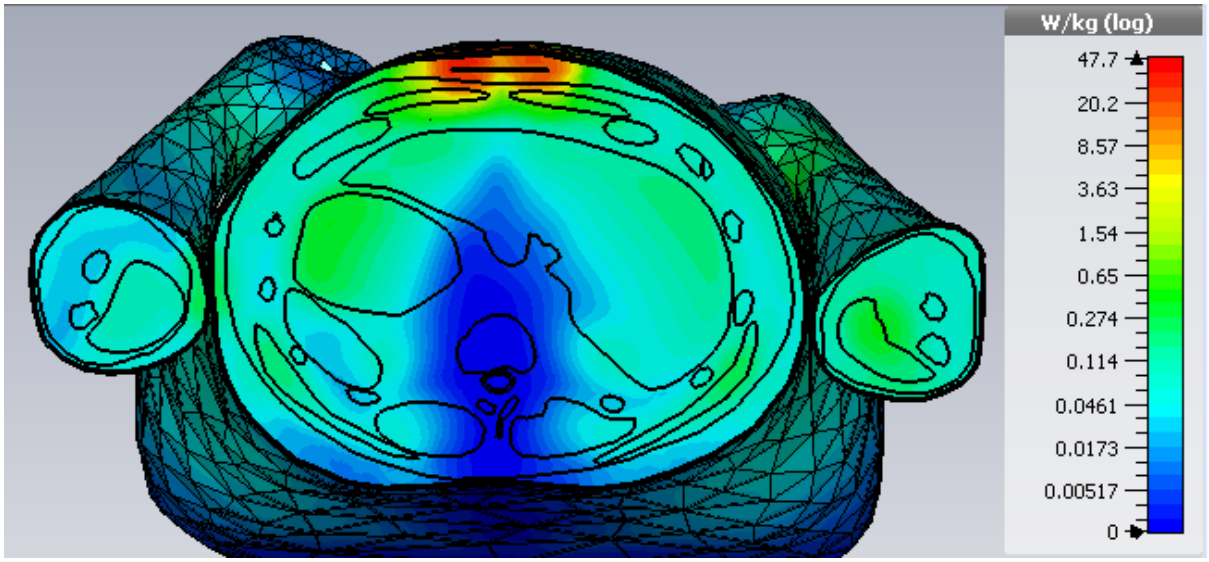


Figure 4.29: SAR distribution: maximum link efficiency (longer-range scenario)

The second longer-range simulation aims to reduce the SAR in the chest area by reducing the overall magnetic field at the centre of the receiver coil and the level of coil dissipation, as described in Section 4.2.5. If R_L is set to 3.62 Ω (20 times the optimal load value), the transmitter coil current needs to be increased to 43.5 A to maintain the delivery of 15 W to the load. Figure 4.30 shows the cross-sectional distribution of SAR through the centre of the receiver coil and the chest area of the Nelly model for these values. The maximum SAR in this plot has decreased to 7.75 W kg^{-1}. The link efficiency of this new set-up has decreased to 6.25 %, the receiver coil current is 2.88 A and the magnetic flux density at the centre of the receiver coil is 167 µT.

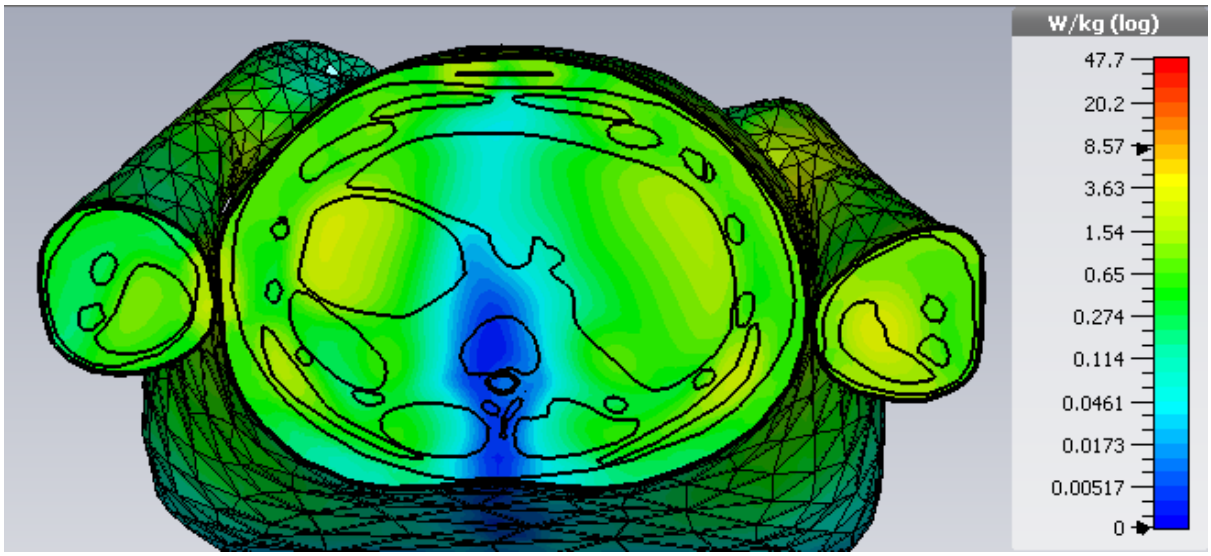


Figure 4.30: SAR distribution: increased load (longer-range scenario)

Figure 4.31 shows the cross-sectional temperature distribution through the centre of the receiver coil and the chest area of the Nelly model for the simulation, in which the load resistance was chosen such that it would maximise link efficiency. The maximum temperature of the tissue in this plot is 97.8 °C, which means that there is an increase of 60.8 °C from a normal body temperature of 37.0 °C.

If the load resistance is set to 3.62 Ω in order to increase the receiver efficiency and to reduce the magnetic field at the centre of the receiver coil (as explained in Section 4.2.5), the resulting temperature distribution plot is shown in Figure 4.32. The maximum temperature of the tissue in this scenario is 39.9 °C, which means that there is a rise in body temperature of only 2.9 °C.

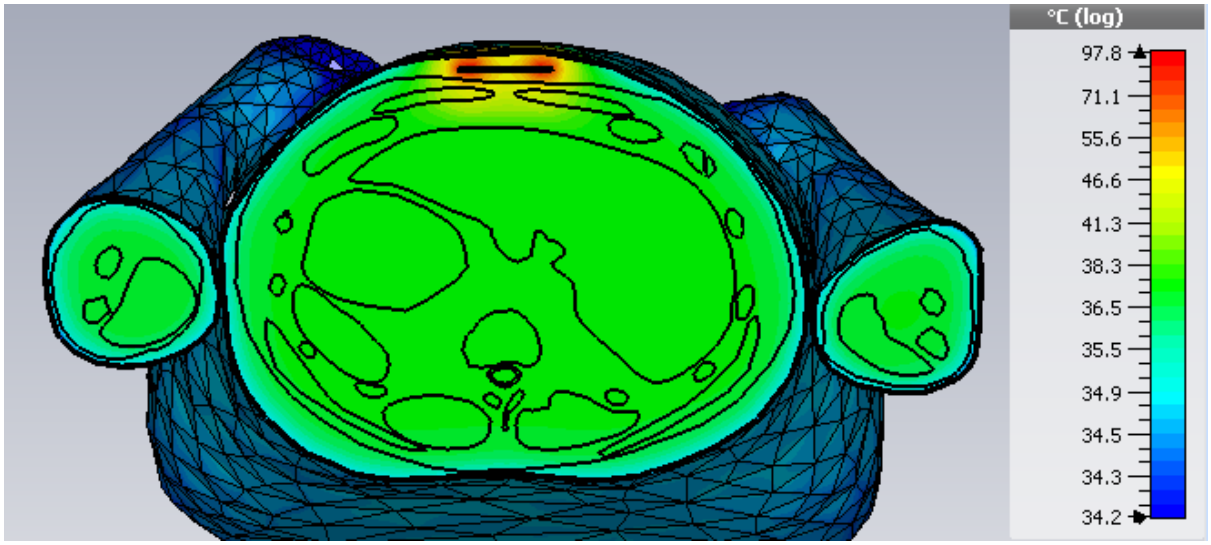


Figure 4.31: Temperature distribution (°C): maximum link efficiency (longer-range scenario)

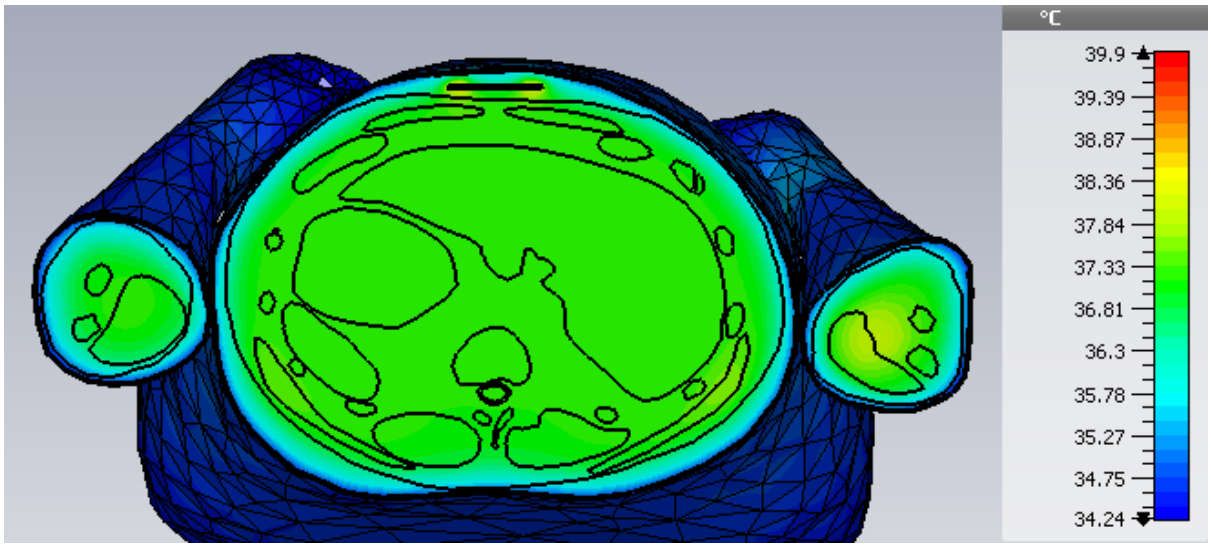


Figure 4.32: Temperature distribution (°C): increased load (longer-range scenario)

4.3 Design trade-offs

The high-level design trade-offs for the short range scenario are summarised in Table 4.9, assuming a constant received power. The table shows the effect of increasing the frequency, increasing the number of receiver coil turns, increasing the receiver load and changing the tuning method from optimal to resonant, on the coil voltages and currents, the link efficiency, receiver coil dissipation, power dissipation in the human model, SAR and temperature rise.

	Increase f	Increase N_{RX}	Increase R_L	Optimal to resonant tuning
V_{TX}	$\uparrow$	$\star$	$\uparrow$	$\uparrow$
I_{TX}	$\downarrow$	$\star$	$\uparrow$	$\downarrow$
V_{RX}	$\uparrow$	$\downarrow$	$\downarrow$	$\uparrow$
I_{RX}	$\downarrow$	$\uparrow$	$\downarrow$	$\downarrow$
η_{link}	$\ddagger$	$\bowtie$	$\downarrow$	$\downarrow$
P_{body}	$\uparrow$	$\uparrow$	$\uparrow$	$\uparrow$
$P_{\mathrm{coil\text{-}RX}}$	$\downarrow$	$\downarrow$	$\downarrow$	$\downarrow$
Max. SAR	$\uparrow$	$\uparrow$	$\downarrow$	$\uparrow$
Temp. rise	$\bigcirc$	$\star$	$\downarrow$	$\uparrow$

Table 4.9: High level design trade-offs ($\uparrow$: increases, $\downarrow$: decreases, $\star$: decreases at 6.78 MHz and increases at 13.56 MHz, $\bowtie$: increases at 6.78 MHz and decreases at 13.56 MHz, $\ddagger$: increases with $N_{\mathrm{RX}} = 1$ and decreases with $N_{\mathrm{RX}} = 2$, $\bigcirc$: decreases with $N_{\mathrm{RX}} = 1$ and increases with $N_{\mathrm{RX}} = 2$)

In Chapter 3, it was explained that a wireless power transfer system operating at frequencies above 100 kHz with an implanted receiver causes both eddy current heating (can be evaluated in terms of the maximum SAR in the body) and receiver coil dissipation (not captured by SAR as it is not a direct effect of exposure to a high frequency magnetic field). Both forms of heating play an important role in the overall temperature rise in the body. Assuming always a constant receiver power, there is an increase in eddy current heating and a decrease in coil dissipation with higher frequency, higher number of receiver coil turns, higher load resistance and when changing from optimal to resonant tuning. The maximum SAR increases with the use of higher frequency, greater number of coil turns and when moving to resonant tuning, and decreases with the use of a higher load resistance. The magnitude of temperature rise is greater with resonant tuning and smaller receiver loads, but how temperature rises vary with frequency depends on the

number of receiver coil turns, and how they change with the number of receiver coil turns depends on frequency. Consequently, thermal simulations should be performed as they can show the combined effect of eddy current heating and coil dissipation on the tissue temperature, and their relative importance depends on the various design parameters described in this chapter.

By looking at Table 4.9, some intuition regarding the relative distribution of the two forms of power losses/heating can be gained:

- Increasing the frequency causes the receiver coil current to fall, leading to a decrease in the magnetic field at the receiver end. However, a higher frequency results in greater eddy current losses in the body as mentioned in Section 4.2.2, causing maximum SAR to rise. As for how the magnitude of temperature rise changes, this depends on the geometry of the receiver coil. With only one turn, the temperature rise at the receiver site decreases. This is due to a lower level of coil dissipation as a consequent of a lower receiver current, so this form of heating is dominant with a one-turn receiver coil. However, with a two-turn receiver coil, the temperature rise increases, which means that eddy current heating has a larger effect on overall thermal dissipation.

- Increasing the receiver load leads to a fall in receiver coil current, resulting in a decrease in the magnetic field at the receiver end. Maximum SAR falls accordingly, as localised eddy current heating near the receiver has decreased. On the other hand, total eddy current heating has risen, owing to higher transmitter currents required for higher receiver load resistances. This means there is more heating on the surface of the human body near the transmitter coil. Nevertheless, the values of SAR in the body nearest to the transmitter are still smaller than those at the implanted receiver site. In addition, the reduced receiver coil current has led to a lower level of coil dissipation. Consequently, temperature rise has fallen with the use of an increased load, as both coil dissipation and localised eddy current heating at the receiver have decreased.

4.4 Summary

The process of designing a WPT system for higher-power implantable biomedical devices such as LVADs requires a different set of objectives and constraints compared to that for a system operating in free space. This is due to the need for reducing the magnitude of temperature increases in the body, caused by dielectric heating, eddy current heating and coil losses. Selecting different combinations of frequency, coil turns and tuning method can lead to a reduction in the amount of heating and temperature rises in the human body. Modifying the load resistance to reduce the loaded Q factor of the receiver can help to improve the receiver efficiency and minimise the overall magnetic field inside the body, leading to lower SAR and magnitude of temperature rise in the tissue. However, a consequence of this is that the transmitter coil current needs to be raised in order to generate a greater EMF in the receiver coil (due to a higher magnetic field produced by the transmitter coil and Faraday's Law of Induction) to maintain the required received power of 15 W. Although link efficiency may drop as a result, these alternative design objectives may be necessary in order for relevant safety regulations to be met.

Chapter 5

Wireless power experiments in salt water solution

As mentioned in Chapter 3, it is generally very difficult to take direct measurements of the specific absorption rate (SAR) in a human body exposed to the high frequency magnetic field of a wireless power transfer (WPT) system, as this quantity is internal to the body. Hence, the usual procedure to evaluate compliance with the thermal effect basic restriction is to perform electromagnetic simulations of the system with a human body model in order to obtain the magnitude of tissue heating. However, it is also important to validate the numerical simulations, and this can be done by performing experiments with a phantom with known dielectric and thermal properties and recording the field strengths and/or temperature rises in the material. Then, by running both 3D electromagnetic and thermal simulations of the experimental setup with a model of the phantom, the simulation outcomes can compared with the experimental results to see if they agree.

In this chapter, an experiment involving the transfer of power wirelessly to a receiver immersed in a salt water solution is demonstrated, with results showing the effect of varying the receiver load on the magnitude of temperature rises in the surroundium conductive medium. Electromagnetic and thermal simulations of the real-world experimental set-up with salt water are then performed in order to validate the results of the experiment.

The selected frequency of operation for the experiments in this chapter is 13.56 MHz, which is an industrial, scientific and medical (ISM) band frequency. The receiver load power is chosen to be 10 W.

5.1 Coils, coating and salt water preparation

The transmitter coil consists of a 4-turn printed circuit board (PCB) circular spiral coil with an outer diameter of 10 cm, a trace width of 4 mm, and a turn spacing of 4 mm. The receiver is a 2-turn PCB circular spiral coil, with an outer diameter of 5 cm, a trace width of 3 mm, and a turn spacing of 3 mm. The transmitter coil and the receiver coil were chosen to have the same outer dimensions as in the short-range scenario that was presented in Chapter 4. Such coil dimensions are suitable for the wireless powering of a higher-power biomedical implant over a short distance with a transmitter coil worn on the body in a vest. Figures 5.1 and 5.2 are photographs of the transmitter coil and the receiver coil PCBs, respectively. Both coil PCBs are manufactured using 1 oz copper, giving an equivalent trace thickness of 35 µm.

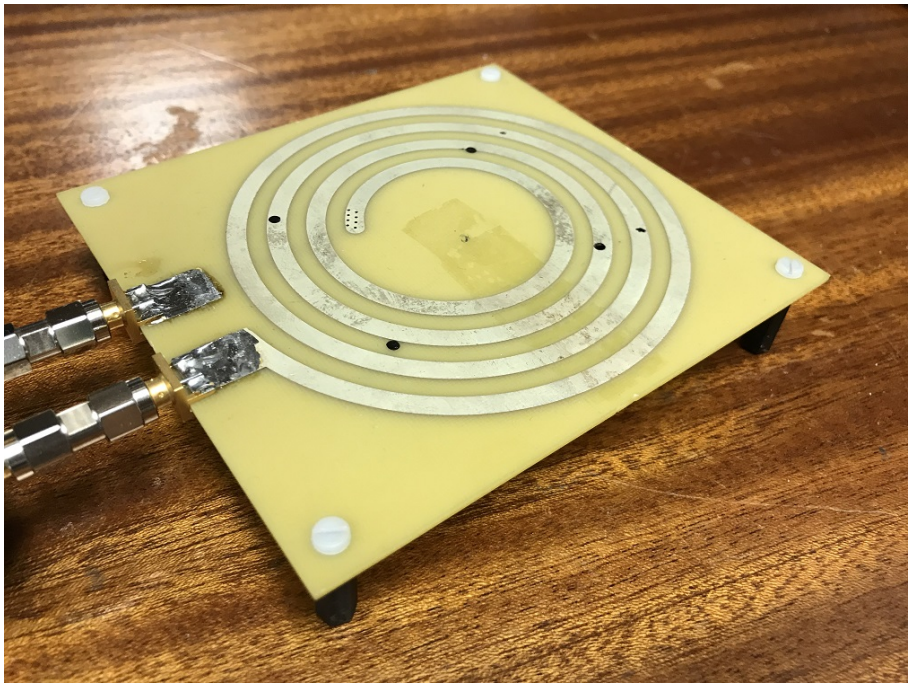


Figure 5.1: Transmitter coil PCB

A plastic tank with dimensions of 15 cm (L) × 9 cm (W) × 14 cm (H) is used to hold

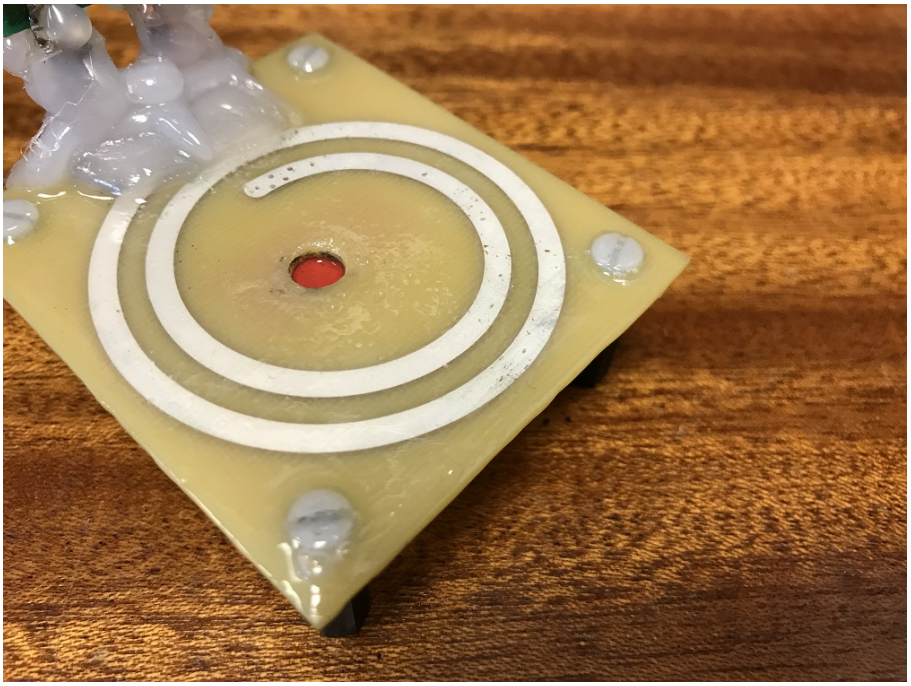


Figure 5.2: Receiver coil PCB

the salt water solution. The conductivity of the solution is chosen to be four times that of muscle, in order to obtain more prominent temperature rises in a shorter period of time. At 13.56 MHz, the conductivity of muscle is $0.628\,\mathrm{S\,m^{-1}}$ [84, 77]. To produce a solution with the desired level of conductivity, the correct mass of table salt (sodium chloride) is to be weighed and added to de-ionised water (which has negligible conductivity to start with). Since a conductivity of $0.628\,\mathrm{S\,m^{-1}} \times 4 = 2.51\,\mathrm{S\,m^{-1}}$ is required, this corresponds to a salinity of 17.1 g per kg of water [85]. The height of the salt water is 2.5 cm which was chosen to just cover the receiver coil, and the resulting volume of the solution was $337.5\,\mathrm{cm^3}$. Since water has a density of $1\,\mathrm{g\,cm^{-3}}$, the mass of table salt required in $337.5\,\mathrm{cm^3}$ of water is $\frac{17.1 \times 337.5}{1000} = 5.77\,\mathrm{g}$.

The receiver coil PCB is coated in an Electrolube flexible silicone conformal coating in order to prevent direct electrical contact of the coil trace with the salt water, when the receiver coil is immersed in the tank. Some hot glue is applied over the coil ends in order to reduce the extra parasitic capacitance seen across the receiver coil, caused by salt water flowing around and between the coil ends. The increased parasitic capacitance is due to the high relative permittivity of salt water solution, which is around 75 [86].

The distance between the transmitter coil and the receiver coil for the experiments

is 4 cm. The salt water tank is placed over the transmitter coil, such that the bottom of the salt water tank is 2 cm above the transmitter coil. The receiver coil is placed in the salt water 2 cm over the bottom of the tank.

5.2 Impedance measurements and link parameters

To be able to design the power electronics and to transfer power wirelessly with maximum link efficiency, the impedance of the coils needs to be measured. This was performed with a Keysight E4990A Impedance Analyzer (20 Hz to 120 MHz), which gives the resistance and inductance of the device under test over a range of frequencies. The connection between the impedance analyzer and the coil is made using the Keysight 42941A Impedance Probe.

The first measurement is performed on the transmitter coil, with the salt water tank situated 2 cm above the coil. This provides the resistance of the transmitter coil, R_{TX}, and the inductance of the transmitter coil, L_{TX}, when loaded by the salt water tank. The second measurement is of the receiver coil placed inside the salt water, 2 cm above the bottom of the tank. This provides the resistance of the receiver coil, R_{RX}, and the inductance of the receiver coil, L_{RX}, when immersed in the salt water tank. The third measurement involves shorting the ends of the receiver coil and placing it in the salt water tank, 2 cm from the bottom of the tank. The tank is then placed 2 cm above the transmitter coil. In this scenario, the resistance of the transmitter coil, $R_{\mathrm{TX,S}}$, and the inductance of the transmitter coil, $L_{\mathrm{TX,S}}$, are measured when loaded with a shorted receiver coil in salt water.

In order to observe the effects of the loading of the salt water tank on the coils, the coil measurements have also been carried out in air without salt water as a comparison. The results of the measurements at 13.56 MHz both with and without salt water are summarised in Table 5.1.

Various quantities can be derived from these measurements, including Q factor, mutual impedance and mutual inductance, coupling factor, receiver tuning capacitance,

Measurement parameter	Air	Salt water
L_{TX}	1.4002 µH	1.4134 µH
R_{TX}	305 mΩ	856 mΩ
L_{RX}	262 nH	265 nH
R_{RX}	124 mΩ	418 mΩ
$L_{\mathrm{TX,S}}$	1.3924 µH	1.4068 µH
$R_{\mathrm{TX,S}}$	312 mΩ	767 mΩ

Table 5.1: Measurements of coil resistance and inductance in air and salt water at 13.56 MHz with impedance analyser

optimal load, reflected impedance on the transmitter coil, link efficiency, and the coil currents and voltages for both the receiver and the transmitter.

The experimental set-up with the two coils and the salt water tank can be considered as a reciprocal two-port network, whose circuit representation in terms of impedance parameters is given in Figure 4.2. The complex impedance quantities in the circuit can be defined in terms of reactances, resistances and inductances, as shown in Equations (4.4), (4.5) and (4.6). All the quantities in Equations (4.4) and (4.5) are known as they are based on measurement results, given in Table 5.1.

The Q factor of a coil, Q, in terms of its complex impedance ($Z = R + j\omega L$) is given by Equation (5.1). The Q factors of the transmitter and receiver coils in both air and salt water are calculated and shown in Table 5.2. The loading of the coils with the salt water leads to a decrease in Q factor.

$$Q = \frac{\Im\left(Z\right)}{\Re\left(Z\right)} = \frac{\omega L}{R} \tag{5.1}$$

	Air	Salt water
Q_{TX}	391	141
Q_{RX}	180	54

Table 5.2: Coil Q factors in air and salt water

According to Table 5.2, the Q factor of the 2-turn receiver coil in air at 13.56 MHz is 180. In contrast, the simulated Q factor of the same coil in air at 13.56 MHz is 263, which is higher than the measured value. The discrepancy between the two values is due to

measurement inaccuracies that occur with high Q factor coils. In general, an impedance analyser measures the magnitude and phase angle of a coil's complex impedance. For high Q coils whose reactance is much bigger than its equivalent series resistance (ESR), errors in the measured phase angle due to the instrument's accuracy can significantly influence the measured Q values. In [87], the authors explain that a Q of 200 corresponds to a phase angle of 0.3°, so to obtain a 5 % accuracy in ESR, the precision of the phase measurement must be 0.014°.

The mutual impedance of a two-port network, Z_M, as shown in Figure 4.2 and Equation (4.6), consists of the well-known mutual inductance M of an inductive link and a mutual resistance R_M. Calculating Z_M involves performing a short-circuit test, where the impedance of the transmitter coil $Z_{\mathrm{TX,S}}$ is measured, when the receiver end is shorted (as shown in Figure 5.3). The expression for $Z_{\mathrm{TX,S}}$ is given by Equation (5.2). The resistive and inductive components of $Z_{\mathrm{TX,S}}$ have been measured with the impedance analyser and their values are found in Table 5.1.

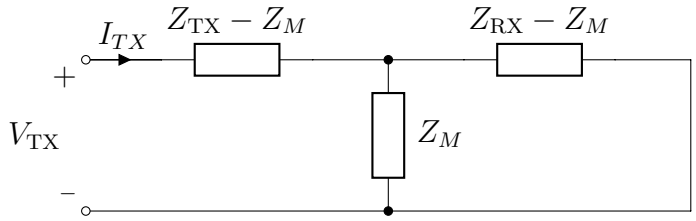


Figure 5.3: Equivalent circuit of reciprocal two-port network in terms of complex impedance parameters, with the receiver end shorted.

$$Z_{\mathrm{TX,S}} = R_{\mathrm{TX,S}} + j\omega L_{\mathrm{TX,S}} \tag{5.2}$$

By observing Figure 5.3, $Z_{\mathrm{TX,S}}$ can be expressed by Equation (5.3):

$$\begin{aligned} Z_{\mathrm{TX,S}} &= Z_{\mathrm{TX}} - Z_M + \frac{Z_M\,(Z_{\mathrm{RX}} - Z_M)}{Z_{\mathrm{RX}} - Z_M + Z_M} \\ &= Z_{\mathrm{TX}} - \frac{Z_M^2}{Z_{\mathrm{RX}}} \end{aligned} \tag{5.3}$$

Rearranging for Z_M, the mutual impedance of the two-coil link is calculated using

Equation (5.4), and is based on measurement results in Table 5.1 taken at 13.56 MHz.

$$Z_M = \sqrt{Z_{\mathrm{RX}} \left(Z_{\mathrm{TX}} - Z_{\mathrm{TX,S}} \right)} \tag{5.4}$$

The calculated values of M and R_M for both the system in air and in salt water at 13.56 MHz are shown in Table 5.3.

	M	R_M
Salt water	42.2 nH	314 mΩ
Air	45.4 nH	9.57 mΩ

Table 5.3: Comparison of mutual impedance between system in air and in salt water

If the system is in air, the coupling factor is given by the well-known equation in (5.5).

$$k_{\mathrm{air}} = \frac{M}{\sqrt{L_{\mathrm{TX}} L_{\mathrm{RX}}}} \tag{5.5}$$

In the presence of salt water, the real part of Z_M is non-negligible, and so an alternative coupling factor formula is proposed by [20] and is given in Equation (5.6).

$$k_{\mathrm{salt}} = \frac{|Z_M|}{\sqrt{\Im\left(Z_{\mathrm{TX}}\right) \Im\left(Z_{\mathrm{RX}}\right)}} = \frac{\sqrt{R_M^2 + (\omega M)^2}}{\omega \sqrt{L_{\mathrm{TX}} L_{\mathrm{RX}}}} \tag{5.6}$$

The coupling factors for the system in air and in salt water are given in Table 5.4.

	k
Salt water	6.92 %
Air	7.50 %

Table 5.4: Coupling factor of system in air and in salt water

In air, as the real part of Z_M becomes negligible ($\omega M \gg R_M$), the equations for a system in air introduced in Chapter 2 are valid for analysing the link and deriving the quantities for optimal link efficiency operation using resonant tuning. Table 5.5 shows the tuning capacitance, optimal load, and maximum link efficiency for the system in air.

The calculation of the tuning capacitance and optimal load resistance for a system in salt water to operate at maximum link efficiency requires a different set of equations due

Parameter	Value
C_{tune}	527 pF
$R_{\text{L,opt}}$	2.47 Ω
η_{link}	90.4 %

Table 5.5: Link parameters for system in air

to the presence of a non-negligible R_M. Equations (4.9) and (4.10) give the optimal load and the tuning capacitance, respectively. The maximum link efficiency is then given by Equations (4.11) and (4.12).

As a comparison, it may be interesting to know how the parameters would differ if the tuning capacitance and the load resistance were calculated using the equations in Chapter 2 for a system in air. They can also be calculated using the Equations (4.9) and (4.10), but with $R_M = 0$, i.e. the mutual resistance is ignored in the calculations, so the equations are identical to the ones for a system in air. However, to calculate the actual link efficiency, a more general expression must be used which allows the calculated of link efficiency for any arbitrary load resistance and tuning capacitance. This was derived in Chapter 4, and the expression of the link efficiency given a tuning capacitance and a load resistance is given in Equation (4.24), where $X_L = -\frac{j}{\omega C_{\text{tune}}}$

Table 5.6 shows the tuning capacitance, load resistance, and the link efficiency, using both the maximum link efficiency objective (referred to as 'optimal tuning') and the equations for the tuning capacitance and optimal load resistance in air (referred to as 'resonant tuning').

Parameter	Resonant tuning	Optimal tuning
C_{tune}	519 pF	551 pF
R_L	2.55 Ω	2.17 Ω
η_{link}	72.8 %	75.5 %

Table 5.6: Link parameters for a system in salt water solution, using both optimal tuning and resonant tuning

Table 5.7 shows the reflected impedances on the transmitter for a system in air, a system in salt water with 'optimal tuning', and a system in salt water with 'resonant tuning'.

Alternatively, it is possible to tune the receiver coil so that a purely real reflected

Scenario	Reflected impedance
Air	$(5.76 + 0.0285\text{j})\,\Omega$
Salt water - resonant tuning	$(4.32 - 0.760\text{j})\,\Omega$
Salt water - optimal tuning	$(3.58 - 2.69\text{j})\,\Omega$

Table 5.7: Reflected impedance on transmitter of a system in air, a system in salt water with 'optimal tuning', and a system in salt water with 'resonant tuning'

impedance is obtained at the transmitter. Expanding the expression for reflected impedance in Equation (4.32), we can obtain:

$$\begin{aligned} & -\frac{Z_M^2}{Z_{\mathrm{RX}} + Z_L} \\ = & -\frac{R_M^2 - X_M^2 + j2R_M X_M}{(R_{\mathrm{RX}} + R_L) + j(X_{\mathrm{RX}} + X_L)} \cdot \frac{(R_{\mathrm{RX}} + R_L) - j(X_{\mathrm{RX}} + X_L)}{(R_{\mathrm{RX}} + R_L) - j(X_{\mathrm{RX}} + X_L)} \\ = & \frac{-(R_M^2 - X_M^2 + j2R_M X_M)((R_{\mathrm{RX}} + R_L) + j(X_{\mathrm{RX}} + X_L))}{(R_{\mathrm{RX}} + R_L)^2 + (X_{\mathrm{RX}} + X_L)^2} \end{aligned} \tag{5.7}$$

Taking the imaginary part of Equation (5.7) and setting to zero:

$$\frac{-2R_M X_M(R_{\mathrm{RX}} + R_L) + (R_M^2 - X_M^2)(X_{\mathrm{RX}} + X_L)}{(R_{\mathrm{RX}} + R_L)^2 + (X_{\mathrm{RX}} + X_L)^2} = 0 \tag{5.8}$$

Re-arranging and solving for $X_L = X_{\mathrm{L,real}}$:

$$X_{\mathrm{L,real}} = \frac{2R_M X_M(R_{\mathrm{RX}} + R_L)}{R_M^2 - X_M^2} - X_{\mathrm{RX}} \tag{5.9}$$

Note that in this 'real tuning' scenario, the reactance load depends on the resistive load.

Substituting Equation (5.9) into (4.24), differentiating the result with respect to R_L, setting the derivative to zero, and re-arranging for $R_L = R_{\mathrm{L,real}}$, the following load resistance for a purely resistive reflected load on the transmitter can be obtained:

$$R_{\mathrm{L,real}} = R_{\mathrm{RX}} \sqrt{\frac{X_M^2 - R_M^2 + R_{\mathrm{TX}} R_{\mathrm{RX}}}{R_{\mathrm{TX}} R_{\mathrm{RX}}}} \tag{5.10}$$

This calculated value of load resistance is the one which maximises the link efficiency when a tuning capacitor of $X_{\mathrm{L,real}}$ is used for obtaining a purely resistive reflected load on the transmitter. Table 5.8 shows the link parameters when real tuning is used.

Parameter	Real tuning
C_{tune}	508 pF
R_L	2.54 Ω
η_{link}	70.6 %
Z_{refl}	4.34 Ω

Table 5.8: Link parameters for a system in salt water solution, using real tuning

Table 5.9 shows the currents through and the voltages across the transmitter and receiver coils for the system in air, the system in salt water with 'resonant tuning', and the system in salt water with 'optimal tuning', and the system in salt water with 'real tuning'. The expressions for currents and voltages were derived in Chapter 4 and are given by Equations (4.33), (4.34), (4.36) and (4.37).

Medium	Tuning	V_{TX}	I_{TX}	V_{RX}	I_{RX}
Air	Optimal/Resonant	228 V	1.91 A	63.8 V	2.84 A
Salt water	Resonant	276 V	2.30 A	63.7 V	2.80 A
Salt water	Optimal	288 V	2.44 A	65.0 V	3.04 A
Salt water	Real	282 V	2.33 A	65.3 V	2.81 A

Table 5.9: Comparison of currents and voltages for system in air and in salt water

Resonant tuning will be used in the experiments, as it results in a smaller reflected reactance on the transmitter than optimal tuning, but unlike tuning for a purely real reflected impedance, does not require changing the tuning capacitance whenever the load is varied. The smaller reflected reactance is beneficial in terms of maintaining the zero-voltage switching and constant current operation of the load-independent Class EF inverter that will be used in the experiment to drive the transmitter coil [88].

The purpose of the experiment is to show how increasing the load resistance can reduce the temperature rise of the salt water, given a constant received power of 10 W. The increased load resistance will be 1.5 times that of the original load, whilst the tuning capacitance is kept the same. Table 5.10 shows how link efficiency, reflected impedance, coil currents and coil voltages change when the load is increased by 1.5 times (using resonant tuning).

Parameter	Original load	Increased load
R_L	$2.55\,\Omega$	$3.82\,\Omega$
η_{link}	$72.8\,\%$	$71.3\,\%$
Z_{refl}	$(4.32 - 0.760\text{j})\,\Omega$	$(3.02 - 0.532\text{j})\,\Omega$
V_{TX}	$276\,\text{V}$	$322\,\text{V}$
I_{TX}	$2.30\,\text{A}$	$2.69\,\text{A}$
V_{RX}	$63.7\,\text{V}$	$52.4\,\text{V}$
I_{RX}	$2.80\,\text{A}$	$2.29\,\text{A}$

Table 5.10: Comparison of link parameters of system with original load (using resonant tuning) and increased load (1.5 times original load)

5.3 Power electronics

The receiver coil PCB is connected via short copper tape to another PCB, which contains the series tuning capacitor and a current-driven half-wave Class D rectifier. A photograph of this rectifier PCB is shown in Figure 5.4.

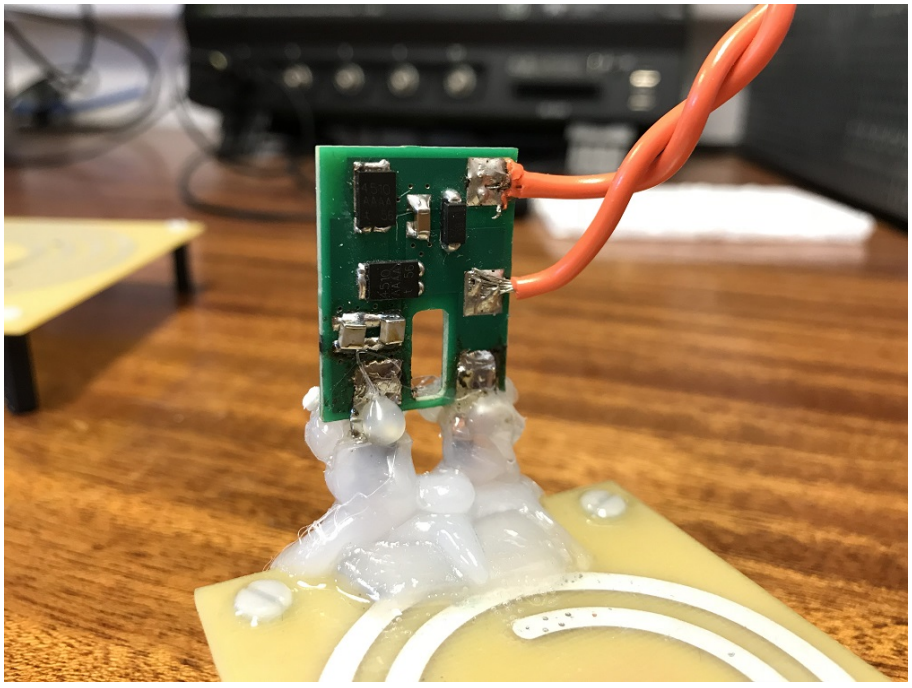


Figure 5.4: Current driven Class D rectifier PCB

The rectifier, which was first introduced and described in Chapter 2, converts the alternating current (AC) current in the coil to a direct current (DC) current. It consists of two Schottky rectifier diodes (Nexperia PMEG45A10EPD - 45 V, 10 A) and a 1 µF output filter capacitor. The output of the rectifier is connected to a variable DC load resistor, so that the load can be easily modified after each experiment run.

Figure 5.5 shows a schematic diagram of the receiver system, with the receiver coil (modelled by the induced electromotive force (EMF) V_{ind}, the coil inductance L_{RX} and the combined coil resistances R_{RX}), the series tuning capacitor C_{ser}, the current-driven half-wave Class D rectifier (consisting of diodes D_1 and D_2 and capacitor C_f) and the variable DC load $R_{\text{L,DC}}$. For the system in salt water under 'resonant tuning', the circuit parameters and variables are given in Table 5.11.

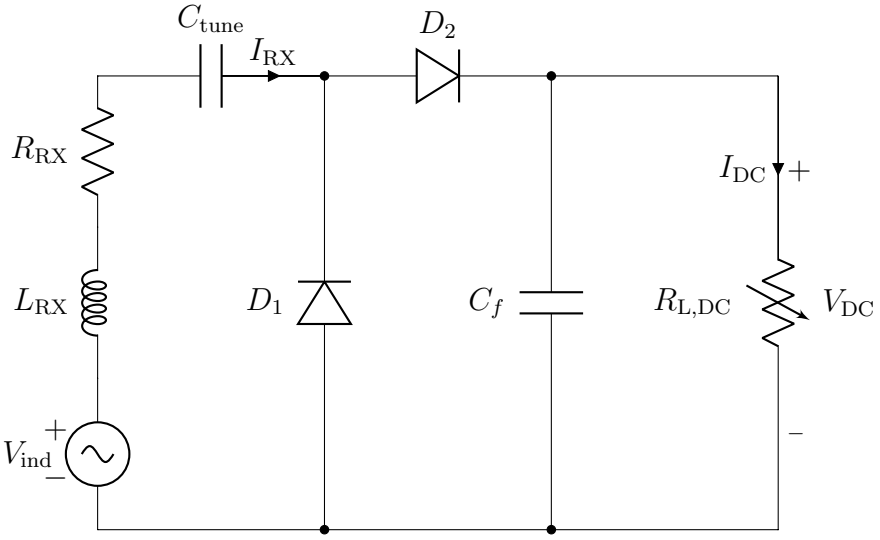


Figure 5.5: Schematic diagram of receiver system

Parameter	Value
V_{ind}	8.31 V
L_{RX}	265 nH
R_{RX}	418 mΩ
C_{tune}	519 pF
C_f	1 µF
$R_{\text{L-DC}}$	12.6 Ω

Table 5.11: Receiver system parameters

The relationship between the AC load at the input of the rectifier (R_L) and output DC load ($R_{\text{L,DC}}$) is given by Equation (5.11) [48, 89]. Therefore, given the AC load values in Table 5.10, the original DC load is 12.6 Ω and the increased DC load is 18.9 Ω.

$$R_{\text{L,DC}} = \frac{\pi^2}{2} R_L \tag{5.11}$$

Equation 5.12 gives the relationship between the AC input current and the DC output

current. The DC output voltage can be calculated using Equation 5.13.

$$I_{\mathrm{DC}} = \frac{I_{\mathrm{RX}}}{\pi} \tag{5.12}$$

$$V_{\mathrm{DC}} = I_{\mathrm{DC}} R_{\mathrm{L,DC}} = \frac{I_{\mathrm{RX}} R_{\mathrm{L,DC}}}{\pi} \tag{5.13}$$

The simulated AC input voltage (V_{in}), AC input current (I_{in}), DC output voltage (V_{DC}) and DC output current (I_{DC}) of the Class D current-driven rectifier with idealised diodes are shown in Figure 5.6. Table 5.12 shows the root mean square (RMS) value at the fundamental frequency (first harmonic) of the AC input waveforms and the value of the DC output waveforms in Figure 5.6. The input impedance of the rectifier is considered to be resistive as the first harmonic components of the input voltage and the input current are in phase, and the amplitude ratio of the input voltage to the input current at the fundamental frequency is constant [48, 89].

Quantity	Value
V_{in}	5.03 V (RMS)
I_{in}	1.97 A (RMS)
V_{DC}	11.2 V
I_{DC}	0.891 A

Table 5.12: Simulated Class D rectifier waveform values

The transmitter coil is driven by a load-independent Class EF inverter [82]. The schematic diagram of the inverter and the transmitter is shown in Figure 5.7. It has a similar topology to the Class EF_2 and the Class $\mathrm{E/F}_3$, where a series inductor-capacitor (LC) network is placed in parallel with the switching device of a Class E inverter in order to reduce the current or voltage stresses of the switching device. However, instead of tuning the LC network to either the second or third harmonic of the switching frequency, it is tuned to a certain value in between the switching frequency and the second harmonic. With the appropriate selection of component values for this circuit, a load-independent Class EF inverter can be designed, which is able to sustain a constant output current over a range of load resistances without losing zero-voltage switching. This means that when a

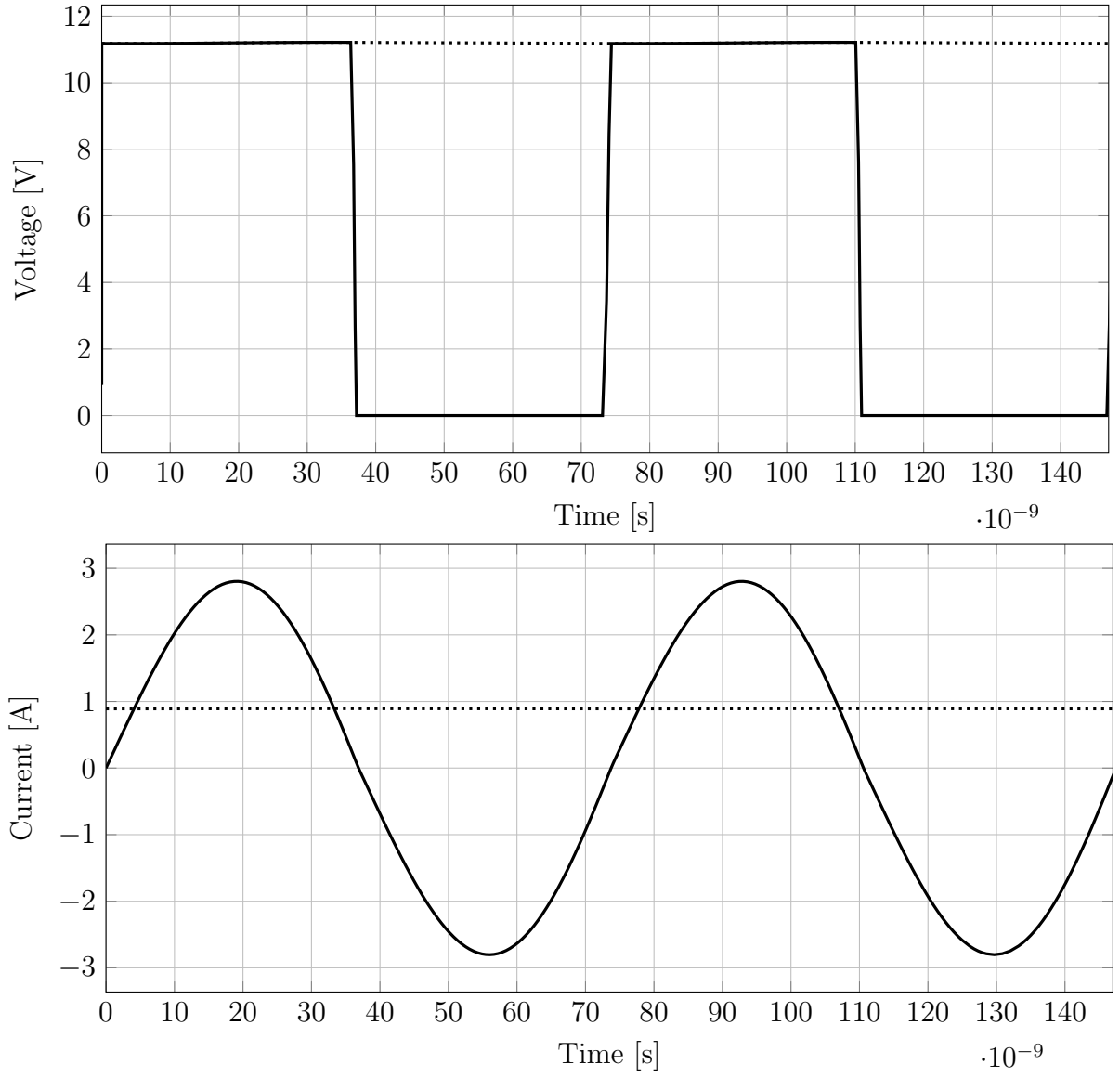


Figure 5.6: Simulated current-driven Class D rectifier waveforms: [Top] Input (solid) and output (dotted) voltage; [Bottom] Input (solid) and output (dotted) current

different receiver load is used, the inverter does not need to be retuned and reconfigured.

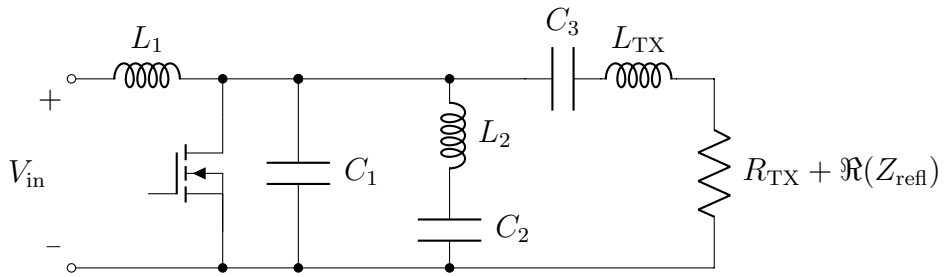


Figure 5.7: Schematic diagram of load independent Class EF inverter and coil

Table 5.13 shows the circuit parameters and variables used for the system in salt water under 'resonant tuning'. Figure 5.8 shows the voltage waveform across the inverter's switch and the output current waveform, using the values in Table 5.13.

Parameter	Value
L_{TX}	1.41 µH
R_{TX}	856 mΩ
Z_{refl}	$(4.32 - 0.760\mathrm{j})\,\Omega$
C_1	261 pF
C_2	196.4 pF
C_3	120 pF
L_1	50 µF
L_2	251.4 nF

Table 5.13: Transmitter system parameters

In order to deliver 10 W to the receiver load, a transmitter coil current of 2.30 A is required as previously calculated. Therefore, an input voltage of 39.5 V is needed. The resulting input current is 328 mA and the switch voltage reaches a maximum of 95.3 V.

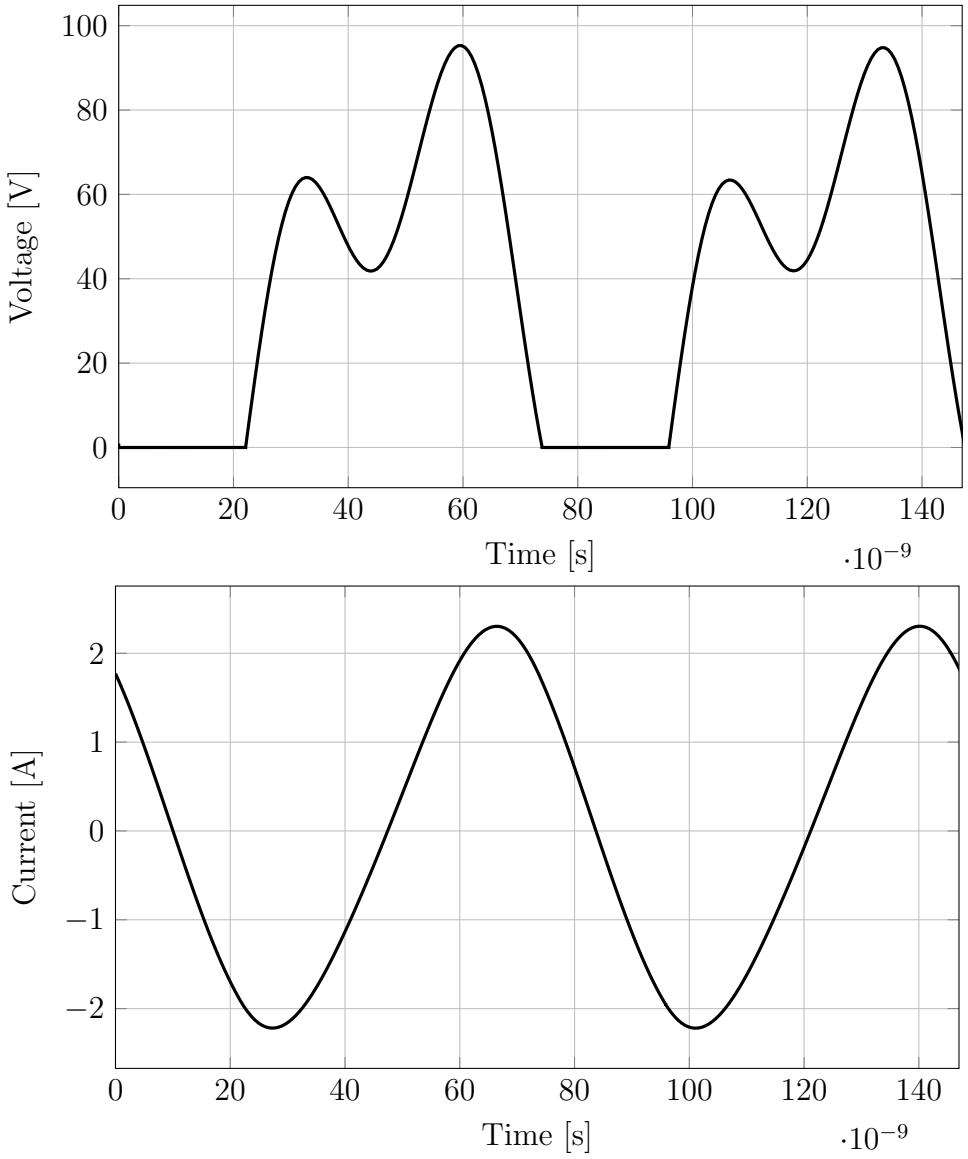


Figure 5.8: Simulated load-independent Class EF inverter waveforms: [Top] Switch voltage; [Bottom] Output current

5.4 Thermal insulation and temperature measurement

Expanded polystyrene foam sheets of 1 cm thickness are used to insulate the tank containing the salt water. A foam holder was made that covered the bottom and the sides of the tank. Another piece of foam was constructed so that it could fit just over the top of the water, with holes cut allowing for copper tape to connect the coil below the foam to the rectifier which was placed above the foam. This would ensure that the heat dissipated by the rectifier would not greatly influence the temperature measurement of the water. Figure 5.9 shows the salt water tank sitting in the foam holder.

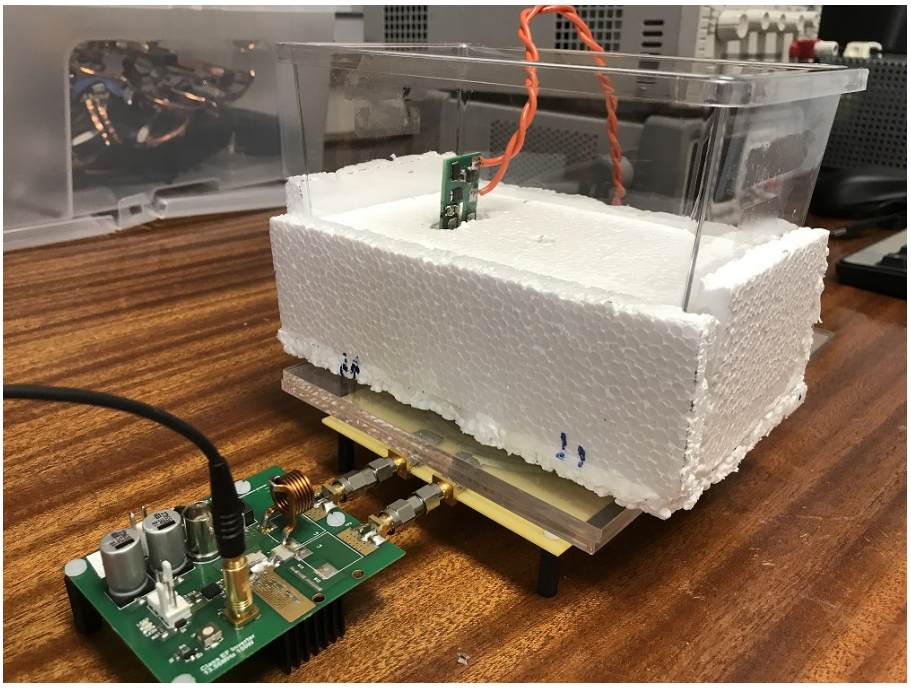


Figure 5.9: Polystyrene foam holder insulating the salt water solution in the tank

Temperature measurement was done via a K-type thermocouple and a Keysight U1251B Handheld Digital Multimeter. The thermocouple probe is unable to measure temperature during the operation of the system as the high frequency magnetic field induces voltage in the thermocouple, leading to interference. In addition, the thermocouple has to be removed from the salt water during the operation of the system. Otherwise, the high frequency magnetic field would induce currents in the thermocouple, which can pose as an additional source of heating. Therefore, the thermocouple measures the starting

temperature of the water, and is removed just before the system is turned on. After the system operates for a certain amount of time, it is then switched off and the thermocouple is placed in the water once again to take the final temperature. Thermocouples have a very quick response time, so temperature readings can be made soon after the thermocouple is placed in the water. The location of temperature measurement is chosen to be the surface of the receiver coil PCB in the centre of the coil.

Thermistor probes were considered as an alternative method of measuring temperature, as they tend to be more accurate. However, when left in the water, they also produce additional heating, adding to the rise in the temperature of the water. They could also be used in the same way as thermocouples, where temperature is only measured when the system is switched off, but removed from the water when power is transferred; however, their response times can be longer than those of thermocouples, so thermocouples were used in favour of thermistors. Figure 5.10 is a thermal imager capture showing the heating of the thermistor probe when the system is running.

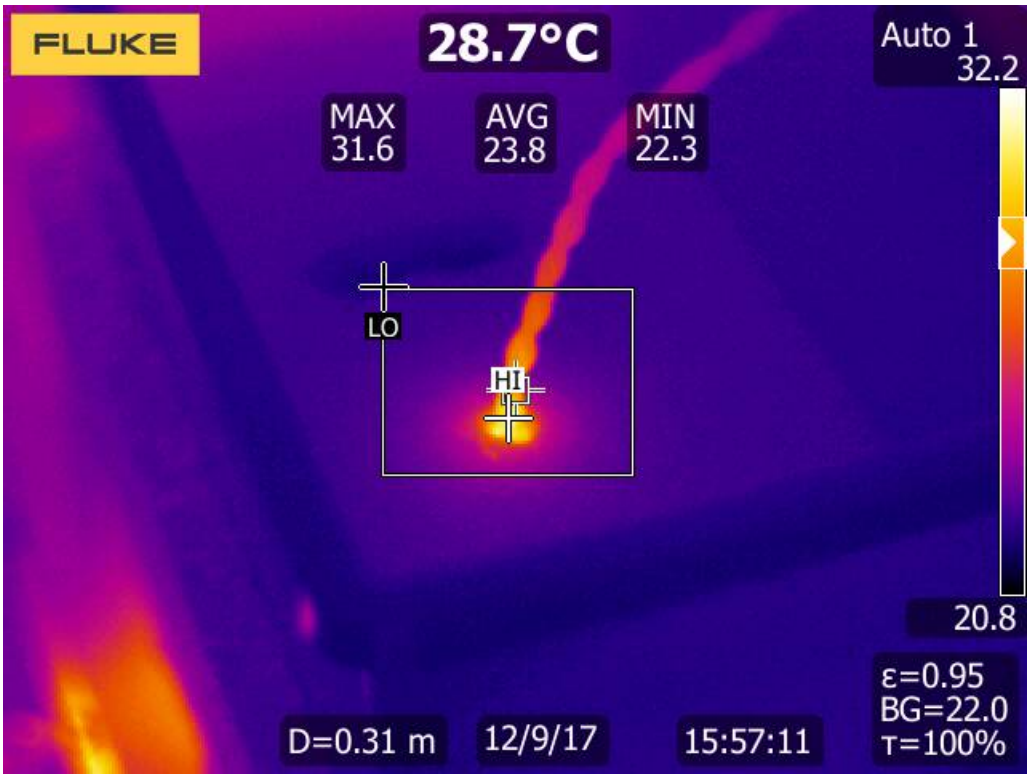


Figure 5.10: Thermal imager capture showing thermistor probe heating up in the salt water solution

5.5 Results

For the experimental runs, the power transferred to the receiver load was chosen to be 10 W, so the DC input voltage to the inverter needed to be constantly monitored and adjusted manually to ensure the power received was as stable as possible. Small changes to the input voltage needed to be made over time, due to the temperature dependence of several parameters such as the GaN FET and diode capacitance. Power in the resistive variable load was monitored using a Yokogawa WT310 Power Meter.

Figure 5.11 is a scatter plot of the experimental results, showing the temperature rise of the salt water solution for each run. For each type of load (original and increased), twelve 20-minute runs were performed. The temperature rise is normalised with respect to the change in ambient temperature for the duration of the experimental run.

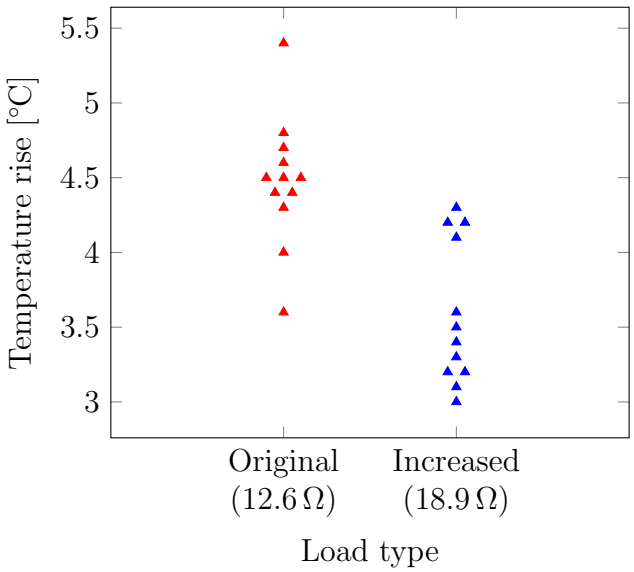


Figure 5.11: Scatter plot of experimental results, showing temperature rise of salt water solution with both original and increased DC load

For the original load, the mean temperature rise was 4.48 °C and the standard deviation was 0.43 °C. For the increased load (which aimed to reduce the receiver coil current and the magnitude of the magnetic field in the centre of the receiver coil), the mean temperature rise was 3.59 °C and the standard deviation was 0.48 °C. Therefore, the difference in the mean temperature rise between the original load and the increased load is 0.89 °C.

There is variation in the temperature rise measurements for each type of load, as a result of experimental error. Despite having normalised the results with respect to the change in ambient temperature for the duration of the experimental run, the experiments were run at different ambient temperatures and different rates of change in ambient temperature (this is largely dependent on the time of day), which would have had an effect on the thermal characteristics. Running the experiments in a climate-controlled environment would help to reduce some of the variations.

5.6 Simulation verification

After the full system experiments have been carried out, electromagnetic and thermal simulations of the experimental setup are performed. By verifying the experimental results with simulations, it can be determined whether the simulations involving the human body models are likely to be valid or not.

The transmitter and receiver coils in the simulations have the same geometries as the actual planar circular spiral coils used in the experiment.

The conformal coating is modelled as a thin box in which the receiver coil is placed. The coating material has a dielectric constant of 2.7 and a dissipation factor of 0.001, as taken from the datasheet [90]; with the use of these values, the dielectric properties of the coating can be considered in electromagnetic field simulations. Thermal properties of silicone have been obtained from other sources and are input into the thermal simulations [78]. The thermal conductivity is taken to be $0.15\,\mathrm{W\,K^{-1}\,m^{-1}}$ and the specific heat capacity is $1.46\,\mathrm{kJ\,K^{-1}\,kg^{-1}}$. The material density is $970\,\mathrm{kg\,m^{-3}}$.

The thickness of the coating is 100 µm; this was selected by optimising the coating thickness so that the simulated receiver coil impedance closely matches the measured coil impedance of the receiver coil.

The salt water is modelled as a rectangular block with dimensions of $150\,\mathrm{mm} \times 90\,\mathrm{mm} \times 25\,\mathrm{mm}$. The conductivity of the block is $2.512\,\mathrm{S\,m^{-1}}$ as required, and its dielectric constant is set at 78 [86]. The dielectric constant of pure water is 80 at 20 °C, but the

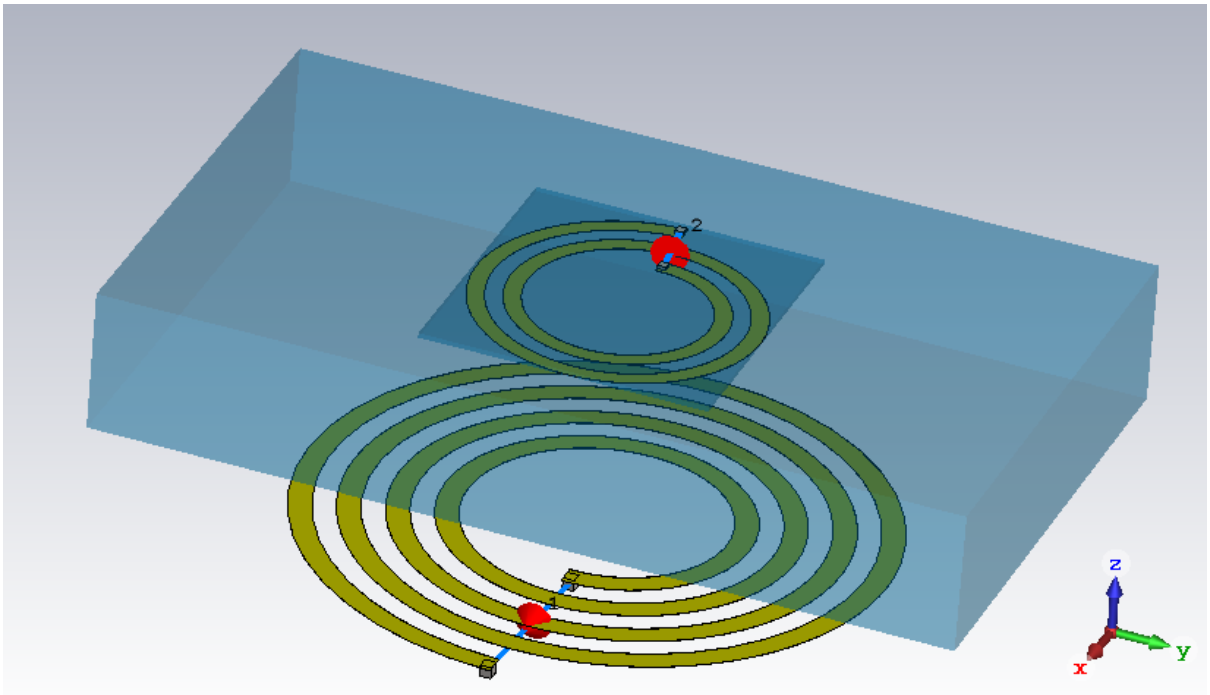


Figure 5.12: Experimental setup modelled in CST Microwave Studio

addition of sodium chloride serves to lower it.

Figure 5.12 shows how the set up is modelled in the CST Microwave Studio electromagnetic simulator. The distance between the coils is 4 cm, with the bottom of the salt water block 2 cm above the transmitter coil, and the receiver coil placed in the salt water block 2 cm above the bottom of the salt water block. There is 5 mm of salt water above the receiver coil, as in the experiments. For the subsequent thermal simulations, the ambient and initial temperature is 20 °C.

For the first simulation, the load resistance and tuning capacitance is calculated with 'resonant tuning' equations in Chapter 2. Therefore, R_L is set to 3.07 Ω (and referred to as the 'original load') and C_{tune} is set to 549 pF. To deliver 10 W to this load, a transmitter coil current of 2.18 A is required. Figure 5.13 shows the cross-sectional distribution of SAR through the centre of the receiver coil in the salt water solution. When averaged over 1 g of water, the maximum SAR in this plot is 31.1 W kg^{-1}. The link efficiency of the system using this load is 76.2 %. Figure 5.14 shows the variation of the magnetic field strength with distance on axis from the transmitter coil, with the receiver coil at 4 cm. At the centre of the receiver coil, the magnetic field strength is 140 A m^{-1}, which

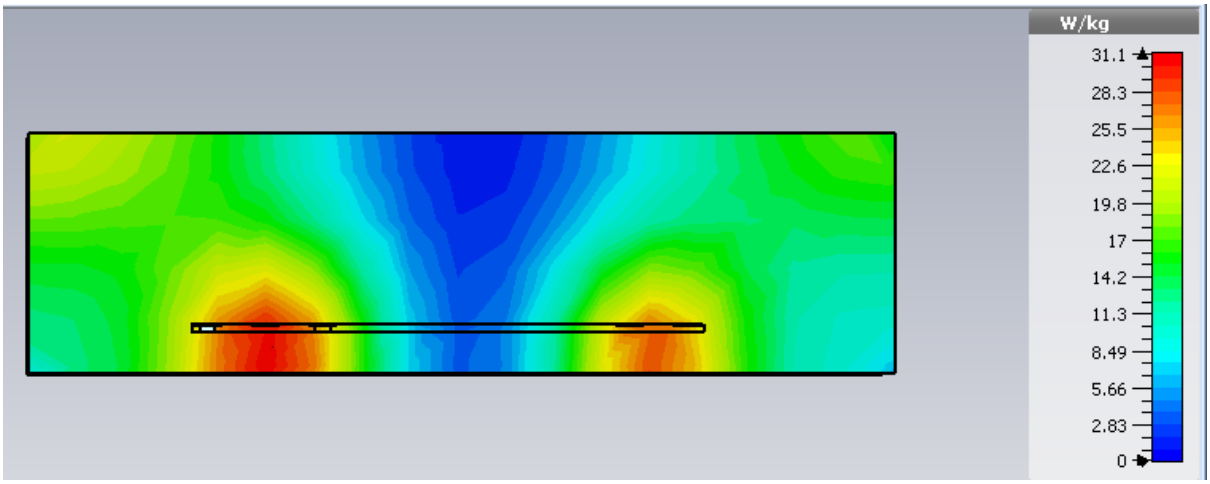


Figure 5.13: SAR distribution with original load

corresponds to a magnetic flux density of 175 µT. Table 5.14 shows the level of power dissipation in the transmitter coil, the receiver coil and the salt water block.

Component	Power dissipation
Transmitter coil	0.58 W
Receiver coil	0.36 W
Salt water block	2.2 W

Table 5.14: Power dissipation in coils and salt water with original load

The second simulation aims to reduce the SAR near the receiver coil, by reducing the overall magnetic field strength at the centre of the receiver. Tuning capacitance is kept the same as in the previous simulation, but $R_L = 4.60\,\Omega$, which is 1.5 times the original value (the 'increased load'). To deliver 10 W to this load, a transmitter coil current of 2.56 A is required. Figure 5.15 shows the cross-sectional distribution of SAR through the centre of the receiver coil in the salt water solution. When averaged over 1 g of water, the maximum SAR in this plot is 28.25 W kg^{-1}. However, it is important to note that this value is found close to the transmitter coil (due to the increased transmitter coil current), whilst the SAR values near the receiver coil has decreased to much lower levels. The link efficiency of using the increased load is 74.9 %. Figure 5.16 shows the variation of the magnetic field strength with distance on axis from the transmitter coil, with the receiver coil at 4 cm. At the centre of the receiver coil, the magnetic field strength is 117 A m^{-1}, which corresponds to a magnetic flux density of 147 µT. Table 5.15 shows the level of power dissipation in the transmitter coil, the receiver coil and the salt water block.

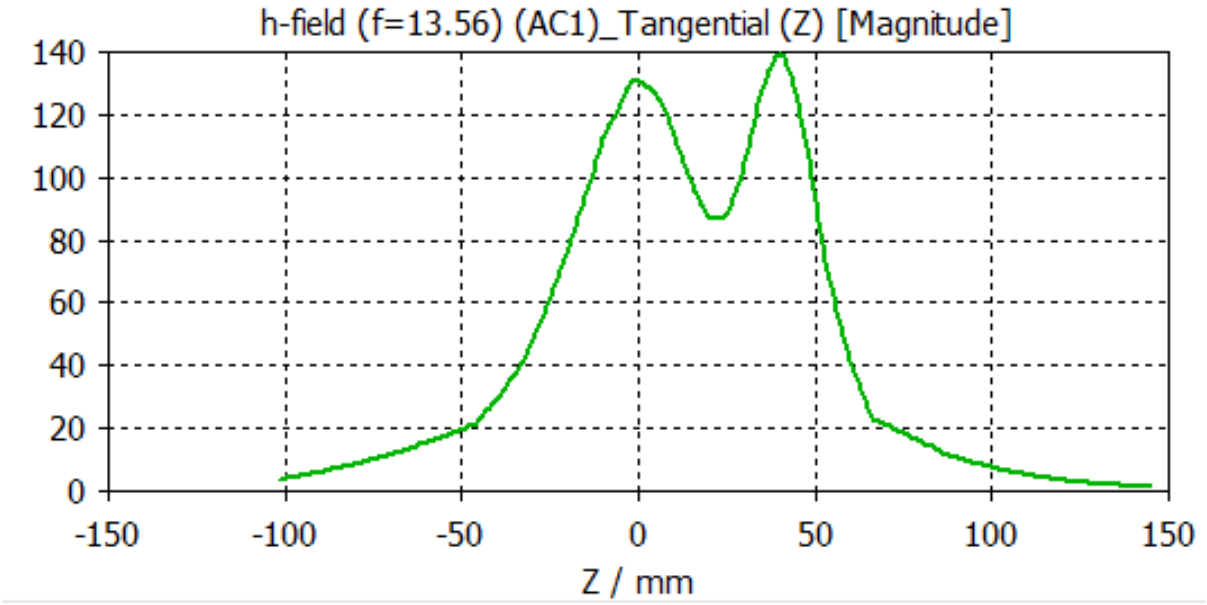


Figure 5.14: Variation of magnetic field strength with distance on axis from transmitter, when original load is used

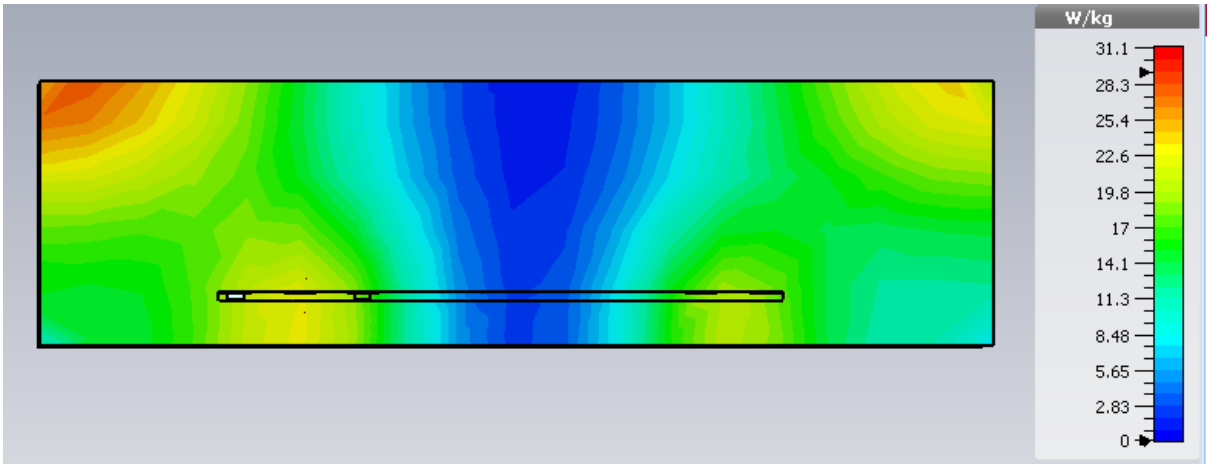


Figure 5.15: SAR distribution with increased load

Component	Power dissipation
Transmitter coil	0.80 W
Receiver coil	0.24 W
Salt water block	2.3 W

Table 5.15: Power dissipation in coils and salt water with increased load

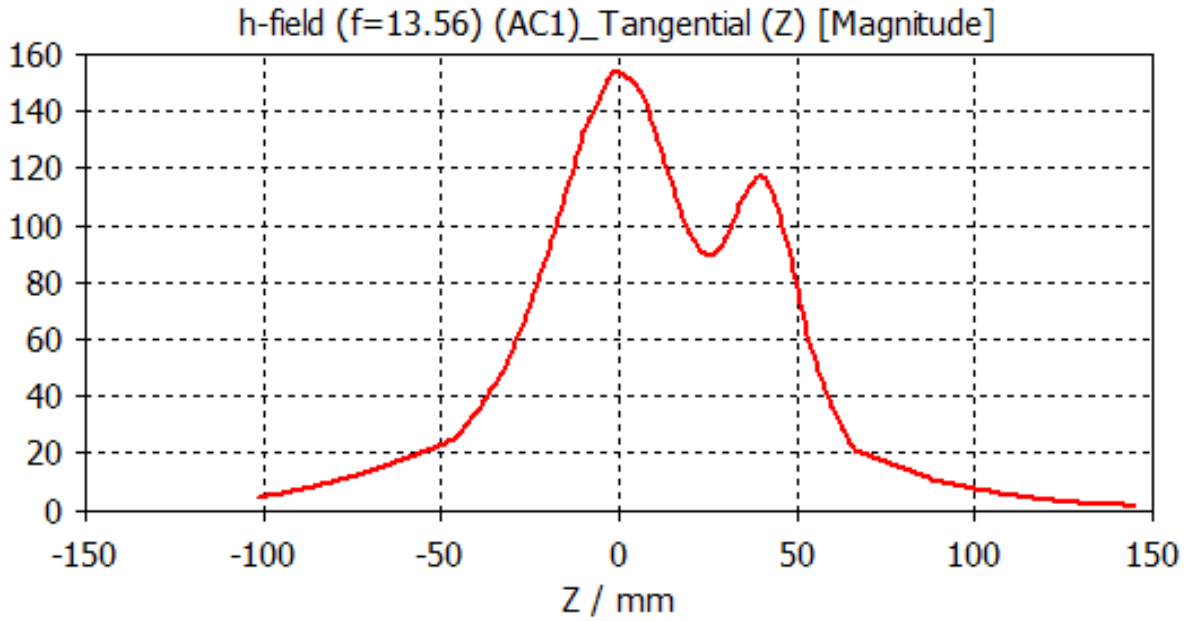


Figure 5.16: Variation of magnetic field strength with distance on axis from transmitter, when increased load is used

Figure 5.17 shows the cross-section temperature distribution through the centre of the receiver coil and the salt water block for the simulation in which the 'original load' was used, 20 minutes after the start of the simulation. The temperature on the surface of the receiver coil at the centre of the coil rose by 4.45 °C to 24.45 °C.

Figure 5.18 shows the cross-section temperature distribution through the centre of the receiver coil and the salt water block for the simulation in which the 'increased load' was used, 20 minutes after the start of the simulation. The temperature on the surface of the receiver coil at the centre of the coil increased by 3.48 °C to 23.48 °C. The difference in temperature rise between the original load and the increased load is 0.97 °C. Note that the temperatures in the upper corners of the salt water box have increased due to the higher voltages and currents on the transmitter coil when the increased load is used.

Figure 5.19 shows the variation of temperature with time during the 20-minute simulation run for both the original load (solid) and the increased load (dashed) at the centre of the receiver coil.

Table 5.16 compares the temperature rises of the experiment with that of the simulation, for both the original load and increased load.

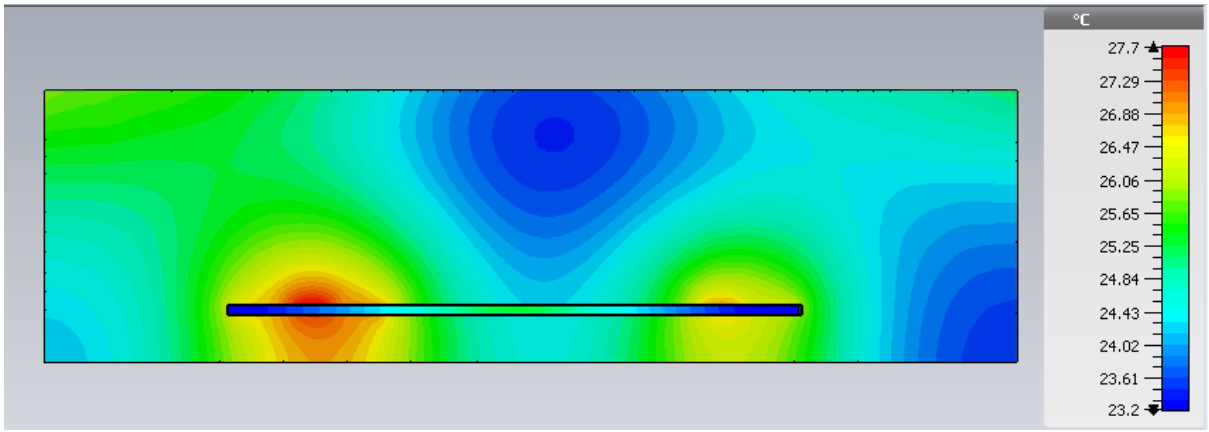


Figure 5.17: Temperature distribution with original load

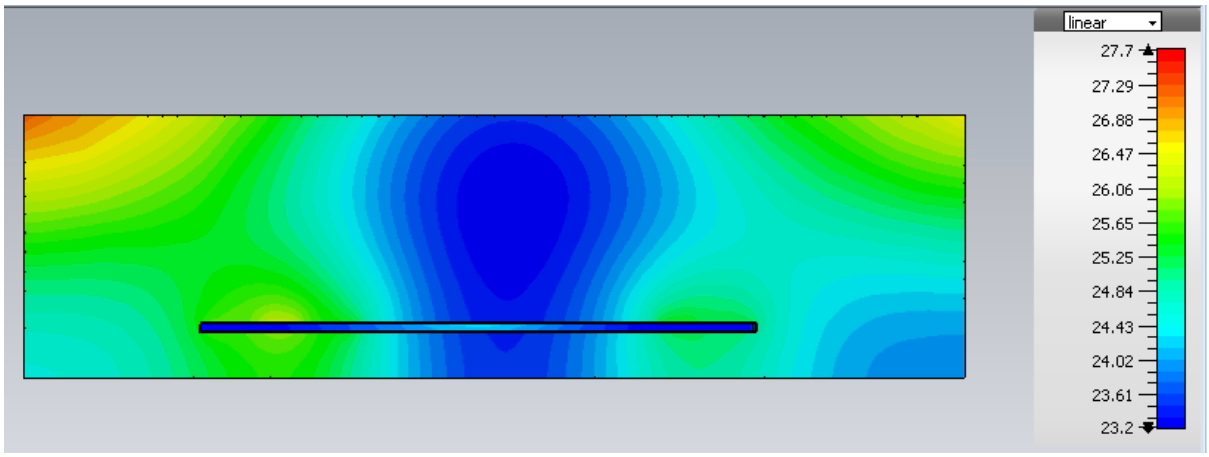


Figure 5.18: Temperature distribution with increased load

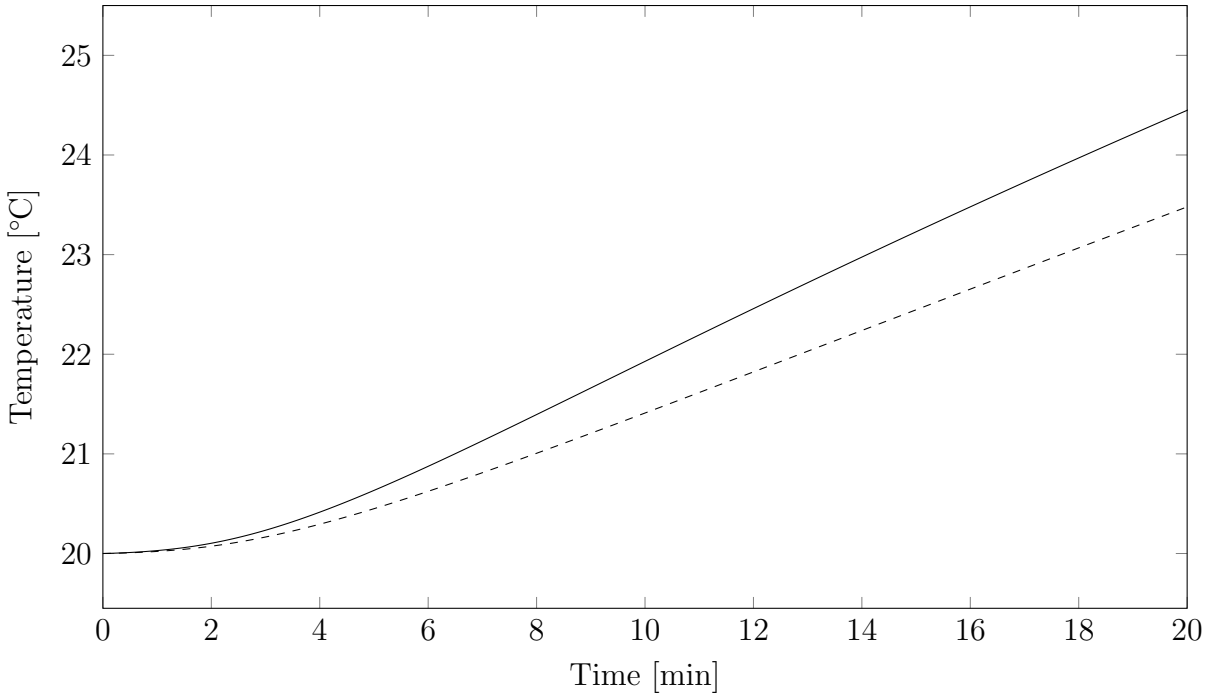


Figure 5.19: Variation of temperature with time for original (solid) and increased (dashed) load at centre of receiver coil

	Experiment	Simulation
Original load temp. rise	4.48 °C	4.45 °C
Increased load temp. rise	3.59 °C	3.48 °C
Difference in temp. rise	0.89 °C	0.97 °C

Table 5.16: Comparison of temperature rises of experiment and simulation

5.7 Summary

This chapter presented an experimental setup consisting of a WPT system with a receiver immersed in a salt water solution. The system was run with two different loads: a load for achieving maximum link efficiency and an increased load to reduce coil dissipation and the overall magnetic field at the centre of the receiver coil. For each experimental run, the temperature rise of the salt water solution was measured after a period of time, and it was found that the experimental runs with the increased load generally resulted in lower temperature rises.

The experimental setup was also modelled in CST Microwave Studio and CST MPhysics Studio as closely to real-life as possible. Electromagnetic and thermal simulation results show good agreement with the experimental results, thus validating the hypothesis that changing the load leads to a fall in the temperature rise of the surrounding conductive medium.

Chapter 6

Towards long-range powering of low-power medical implants and wearables

Chapter 4 presented the design process of a wireless power transfer (WPT) system for high-power implantable medical devices that can operate efficiently and within safety limits. In reality, these systems can only operate feasibly over a relatively short distance without link efficiency suffering too much, current and voltages levels being too impractically high, or safety limits being exceeded. However, there are many types of small medical implants and wearable devices requiring an external source of power, whose power consumption is very low. Thus, for such devices, there is the possibility of being wirelessly powered over a longer range.

A common characteristic among WPT systems for medical implants and wearable devices is that the implanted or body-worn receiver coil is highly constrained in size (no more than a few cm), and therefore the transmitter coil is likely to be larger than the receiver coil. For the long range delivery of power to small medical devices and wearables, this asymmetry in size will be much more apparent than that for the shorter-range powering of higher-power left ventricular assist devices (LVADs). The transmitter coil needs to be larger in order to maintain good coverage of magnetic flux that will

be picked up by the receiver coil some distance away. Also, a larger transmitter coil is required to sustain the high magnetic field levels that smaller receiver coils, with their decreased flux capture areas, need in order to deliver adequate power to the load.

This chapter introduces a position-insensitive approach to powering sensor networks remotely over a long range. It is envisioned that such an approach will also be suitable for low-power medical implantables and wearables. The method uses an open-loop method of impedance emulation to ensure that maximum power is received, and transmitter power modulation so that the sensor node electronics will not be damaged as the receiver moves close to the transmitter end. This method allows the system to operate reliably as the distance between the transmitter and the receiver changes. At the end of this chapter, an approach to detecting living objects using a high frequency magnetic field is presented, making use of some of the concepts introduced in Chapter 4. Such an approach could be used in the detection of foreign objects in the vicinity of a WPT system for safety reasons. Another example of its potential use could be in rescue operations to find people trapped underneath collapsed buildings following an earthquake.

6.1 Motivation

Inductive power transfer (IPT) systems, which operate in the near field, are a particularly attractive alternative to existing far-field techniques for transferring power with electromagnetic (EM) fields over long distances (up to 10 m). In a previous system [42], it was shown that more than 10 mW can be transferred to a load up to 6 m from the transmitter. An issue with this system, though, is that different levels of load current draw in the sensor node changes the load impedance seen by the receiver's resonant tank, resulting in poorer efficiency and a significant drop in received power. Also, moving the receiver too close to the transmitter could cause damage to the receiver electronics due to excessive received voltage. An improved long-range IPT system for reliable long-range powering of sensors with milliwatt-level consumption is proposed. It overcomes the problems of the previous system by using an ultra-low power switch-mode impedance emulator to present

a constant impedance and wireless feedback to modulate the transmitter power.

6.2 System specifications and simulations

The transmitter used in the previous long-range system in [42] was a 2-turn 1 m square coil with a turn spacing of 30 mm, and was made from 28 mm copper pipe with a wall thickness of 0.9 mm. At the other end, the receiver was a 5-turn 17 cm square coil, made from three strands of 1.3 mm Litz wire. The same coils will be used in the simulation and experimental work in this chapter, which involves the development of an improved long-range remote powering system for sensor networks. Table 6.1 shows the simulated inductance, resistance and Q factor of both of the coils at 3 MHz, which is the same frequency that was used in [42].

Quantity	Symbol	Value
TX coil inductance	L_{TX}	8.67 µH
RX coil inductance	L_{RX}	9.14 µH
TX coil resistance	R_{TX}	52.0 mΩ
RX coil resistance	R_{RX}	450 mΩ
TX coil Q factor	Q_{TX}	3140
RX coil Q factor	Q_{RX}	383

Table 6.1: Simulated transmitter and receiver coil properties at 3 MHz

For this long-range system, the distance between the transmitter and receiver coils is to be varied from 1 m to 6 m. Figure 6.1 shows how the coupling factor changes with distance (obtained by electromagnetic simulation). Looking at the results from 3 m to 6 m, when the receiver is sufficiently far away from the transmitter coil, the relationship between the coupling factor k and the coil separation distance d is:

$$k \propto \frac{1}{d^{2.87}} \tag{6.1}$$

In comparison, the variation of the magnetic field strength of a magnetic dipole with distance follows the inverse cube law [83].

Figure 6.2 shows the change in link efficiency with distance at 3 MHz (obtained by electromagnetic simulation). The relationship between the link efficiency η_{link} and dis-

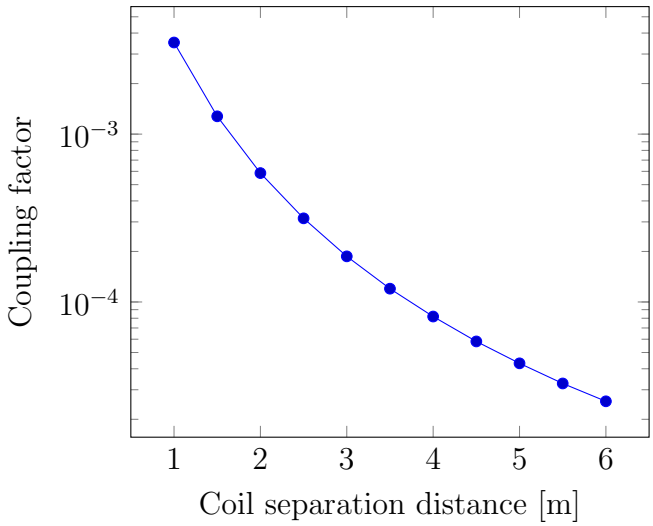


Figure 6.1: Variation of coupling factor with distance on axis from transmitter coil (from simulation)

tance d is:

$$\eta_{\text{link}} \propto \frac{1}{d^{5.74}} \tag{6.2}$$

Assuming a constant transmitter coil current and a negligible reflected resistance (resulting in near constant input power), this means that the received power also follows the same relationship with distance as link efficiency. For a magnetic dipole, power falls with distance to the power of six.

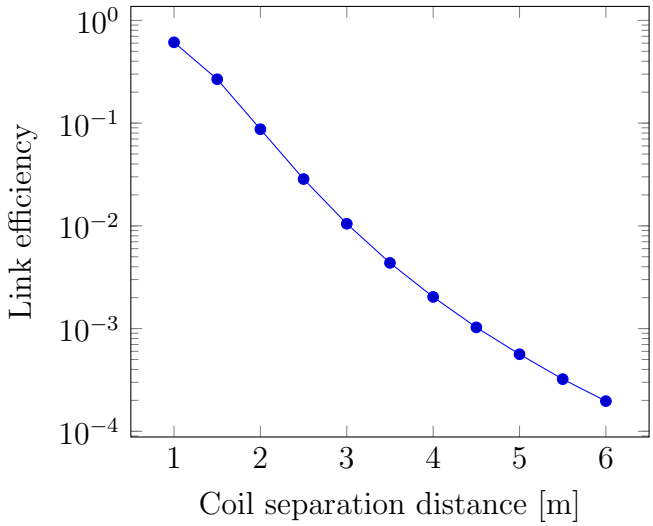


Figure 6.2: Variation of link efficiency with distance on axis from transmitter coil (from simulation)

A Class E inverter is used to drive the transmitter coil with a high-frequency alter-

nating current (AC) in order to generate the required magnetic field for the receiver end. Since coupling is very low over distances of several coil diameters, the reflected resistance of the receiver on the transmitter coil is also very low. For example, at a distance of 6 m, the coupling factor is 0.0026 %, leading to a reflected resistance of only 20.4 µΩ. Therefore, the inverter only needs to be designed with the transmitter coil impedance in mind, without needing to refer to the link and receiver parameters via reflected impedances [42].

Figure 6.3 shows the circuit diagram of the semi-resonant Class E inverter used for the long-range system. Table 6.2 lists the component values used for the Class E inverter that results in zero-voltage switching; these were calculated using the design procedure described in [91]. Figure 6.4 shows the simulated drain-source voltage of the Class E inverter metal–oxide–semiconductor field-effect transistor (MOSFET) switch, when the input direct current (DC) voltage V_{in} is 16.0 V and the output AC current I_{TX} is 27.0 A.

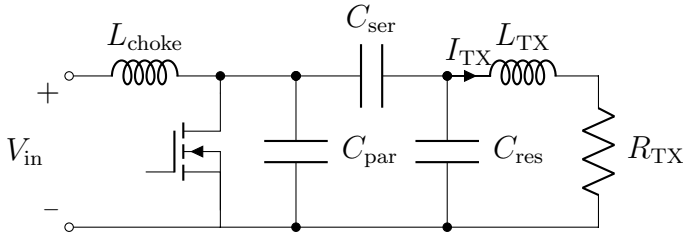


Figure 6.3: Semi-resonant Class E inverter from [2]

Component	Value
L_{choke}	47 µH
C_{par}	1.62 nF
C_{ser}	30.3 pF
C_{res}	294 pF

Table 6.2: Components values for semi-resonant Class E inverter

At the receiver end, link efficiency is maximised when receiver resonance is used to cancel the secondary leakage inductance and the optimal load is connected to the receiver's resonant tank [1]. Parallel tuning is employed instead of series tuning, due to the low induced electromotive force (EMF) in the receiver coil for the long-range low-power scenario. Figure 6.5 shows a schematic diagram of the receiver coil with the parallel tuning capacitor C_{tune} and the AC load R_L.

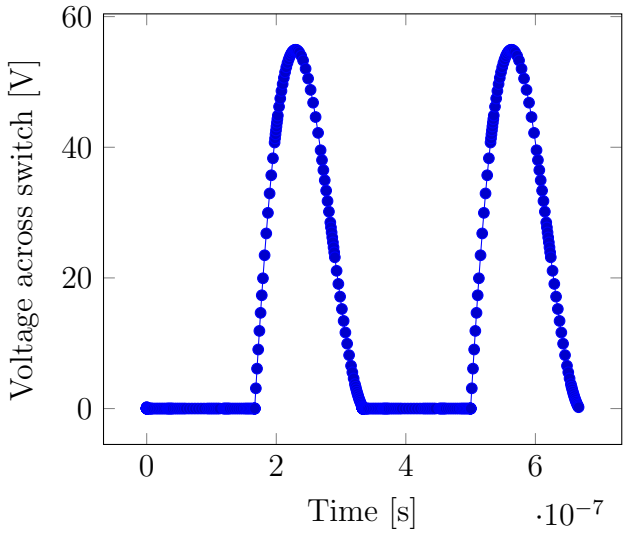


Figure 6.4: Voltage across MOSFET switch of Class E inverter ($V_{\text{in}} = 16.0\,\text{V}$, $I_{\text{TX}} = 27.0\,\text{A}$)

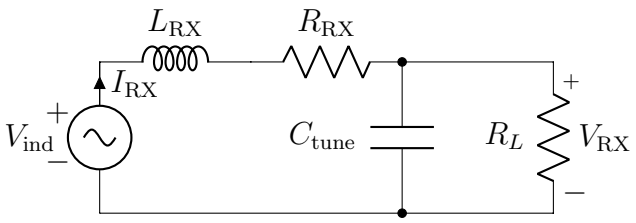


Figure 6.5: Equivalent circuit of parallel-tuned receiver with tuning capacitor and load

The expressions for the tuning capacitance and the optimal load for a parallel-tuned secondary are given by Equations (2.9) and (2.12), respectively [1]. As a result of using secondary tank resonance, the maximum link efficiency can be evaluated using Equation (2.13) [1].

However, in the case of a long-range system where coupling between the transmitter and the receiver is extremely weak, the link efficiency will be very poor. In fact, as coupling factor k is very low, the expression for the (complex) optimal load $Z_{\mathrm{L,opt}}$ can then be easily determined as it is simply the complex conjugate of the receiver's resonant tank at the operating frequency [42]. Therefore, the goal of link efficiency maximisation converges to that of achieving maximum power transfer from a voltage source (the induced voltage) with a finite impedance (the resonant tank). Thus, for a parallel tuned secondary,

$$Z_{\mathrm{L,opt}} = \left(\frac{1}{\frac{1}{R_{\mathrm{RX}}+j\omega L_{\mathrm{RX}}} + j\omega C_{\mathrm{tune}}} \right)^{*} \tag{6.3}$$

where R_{RX} is the parasitic resistance of the receiver coil, and $(x)^{*}$ denotes the complex conjugate of x. Due to the use of parallel receiver resonance and the relatively large coil Q factor, $Z_{\mathrm{L,opt}}$ is real and can be denoted by the optimal resistive load $R_{\mathrm{L,opt}}$.

Table 6.3 lists the values of the tuning capacitance and AC load resistance for maximising the link efficiency of the long-range system at 6 m.

Quantity	Value
C_{tune}	308 pF
$R_{\mathrm{L,opt}}$	66.0 kΩ

Table 6.3: Tuning and loading parameters for maximising link efficiency at 6 m

Figure 6.6 shows the variation of the magnetic flux density per square root of receiver power in mW with distance on axis from the transmitter coil, when the receiver coil (located at 6 m) is tuned and loaded with the values given in Table 6.3.

R_L in Figure 6.5 represents the AC load, but in most applications a DC output is required. Therefore, at the receiver side of an IPT system, a rectifier needs to be present in order to convert the AC voltage across the coils to a DC voltage to supply a DC load. For the long-range system, a full-wave bridge rectifier consisting of four diodes is selected

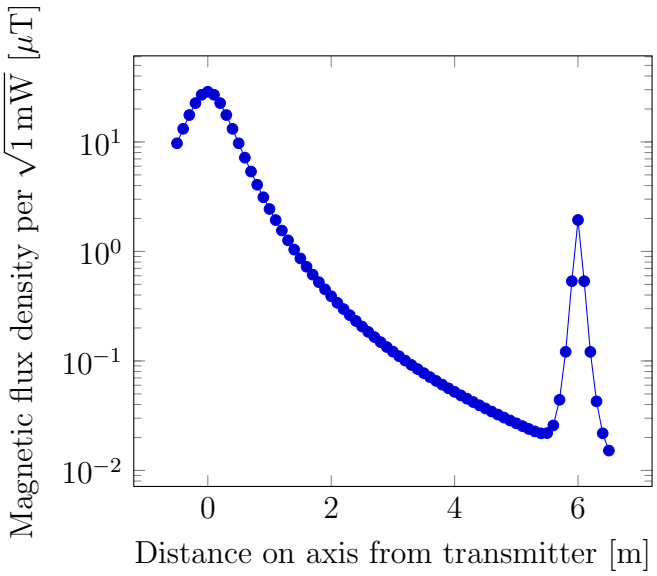


Figure 6.6: Variation of magnetic flux density per square root of receiver power in mW with distance on axis from transmitter (receiver at 6 m)

to perform the task of rectification. The relationship between the output DC load ($R_{\mathrm{L,DC}}$) and the AC resistance at the input of the rectifier (R_L) is given by [1]:

$$R_{\mathrm{L,DC}} = 2R_L \tag{6.4}$$

This rectifier needs to present to the resonant tank the optimal impedance in order for the maximum power to be collected.

The maximum receiver coil voltage, V_{RX}, was limited to 50 V (higher voltages could damage the receiver electronics), so the transmitter coil current is to be modified in order to achieve the desired receiver coil voltage. The transmitter coil current can be varied by changing DC input voltage of the Class E inverter. The received power P_L can be calculated by using the receiver coil voltage V_{RX} and the attached load R_L:

$$P_L = \frac{V_{\mathrm{RX}}^2}{2R_L} \tag{6.5}$$

6.3 Impedance emulation

Different levels of sensor node activity, resulting in variations in load current draw, can cause the link efficiency and power available to the load to collapse. Therefore, a method of impedance emulation is required so that a constant impedance is always presented to the output of the bridge rectifier in the receiver (and hence, to the receiver's resonant tank). Switch-mode DC-to-DC converters can be controlled in such a way that the desired impedance is presented. An open-loop control scheme is preferred as the power consumption requirements can be minimised. A converter operating in discontinuous conduction mode presents the potential ability to operate in open loop as the input current always starts from zero every switching cycle. The shape of the input current is then hopefully dependent only on switching characteristics and the value of circuit components such as the inductor. Step-down topologies are required as the expected rectified receiver voltage is 50 V whilst the sensor-node electronics run on 3 V to 5 V. A lithium (Li)-ion rechargeable coin cell is placed across the output of the impedance emulator in order to fix the output voltage at 3.7 V. Any excess power not consumed by the sensor node is stored in the cell, whilst the cell can also be used to power up the sensor node and the impedance emulator if the receiver is out of the transmit power range.

The buck converter, buck-boost converter, and the flyback converter are candidates for a step-down open-loop impedance emulation circuit [92], which is to be inserted between the bridge rectifier and the sensor node.

6.3.1 Buck topology

Figure 6.7 shows a buck converter, which steps down the voltage at its input, V_i (the rectified receiver coil voltage) to its output, V_o (fixed by a 3.7 V rechargeable Li-ion button cell).

In discontinuous mode, the input current, I_i (which is equal to the inductor current when the switch is on) is zero at the start of the switching cycle and increases at a rate

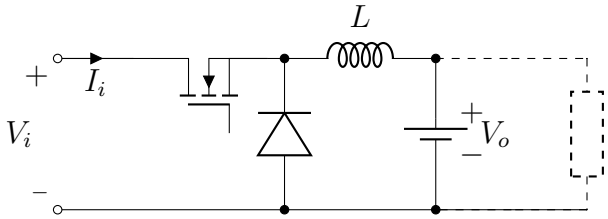


Figure 6.7: Buck converter

of:

$$\frac{\mathrm{d}I_i}{\mathrm{d}t} = \frac{V_i - V_o}{L} \tag{6.6}$$

Given a duty cycle of δ and a switching frequency of f, the on-time of the switch is:

$$T_{\text{on}} = \frac{\delta}{f} \tag{6.7}$$

Therefore, the maximum current in the inductor is:

$$\begin{aligned} I_{\text{max}} &= \frac{V_i - V_o}{L} T_{\text{on}} \\ &= \frac{V_i - V_o}{L} \frac{\delta}{f} \end{aligned} \tag{6.8}$$

Since the input current is zero when the switch is off, the average input current is then:

$$\begin{aligned} I_{\text{i,average}} &= \frac{1}{2} I_{\text{max}} \delta \\ &= \frac{V_i - V_o}{2L} \frac{\delta^2}{f} \end{aligned} \tag{6.9}$$

The input impedance is therefore:

$$\begin{aligned} Z_{\text{in}} &= \frac{V_i}{I_{\text{i,average}}} \\ &= \frac{V_i}{V_i - V_o} \frac{2fL}{\delta^2} \end{aligned} \tag{6.10}$$

The buck converter remains in discontinuous conduction mode only if the current through the inductor when the MOSFET is off is allowed to fall back to zero (before the

switch turns on again). From this, we obtain an upper bound for the operating duty cycle:

$$\begin{aligned} \frac{V_i - V_o}{L} t_{\text{on}} &\leq \frac{V_o}{L} (T - t_{\text{on}}) \\ V_i t_{\text{on}} &\leq V_o T \\ \delta &\leq \frac{V_o}{V_i} \end{aligned} \tag{6.11}$$

From Equation (6.11), the maximum expected value of $V_i = 55\,\text{V}$ and the chosen output value of $V_o = 3.7\,\text{V}$, the maximum duty cycle for which the converter remains in discontinuous mode is $\delta = 0.0673$. This would mean that the MOSFET would have to switch at unrealistic speeds since the duty cycle is very short as a result of the large step-down ratio.

Although the buck impedance emulator is working in open loop (no control circuitry is required), the input impedance does vary with the input voltage. If the expected input voltage range is from 20 V to 55 V, then the emulated impedance changes from 114 kΩ to 100 kΩ. Although the emulated impedance change is small, it would be more desirable to have a topology that can emulate a constant impedance that does not depend on the input voltage (i.e. emulating a linear resistor).

6.3.2 Buck-boost topology

A buck-boost converter operating in discontinuous conduction mode and with open-loop control (i.e. fixed duty cycle) can act as an impedance emulator. Buck-boost circuits, as shown in Figure 6.8, were used in [93] as part of the power processing circuitry for PowerMEMS generators in order to present the correct electrical impedance to the generator.

To determine the impedance seen at the input of a buck-boost converter in discontinuous conduction mode, the average current into the converter $I_{\text{i,average}}$ when a voltage V_i is applied at the input is first calculated:

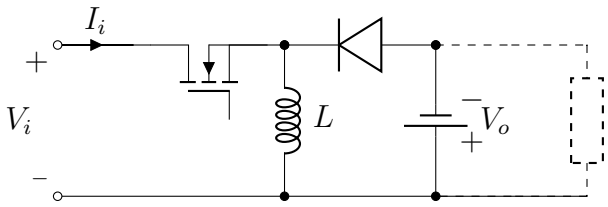


Figure 6.8: Buck-boost converter

$$\begin{aligned} I_{\text{i,peak}} &= \frac{V_i}{L} t_{\text{on}} \\ &= \frac{V_i}{L} \frac{\delta}{f} \end{aligned} \tag{6.12}$$

$$\begin{aligned} I_{\text{i,average}} &= \frac{1}{2} I_{\text{i,peak}} \frac{t_{\text{on}}}{T} \\ &= \frac{1}{2} I_{\text{i,peak}} \delta \\ &= \frac{V_i \delta^2}{2Lf} \end{aligned} \tag{6.13}$$

where $f = \frac{1}{T}$ is the switching frequency of the buck-boost, L is the value of the inductor, t_{on} is the time during which the MOSFET is switched on, and $\delta = \frac{t_{\text{on}}}{T}$ is the duty cycle of the switching signal.

Therefore, the input impedance of the buck-boost converter is:

$$\begin{aligned} Z_{\text{in}} &= \frac{V_i}{I_{\text{i,average}}} \\ &= \frac{2fL}{\delta^2} \end{aligned} \tag{6.14}$$

The buck converter remains in discontinuous conduction mode only if the current through the inductor when the MOSFET is off is allowed to fall back to zero (before the switch turns on again). From this, we obtain an upper bound for the operating duty cycle:

$$\frac{V_i}{L} t_{\text{on}} \leq \frac{V_o}{L} (T - t_{\text{on}})$$

$$(V_i + V_o) t_{\text{on}} \leq V_o T$$

$$\delta \leq \frac{1}{1 + \frac{V_i}{V_o}} \tag{6.15}$$

From Equation (6.15), the maximum duty cycle for which the converter remains in discontinuous mode is $\delta = 0.0630$. This would mean that, as with the buck impedance emulator, the MOSFET would have to switch at unrealistic speeds since the duty cycle is very short as a result of the large step-down ratio. Another issue with the buck-boost impedance emulator is that the output voltage is negative.

6.3.3 Flyback topology

To overcome the limitations of the buck and buck-boost impedance emulators, a flyback impedance emulator was designed. Flyback circuits, as shown in Figure 6.9, are used in [94] for emulating an impedance in low-power radio frequency (RF) and wind energy harvesters, and in [95] as part of a high-power-factor rectifier.

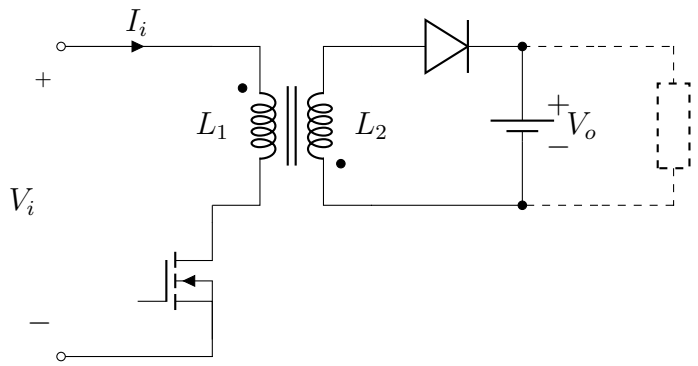


Figure 6.9: Flyback converter

The expression for emulated resistance is the same as Equation (6.14), but with the buck-boost inductor L replaced by the primary inductance of the flyback transformer, L_1:

$$Z_{\text{in}} = \frac{2 f L_1}{\delta^2} \tag{6.16}$$

The flyback converter remains in discontinuous conduction mode only if the current through the secondary winding of the transformer when the MOSFET is off is allowed to fall back to zero (before the switch turns on again):

$$\begin{aligned}\frac{V_i}{L_1}t_{\text{on}} &\leq \frac{V_o}{nL_2}\left(T - t_{\text{on}}\right)\\ \frac{V_i}{n}t_{\text{on}} &\leq V_o\left(T - t_{\text{on}}\right)\\ \delta &\leq \frac{1}{1+\frac{V_i}{nV_o}}\end{aligned} \tag{6.17}$$

where n is the turns ratio and is equal to:

$$\begin{aligned}n &= \frac{N_1}{N_2}\\ &= \sqrt{\frac{L_1}{L_2}}\end{aligned} \tag{6.18}$$

With $V_o = 3.7\,\text{V}$, $V_i = 55\,\text{V}$ and $n = 10$, the maximum allowable duty cycle for maintaining discontinuous conduction mode is $\delta = 0.402$, which means the MOSFET can be switched at more reasonable speeds. In addition, the output voltage of a flyback converter is positive. Like the buck-boost impedance emulator in Section 6.3.2, the flyback can be operated in discontinuous conduction mode and in open loop, keeping power consumption low.

The implemented flyback impedance emulator has the following parameters: $f = 19\,\text{kHz}$, $L_1 = 140\,\text{mH}$, $L_2 = 1.6\,\text{mH}$, $\delta = 0.24$. This gives an emulated impedance of $92.3\,\text{k}\Omega$, which is close to the optimal load (based on measured receiver coil properties in [42]) presented to the rectifier. As $n = 9.35$ here, the maximum allowable duty cycle is 0.386, which means that the flyback circuit will remain in discontinuous conduction mode.

Figure 6.10 shows the simulated current through the primary winding of the flyback transformer, whilst Figure 6.11 shows the simulated current through the secondary winding. The ratio of the peak current at the secondary side to that at the primary side is the turns ratio of the flyback transformer.

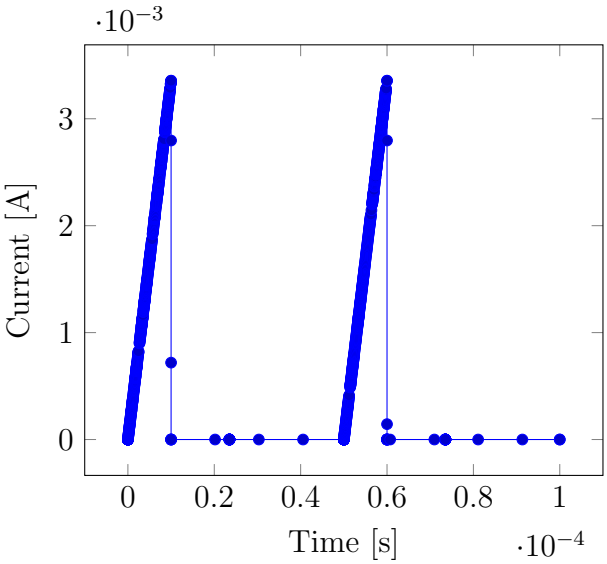


Figure 6.10: Simulated current through primary winding of flyback transformer

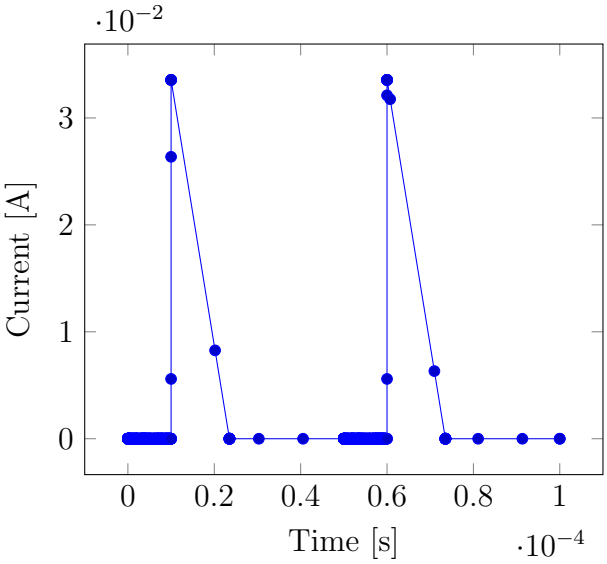


Figure 6.11: Simulated current through secondary winding of flyback transformer

Figure 6.12 shows the simulated voltage across the diode at the secondary side of the flyback impedance emulator. When the MOSFET is switched on, the primary current

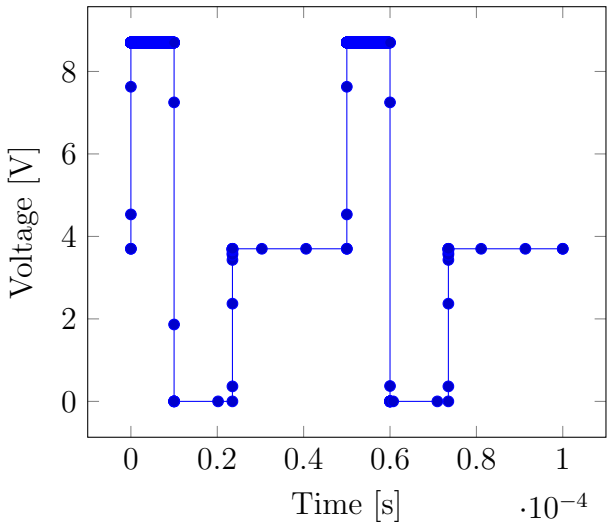


Figure 6.12: Simulated voltage across diode at secondary side of flyback transformer

starts to increase and the voltage seen by the diode is the sum of the output battery voltage, and the input voltage of the flyback impedance emulator divided by the turns ratio. Once the MOSFET is switched off, current flows in the secondary coil and through the diode, causing the diode to be forward biased and the voltage to drop to its forward voltage. However, when the secondary current falls to zero, the diode voltage becomes that of the output voltage (which is 3.7 V because of the battery).

Due to the extremely low magnetic coupling in this system, the optimal impedance presented to the rectifier is high (around 100 kΩ in this case), causing the received current to be very small (100s of µA). In reality the emulated impedance is not perfectly constant with variations in input voltage due to parasitic oscillations in discontinuous conduction mode (Figure 6.13). Nevertheless, the emulator performance was sufficient, restricting impedance changes to within $+20/-50\,\%$ of the optimal value. Figure 6.14 shows the efficiency of the impedance emulator with input voltage.

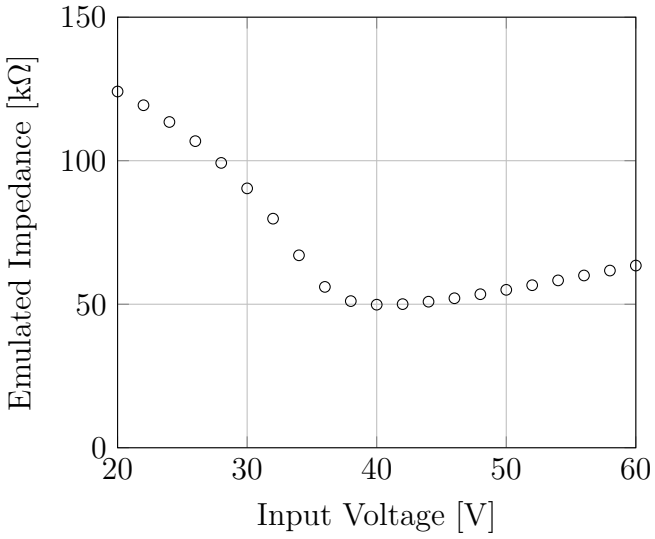


Figure 6.13: Variation of emulated impedance of flyback impedance emulator with input voltage

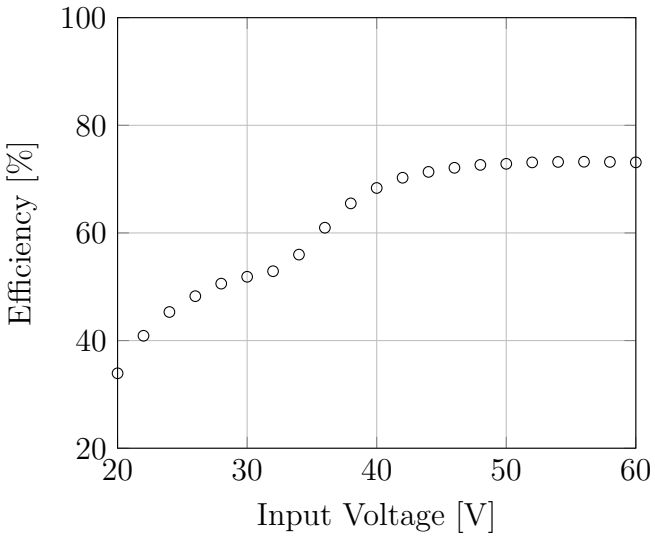


Figure 6.14: Variation of efficiency of flyback impedance emulator with input voltage

6.4 Transmitter power control

In order to maintain constant received power as the receiver position is changed and to prevent damage to the receiver electronics due to excessive received voltage, transmitter power modulation was implemented. At the receiver side, the rectifier output voltage $V_{\mathrm{RX,DC}}$ (and the flyback impedance emulator input voltage), is measured by a microcontroller in the sensor node. This voltage measurement is then sent to a microcontroller at the power transmitter side via a separate 433 MHz frequency-shift keyring (FSK) wireless data link.

Figure 6.15 shows the power transmitter coil and the associated electronics. The microcontroller at the power transmitter side obtains the measured $V_{\mathrm{RX,DC}}$ value with an FSK data receiver, and this value is used to control the voltage of the DC power supply to the Class E inverter, V_{inv}, in order to modulate the input power. The objective of the control algorithm is to keep $V_{\mathrm{RX,DC}}$ close to 50 V. Any voltage above 55 V is deemed 'excessive' and could potentially cause damage to the receiver electronics.

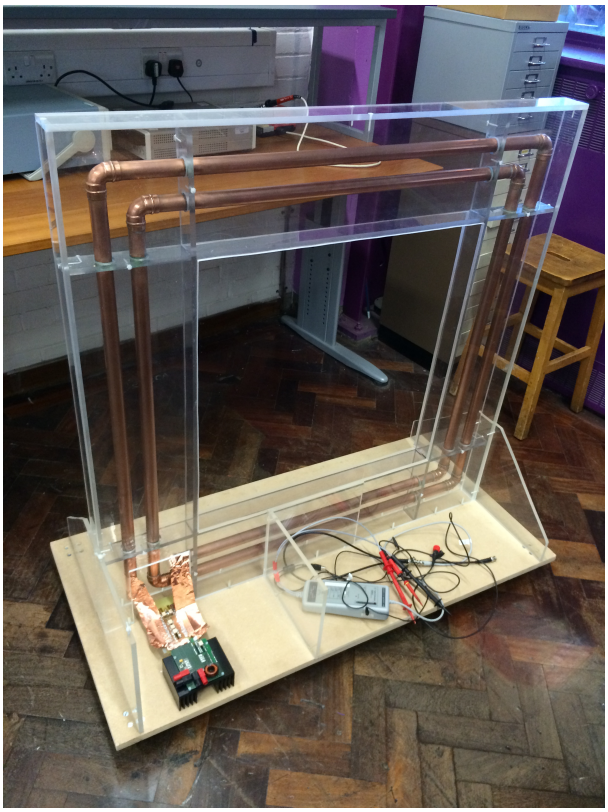


Figure 6.15: Transmitter coil and electronics

The method of V_{inv} control is as follows: if $V_{\text{RX,DC}}$ is greater than 55 V, then V_{inv} is decreased by 10 V. If $V_{\text{RX,DC}}$ is less than 45 V, then V_{inv} is increased by 2 V, but only if V_{inv} is less than a certain value called $V_{\text{inv,max}}$. $V_{\text{inv,max}}$ is an upper limit on V_{inv} that is set in order to keep V_{DS} of the MOSFET in the Class E inverter less than 1000 V, which is its breakdown voltage. A hysteresis band for $V_{\text{RX,DC}}$ (between 45 V and 55 V) is used to prevent frequent fluctuations in input power.

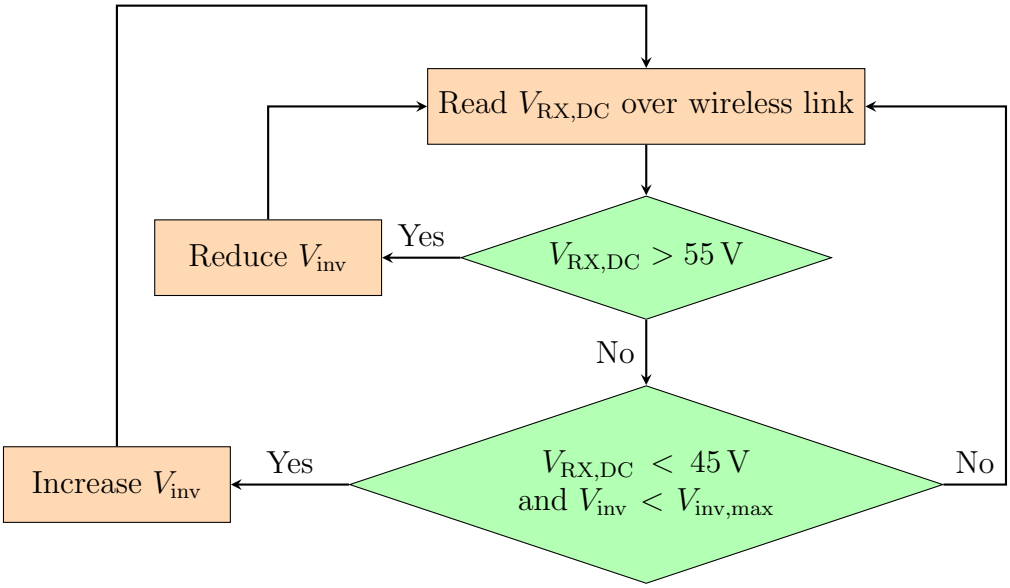


Figure 6.16: Transmitter power modulation flow diagram

6.5 Class E inverter board modifications

As part of the work on the long-range IPT system, the Class E inverter printed circuit board (PCB) was also modified in order to solve some existing practical issues. One problem with the previous PCB was that the high voltage node at the coil resonant tank, which could potentially reach a peak amplitude of 7 kV, was only 3 mm away from the heat sink (through air) and this caused arcing between the high voltage node and the heat sink. The photographs in Figures 6.17 and 6.18 show the damage done to the board and its heat sink due to arcing.

The new design consisted of a smaller heat sink with active cooling via a small fan, which was placed away from the high voltage node to prevent any arcing. Also a small copper block was placed in between the MOSFET's exposed pad and the heat sink, so



Figure 6.17: Old Class E inverter board damaged by arcing



Figure 6.18: Heat sink of old Class E inverter board damaged by arcing

that there would not be any arcing between the heat sink and the MOSFET's drain pin (the drain could reach a maximum 1000 V). The new board is shown in Figure 6.19.

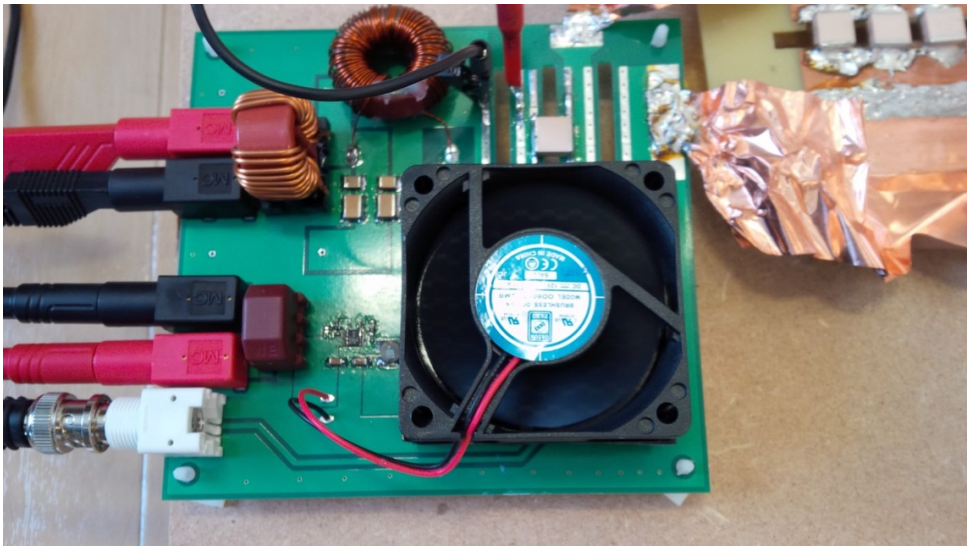


Figure 6.19: New Class E inverter board

Since the capacitors in the resonant tank (represented by C_{res} in Figure 6.3), which have a voltage rating of 7.2 kV [96], were subjected to the entire transmitter coil voltage of around 7 kV, they constantly broke down when running the transmitter at full power (full power being determined by the point at which the MOSFET's drain-source voltage is just below its breakdown voltage). To fix this, each capacitor was replaced with two in series and two in parallel, so that the voltage would be distributed between the two capacitors in series. This change meant that the capacitors were no longer breaking down as they did not have the full transmitter coil voltage across them.

6.6 Results

Figure 6.20 shows a schematic diagram of the receiver coil and electronics, with the resonant tank on the left hand side, followed by the bridge rectifier, the impedance emulator and the sensor node with an RF data transmitter.

Figure 6.21 is a photograph of the receiver coil and electronics. In the final implementation, the p-n diodes in the bridge rectifier (1N4148W [97]) were replaced by Schottky diodes (BAT46W [98]) in order to reduce conduction loss, since Schottky diodes have a

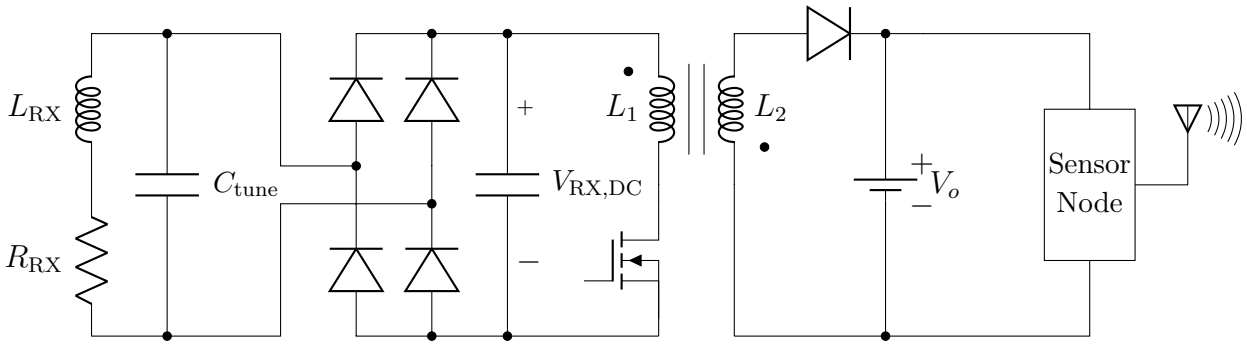


Figure 6.20: Receiver coil and electronics - schematic diagram

smaller forward voltage drop when they are conducting current.

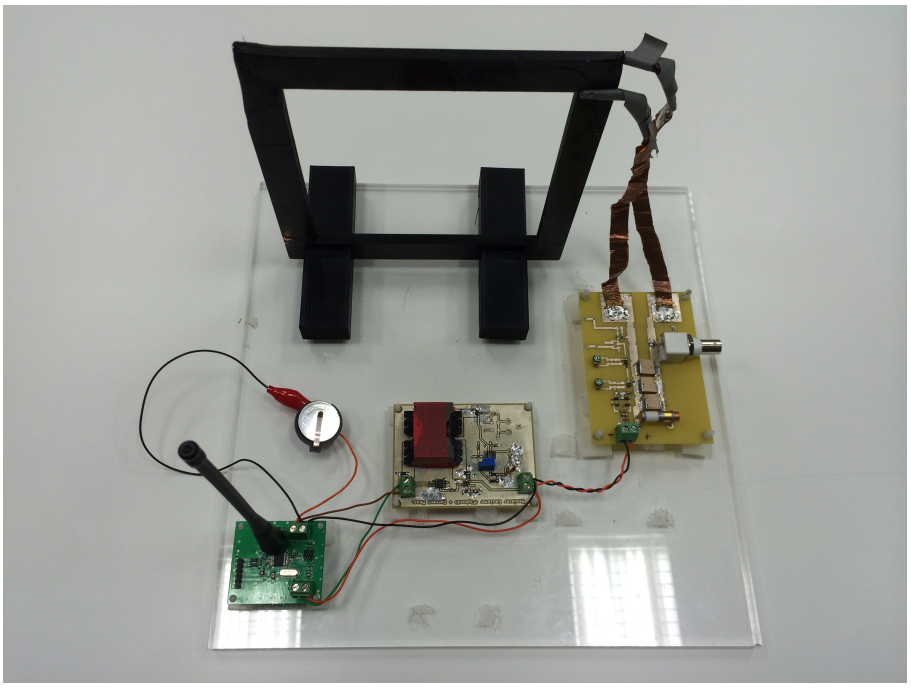


Figure 6.21: Receiver coil and electronics - photograph

Figure 6.22 shows post-emulator received power with distance between the receiver and the transmitter. Received power is constant at around 30 mW up to 3 m as the power is modulated, but beyond 3 m the transmit power saturates (limitations in the MOSFET voltage rating of the inverter) and the received power decreases. The receiver electronics and feedback system consumes 3.1 mW and so with a transmitter input power of 163.3 W the receiver becomes 'power neutral' at 4.75 m. At 5 m, received power falls to 2 mW. From 3 m to 6 m, the relationship between the received power and distance is:

$$P_{RX} \propto \frac{1}{d^{6.88}} \tag{6.19}$$

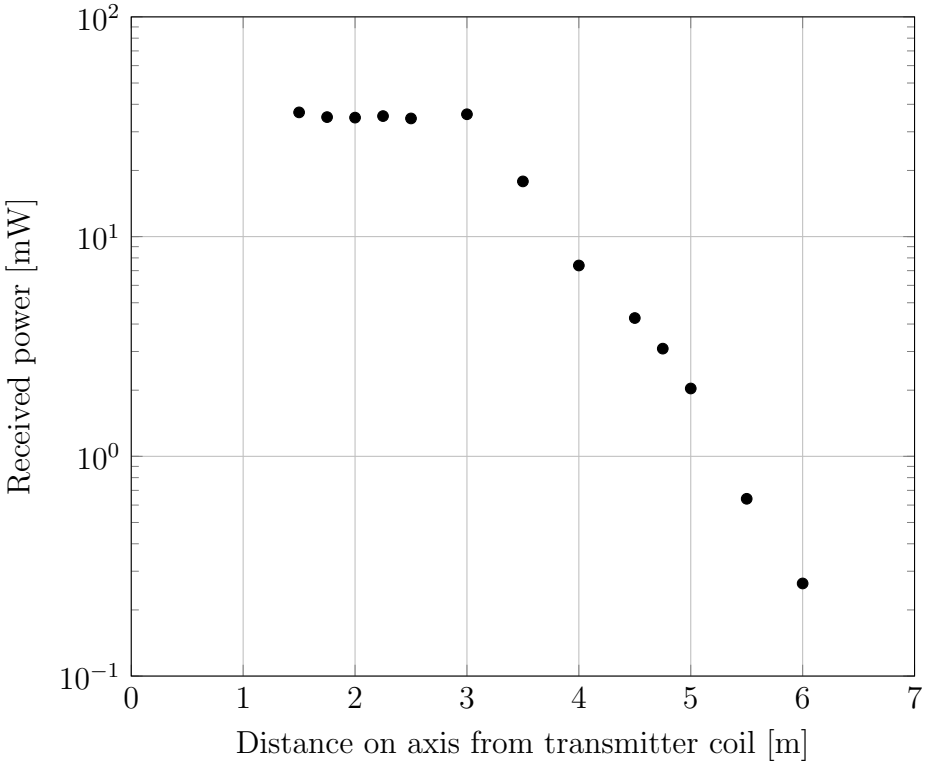


Figure 6.22: Received power with distance between transmitter and receiver coil

6.7 Safety

Simulations for the long range IPT system were performed in the absence of a human body model. Since the main causes of heating in the human body are receiver coil dissipation and energy absorption in the tissue due to the magnetic fields generated by the receiver coil, a WPT system for a low-power medical implant (up to 30 mW) should be safer than that for a higher-power medical device such as an LVAD (up to 15 W). As an example, in the short-rage scenario of the high-power system described in Section 4.2.5, the receiver coil has a current of 2.78 A and the magnetic field at the centre of the receiver is 155 µT, when the optimal load is used. In contrast, for the long range medical implant described in this chapter, the receiver coil current is only 289 mA, and the magnetic field in the centre of the receiver is 10.5 µT. Hence, it is expected that tissue heating effects will be less significant with a long range IPT system for a low-power medical implant than a

short-range system for a higher-power device.

A person with an implantable medical device and a receiver coil would remain safe when walking towards the transmitter coil. With the use of transmitter power control and impedance emulation, the receiver end would sense that too much power was received, so it would tell the transmitter end to step down the input power. For people without an implanted receiver that can communicate with the transmitter, there are several ways of ensuring their safety when moving close to the transmitter coil. One method is to implement foreign object detection and an approach for doing so will be described in Section 6.9. In addition, electromagnetic simulations could be performed to determine whether exclusion zones need to be established, outside of which the reference levels or limits on specific absorption rate (SAR) are not exceeded.

6.8 System comparison

Table 6.4 presents a comparison of the various link and coil parameters of a WPT system for LVADs over a short distance presented in Chapter 4 and those for sensor networks over much greater coil separations described in this chapter.

	High power	Long range
TX size	10 cm	1 m
RX size	5 cm	17 cm
Received power	15 W	$\leq$ 30 mW
Coupling factor	10 % - 20 %	0.0026 %
Link efficiency	95 %	0.02 %
Distance	2 cm	up to 6 m

Table 6.4: Comparison of coil and link parameters

6.9 An approach to detection of living objects

The analysis of WPT systems for medical devices involves investigating and modelling the interaction of the high-frequency magnetic field with the human body, as described in Chapter 4. Since there is an effect of the human body on the distribution of the magnetic

field, operating in the near field of the coil means that any changes in the field is reflected (referred back) to the transmitter coil. This information can be used potentially to detect the presence and location of humans and other living objects in the vicinity of at least one large coil, such as the one used as the transmitter for the long range system in this chapter.

Useful and suitable applications of this technology might revolve around disaster relief after a humanitarian crisis, such as locating people trapped under collapsed buildings and structures following an earthquake. A network of drones, each with its own receiver coil, could form a coil array to increase the degrees of freedom in order to implement object localisation and tracking. Therefore, a group of wireless-powered drones could fly over collapsed buildings and use the high-frequency magnetic fields to search for trapped human beings.

Another example of the potential use of this technology could be the detection of foreign objects in the vicinity of a mid-range WPT system. These foreign objects could be metallic objects (e.g. CDs, chewing gum wrappers etc.) that heat up and catch on fire or living objects (e.g. humans, cats etc.) that suffer from tissue damage or nervous system effects, when situated in a strong magnetic field. As soon as a foreign object is detected, the entire system could then be turned off.

6.9.1 Theory and modelling

The general idea is to use a low frequency magnetic field ($< 10\,\mathrm{MHz}$) in order to detect objects of interest within the near-field. This alternating magnetic field could be set up using a transmitter coil, such as the large $1\,\mathrm{m} \times 1\,\mathrm{m}$ coil used in the long range system described in this chapter. The eddy currents that are induced in an electrically conductive object of interest (e.g. a person or an animal) by the transmitter-generated magnetic field can be detected by either the same transmitter coil or another 'receiver' coil, due to a corresponding change in the magnetic field distribution. The amplitude and phase response of the field can provide information about the relative distance and material of the detected object.

The transmitter coil and the object of interest are considered to be mutually coupled, and the resulting system can be modelled as an air-core transformer (just like with a WPT system). The electrically-conductive object can be represented by a resistor-inductor (RL) receiver coil model, which loads the transmitter coil in a way that depends on the mutual impedance between the two.

When a current is injected into the square transmitter coil, it generates a magnetic field with an on-axis distribution given by [83]:

$$H_{\mathrm{TX}}(z) = \frac{2I_{\mathrm{TX}}a_{\mathrm{TX}}^2 N_{\mathrm{TX}}}{\pi\left(a_{\mathrm{TX}}^2 + z^2\right)\left(2a_{\mathrm{TX}}^2 + z^2\right)^{\frac{1}{2}}} \tag{6.20}$$

where N_{TX} is the number of turns, $2a_{\mathrm{TX}}$ is the average length of one side, I_{TX} is the transmitter coil current and z is the distance on axis from the centre of the transmitter coil.

The induced voltage in the 'receiver' object as a result of the transmitter-generated magnetic field can be calculated using Faraday's Law of Induction, and the resulting expression in time-harmonic form is given by Equation (6.21):

$$\begin{aligned} V_{\mathrm{ind,RX}} &= -j\omega\Phi \\ &= -j\omega\mu_0 A_{\mathrm{RX}} H_{\mathrm{TX}}(D) \end{aligned} \tag{6.21}$$

where Φ is the total flux over the effective area A_{RX} of the object, and D is the distance between the transmitter coil and the object. $H_{\mathrm{TX}}(D)$, the magnetic field strength at the object of interest, is assumed to be constant over A_{RX}.

The phase, amplitude and frequency dependence of the 'receiver' object current I_{RX} and the resulting 'reflected' magnetic field H_{RX} will depend on the induced voltage $V_{\mathrm{ind,RX}}$ in the object, and the effective inductance L_{RX} and resistance R_{RX} of the object. This 'reflected' magnetic field is detected as an induced voltage in the transmitter coil $V_{\mathrm{ind,TX}}$.

6.9.2 Simulation study

CST Microwave Studio was used to verify and quantify the basic approach to detecting objects in the near field. The amplitude and phase response of the 'reflected' magnetic field and the induced voltage in the transmitter coil to different materials at varying distances from the transmitter coil were simulated.

A 1 m × 1 m 2-turn helical coil is used as the transmitter, and is fed by a 1 A current source at a frequency of 1 MHz. Coil losses are irrelevant for this study, so the coil was modelled as a perfect electrical conductor instead of copper (lossy metal). Human-sized blocks of different materials were placed at distances between 50 cm and 10 m from the centre of the coil on axis at 25 cm intervals. The materials simulated were human fat and polypropylene. The blocks have a dimension of 1.8 m × 80 cm × 20 cm. Figure 6.23 shows the simulation setup in CST Microwave Studio for the detection of a human sized block by a transmitter coil.

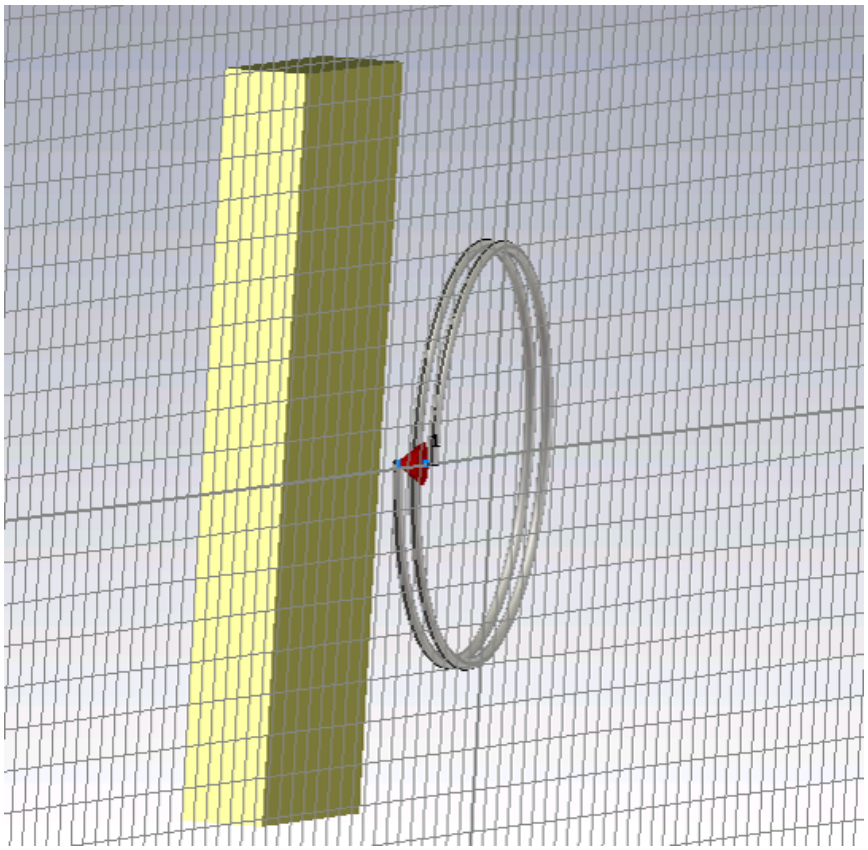


Figure 6.23: Simulation setup for detection of a human sized block by a transmitter coil

The real and imaginary components of the magnetic fields on the central axis were

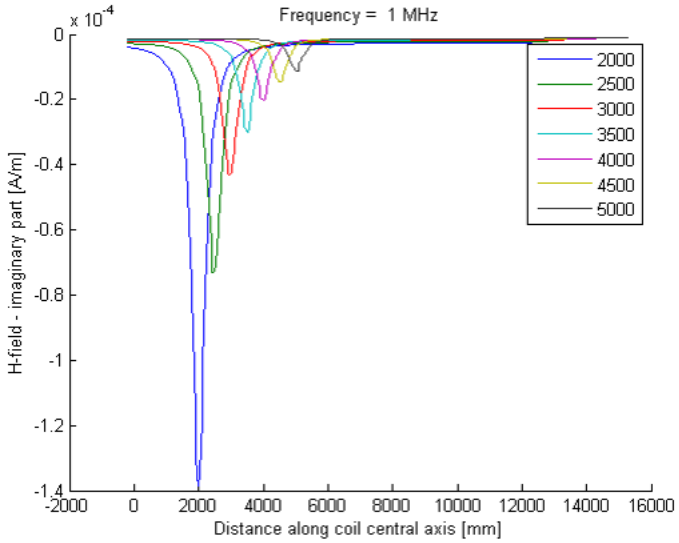


Figure 6.24: Variation of the imaginary part of the magnetic field with distance along coil central axis, with block of fat placed at distances between 2 m and 5 m

simulated and recorded for different distances between the object of interest and the transmitter coil. The corresponding transmitter coil voltage at the current source port was measured.

The first simulation involved placing a block of fat at distances varying from 2 m to 10 m. Fat has a dielectric constant of 27.2 and loss tangent of 16.6 at 1 MHz [77, 84]. As can be seen from the field distribution results in Figures 6.24 and 6.25, the imaginary part of the magnetic field (90° out of phase with the input current) clearly indicates the location of the electrically-conductive biological material.

The imaginary part of the magnetic field can be detected at the transmitter coil. Figures 6.26 and 6.27 shows the real part of the voltage across the transmitter coil. There is a clear correlation between the real part of the transmitter coil voltage and the distance between the block of fat and the coil. This voltage corresponds to the imaginary 'reflected' magnetic field from the fat coupled back to the transmitter coil, in the form of an induced voltage. Such changes in voltage amplitudes are detectable.

In the second simulation, the block of fat was replaced with a block of polypropylene plastic of the same dimensions. Polypropylene has a dielectric constant of 2.3 and a loss tangent of 0.00041 [78, 99] (much less lossy and conductive compared to fat). Figure 6.28 shows the variation of real part of the voltage across the transmitter coil with distance be-

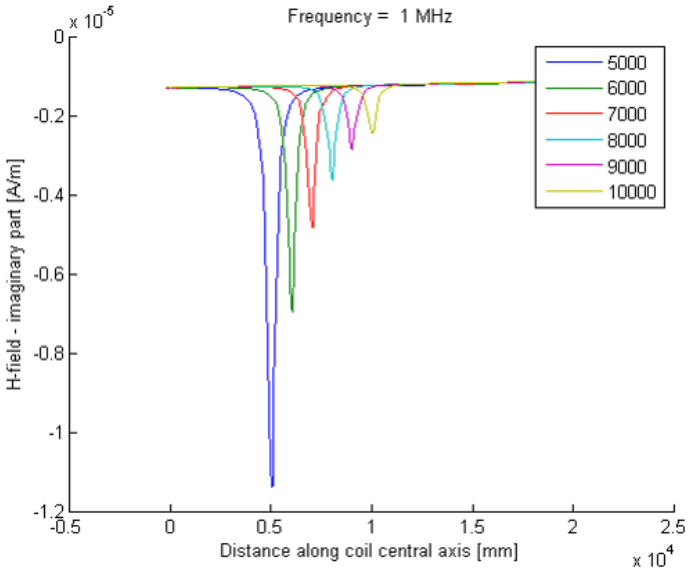


Figure 6.25: Variation of the imaginary part of the magnetic field with distance along coil central axis, with block of fat placed at distances between 5 m and 10 m

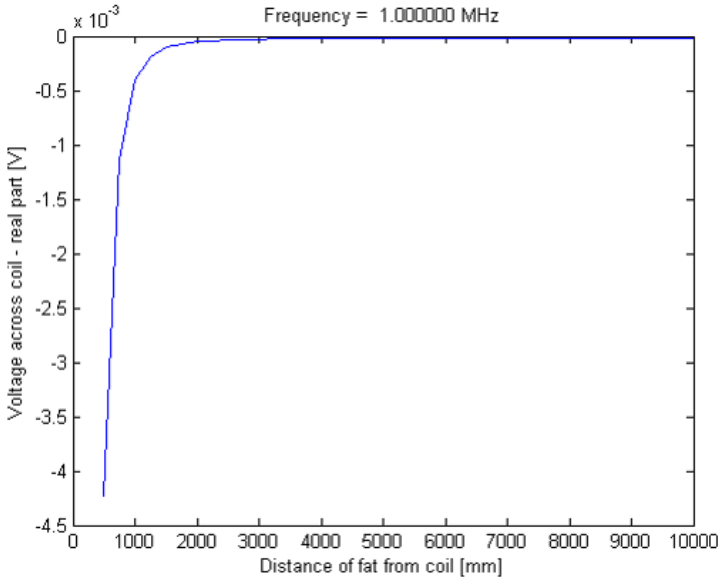


Figure 6.26: Variation of the real part of transmitter coil voltage with distance between fat block and transmitter, between 2 m and 5 m

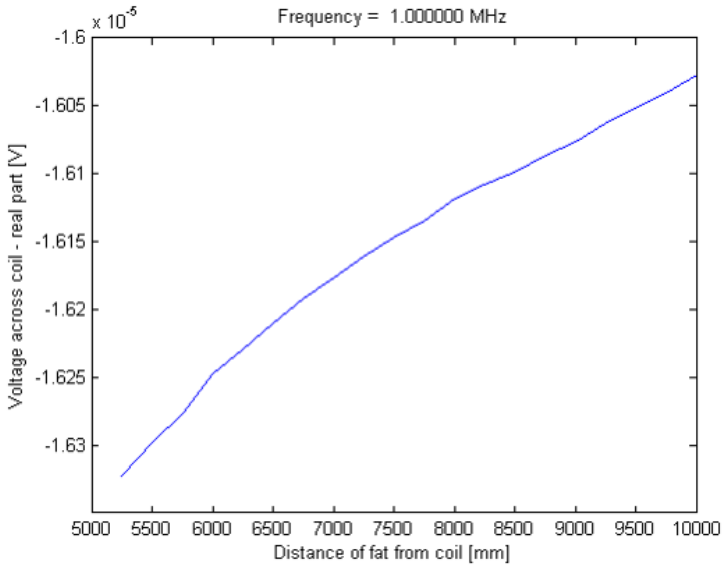


Figure 6.27: Variation of the real part of transmitter coil voltage with distance between fat block and transmitter, between 5 m and 10 m

tween the coil and the plastic block. The same trend can be seen in voltage with distance between the polypropylene plastic block and the transmitter coil; however, compared to fat, the voltage amplitudes for polypropylene plastic are much smaller.

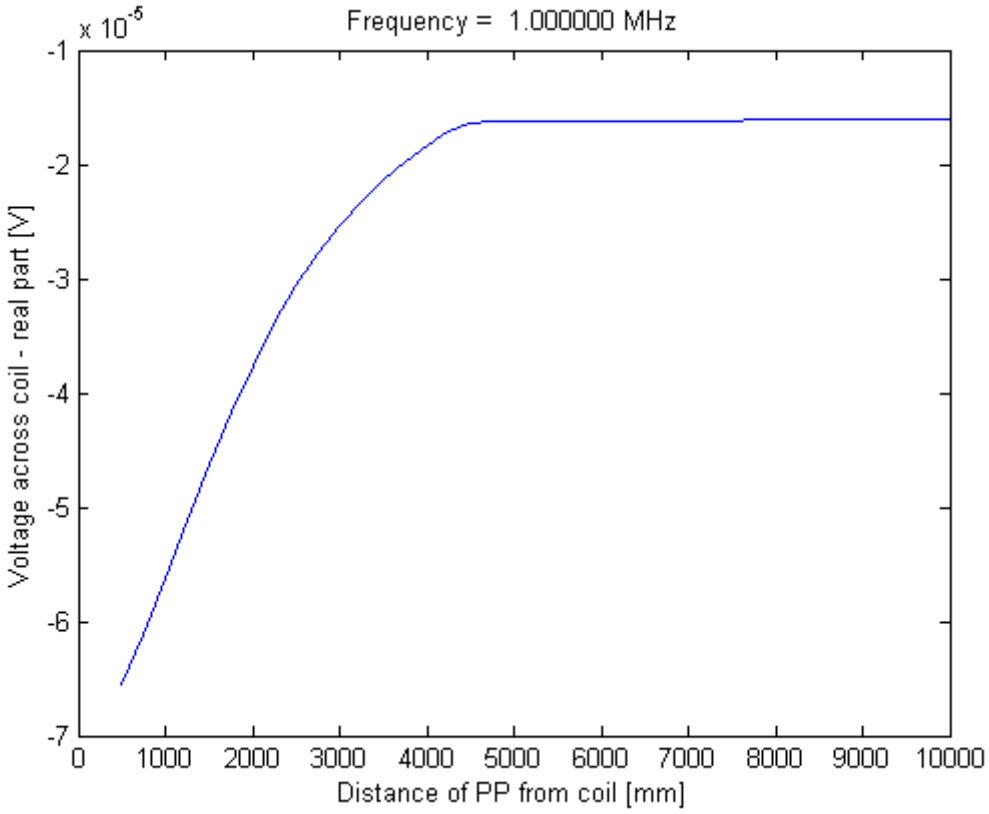


Figure 6.28: Variation of the real part of transmitter coil voltage with distance between polypropylene block and transmitter, between 50 cm and 10 m

6.9.3 Experimental work

An experiment is conducted where a person is stood at different distances in the near field of the transmitter coil. The transmitter power used was 50 W, and the drain-source voltage of the MOSFET switch of the Class E inverter was measured as the distance between the person and the transmitter varied from 50 cm to 5 m. Figure 6.29 shows the results of this experiment, where a clear correlation of distance with the drain-source voltage can be observed.

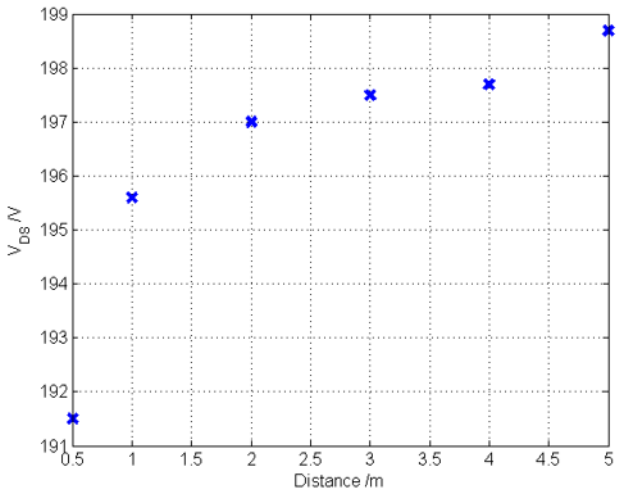


Figure 6.29: Variation of MOSFET drain-source voltage with distance between standing person and transmitter coil (Transmitter power: 50 W)

6.10 Summary

An ultra-low power switch mode impedance emulator was designed and implemented into a previous long range IPT system to provide constant loading for maximum power transfer. Transmitter power control via wireless feedback was also added in order to maintain constant received power and to prevent excessive received voltage damaging the electronics. These improvements resulted in a position-insensitive long-range inductive power transfer system that could be used to reliably supply power to a network of sensors with milliwatt-level power consumption. IPT systems are therefore a viable alternative to existing far-field methods such as RF energy harvesters for supplying power concurrently

to multiple remote sensors.

An approach to the detection of living objects was presented as well, with simulations showing that when an electrically conductive object is placed in the magnetic field produced by a coil, the real part of the coil voltage varies with the distance between the object and the coil. These voltages are large enough to be detectable, and are caused by a peak in the imaginary part of the magnetic field at the object of interest. An experiment was also performed, in which a person stood at varying distances from the large transmitter coil used in the system described in this chapter. There was a strong correlation between the drain-source voltage of the Class E inverter's MOSFET switch and the distance between the person and the transmitter coil, due to the change in loading of the coil by the person.

Chapter 7

Conclusion

This thesis covered a variety of topics that relate to the design of wireless power transfer (WPT) systems in the presence of living objects. Firstly, an overview of the design of a multi-MHz mid-range WPT system in free-space was presented, using link efficiency-led principles and incorporating high-frequency power electronics (semiconductor devices, inverters and rectifiers). This was followed by an identification of the safety guidelines and regulations concerning exposure to electromagnetic fields and temperature rises that apply to WPT systems in the presence of living objects and for implantable medical devices. Afterwards, an explanation of how to evaluate safety and compliance with safety limits using 3D electromagnetic and thermal numerical simulations was given, using a wirelessly-powered drone as an example.

With safety considerations in mind, the thesis then discussed the design, analysis and simulation of a WPT system with an implanted receiver for high-power medical devices. This included an investigation into how changing different system and coil parameters can lead to a lower level of tissue heating and temperature rises in the human body, despite moving away from the widely-accepted maximum link efficiency objective. Subsequently, a detailed account of the experimental work carried out was provided, in order to show the effect of changing certain design parameters on the maximum link efficiency, heating and temperature rises of the surrounding conductive medium.

The development of a position-insensitive long range inductive power transfer (IPT)

system for sensors networks was also covered; such a system could also be used for remotely powering low-power medical implants and wearable devices. Lastly, an approach to detection of living objects using high-frequency magnetic fields was introduced.

7.1 Main research outcomes

The key outcomes and findings arising from the PhD research are as follows:

- A method of designing multi-MHz mid-range IPT systems in air using link efficiency-led principles was devised, where for a given coupling factor between two coils (constant distance and fixed coil geometries), the operating frequency of the WPT system should be chosen to maximise the product of the coil Q factors in order to maximise link efficiency. This has been completed in collaboration with my colleagues (co-authors of [3]), who researched, designed and implemented efficient high-frequency power converters (soft-switching inverters and rectifiers) that are able to support the MHz frequencies used in such IPT systems.

- For WPT systems with an implanted receiver for a high-power medical device, a general link efficiency expression was derived with an arbitrary receiver tuning capacitance and load. In addition, a simple equivalent circuit model of an implanted coil was devised, with an insight into how an extra resistance representing eddy current looses in the body varies with tissue type and frequency.

- It was discovered that to minimise tissue temperature rises, the optimal selection of frequency and number of turns should be made so as to balance out tissue heat absorption due to an electromagnetic (EM) field and heat dissipation due to coil currents. Increasing the frequency or the number of coil turns leads to greater tissue heat absorption but lower coil dissipation.

- A method of reducing temperature rises and specific absorption rate (SAR) was presented, which involved setting the receiver load away from its optimal value. The relationship between the overall magnetic field at centre of the receiver coil

and the output load for a particular received power was derived, using Biot-Savart law and Faraday's Law of Induction. Despite a fall in maximum link efficiency with a non-optimal load, such a method is necessary to ensure a system is safe for patients. In addition, the receiver load which minimised the overall magnetic field through the centre of receiver coil to reduce eddy current heating in the tissue was calculated. Alternatively, a load value which minimised the coil voltage was identified, and this could be used to reduce electric fields and dielectric heating.

- It was found that although switching from optimal tuning to resonant tuning leads to a small decrease in link efficiency and slightly higher heating and temperature rises for the short-range scenario, there is a noticeable reduction in the reactance of the reflected impedance, which may have implications for inverter design.

- A position-insensitive long-range IPT system for sensor networks was successfully developed. An ultra-low power open-loop flyback impedance emulator was designed to maintain maximum power transfer even when the receiver is relatively far from the transmitter. A method of transmitter power modulation using wireless data feedback was implemented to prevent receiver damage when moving close to the transmitter. These improvements were required in order to deliver power reliably to a direct current (DC) load at varying distances from the transmitter.

- The potential use of high-frequency magnetic fields for detecting living objects was found to be possible. Since the electrically conductive human tissue alters the distribution of the transmitter-generated magnetic field, this results in an induced voltage across the transmitter coil that can be detected; the amplitude and phase response can provide information regarding the distance and material composition of the object of interest.

7.2 Comparison with other work

The long range IPT system described in Chapter 6 builds on a previous system developed by James Lawson [42], which used an alternating current (AC) load at the receiver. There have been various implementations of far-field methods, such as radio frequency (RF) ambient energy harvesting [41] and radiative power transfer [40], but their received power levels have been limited to less than 1 mW. Using near-field inductive power transfer to deliver several milliwatts of power over a long range (up to 10 m) was introduced in [42], and the improved system developed in this thesis provides reliable power transfer over long distances by using impedance emulation to maximise power transfer and transmitter power control to prevent receiver damage when moving close to the transmitter.

With respect to WPT systems for high-power implantable medical devices such as left ventricular assist devices (LVADs), Table 7.1 shows the key results of other research groups who have developed systems with similar specifications as those for the short-range scenario described in Chapter 4, where f is the frequency of operation, P_{RX} is the received power, D is the coil separation distance, and η is the overall system efficiency.

In this thesis, a link efficiency-led approach to the design of a WPT system for an LVAD has been taken. To this end, it was found that working at the industrial, scientific and medical (ISM) bands of 6.78 MHz or 13.56 MHz results in higher link efficiencies. This is in contrast to the various systems in [30, 100, 101, 102, 29], where frequencies in the 100s of kHz range were used. Therefore, for many of the aforementioned systems, Litz wire coils were chosen in order to boost the coil Q factors as a means of maximising link efficiency. In addition, a few of these systems [30, 102] used ferrite cores in the coils to enhance the coupling coefficient so as to further increase link efficiency. However, Litz wire can be expensive, and ferrite cores are brittle and can heat up significantly in the presence of an AC magnetic field. To summarise, these systems have overall efficiencies ranging between 82 % to 88 %. However, with the exception of [29] in which the receiver coil was implanted in a sheep, the experiments of the other research groups were performed in air.

The WPT system developed in [103] operated at a frequency of 6.78 MHz. A good

Ref.	f	P_{RX}	D	TX coil	RX coil	η	Temp.	Scenario
[30]	163 kHz	20 W	5 mm	92 mm, 7-turn Litz	53 mm, 12-turn Litz, ferrite	85 %	46.1 °C (ferrite)	Air
[100]	470 kHz	15 W	5 mm	90 mm	66 mm	82 %	-	Air
[101]	250-320 kHz	12-60 W	20 mm	64 mm x 50 mm, 19-turn Litz	64 mm x 50 mm, 17-turn Litz	88 %	-	Air
[102]	160 kHz	27.4 W	20 mm	90 mm, 18-turn Litz, ferrite	72 mm, 9-turn Litz	85.5 %	10.1 °C rise (MOS-FET)	Air
[29]	155-168 kHz	15 W	16 mm	50 mm, 21-turn Litz	50 mm, 10-turn Litz	82.1 %	2.7 °C rise (RX Coil)	Sheep
[103]	6.78 MHz	48.2 W	77 mm	24 cm x 30 cm, 2 turns	53 mm, 12 mm thick-ness	80 %	-	Air
[31]	8 MHz	-	20 mm	200 mm, 6-turn Litz	60 mm, 8-turn Litz	70 %	-	Agar gel

Table 7.1: Comparison of other systems in literature with similar specifications for wirelessly powering an LVAD

overall efficiency was achieved in air, despite having a coil separation that was greater than those of other work listed in Table 7.1. However, it relied on a receiver coil with a thickness of 12 mm (comprising 4 layers of 10 parallel turns), which may not be suitable as part of an implantable device. The work in [31] also used MHz frequencies to drive their system, and they obtained an overall frequency of 70 % in the presence of an agar gel human phantom. However, their system could have been further optimised by having fewer turns on the coils.

From the simulation studies with human body models presented in this thesis, the short-range system for wirelessly powering an LVAD had a link efficiency of 95 % over a distance of 20 mm at a frequency of 6.78 MHz. Lightweight, thin, low-cost PCB coils were used for the transmitter (10 cm, 4 turns) and the receiver (5 cm, 2 turns) ends. Due to the use of an increased load, the temperature rise in the human body model was only 1.2 °C. Though the overall efficiency would not be as high as the link efficiency due to losses in the power electronics, with the use of efficient topologies introduced in Chapter 2 switching losses in the power converters can be minimised.

7.3 Publications, patents and presentations

The PhD programme has resulted in a number of publications and presentations:

- A conference paper on the long range IPT work described in Chapter 6 was accepted as a poster presentation at The 14th International Conference on Micro and Nanotechnology for Power Generation and Energy Conversion Applications (PowerMEMS 2014) in Awaji Island, Hyogo, Japan (18-21 November 2014). It is titled 'Position-insensitive long range inductive power transfer' and is published by the Institute of Physics in the Journal of Physics: Conference Series.

- A conference paper on the use of link efficiency-led principles for designing mid-range multi-MHz WPT systems in air presented in Chapter 2 was accepted as an oral presentation at the 2015 Institute of Electrical and Electronics Engineers (IEEE) PELS Workshop on Emerging Technologies: Wireless Power (IEEE WoW

2015) in Daejeon, South Korea (5-6 June 2015). It is titled 'Link efficiency-led design of mid-range inductive power transfer systems' and was awarded 'Best Paper'.

- A conference paper on the design of WPT systems with a human-implantable receiver that was described in Chapter 4 was accepted as a poster presentation at the 2016 IEEE Wireless Power Transfer Conference (IEEE WPTC 2016) in Aveiro, Portugal (5-6 May 2016). It is titled 'Design objectives and power limitations of human implantable wireless power transfer systems'.

- An invited talk was given at the Biological + Chemical Sensors Summit 2016: Implantable Biomedical Systems Symposium in La Jolla, U.S.A. (7 December 2016). The topic of the talk was on the design of WPT systems for high-power implantable medical devices such as LVADs and is based on the contents of Chapters 3 and 4 and the paper presented at IEEE WPTC 2016.

- A patent application titled 'Inductive power transfer system' has been submitted, and is based on the novel improvements to the long range inductive power transfer system that was developed in Chapter 6.

- A co-authored journal paper has been accepted for publication on 13 September 2018 in IEEE Transactions on Power Electronics (first author: Juan M. Arteaga). It is titled 'Dynamic capabilities of multi-MHz inductive power transfer systems demonstrated with batteryless drones' and includes the drone safety simulations discussed in Chapter 3.

- A conference paper on the wireless power experiments in salt water solution described in Chapter 5 was accepted as a poster presentation at The 18th International Conference on Micro and Nanotechnology for Power Generation and Energy Conversion Applications (PowerMEMS 2018) in Daytona Beach, Florida, U.S.A. (4-7 December 2018). It is titled 'Reducing human body heating and temperature rises due to inductively-powered implantable medical devices'.

7.4 Future work

There are many avenues for a future researcher to pursue in order to further the research in the design of WPT systems for implantable medical devices and for sensor networks, and in the detection of living objects with a high-frequency magnetic field:

- Based on future discussions and collaborations with medical professionals e.g. cardiothoracic surgeons, the specifications for the implanted receiver coils (e.g. size, thickness, flexibility, location) could be refined. In addition, practical safety limits, such as maximum temperature rise at different locations of the body and the maximum period of time a patient can endure elevated tissue temperatures could be determined through co-operation with a medical team.

- For delivering power to a high-power medical implant described in Chapter 4, a three-coil system could combine both the benefits of the short range scenario with the smaller body-worn transmitter coil acting as a relay and the longer-range scenario with a larger transmitter coil attached to furniture. The design of the implanted receiver coil could be optimised, in terms of electromagnetic characteristics (coil Q improvements, use of ferrite materials) and thermal properties (coating thickness, encapsulation, choice of materials). A greater implant depth could be explored where the receiver coil could be placed inside the chest cavity (i.e. attached to the LVAD itself); heating issues would need to be investigated due to the greater distance of human tissue through which the high-frequency magnetic field passes.

- For the long range inductive power transfer system in Chapter 6, future work to improve the present system could include incorporating the data transfer within the same 3 MHz inductive link used for power, instead of having a separate 433 MHz frequency-shift keyring (FSK) RF wireless data link. Otherwise, the data link could be optimised further, such as by increasing the baud rate and data rate. In addition, the receiver power electronics (including the impedance emulator) could be optimised and miniaturised, to increase efficiency and reduce their size and weight.

Lastly, improvements could be made to the secondary coil in order to increase its Q factor per unit volume.

- In terms of the detection of living objects with a high-frequency magnetic field, the use of a multiple coil array to increase the degrees of freedom should be investigated in order to implement object localisation and tracking. A dynamic system applied to a network of drones could be implemented, where wirelessly-powered drones fly over collapsed buildings, and use magnetic fields to search for trapped objects. Foreign object detection for wireless power transfer systems could also be considered for safety reasons; such technology is particularly desirable for applications such as electric vehicle charging.

References

[1] K. V. Schuylenbergh and R. Puers, *Inductive Powering: Basic Theory and Application to Biomedical Systems*. Springer Publishing Company, Incorporated, 1st ed., 2009.

[2] M. Pinuela, D. C. Yates, S. Lucyszyn, and P. D. Mitcheson, "Maximizing dc-to-load efficiency for inductive power transfer," *IEEE Transactions on Power Electronics*, vol. 28, pp. 2437–2447, May 2013.

[3] C. H. Kwan, G. Kkelis, S. Aldhaher, J. Lawson, D. C. Yates, P. C. K. Luk, and P. D. Mitcheson, "Link efficiency-led design of mid-range inductive power transfer systems," in *2015 IEEE PELS Workshop on Emerging Technologies: Wireless Power (2015 WoW)*, pp. 1–7, June 2015.

[4] D. C. Ng, S. Bai, J. Yang, N. Tran, and E. Skafidas, "Wireless technologies for closed-loop retinal prostheses," *Journal of Neural Engineering*, vol. 6, p. 065004, oct 2009.

[5] B. H. Waters, J. R. Smith, and P. Bonde, "Innovative free-range resonant electrical energy delivery system (free-d system) for a ventricular assist device using wireless power," *ASAIO Journal (American Society for Artificial Internal Organs)*, vol. 60, pp. 31–37, Jan-Feb 2014.

[6] K. N. Bocan and E. Sejdić, "Adaptive transcutaneous power transfer to implantable devices: A state of the art review," *Sensors*, vol. 16, no. 3, 2016.

[7] C. Watkins, B. Shen, and R. Venkatasubramanian, "Low-grade-heat energy harvesting using superlattice thermoelectrics for applications in implantable medical devices and sensors," in *ICT 2005. 24th International Conference on Thermoelectrics, 2005.*, pp. 265–267, June 2005.

[8] Y. Hu and M. Sawan, "A fully integrated low-power bpsk demodulator for implantable medical devices," *IEEE Transactions on Circuits and Systems I: Regular Papers*, vol. 52, pp. 2552–2562, Dec 2005.

[9] B. Smith, Z. Tang, M. W. Johnson, S. Pourmehdi, M. M. Gazdik, J. R. Buckett, and P. H. Peckham, "An externally powered, multichannel, implantable stimulator-telemeter for control of paralyzed muscle," *IEEE Transactions on Biomedical Engineering*, vol. 45, pp. 463–475, April 1998.

[10] Q. Huang and M. Oberle, "A 0.5-mw passive telemetry ic for biomedical applications," *IEEE Journal of Solid-State Circuits*, vol. 33, pp. 937–946, Jul 1998.

[11] M. Piedade, J. Gerald, L. A. Sousa, G. Tavares, and P. Tomas, "Visual neuroprosthesis: a non invasive system for stimulating the cortex," *IEEE Transactions on Circuits and Systems I: Regular Papers*, vol. 52, pp. 2648–2662, Dec 2005.

[12] W. Liu, K. Vichienchom, M. Clements, S. C. DeMarco, C. Hughes, E. McGucken, M. S. Humayun, E. D. Juan, J. D. Weiland, and R. Greenberg, "A neuro-stimulus chip with telemetry unit for retinal prosthetic device," *IEEE Journal of Solid-State Circuits*, vol. 35, pp. 1487–1497, Oct 2000.

[13] T. Akin, K. Najafi, and R. M. Bradley, "A wireless implantable multichannel digital neural recording system for a micromachined sieve electrode," *IEEE Journal of Solid-State Circuits*, vol. 33, pp. 109–118, Jan 1998.

[14] H. Yu and K. Najafi, "Low-power interface circuits for bio-implantable microsystems," in *2003 IEEE International Solid-State Circuits Conference, 2003. Digest of Technical Papers. ISSCC.*, pp. 194–487 vol.1, Feb 2003.

[15] U. M. Jow and M. Ghovanloo, "Design and optimization of printed spiral coils for efficient transcutaneous inductive power transmission," *IEEE Transactions on Biomedical Circuits and Systems*, vol. 1, pp. 193–202, Sept 2007.

[16] U. M. Jow and M. Ghovanloo, "Modeling and optimization of printed spiral coils in air, saline, and muscle tissue environments," *IEEE Transactions on Biomedical Circuits and Systems*, vol. 3, pp. 339–347, Oct 2009.

[17] M. Zargham and P. G. Gulak, "Fully integrated on-chip coil in 0.13 *murmm* cmos for wireless power transfer through biological media," *IEEE Transactions on Biomedical Circuits and Systems*, vol. 9, pp. 259–271, April 2015.

[18] A. K. RamRakhyani, S. Mirabbasi, and M. Chiao, "Design and optimization of resonance-based efficient wireless power delivery systems for biomedical implants," *IEEE Transactions on Biomedical Circuits and Systems*, vol. 5, pp. 48–63, Feb 2011.

[19] M. Zargham and P. G. Gulak, "Maximum achievable efficiency in near-field coupled power-transfer systems," *IEEE Transactions on Biomedical Circuits and Systems*, vol. 6, pp. 228–245, June 2012.

[20] D. Ahn and M. Ghovanloo, "Optimal design of wireless power transmission links for millimeter-sized biomedical implants," *IEEE Transactions on Biomedical Circuits and Systems*, vol. 10, pp. 125–137, Feb 2016.

[21] E. J. Molina and S. W. Boyce, "Current status of left ventricular assist device technology," *Semin. Thorac. Cardiovasc. Surg.*, vol. 25, no. 1, pp. 56–63, 2013.

[22] G. Gerosa, S. Scuri, L. Iop, and G. Torregrossa, "Present and future perspectives on total artificial hearts," *Ann Cardiothorac Surg*, vol. 3, pp. 595–602, Nov 2014.

[23] "Heartmate II® LVAS Operating Manual." `http://www.thoratec.com/_assets/download-tracker/HM%20II%20Op%20Man%20_EU_%20103878E_ENGLISH.pdf`, April 2015.

[24] M. S. Slaughter and T. J. Myers, "Transcutaneous energy transmission for mechanical circulatory support systems: History, current status, and future prospects," *Journal of Cardiac Surgery*, vol. 25, no. 4, pp. 484–489, 2010.

[25] J. X. Wang, J. R. Smith, and P. Bonde, "Energy transmission and power sources for mechanical circulatory support devices to achieve total implantability," *Ann. Thorac. Surg.*, vol. 97, pp. 1467–1474, Apr 2014.

[26] B. H. Waters, A. P. Sample, P. Bonde, and J. R. Smith, "Powering a ventricular assist device (vad) with the free-range resonant electrical energy delivery (free-d) system," *Proceedings of the IEEE*, vol. 100, pp. 138–149, Jan 2012.

[27] B. Waters, A. Sample, J. Smith, and P. Bonde, "Toward total implantability using free-range resonant electrical energy delivery system: Achieving untethered ventricular assist device operation over large distances," *Cardiology Clinics*, vol. 29, no. 4, pp. 609 – 625, 2011. Left Ventricular Assist Devices.

[28] T. D. Dissanayake, D. M. Budgett, P. Hu, L. Bennet, S. Pyner, L. Booth, S. Amirapu, Y. Wu, and S. C. Malpas, "A novel low temperature transcutaneous energy transfer system suitable for high power implantable medical devices: Performance and validation in sheep," *Artificial Organs*, vol. 34, no. 5, pp. E160–E167, 2010.

[29] T. D. Dissanayake, A. P. Hu, S. Malpas, L. Bennet, A. Taberner, L. Booth, and D. Budgett, "Experimental study of a tet system for implantable biomedical devices," *IEEE Transactions on Biomedical Circuits and Systems*, vol. 3, pp. 370–378, Dec 2009.

[30] E. Okamoto, Y. Yamamoto, Y. Akasaka, T. Motomura, Y. Mitamura, and Y. Nosé, "A new transcutaneous energy transmission system with hybrid energy coils for driving an implantable biventricular assist device," *Artificial Organs*, vol. 33, no. 8, pp. 622–626, 2009.

[31] S. Nagato, W. Hijikata, and T. Shinshi, "Evaluation of a transcutaneous energy transmission system with a flexible coil for an implantable ventricular assist device," in *2017 IEEE Wireless Power Transfer Conference (WPTC)*, pp. 1–3, May 2017.

[32] D.-W. Seo, J.-H. Lee, and H. S. Lee, "Study on two-coil and four-coil wireless power transfer systems using z-parameter approach," *ETRI Journal*, vol. 38, no. 3, pp. 568–578.

[33] J. C. Lin, C. C. Johnson, and A. W. Guy, "Power deposition in a spherical model of man exposed to 1-20 mhz em fields," in *1973 IEEE G-MTT International Microwave Symposium*, pp. 257–259, June 1973.

[34] P. J. Dimbylow, "Fdtd calculations of the whole-body averaged sar in an anatomically realistic voxel model of the human body from 1 mhz to 1 ghz," *Physics in Medicine & Biology*, vol. 42, no. 3, p. 479, 1997.

[35] P. Dimbylow, "Development of the female voxel phantom, naomi, and its application to calculations of induced current densities and electric fields from applied low frequency magnetic and electric fields," *Physics in Medicine & Biology*, vol. 50, no. 6, p. 1047, 2005.

[36] L. Lucke and V. Bluvshtein, "Safety considerations for wireless delivery of continuous power to implanted medical devices," in *2014 36th Annual International Conference of the IEEE Engineering in Medicine and Biology Society*, pp. 286–289, Aug 2014.

[37] V. Bluvshtein and L. Lucke, "Safe wireless power design for implanted medical devices1," *Journal of Medical Devices*, vol. 8, p. 020917, apr 2014.

[38] X. Shi, B. H. Waters, and J. R. Smith, "Sar distribution for a strongly coupled resonant wireless power transfer system," in *2015 IEEE Wireless Power Transfer Conference (WPTC)*, pp. 1–4, May 2015.

[39] A. Christ, M. G. Douglas, J. M. Roman, E. B. Cooper, A. P. Sample, B. H. Waters, J. R. Smith, and N. Kuster, "Evaluation of wireless resonant power transfer systems

with human electromagnetic exposure limits," *IEEE Transactions on Electromagnetic Compatibility*, vol. 55, pp. 265–274, April 2013.

[40] H. J. Visser, "Aspects of far-field rf energy transport," in *2012 42nd European Microwave Conference*, pp. 317–320, Oct 2012.

[41] M. Piñuela, P. D. Mitcheson, and S. Lucyszyn, "Ambient rf energy harvesting in urban and semi-urban environments," *IEEE Transactions on Microwave Theory and Techniques*, vol. 61, pp. 2715–2726, July 2013.

[42] J. Lawson, M. Pinuela, D. C. Yates, S. Lucyszyn, and P. D. Mitcheson, "Long range inductive power transfer system," *Journal of Physics: Conference Series*, vol. 476, no. 1, p. 012005, 2013.

[43] S. Ramo, J. R. Whinnery, and T. Van Duzer, *Fields and waves in communication electronics*. New York: Wiley, 3rd ed. ed., 1994. Previous ed.: 1984.

[44] F. Terman, *Radio engineer's handbook*. McGraw-Hill Book Company, inc., 1943.

[45] S. S. Mohan, M. del Mar Hershenson, S. P. Boyd, and T. H. Lee, "Simple accurate expressions for planar spiral inductances," *IEEE Journal of Solid-State Circuits*, vol. 34, pp. 1419–1424, Oct 1999.

[46] C. Balanis, *Antenna Theory: Analysis and Design*. Wiley, 2016.

[47] D. M. Beams and S. G. Annam, "Calculation of mutual inductance from magnetic vector potential for wireless power transfer applications," in *Proceedings of the 2012 44th Southeastern Symposium on System Theory (SSST)*, pp. 209–213, March 2012.

[48] G. Kkelis, D. C. Yates, and P. D. Mitcheson, "Comparison of current driven class-d and class-e half-wave rectifiers for 6.78 mhz high power ipt applications," in *2015 IEEE Wireless Power Transfer Conference (WPTC)*, pp. 1–4, May 2015.

[49] D. C. Yates, A. S. Holmes, and A. J. Burdett, "Optimal transmission frequency for ultralow-power short-range radio links," *IEEE Transactions on Circuits and Systems I: Regular Papers*, vol. 51, pp. 1405–1413, July 2004.

[50] "IXYS RF IXZ4DF12N100 RF Power MOSFET & DRIVER." http://ixapps.ixys.com/Datasheet/ixz4df12n100.pdf, January 2015.

[51] "International Rectifier IRFB812PbF HEXFET® Power MOSFET." http://www.irf.com/product-info/datasheets/data/irfb812pbf.pdf, January 2015.

[52] "C3d10170h - silicon carbide schottky diode." https://www.wolfspeed.com/media/downloads/96/C3D10170H.pdf, January 2015.

[53] S. Aldhaher, P. C. K. Luk, and J. F. Whidborne, "Tuning class e inverters applied in inductive links using saturable reactors," *IEEE Transactions on Power Electronics*, vol. 29, pp. 2969–2978, June 2014.

[54] Z. Kaczmarczyk, "High-efficiency class e,$hboxef_2$, and$hboxe/f_3$inverters," *IEEE Transactions on Industrial Electronics*, vol. 53, pp. 1584–1593, Oct 2006.

[55] S. D. Kee, I. Aoki, A. Hajimiri, and D. Rutledge, "The class-e/f family of zvs switching amplifiers," *IEEE Transactions on Microwave Theory and Techniques*, vol. 51, pp. 1677–1690, June 2003.

[56] S. Aldhaher, G. Kkelis, D. C. Yates, and P. D. Mitcheson, "Class ef2 inverters for wireless power transfer applications," in *2015 IEEE Wireless Power Transfer Conference (WPTC)*, pp. 1–4, May 2015.

[57] G. Kkelis, J. Lawson, D. C. Yates, M. Pinuela, and P. D. Mitcheson, "Integration of a class-e low dv/dt rectifer in a wireless power transfer system," in *2014 IEEE Wireless Power Transfer Conference*, pp. 72–75, May 2014.

[58] A. Ivascu, M. K. Kazimierczuk, and S. Birca-Galateanu, "Class e resonant low dv/dt rectifier," *IEEE Transactions on Circuits and Systems I: Fundamental Theory and Applications*, vol. 39, pp. 604–613, Aug 1992.

[59] C. H. Kwan, J. Lawson, D. C. Yates, and P. D. Mitcheson, "Position-insensitive long range inductive power transfer," *Journal of Physics: Conference Series*, vol. 557, no. 1, p. 012053, 2014.

[60] T. E. Parliament and the Council of the European Union, "Directive 2013/35/EU," *Official Journal of the European Union*, vol. 53, pp. 1–21, June 2013.

[61] I. C. on Non-Ionizing Radiation Protection, "Guidelines for limiting exposure to time-varying electric, magnetic, and electromagnetic fields (up to 300 GHz)," *Health Physics*, vol. 74, no. 4, pp. 494–522, 1998.

[62] I. C. on Non-Ionizing Radiation Protection, "Guidelines for limiting exposure to time-varying electric and magnetic fields (1 Hz to 100 kHz)," *Health Physics*, vol. 99, no. 6, pp. 818–836, 2010.

[63] "Ieee standard for safety levels with respect to human exposure to radio frequency electromagnetic fields, 3 khz to 300 ghz," *IEEE Std C95.1-2005 (Revision of IEEE Std C95.1-1991)*, pp. 1–238, April 2006.

[64] T. C. of the European Communities, "Directive 90/385/EEC," *Official Journal of the European Communities*, vol. 33, pp. 17–36, July 1990.

[65] *BS EN 45502-1:2015 - Implants for surgery. Active implantable medical devices. General requirements for safety, marking and for information to be provided by the manufacturer*. June 2015.

[66] T. C. of the European Union, "Recommendation 1999/519/EC," *Official Journal of the European Communities*, vol. 42, pp. 59–70, July 1999.

[67] "Simplify scanning of patients with mr conditional implants." `https://www.usa.philips.com/c-dam/b2bhc/master/events/ISMRM2016/philips-scanwise-implant-whitepaper.pdf`, April 2016.

[68] "Safety guildlines for magnetic resonance imaging equipment in clinical use." `https://assets.publishing.service.gov.uk/government/uploads/system/uploads/attachment_data/file/476931/MRI_guidance_2015_-_4-02d1.pdf`, March 2015.

[69] D. W. McRobbie, E. A. Moore, M. J. Graves, and M. R. Prince, *MRI from Picture to Proton*. Cambridge University Press, 2 ed., 2006.

[70] *BS EN 60601-2-33:2010+A12:2016 - Medical electrical equipment. Particular requirements for the basic safety and essential performance of magnetic resonance equipment for medical diagnosis*. 2010.

[71] *PD ISO/TS 10974:2018 - Assessment of the safety of magnetic resonance imaging for patients with an active implantable medical device*. 2018.

[72] G. Kkelis, S. Aldhaher, J. M. Arteaga, D. C. Yates, and P. D. Mitcheson, "Hybrid class-e synchronous rectifier for wireless powering of quadcopters," in *2017 IEEE Wireless Power Transfer Conference (WPTC)*, pp. 1–4, May 2017.

[73] S. Aldhaher, P. D. Mitcheson, J. M. Arteaga, G. Kkelis, and D. C. Yates, "Light-weight wireless power transfer for mid-air charging of drones," in *2017 11th European Conference on Antennas and Propagation (EUCAP)*, pp. 336–340, March 2017.

[74] C. H. Kwan, D. C. Yates, and P. D. Mitcheson, "Design objectives and power limitations of human implantable wireless power transfer systems," in *2016 IEEE Wireless Power Transfer Conference (WPTC)*, pp. 1–4, May 2016.

[75] D. Pozar, *Microwave Engineering, 4th Edition*. Wiley, 2011.

[76] "CST Studio Suite 2017 Help Documentation."

[77] S. Gabriel, R. W. Lau, and C. Gabriel, "The dielectric properties of biological tissues: Iii. parametric models for the dielectric spectrum of tissues," *Physics in Medicine & Biology*, vol. 41, no. 11, p. 2271, 1996.

[78] J. Mark, *Polymer Data Handbook*. Oxford University Press, 1999.

[79] Y. Kurazumi, T. Tsuchikawa, J. Ishii, K. Fukagawa, Y. Yamato, and N. Matsubara, "Radiative and convective heat transfer coefficients of the human body in natural convection," *Building and Environment*, vol. 43, no. 12, pp. 2142 – 2153, 2008.

[80] Y. P. Su, X. Liu, and S. Y. R. Hui, "Mutual inductance calculation of movable planar coils on parallel surfaces," *IEEE Transactions on Power Electronics*, vol. 24, pp. 1115–1123, April 2009.

[81] "Surface mount multilayer ceramic capacitors for rf power applications." `https://www.vishay.com/docs/45221/quadhifreq.pdf`, July 2017.

[82] S. Aldhaher, P. D. Mitcheson, and D. C. Yates, "Load-independent class ef inverters for inductive wireless power transfer," in *2016 IEEE Wireless Power Transfer Conference (WPTC)*, pp. 1–4, May 2016.

[83] G. Pollack and D. Stump, *Electromagnetism*. Addison Wesley, 2002.

[84] "An internet resource for the calculation of the dielectric properties of body tissues in the frequency range 10 hz - 100 ghz." `http://niremf.ifac.cnr.it/tissprop/`, February 2015.

[85] *Standard Methods for the Examination of Water and Wastewater. – 20th Edition/ Prepared and Published Jointly by American Public Health Association, American Water Works Association, Water Environment Federation*. AWWA, 1999.

[86] K. Nörtemann, J. Hilland, and U. Kaatze, "Dielectric properties of aqueous nacl solutions at microwave frequencies," *The Journal of Physical Chemistry A*, vol. 101, no. 37, pp. 6864–6869, 1997.

[87] S. Prabhakaran and C. R. Sullivan, "Impedance-analyzer measurements of high-frequency power passives: techniques for high power and low impedance," in *Conference Record of the 2002 IEEE Industry Applications Conference. 37th IAS Annual Meeting (Cat. No.02CH37344)*, vol. 2, pp. 1360–1367 vol.2, Oct 2002.

[88] J. M. Arteaga, S. Aldhaher, G. Kkelis, D. C. Yates, and P. D. Mitcheson, "Design of a 13.56 mhz ipt system optimised for dynamic wireless charging environments," in *2016 IEEE 2nd Annual Southern Power Electronics Conference (SPEC)*, pp. 1–6, Dec 2016.

[89] M. Kazimierczuk and D. Czarkowski, *Resonant Power Converters*. Wiley, 2012.

[90] "Electrolube - flexible silicone coating: Technical data sheet." `https://www.electrolube.com/core/components/products/tds/044/FSC.pdf`, July 2017.

[91] F. Raab, "Idealized operation of the class e tuned power amplifier," *IEEE Transactions on Circuits and Systems*, vol. 24, pp. 725–735, December 1977.

[92] R. Erickson and D. Maksimovic, *Fundamentals of Power Electronics*. Power electronics, Springer US, 2001.

[93] R. D'hulst, P. D. Mitcheson, and J. Driesen, "Cmos buck-boost power processing circuitry for powermems generators," in *Proceedings of PowerMEMS 2006*, pp. 215–218, Nov 2006.

[94] T. S. Paing and R. Zane, "Resistor emulation approach to low-power energy harvesting," in *2006 37th IEEE Power Electronics Specialists Conference*, pp. 1–7, June 2006.

[95] R. Erickson, M. Madigan, and S. Singer, "Design of a simple high-power-factor rectifier based on the flyback converter," in *Fifth Annual Proceedings on Applied Power Electronics Conference and Exposition*, pp. 792–801, March 1990.

[96] "Hi-q high rf power mlc surface mount capacitors." `http://datasheets.avx.com/HQ-Series.pdf`, January 2014.

[97] "Bav16w/1n4148w surface mount fast switching diode." `https://www.diodes.com/assets/Datasheets/ds30086.pdf`, January 2014.

[98] "Bat46w small signal schottky diode." `https://www.vishay.com/docs/85663/bat46wv.pdf`, January 2014.

[99] "Professional plastics: Electrical properties of plastic materials." `https://www.professionalplastics.com/professionalplastics/ElectricalPropertiesofPlastics.pdf`, February 2015.

[100] J. A. Miller, G. Belanger, and T. Mussivand, "Development of an autotuned transcutaneous energy transfer system," *ASAIO J.*, vol. 39, no. 3, pp. M706–710, 1993.

[101] Q. Chen, S. C. Wong, C. K. Tse, and X. Ruan, "Analysis, design, and control of a transcutaneous power regulator for artificial hearts," *IEEE Transactions on Biomedical Circuits and Systems*, vol. 3, pp. 23–31, Feb 2009.

[102] H. Miura, S. Arai, Y. Kakubari, F. Sato, H. Matsuki, and T. Sato, "Improvement of the transcutaneous energy transmission system utilizing ferrite cored coils for artificial hearts," *IEEE Transactions on Magnetics*, vol. 42, pp. 3578–3580, Oct 2006.

[103] S. C. Tang, T. L. T. Lun, Z. Guo, K. Kwok, and N. J. McDannold, "Intermediate range wireless power transfer with segmented coil transmitters for implantable heart pumps," *IEEE Transactions on Power Electronics*, vol. 32, pp. 3844–3857, May 2017.